Structural and Electrical Investigations of Tungsten-Bronze Ferroelectric Ceramics

A thesis submitted

by

Prasun Ganguly

In fulfillment of the requirements
for the award of the degree of

Doctor of Philosophy

to the

University of Delhi
Delhi, India

DEDICATED TO.....

MY FAMILY

CERTIFICATE

This is to certify that the thesis entitled '**Structural and Electrical Investigations of Tungsten-Bronze Ferroelectric Ceramics**' being submitted by **Mr. Prasun Ganguly** to the **Faculty of Technology, University of Delhi, India** for the award of the degree of the **Doctor of Philosophy** is a record of bonafide research carried out by him. He has worked under our guidance and supervision, and has fulfilled the requirements for the submission of this thesis, which in our opinion has reached the requisite standard.

The results contained herein have not been submitted in part or full to any other university or institution for the award of any degree or diploma.

(Prof. K. L. Deori)
Formerly Professor and Head
Department of Applied Physics
Delhi College of Engineering
University of Delhi
Delhi – 110042, India

(Dr. A. K. Jha)
Assistant Professor
Department of Applied Physics
Delhi College of Engineering
University of Delhi
Delhi – 110042, India

(Prof. A. Trivedi)
Head, Department of Applied Sciences & Humanities
Delhi College of Engineering
University of Delhi
Delhi – 110042, India

Acknowledgements

This journey of my research is accomplished with the valuable support of many people. I take a great pleasure in expressing my heartfelt gratitude to my supervisors Prof. K. L. Deori and Dr. A. K. Jha for their immense support and guidance throughout the whole process of the research work and successful completion of this thesis.

I am extremely grateful to Prof. K. L. Deori who has provided me constant motivation and competent advice in my academic quest.

I am truly obliged to Dr. A. K. Jha who was my mentor throughout this journey. He took great care and keen interest to revise each work meticulously and gave valuable suggestions. He has been my support system in carrying out the research work. It is my strong belief that without their guidance and appropriate direction my thesis would never have been complete.

I am thankful to Prof. A. Trivedi, Dean, Faculty of Technology, University of Delhi and Prof. P. B. Sharma, Director, Delhi College of Engineering for their generous support and providing ample infrastructure to carry out the research work.

I would also like to convey my extreme thanks to all the faculty members and technical staff of Department of Applied Physics for their support.

I would like to extend my thankfulness to Dr. A. K. Bandyopadhyay and Dr. Nita Dilawar, NPL, New Delhi who helped me to conduct Raman study on my samples.

I am also gratified towards Council of Scientific and Industrial Research (CSIR), New Delhi, for providing the financial support to carry out the research work.

My colleagues, associates and friends continuously influenced me in a positive way and have an important impact on my thinking. I will always remain grateful to them for their selfless support. I think myself to be fortunate to get friends like Sameer, Sheela, Sugandha, Priyanka and Neelam.

Last but not the least, my parents, pimi, wife, sister, brother-in-law, parents-in-law, all my relatives and well-wishers, have always motivated me and have been by my side in every difficult situation. I am highly indebted towards my parents who have sacrificed endlessly to make this thesis a success. I treasure my beloved wife's support for her unconditional love and having faith in me.

Above all I am thankful to the Almighty my Gurudev and Ranima for their bountiful blessings which have made me competent to face every situation in life with courage and determination.

(Prasun Ganguly)

Abstract

Pyroelectric crystals possess the unusual characteristic of being permanently polarized within a given temperature range. Unlike piezoelectric materials which undergo polarization under stress, the pyroelectric materials are polarized spontaneously and form permanent dipoles in the structure. This polarization also changes with temperature, hence, the term pyroelectricity. A subgroup of the spontaneously polarized pyroelectrics is a very special category of materials known as ferroelectrics. Similar to pyroelectrics, materials in this group are spontaneously polarized and possess spontaneous dipoles. However, unlike pyroelectrics, these dipoles are reversible by an electric field smaller than the dielectric breakdown of the material. Thus, the two conditions necessary in a material to classify it as a ferroelectric are:-

(i) the existence of spontaneous polarization and

(ii) the ability to reverse the direction of polarization.

Ferroelectricity was discovered in single-crystal materials (i.e. in Rochelle Salt $KNaC_4H_4O_6.4H_2O$) in 1921 and then in polycrystalline ceramics (i.e. in Barium Titanate $BaTiO_3$) during the early to mid-1940s. Thereafter, large number of new materials have been discovered which show ferroelectricity that leads to significant number of industrial and commercial applications. The prominent properties of ferroelectric materials such as polarization hysteresis, large dielectric constant and remarkable piezoelectric, pyroelectric and electro-optical effects makes it useful for a number of electronic devices like small size high

capacitance capacitors, piezoelectric sonar, pyroelectric security surveillance devices, medical diagnostic transducers, electrooptic light valves, ferroelectric memories, etc. Because of all these important applications, the field of ferroelectric materials is ever expanding. In this general group of ferroelectric materials, based on the basic structure, the following four types of ceramic ferroelectrics are known:-

(i) the Tungsten-Bronze group

(ii) the Perovskites group

(iii) the Pyrochlore group

(iv) the Bismuth Layer-Structured group.

Of these, the Tungsten-Bronze structure ferroelectrics are a large class of technically important materials. These materials belong to an important family of dielectric materials, which display interesting ferroelectric, pyroelectric, piezoelectric and nonlinear optic properties for applications in various electronic devices, such as transducers, actuators, capacitors and ferroelectric random access memory.

Tungsten Bronze Ferroelectric Ceramic

The Tungsten Bronze (TB)-type structure having a general formula $(A_1)_4(A_2)_2(C)_4(B_1)_2(B_2)_8O_{30}$ consists of a complex array of distorted BO_6 octahedra sharing corners in such a way that three different types of interstices (i.e. A, B and C) are available for cation substitutions in which a wide variety of substitutions can be made for different applications. It is interesting to observe that some compounds of this family, such as $K_2LaNb_5O_{15}$, $Ba_4NaNb_{10}O_{30}$, $Ba_5RTi_3Nb_7O_{30}$ (R = rare earth ions) and $Ba_5YTi_{3-x}Zr_xNb_7O_{30}$ (x = 0, 1, 2, 3), show

diffuse phase transition and relaxor behaviour. It is now a well – known fact that there is a drastic change in some physical properties of materials on suitable substitutions at different atomic sites of TB structure. After extensive literature survey it was felt that although some work has been reported for both A- as well as B- site substitutions in this TB- structure but a comprehensive study of the changes in physical properties due to systematic substitution at the A-site of these materials is lacking.

With this background in mind, systematic A-site substitution in TB-structured BaO-R_2O_3-TiO_2-Nb_2O_5 (R = Rare Earth) quaternary systems was undertaken. The chemical formulas for the different studied compositions are:

Series 1 $Ba_{5-x}Ca_xSmTi_3Nb_7O_{30}$; x = 0 to 5

Series 2 $Ba_5RTi_3Nb_7O_{30}$; R = La, Nd, Sm, Eu, Dy

Series 3 $CaBa_4RTi_3Nb_7O_{30}$; R = La, Nd, Sm, Eu, Dy

All the samples were prepared by solid state reaction method at the optimized sintering condition of 1300 ºC for 10 hours and studied for their structural, dielectric, ferroelectric, piezoelectric, pyroelectric, ac and dc conductivity, impedance and modulus properties. Also $Ba_5SmTi_3Nb_7O_{30}$ have been prepared by Micowave sintering and Mechanical Activation technique by using ball-mill and its properties is compared with that obtained from conventional solid-state reaction method.

Contents

Chapter 2: Experimental Details

Chapter 3: $Ba_5SmTi_3Nb_7O_{30}$: Optimization of Preparation Conditions

Chapter 6: Synthesis by Some Novel Techniques

List of Figures

List of Tables

List of Publications

In International Journals

1. Investigations of structural, dielectric and electrical behaviour of calcium substituted $Ba_5NdTi_3Nb_7O_{30}$ ferroelectric ceramics
   Prasun Ganguly and A. K. Jha
   Integrated Ferroelectrics (In Press).

2. Impedance-spectroscopy analysis of $Ba_5NdTi_3Nb_7O_{30}$ ferroelectric ceramic
   Prasun Ganguly and A. K. Jha
   Physica B, Vol. 405, No. 15, pages 3154–3158, 2010.

3. Structural and electrical properties of $Ba_{5-x}Ca_xSmTi_3Nb_7O_{30}$ (x = 0-5) ferroelectric ceramics
   Prasun Ganguly and A. K. Jha
   Journal of Alloys and Compounds, Vol. 495, No. 1, pages 7–12, 2010.

4. Investigations of dielectric, pyroelectric and electrical properties of $Ba_5SmTi_3Nb_7O_{30}$ ferroelectric ceramic
   Prasun Ganguly, A. K. Jha and K. L. Deori
   Journal of Alloys and Compounds, Vol. 484, No. 1-2, pages 40–44, 2009.

5. Structural, dielectric and electrical studies of $Ba_{5-x}Ca_xSmTi_3Nb_7O_{30}$ (x = 0, 1) ferroelectric ceramics
   Prasun Ganguly, A. K. Jha and K. L. Deori
   Asian Journal of Chemistry, Vol. 21, No. 10, pages 22-27, 2009.

6. Enhancement of dielectric properties by optimization of sintering condition in tungsten-bronze structured $Ba_5SmTi_3Nb_7O_{30}$ ferroelectric ceramics
   Prasun Ganguly, A. K. Jha and K. L. Deori
   Journal of Electroceramics**,** Vol. 22, No. 1, pages 257-262, 2009.

7. Dielectric and pyroelectric studies of tungsten - bronze structured $Ba_5SmTi_3Nb_7O_{30}$ ferroelectric ceramics
   Prasun Ganguly, Sheela Devi, A. K. Jha and K. L. Deori
   Ferroelectrics, Vol. 381, pages 111–119, 2009.

8. Complex impedance studies of tungsten-bronze structured $Ba_5SmTi_3Nb_7O_{30}$ ferroelectric ceramics
   Prasun Ganguly, A. K. Jha and K. L. Deori,
   Solid State Communications**,** Vol. 146, No. 11-12, pages 472-477, 2008.

In National Journals

9. Structural, dielectric and electrical properties of $CaBa_4SmTi_3Nb_7O_{30}$ ferroelectric ceramic
   Prasun Ganguly and A. K. Jha
   Bulletin of Materials Science (Accepted).

Communicated

1. Structural and electrical properties of $Ba_5LaTi_3Nb_7O_{30}$ ferroelectric ceramic
   Prasun Ganguly and A. K. Jha
   Current Applied Physics.

2. Synthesis and characterization of tungsten–bronze structured nanocrystalline $Ba_5SmTi_3Nb_7O_{30}$ ferroelectric ceramics by high-energy ball milling
   Prasun Ganguly and A. K. Jha
   Journal of the American Ceramic Society.

3. Enhanced characteristics of $Ba_5SmTi_3Nb_7O_{30}$ ferroelectric nanocrystalline ceramic prepared by mechanical activation process: A comparative study
   Prasun Ganguly and A. K. Jha
   Materials Research Bulletin.

In International Conferences

1. Structural and electrical properties of $Ba_5LaTi_3Nb_7O_{30}$ ferroelectric ceramic
   Prasun Ganguly and A. K. Jha
   7^{th} Asian Meeting on Ferroelectricity and 7^{th} Asian Meeting on Electroceramics, June 28 – July 1, 2010, Jeju, Korea.

2. Investigations of structural, dielectric and electrical behaviour of calcium substituted $Ba_5NdTi_3Nb_7O_{30}$ ferroelectric ceramics
   Prasun Ganguly and A. K. Jha
   International Conference on Electroceramics (ICE), December 13-17, 2009, University of Delhi, Delhi.

3. Ferroelectric, pyroelectric and piezoelectric studies in $Ba_5SmTi_3Nb_7O_{30}$ ceramic
   Prasun Ganguly, Sheela Devi, A. K. Jha and K. L. Deori
   12^{th} International Meeting on Ferroelectricity (IMF-12) & 18^{th} IEEE-International Symposium on the Applications of Ferroelectrics (ISAF-18), August 23 -27, 2009, Xi'an, China.

4. Dielectric and pyroelectric studies of tungsten - bronze structured $Ba_5SmTi_3Nb_7O_{30}$ ferroelectric ceramics
   Prasun Ganguly, Sheela Devi, A. K. Jha and K. L. Deori
   6th Asian Meeting on Ferroelectrics, August 2-6, 2008, Taipei, Taiwan.

5. Structural, dielectric and electrical studies of $Ba_5SmTi_3Nb_7O_{30}$ ferroelectric ceramics
   Prasun Ganguly, Sameer Jain, A. K. Jha and K. L. Deori
   17th IEEE International Symposium on Applications of Ferroelectrics – ISAF, February 24-27, 2008, Santa Fe, New Mexico, USA.

6. Investigations of dielectric and electrical properties of tungsten-bronze structured $Ba_5SmTi_3Nb_7O_{30}$ ferroelectric ceramics: Effect of sintering conditions
   Prasun Ganguly, A. K. Jha and K. L. Deori
   10th International Conference on Advanced Materials, October 8-13, 2007, Bangalore, India.

7. Impedance-spectroscopic analysis of $Ba_5SmTi_3Nb_7O_{30}$ ferroelectric ceramics: Effect of sintering conditions
   Prasun Ganguly, A. K. Jha and K. L. Deori
   2nd International Workshop on Smart Materials and Structures, August 29-31, 2007, Kiel, Germany.

8. Enhancement of dielectric properties by optimization of sintering condition in tungsten-bronze structured $Ba_5SmTi_3Nb_7O_{30}$ ferroelectric ceramics
   Prasun Ganguly, A. K. Jha and K. L. Deori
   International Conference on Electroceramics (ICE), July 31- August 3, 2007, Arusha, Tanzania, Africa.

In National Conferences

1. Structural, dielectric and electrical studies of $Ba_{5-x}Ca_xSmTi_3Nb_7O_{30}$ (x = 0, 1) ferroelectric ceramics
   Prasun Ganguly, A. K. Jha and K. L. Deori
   National Conference on Advanced Materials and Radiation Physics (AMRP-2009) March 9-10, 2009, Sant Longowal Institutes of Engineering and Technology, Sangrur, Punjab.

2. Effect of sintering conditions on the electrical properties of $Ba_5SmTi_3Nb_7O_{30}$ ferroelectric ceramics
   Prasun Ganguly, Sheela Devi A. K. Jha and K. L. Deori
   15th National Seminar on Ferroelectrics & Dielectrics-2008 (NSFD-15), November 6-8, 2008, Thapar University, Patiala.

CHAPTER 1

Chapter 1

Introduction

1.1 History

The history of ferroelectrics can be traced back to Rochelle or Siegnette salt (sodium potassium tartrate tetrahydrate, $NaK(C_4H_4O_6).4H_2O$), which was synthesized more than 400 years ago, initially for medicinal purpose. In this material ferroelectric properties were discovered subsequently by Joseph Valasek in 1921 [1]. The new effect discovered by Valasek was a dielectric hysteresis which resembles to a ferromagnetic hysteresis loop. It is to this analogy with ferromagnetism that ferroelectricity owes its name. Before this discovery, ferroelectricity was only a hypothetical property of solid materials at the turn of the 20th century. However, the practical application of this material is largely limited due to its water solubility. It was after the discovery of ferroelectric ceramics that this class of materials became extremely useful for a variety of applications.

The first ferroelectric ceramic material is barium titanate ($BaTiO_3$), which was discovered in the mid-1940s [2-4]. Before the discovery of $BaTiO_3$, the most widely used dielectric materials for capacitors were steatite, mica, TiO_2, $MgTiO_3$ and $CaTiO_3$, with dielectric constant of ≤ 100. During the World War II, there was pressing needs for high dielectric constant materials to fabricate high capacitance capacitors. Before publication was available in the literature, $BaTiO_3$ has already

been studied as a high dielectric constant material concurrently. Shortly thereafter, ferroelectricity was reported in this material by Wul and Goldman in 1945 [5].

The history of ferroelectric ceramics also includes the report of lead zirconate titanate ($PbZr_{1-x}Ti_xO_3$ or PZT) piezoelectric ceramics, the development of transparent electrooptical lead lanthanum zirconate titanate ($Pb_{1-x}La_xZr_{1-y}Ti_yO_3$ or PLZT), the research on lead magnesium niobate ($PbMg_{1/3}Nb_{2/3}O_3$ or PMN) relaxor ferroelectric ceramics and the discovery of many other non-perovskite ferroelectric ceramics [2,4].

1.2 Dielectrics

Dielectrics are insulating materials, in which the electrons are bound to their parent molecules and thus ordinarily do not contain any free charge carriers for conduction [6]. Even with a small applied voltage or thermal energy at normal temperature, electrons are not free for conduction. However, they do contain positive and negative charges, as usual; those are bound together and can be affected by a strong applied electric field. In certain dielectric materials, called polar dielectrics, the constituent atoms are ionized to a certain degree and contain positively or negatively charged ions [7]. Dielectric materials offer a very high resistance to the passage of electric current and therefore differ in their basic electrical properties from conductive materials [8]. An applied electric field produce an electric current in a conducting material while in the case of dielectrics the applied field redistribute the charge without removing it from the vicinity of the individual atoms or molecules [9]. When a sufficient electric field is applied, cations are attracted to the cathode and anions to the anode due to

electrostatic attraction and the electron clouds get deformed forming electric dipoles [7]. A material is said to be polarized when the centres of positive charges do not coincide with that of negative charges and the phenomenon is known as polarization of the dielectric. Since in general, dielectric materials contain both bound and a smaller number of mobile charges, applied electric fields produce both current and polarization.

1.2.1 Dielectric Polarization

1.2.1.1 Macroscopic and microscopic view

The most important property of dielectrics is their ability to get polarized under the action of an external electric field. The phenomenon of polarization leads to the alignment of the dipoles of a dielectric in space and acquires an electric dipole moment **p** [8]. From a macroscopic viewpoint the entire negative charge of the dielectric material is displaced relative to the positive charge and the material is said to be polarized [9].

The state of dielectric acted upon by an electric field can be described by two vector quantities: intensity of the applied electric field ***E*** and polarization ***P***. The magnitude of polarization ***P*** of a dielectric numerically describes the phenomenon of polarization of a dielectric in an external electric field. In the absence of an external electric field each volume element of the dielectric has no electric dipole moment because the algebraic sum of the charges in each molecule of the dielectric is equal to zero [10]. The action of an external electric field forces the charges of the molecules of the dielectric into a certain ordered arrangement in space, as is schematically shown in Fig. 1.1. In such a case each volume

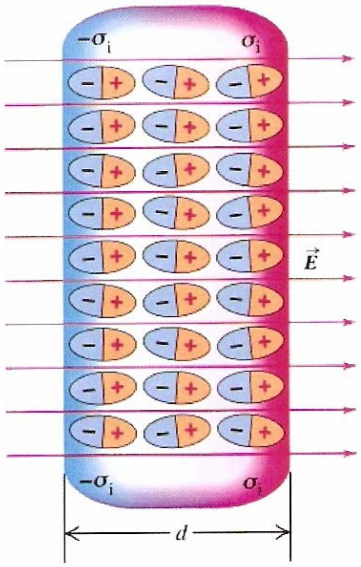

Fig. 1.1 Dielectric polarization

element of dielectric will have an electric moment other than zero and equal to the vector sum $\Sigma \boldsymbol{p}$ of the moments of all the polarized molecules present in this volume element. The polarization $\boldsymbol{P}$ can be expressed quantitatively as the sum of the electric dipole moment per unit volume,

$$\boldsymbol{P} = \frac{\Sigma \boldsymbol{p}}{V} \tag{1.1}$$

Apart from the vector quantities $\boldsymbol{P}$ and $\boldsymbol{E}$ mentioned above, the macroscopic behaviour under static or low frequency conditions, can also be described by another vector quantity – electric displacement vector $\boldsymbol{D}$ [11].

Compared to air-filled capacitors, dielectric capacitors can store more electric charge due to the dielectric polarization $\boldsymbol{P}$. The physical quantity corresponding to the stored electric charge per unit area is called the electric displacement $\boldsymbol{D}$ and is related to the electric field $\boldsymbol{E}$ by the following expressions [11]:

$$\boldsymbol{D} = \varepsilon_r \varepsilon_o \boldsymbol{E} \tag{1.2}$$

$$\boldsymbol{D} = \varepsilon_o \boldsymbol{E} + \boldsymbol{P} \tag{1.3}$$

Comparing Eqs. (1.2) and (1.3), we get the relation between **P** and **E** for an isotropic material as:

$$\boldsymbol{P} = \varepsilon_o (\varepsilon_r - 1) \boldsymbol{E} = \varepsilon_o \chi_e \boldsymbol{E} \tag{1.4}$$

where ε_o is the permittivity of the free-space = 8.854 x 10^{-12} F/m and ε_r the relative permittivity. The quantity (ε_r -1) is termed as the electrical or dielectric susceptibility χ_e.

Permittivity is essentially a macroscopic description of the properties of a dielectric [12]. To understand exactly what is happening in the material when an electric field is applied, we have to link the permittivity to atomic or molecular mechanisms that describe the process of polarization of the material [12]. On the macroscopic scale we use the polarization ***P***, to represent the bound charges at the surface of the material. Polarization reduces the effective electric field inside a material. If the polarizing entities in a solid are close enough to each other, the field component due to induced polarization can help produce dipoles [9]. Strictly, the induced polarization depends on the actual field experienced by the individual molecule that is different from the applied field ***E*** [10]. As depicted in Fig. 1.2, as we move through the dielectric, the field is not constant but its value

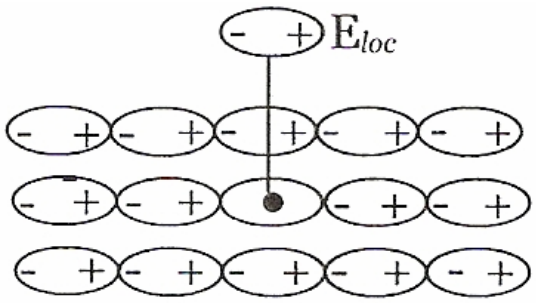

Fig. 1.2 Local electric field inside a polarized dielectric at the atomic scale

depends not only on the charges on the plates but also on the orientations of all the other dipoles around this point in the dielectric.

The actual field experienced by a molecule in a dielectric is the local field $\boldsymbol{E}_{loc}$. The microscopic polarization response, described by direct analogy to Eq. (1.4), is proportional to the $\boldsymbol{E}_{loc}$ at the site of the polarizing entity [9] and is expressed as:

$$\boldsymbol{P} = \varepsilon_o \chi_e \boldsymbol{E}_{loc} \tag{1.5}$$

The simplest case that illustrates this important concept is that of a spherical specimen of a crystal having a simple cubic lattice; the local field $\boldsymbol{E}_{loc}$ acting on a molecule increases with polarization as [10]:

$$\boldsymbol{E}_{loc} = \boldsymbol{E} + \frac{\boldsymbol{P}}{3\varepsilon_0} \tag{1.6}$$

The induced polarization in the molecule now depends on this local field $\boldsymbol{E}_{loc}$ rather than the average or applied field $\boldsymbol{E}$. Thus,

$$p_{induced} = \alpha \boldsymbol{E}_{loc} \tag{1.7}$$

where the constant α is called the polarizability. Thus, the polarizability of an atom is the ratio of the average dipole moment induced in a unit volume of the dielectric to the effective local field. Polarizability reflects the properties of an individual particle of a matter and not of a certain very large volume of it and is the most important microscopic electrical parameter of a dielectric [6]. For a dielectric containing N atoms or molecules per unit volume, the total dipole moment or polarization $\boldsymbol{P}$, is equal to

$$\boldsymbol{P} = \mathrm{N}\alpha\boldsymbol{E}_{loc} \tag{1.8}$$

Using Eqs. (1.4), (1.6), (1.7) and (1.8), we can obtain a relationship between ε_r and α. This is the **Clausius-Mossotti equation** [6,13] expressed as:

$$\frac{\varepsilon_r - 1}{\varepsilon_r + 2} = \frac{N\alpha}{3\varepsilon_0} \tag{1.9}$$

This equation relates a macroscopic quantity relative permittivity or dielectric constant (ε_r) to a microscopic quantity the polarizability (α).

1.2.1.2 Types of polarization

In general, there are four different types of polarization which can contribute to the dielectric response [13]:

(i) **Electronic polarization** occurs in all dielectric materials. It is due to the displacement of the negatively charged electrons with respect to the positively charged core. The electronic polarizability α_e is approximately proportional to the volume of the electron shell [11]. In general α_e is temperature independent and large atoms have a large electronic polarizability.

(ii) **Ionic polarization** is observed in ionic crystals and describes the displacement of the positive and negative ions with respect to each other under an applied electric field.

(iii) **Orientation (or Dipolar) polarization** describes the alignment of permanent dipoles. At ambient temperatures, usually all dipole moments have statistical distributions of their directions [14]. An electric field generates a preferred direction for the dipoles, while the thermal movement of the atoms perturbs the alignment.

(iv) **Space charge polarization** exists in dielectric materials having multiphase structure and which show spatial inhomogeneities of charge carrier densities. In a real crystal there exist a large number of defects such as impurity centres, dislocations and so on. Free charge carriers, migrating through the crystal under the influence of an applied field may be trapped by, or piles near a defect. This results in localized accumulation of charges that induce its image charges on an electrode and give rise to a dipole moment. This is called interfacial or space-charge polarization.

The total polarization of dielectric material results from all the contributions mentioned above. Accordingly, the total polarizability is the sum of individual polarizabilities and is expressed as:

$$\alpha = \alpha_e + \alpha_i + \alpha_o + \alpha_s \tag{1.10}$$

where α represents the total polarizability and α_e, α_i, α_o and α_s are the polarizability of the respective polarization mechanisms; electronic, ionic, orientation and space charge polarizations.

Each contribution stems from a short-range movement of charges that responds to an electric field on different time scales and, hence, through a Fourier transform, in different frequency regimes. If the oscillating masses experience a restoring force, a relaxation behaviour is found (for orientation and space charge polarization). Resonance effects are observed for the ionic and electronic polarization [14].

The space charge polarization is caused by a drift of mobile ions or electrons which are confined to outer or inner interfaces. Depending on the local

conductivity, the space charge polarization may occur at frequencies as low as 100 Hz to 1 kHz [11,15]. However, in certain cases it is known to exceed upto 100 kHz too [11]. The polarization due to the orientation of electric dipoles takes place in the frequency regime upto a few GHz. It is often possible to distinguish between space charge and orientation polarization because of the temperature dependence of α_o. In the infrared region between 1 and 10 THz, resonances of the

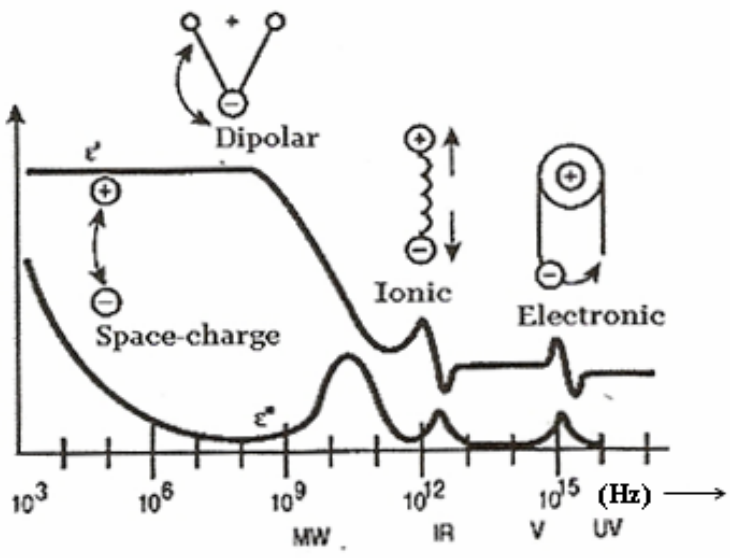

Fig. 1.3 The frequency dependence of the real and imaginary parts of dielectric constant

molecular vibrations and ionic lattices constituting the upper frequency limit of the ionic polarization are observed. The resonance of the electronic polarization is around 10^{15} Hz. It can be investigated by optical methods.

The dispersion of the dielectric response of each type leads to dielectric losses which can mathematically expressed by a complex dielectric permittivity:

$$\varepsilon_r = \varepsilon_r' - j\,\varepsilon_r'' \qquad (1.11)$$

Dielectric losses are usually described by the loss tangent given by

$$\tan \delta = \frac{\varepsilon_r''}{\varepsilon_r'} \tag{1.12}$$

It is worth mentioning that the general definition of the tan δ is related to the ratio of loss energy and reactive energy, i.e. all measurements of the loss tangent also include possible contributions of conductivity σ of a non-ideal dielectric given by

$$\tan \delta = \frac{\sigma}{\omega \varepsilon_0 \varepsilon_r'} \tag{1.13}$$

1.2.2 Classification of dielectrics

The dielectrics can be classified into two classes [8]:

(1) **Polar dielectrics**: Polar dielectrics have molecules inside which the centres of the positive and negative charges do not coincide with each other. They consists of molecules with non-zero dipole moment. They all are of asymmetric shape.

(2) **Non-polar dielectrics:** In case of non-polar dielectrics, centres of both positive as well as negative charges inside the molecule coincide. Dipole moment of each molecule in non-polar system is zero. These molecules are symmetric in nature.

Experimental investigations of polar crystals have demonstrated that they can further be divided into linear and nonlinear dielectrics in accordance with their behaviour in electric fields [16], as discussed below.

(i) **Linear dielectrics**

The "linear" dielectrics are characterized by the fact that their polarization $\boldsymbol{P}$ and electric displacement $\boldsymbol{D}$ are directly proportional to the intensity of the applied electric field $\boldsymbol{E}$ [8],

$$\boldsymbol{D} = \varepsilon_r \varepsilon_o \boldsymbol{E} \quad \text{and}$$
$$\boldsymbol{P} = \varepsilon_o \chi_e \boldsymbol{E} \tag{1.14}$$

Thus, in such substances the permittivity ε and the dielectric susceptibility χ_e do not depend on the intensity of the electric field. Therefore,

$$C = \varepsilon_r \varepsilon_o \frac{A}{d} \tag{1.15}$$

i.e., the capacitance of a capacitor with a linear dielectric does not depend on the voltage V applied to the capacitor while the charge

$$Q = CV \tag{1.16}$$

of the capacitor is directly proportional to the voltage applied to it.

(ii) **Nonlinear dielectrics**

The electric polarization of nonlinear dielectrics is a nonlinear function of the applied electric field. Ferroelectric materials belong to this class of dielectrics.

1.3 Ferroelectricity

The property of certain polar dielectric crystal that exhibit spontaneous electric polarization (i.e. electric polarization in the absence of an external electric field) that can be reversed in direction by the application of an appropriate electric field is termed as *ferroelectricity* [17,18]. Thus, ferroelectrics can be considered as a subclass of polar crystals whose electric dipoles can be reversed in direction by means of an applied electric field.

The ferroelectric properties of a ferroelectric material disappear above a critical temperature called Curie temperature (T_c) where material becomes paraelectric [19]. The phase transition from the ferroelectric to the paraelectric phase is associated with anomalies in the physical properties like specific heat, dielectric constant, spontaneous polarization etc. The ferroelectric structure has a lower crystal symmetry than the paraelectric (nonpolarized) state; thus at the transition temperature a change in the crystal structure is observed [19].

1.3.1 Phenomenology of ferroelectricity

The interpretation of ferroelectric properties is based on one hand on the thermodynamic considerations that is independent of any particular model; on the other hand, theories have been developed on the basis of atomic models. The latter require for their verification detailed studies of the structure of the crystal as a function of temperature [19].

About ten years ago, it was believed that there were two different types of ferroelectric transition mechanism: displacive type and order-disorder type [13]. However, many ferroelectric phenomena cannot be explained unequivocally either by displacive type mechanism or by order-disorder type mechanism [20].

Ferroelectric phase transitions can be described mathematically with some success by Landau theory, often called Landau-Devonshire theory, as a credit to Devonshire, who developed it specifically for the ferroelectric case. An exhaustive description of ferroelectric phase transitions has been given by Strukov and Lavanyuk [20].

Landau Theory of the Phase Transition

Based on the phase transition theory of Landau-Ginzburg [21-23], Devonshire [21,24] developed a phenomenological theory of ferroelectricity by choosing the polarization *P* as order parameter [21]. It is convenient to treat the ferroelectric phase transition by choosing Gibbs function *G* as a state function of the ferroelectric system and the temperature *T* and polarization *P* as independent variables. Since the Gibbs free energy *G* is not changed by reversing the direction of the axes of the space coordinate system and is independent of the direction of the polarization *P*, *G* can be expressed in an even power series of polarization

$$G(T) = G_0 + \frac{1}{2}\alpha(T)^2 + \frac{1}{4}\beta(T)^4 + \frac{1}{6}\gamma(T)^6 + \ldots\ldots\ldots\ldots \quad (1.17)$$

where G_0 is the elastic Gibbs free energy of the system when polarization $P = 0$ and the coefficients $\alpha, \beta, \gamma \ldots\ldots$ are functions of temperature *T*.

A stable state of the thermodynamic system is characterized by a minimum value of the free energy *G*. The conditions for a minimum of *G* are:

$$\frac{\partial G}{\partial P} = 0; \qquad \frac{\partial^2 G}{\partial P^2} \geq 0 \quad \text{or} \quad \frac{\partial E}{\partial P} = \chi^{-1} > 0 \quad (1.18)$$

where χ is susceptibility.

By combining Eqs. (1.17) and (1.18), the equation of state for the ferroelectric system takes the form

$$P(\alpha(T) + \beta(T)P^2 + \gamma(T)P^4) = 0; \quad \beta^2(T) - 4\alpha(T)\gamma(T) > 0 \quad (1.19)$$

$$\chi^{-1} = \alpha(T) + 3\beta(T)P^2 + 5\gamma(T)P^4 > 0 \quad (1.20)$$

Two roots can be found for the left side of Eq. (1.19). The first root $P = 0$ corresponds to a paraelectric phase and the second root $P \neq 0$ to a ferroelectric phase [21].

Paraelectric phase

When $P = 0$, then Eq. (1.20) becomes,

$$\chi^{-1} = \alpha(T) > 0 \tag{1.21}$$

Hence, we see that α must have a positive value when a stable state of the crystal is a paraelectric phase. Expanding $\alpha(T)$ as a Taylor series in $(T\text{-}T_0)$ and taking into account only the first order-term, we have [21],

$$\alpha(T) = \alpha_0 (T - T_0) \tag{1.22}$$

Combining Eqs. (1.21) and (1.22), we obtain

$$\chi = C[4\pi(T - T_0)]^{-1}, \; T > T_0 \tag{1.23}$$

where $C = 4\pi / \alpha$. This is the Curie-Weiss law with C being the Curie-Weiss constant.

Ferroelectric phase

When $P \neq 0$, there are two results corresponding to:

(a) second-order phase transition when $\beta > 0$, and

(b) first-order phase transition when $\beta < 0$.

Second-order phase transition or continuous phase transition ($\beta > 0$)

When β is positive, γ is often neglected [7]. Combining Eqs. (1.18) and (1.23), we get

$$\left(\frac{T - T_0}{\varepsilon_0 C} \right) P + \beta P^3 = 0 \tag{1.24}$$

so that either $P = 0$ or $P^2 = (T\text{-}T_0)/\beta \, \varepsilon_0 \, C$.

For $T > T_0$, the unique solution $P = 0$ is obtained. For $T < T_0$, the minimum of the Landau free energy is obtained at:

$$P = \sqrt{\frac{(T_0 - T)}{\beta \varepsilon_0 C}} \tag{1.25}$$

The phase transition occurs at $T_c = T_0$ and the polarization reduces continuously to zero at this temperature; this is called a second-order transition. The relative permittivity ε is calculated as [7]:

$$\frac{1}{\varepsilon} = \frac{\varepsilon_0}{(\partial P / \partial E)} = \varepsilon_0 (\alpha + 3\beta P^2) \tag{1.26}$$

Then,

$$\varepsilon = \frac{C}{T - T_0} \qquad (T > T_0) \tag{1.27}$$

$$= \frac{C}{2(T - T_0)} \qquad (T < T_0) \tag{1.28}$$

The variation of P and ε with temperature is shown in Fig. 1.4. P is a continuous function of temperature; a transition of this type is associated with a discontinuity in the specific heat. Tri-glycine sulphate (TGS) exhibits a second-order ferroelectric phase transition.

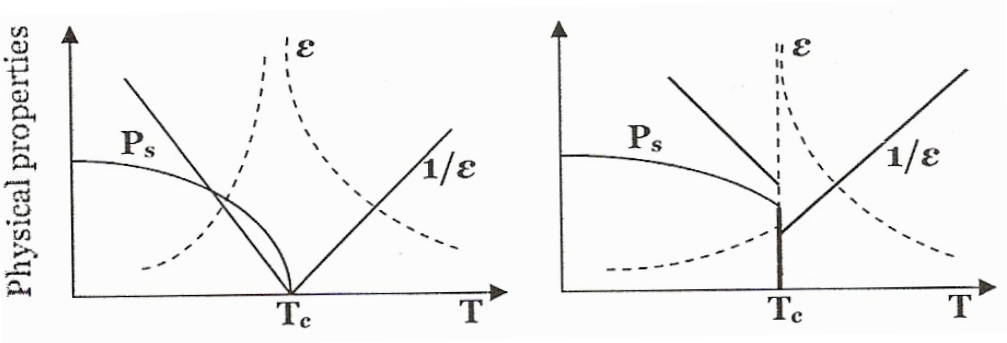

(a) (b)

Fig. 1.4 Variation of P_s and ε with temperature in the case of (a) second order and (b) first order phase transition

First-order phase transition (β < 0)

When β is negative and γ is taken positive, the transition becomes first order. The equilibrium condition gives,

$$\frac{(T-T_0)}{\varepsilon_0 C}P + \beta P^3 + \gamma P^5 = 0 \tag{1.29}$$

This leads to either $P = 0$ or

$$P^2 = \left[-\beta + \sqrt{\frac{\beta^2 - 4\gamma(T-T_0)}{\varepsilon_0 C}}\right]2\gamma \tag{1.30}$$

A transition from the non-polarized to a spontaneously polarized state occurs when the free energies of the paraelectric and ferroelectric phases are equal, i.e., $G = 0$. Therefore, we get

$$T_c = T_0 + \left(\frac{3}{16}\right)\left(\frac{\beta^2 \varepsilon_0 C}{\gamma}\right) \tag{1.31}$$

It is evident that the Curie temperature T_c is slightly higher than the Curie-Weiss temperature T_0 and the polarization shows a discrete jump at the critical temperature from zero to some to non-zero value, as shown in Fig. 1.4. Barium titanate ($BaTiO_3$) is an example of a ferroelectric that undergoes a first-order phase transition.

1.3.2 General properties of ferroelectrics

1.3.2.1 Crystal symmetry

Of the 32 possible crystal classes (i.e. point groups), 11 are centrosymmetric and do not exhibit polar properties [25,26]. The remaining 21 lack a center of symmetry, i.e., they are non-centrosymmetric and therefore posses one or more polar axes. Of these, 20 classes are piezoelectric (the one exception is cubic class

432) (Fig. 1.5). Piezoelectric crystals have the property that the application of mechanical stress induces polarization, and conversely, the application of an electric field produces mechanical deformation. Of the 20 piezoelectric classes, 10 have a unique polar axis and thus are spontaneously polarized, i.e. polarized even in the absence of an externally applied electric field. Crystals belonging to these 10 classes are called pyroelectric because this polarization varies with temperature. Ferroelectric crystals belong to the pyroelectric family. They additionally also exhibit the property that the direction of the spontaneous polarization can be reversed by the application of a suitable electric field. Therefore, materials that can be defined as ferroelectrics must have two characteristics: the presence of spontaneous polarization and reversibility of the polarization under electric field [2,3].

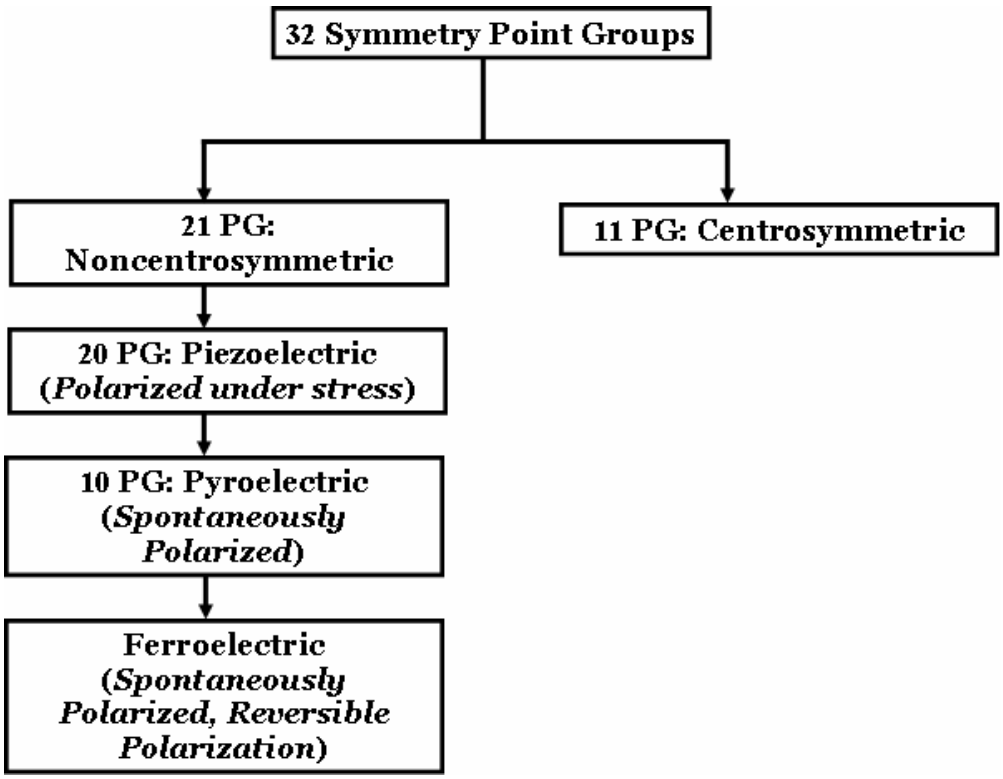

Fig. 1.5 Classification scheme on the basis of crystal symmetry

1.3.2.2 Spontaneous polarization and pyroelectric effect

The spontaneous polarization is given by the value of the dipole moment per unit volume or by the value of the charge per unit area on the surface perpendicular to the axis of spontaneous polarization. The axis of spontaneous polarization is usually along a given crystal axis. Although a crystal with polar axes (20 non-centrosymmetric point groups) shows the piezoelectric effect, it is not necessary for it to have a spontaneous polarization vector. It could be due to the canceling of the electric moments along the different polar axes to give a zero net polarization [27]. Only crystals with a unique polar axis (10 out of 21 non-centrosymmetric point groups) show a spontaneous polarization vector $\boldsymbol{P}_s$ along this axis. When the value of the spontaneous polarization depends on the temperature, this is called the pyroelectric effect which was first discovered in tourmaline by Teophrast in 314 B.C. and so named by Brewster in 1824 [28]. Pyroelectric crystals show a spontaneous polarization $\boldsymbol{P}_s$ in a certain temperature range. If the magnitude and direction of $\boldsymbol{P}_s$ can be reversed by an external electric field, then such crystals are said to show ferroelectric behavior. Hence, all single crystals and poled ceramics which show ferroelectric behavior are pyroelectric, but not vice versa. For example, tourmaline shows pyroelectricity but not ferroelectricity.

1.3.2.3 Ferroelectric domains and hysteresis loop

Ferroelectric crystals possess small regions with unidirectional polarization called ferroelectric domains. Within a domain, all the electric dipoles are aligned in the same direction. There may be many domains in a crystal separated by

interfaces called domain walls. A ferroelectric single crystal, when grown, has multiple ferroelectric domains. A very strong field in opposite direction could lead to the reversal of the polarization in the domain, known as domain switching [29,30].

The main difference between pyroelectric and ferroelectric materials is that the direction of the spontaneous polarization in ferroelectrics can be switched by an applied electric field. The polarization reversal can be observed by measuring the ferroelectric hysteresis as shown in Fig. 1.6. As the electric field strength is increased, the domains start to align in the positive direction giving rise to a rapid increase in the polarization (OB). At very high field levels, the polarization reaches a saturation value (P_{sat}). The polarization do not reduce to zero when the

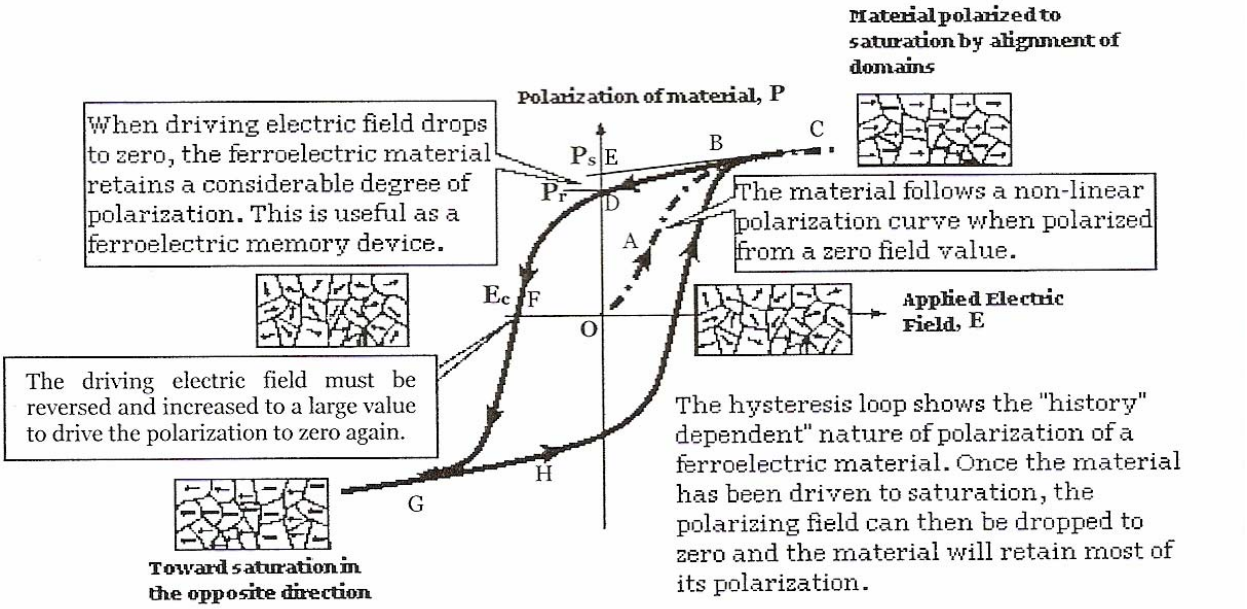

Fig. 1.6 A Polarization vs. Electric Field (P-E) hysteresis loop for a typical ferroelectric crystal

external field is removed. Even after removal of the external field, some of the domains remain aligned in the positive direction; hence the material show a remanent polarization P_r. The crystal do not get completely depolarized until a field of magnitude OF is applied in the negative direction. The corresponding external field needed to reduce the polarization to zero is called the coercive field strength E_c. If the field is increased to a more negative value, the direction of polarization flips and a hysteresis loop is obtained. The value of the spontaneous polarization P_s (OE) is obtained by extrapolating the curve onto the polarization axes (CE).

1.3.2.4 Curie temperature and phase transitions

All ferroelectric materials posses a characteristic transition temperature called the Curie temperature (T_c). At a temperature $T \geq T_c$, they do not exhibit ferroelectricity. On decreasing the temperature through the Curie point, a ferroelectric crystal undergoes a phase transition from a non-ferroelectric (paraelectric) phase to a ferroelectric phase. If there are more than one ferroelectric phases, the temperature at which the crystal transforms from one ferroelectric phase to another is called the transition temperature. Early research work on ferroelectric transitions has been summarized by Nettleton [31,32]. Near the Curie temperature or transition temperatures, thermodynamic, dielectric, elastic, optical and other properties show an anomalous behavior. This is due to a distortion in the crystal structure due to the phase change. The temperature dependence of the dielectric constant above the Curie temperature ($T > T_c$) in ferroelectric crystals is governed by the Curie-Weiss law:

$$\varepsilon = \varepsilon_0 + \frac{C}{T - T_0} \tag{1.32}$$

where ε is the permittivity of the material, ε_0 is the permittivity of free space, C is a constant called the Curie constant and T_0 is the Curie temperature. The Curie Temperature T_0 is different from the Curie point T_c. T_0 is a constant obtained by extrapolation, while T_c is the actual temperature where the crystal structure changes. For the first order transitions, $T_0 < T_c$; while for the second order phase transitions $T_0 = T_c$ [33].

1.3.3 Classification of ferroelectric materials

Ferroelectric materials can be classified on the basis of:

(a) the mechanism of the appearance of spontaneous polarization

(b) the crystal structure

(a) The mechansim of the appearance of spontaneous polarization

There are two mechanisms under this category as discussed below.

(i) Displacive type

In this case, a rearrangement of the structure, due to the displacements of certain ions, produces spontaneous polarization. The direction of the polarization coincides with the direction of the displacements. The polarization of such ferroelectrics is usually associated with the displacement of a cation from the centre of the surrounding oxygen octahedron. Depending on the geometry of the structure (e.g., dimensions, positions of the ions etc.), the nature of the binding and the electronic configuration of the atoms, the resulting dipole moments are oriented either parallel or antiparallel in a given

structure. Most of the oxide ferroelectrics including Barium titanate ($BaTiO_3$) fall under this category [13,16].

(ii) Order-disorder type

Certain ferroelectrics exhibit a transition which involves the ordering of certain structure elements which were disordered before the transition. The polarization process in these ferroelectrics can be considered to take place in two stages: the appearance of dipoles due to the deformation of the atomic groups and the alignment (to produce a parallel or antiparallel orientation) of dipole due to the ordering of the structural elements. The ordering mechansim acts as a "trigger". Tri-glycine sulphate (KH_2PO_4) belongs to this type.

(b) The crystal structure

Ferroelectric materials on the basis of the crystal structure can broadly be classified into four subcategories:

(i) Perovskite group

Perovskite is a family name of a group of materials and the mineral name of calcium titanate ($CaTiO_3$) having a structure of the type ABO_3 (Fig. 1.7). Many piezoelectric (including ferroelectric) ceramics such as Barium Titanate ($BaTiO_3$), Lead Titanate ($PbTiO_3$), Lead Zirconate Titanate (PZT), Lead Lanthanum Zirconate Titanate (PLZT), Lead Magnesium Niobate (PMN), Potassium Niobate ($KNbO_3$), Potassium Sodium Niobate ($K_xNa_{1-x}NbO_3$) and Potassium Tantalate Niobate ($K(Ta_xNb_{1-x})O_3$) have a perovskite type structure.

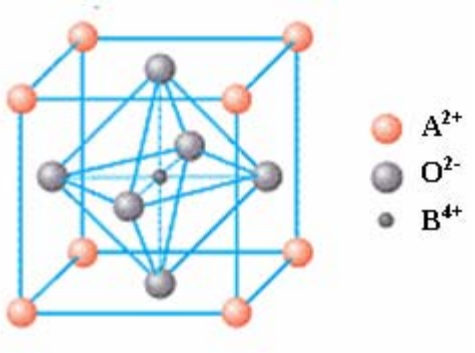

Fig. 1.7 Crystal structure of perovskites

(ii) Tungsten-Bronze group

The tungsten bronze type ferroelectric crystals have a structure similar to tetragonal tungsten bronze K_xWO_3 ($x < 1$). Lead niobate ($PbNb_2O_6$) was one of the first crystals of the tungsten bronze type structure to show useful ferroelectric properties. The site occupancy formula for this type of structure is given by $(A_1)_4(A_2)_2(C)_4(B_1)_2(B_2)_8O_{30}$ [34]. Fig. 1.8 shows the schematic of the projection of the tungsten bronze type structure. For lead niobate the B_1 and B_2 sites are occupied by Nb^{5+} ions. The open nature of the structure as compared to the perovskite allows a wide range of cation and anion substitutions without loss of ferroelectricity [21,35,36].

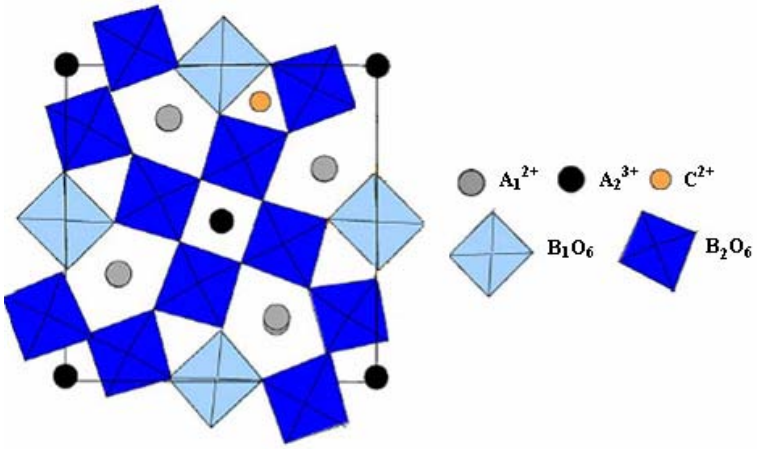

Fig. 1.8 Projection of the tungsten-bronze crystal structure

(iii) Bismuth Oxide Layer Structured group

The two most important piezoelectric materials with the $(Bi_2O_2)^{2+}$ layer structure are bismuth titanate ($Bi_4Ti_3O_{12}$) and lead bismuth niobate ($PbBi_2Nb_2O_9$). As shown in Fig. 1.9, the structure consists of corner linked perovskite-like sheets, separated by $(Bi_2O_2)^{2+}$ layers [37,38]. The plate like crystal structure of these compounds leads to highly anisotropic ferroelectric properties. The bismuth oxide layer structured ferroelectrics may become important piezoelectric ceramics because of their higher stability, higher operating temperature and higher operating frequency. These ceramics are mainly useful for piezoelectric resonators which need to exhibit a very stable resonant frequency [33,39,40].

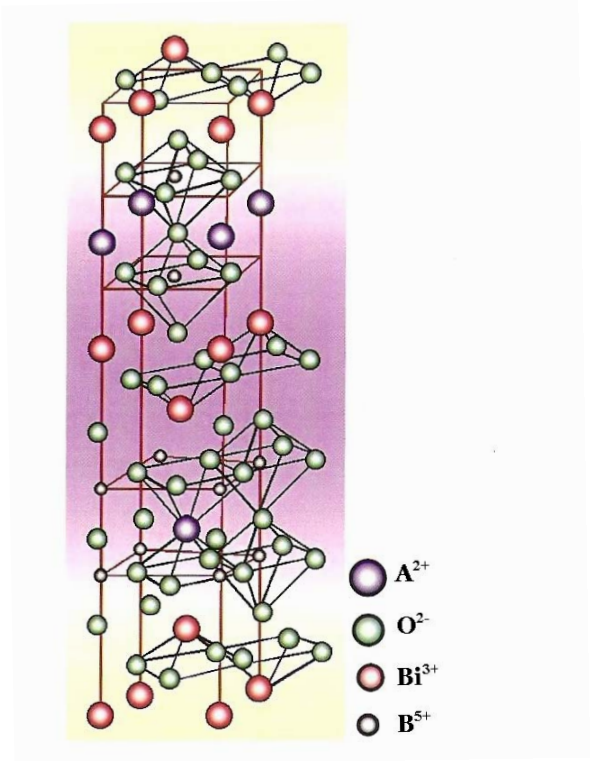

Fig. 1.9 Crystal structure of bismuth oxide layer structured (BLSF) ferroelectric compounds

(iv) Pyrochlore group

Members of this group have the general formula $A_2B_2O_7$ and the crystal structure is shown in Fig. 1.10. The A-site can be represented by any of a long list of metal ions: lead, calcium, potassium, bismuth, sodium, barium, cadmium, cerium etc. while the B-site can be represented by any of these metal ions: niobium, tungsten, tantalum, titanium etc. $Cd_2Nb_2O_7$, $Y_2Ti_2O_7$, $Mn_2Sb_2O_7$, etc. belong to this family.

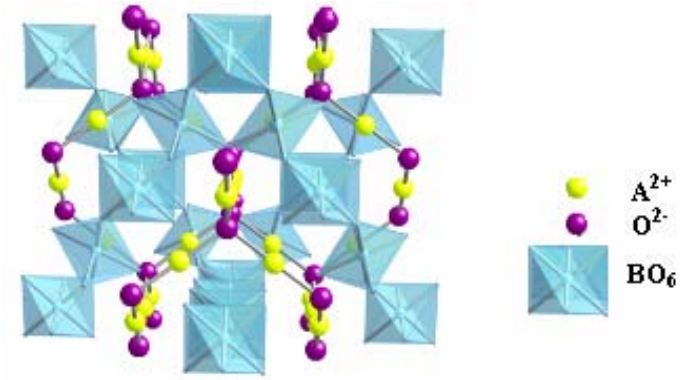

Fig. 1.10 Crystal structure of pyrochlores

1.3.4 Applications of ferroelectric materials

Ferroelectric ceramics have been found to be useful for various practical applications, such as high dielectric constant capacitors, piezoelectric sonar and ultrasonic transducers, radio and communication filters, pyroelectric devices, medical diagnostic transducers, positive temperature coefficient (PTC) sensors, ultrasonic motors and electrooptic light valves, to name a few [2,3]. The following section discusses the applications on the basis of the properties.

(i) Capacitors

The major application of ferroelectrics is for capacitors, utilizing their high dielectric constants around the Curie temperature. A capacitor consists of a dielectric material sandwiched between two electrodes. The total capacitance for this device is given by Eq. (1.15). To get a high volumetric efficiency (capacitance per unit volume) the dielectric material between the electrodes should have a large dielectric constant, a large area and small thickness. $BaTiO_3$ based ceramics show dielectric constant values as high as 15,000 as compared to 5 or 10 for common ceramic and polymer materials. The volumetric efficiency can be further enhanced by using multilayer ceramic (MLC) capacitors, which consists of alternate layers of dielectric and electrode material. Each individual dielectric layer contributes capacitance to the MLC capacitor. The high dielectric constants of the relaxor materials such as PMN ($\varepsilon_r \approx 25{,}000$) make them ideal for MLC capacitor applications [41,42]. Another added advantage of ferroelectric materials is due to their nonlinear nature they can be used to make capacitors with tunable capacitance.

(ii) Ferroelectric memories

Recently, very large scale integrated semiconductor memories using ferroelectric films have been investigated intensively. Utilization of ferroelectric material with high permittivity or polarization hysteresis has been considered as a possible solution to the problem of limitation in production of fine-scale capacitors using the conventional silicon micromachining technology [7].

There are volatile and non-volatile memory devices in semiconductor memories [43]. Dynamic Random Access Memories (DRAMs) and Static Random Access Memories (SRAMs), widely used because of its high integration capability, are volatile memories. Data stored in volatile memory is lost when power fails. The non-volatile memories which retain the data even when power fails, include Electrically Erasable Programmable Read Only Memories (EEPROMs) and Si-surface-potential control CMOS (Complimentary Metal Oxide Semiconductor) FET channel. However both types, in general, have problems in integration density and writing time.

Ferroelectric memories are attractive for DRAM devices because of their high permittivity [44], since, because of the high dielectric constant, higher memory integration is possible. $SrTiO_3$ and $Ba_xSr_{1-x}TiO_3$ (BST) films are the ferroelectric materials used for DRAM devices.

The non-volatile memories, named above, are very expensive. The advantages offered by Ferroelectric Random Access Memories (FeRAMs) include non-volatility, radiation hardened compatibility with CMOS and GaAs circuitry, high density, low power consumption and high speed (Fig. 1.11). Data in the FeRAM is stored by localized polarization switching in the microscopic regions of ferroelectric thin films. The radiation hardness of FeRAMs allow for the use of devices containing these memories in harsh environments such as outer space [45,46]. For good performance of the device, the ferroelectric thin film should fulfill certain requirements. As the FeRAM operates on the basis of polarization

switching, the ferroelectric material should have a large remanent polarization and a small coercive field.

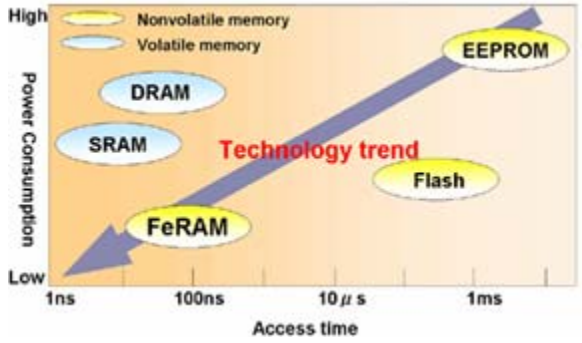

Fig. 1.11 Comparison of FeRAM with other memory devices

(iii) Pyroelectric Devices

Pyroelectricity is utilized in the fabrication of pyrodetectors like temperature / infrared light sensors and infrared image sensors. The pyroelectric sensor is a device for transducing thermal energy to electrical energy. The principle on which the pyroelectric sensors work is based on the change in spontaneous polarization with change in temperature.

The merits of pyrosensors as compared to semi-conducting infrared sensor materials are high sensitivity, quick response and high quality. Thin films of PZT, $PbTiO_3$ and $(Pb,La)TiO_3$ are widely used for pyroelectric sensing applications [47,48].

(iv) Piezoelectric Devices

Piezoelectricity is extremely utilized in the fabrication of various devices such as transducers, actuators, surface acoustic wave (SAW) devices and so on.

High voltage generated in a piezoelectric ceramic under applied mechanical stress can cause sparking and ignite the gas. Usually PZT ceramic disks are used for application like gas-ignitors [49].

Piezoelectric materials can be used for both active and passive transducer applications. In the passive mode, the transducer acts as a sound receiver i.e. there is conversion of sound energy into an electrical signal. The converse piezoelectric effect permits a transducer to act as an active sound transmitter [50]. In medical ultrasonography, piezoelectric transducers convert electrical energy into mechanical form when generating an acoustic pulse and convert mechanical energy into an electrical signal when detecting its echo. The transmitted waves propagate into a body and echoes are generated which travel back to be received by the same transducer. These echoes vary in intensity according to the type of tissue or body structure, thereby creating images [51].

Recent laptops and computers with a liquid crystal display require a very thin, no electromagnetic-noise transformer to start the glow of a fluorescent back-lamp. For this a piezoelectric transformer is used. The original piezo-transformer was proposed by C. A. Rosen [52].

(v) Electro-optic devices

The ferroelectric materials for electro-optic applications include an optically transparent film with a high degree of crystallinity. The electro-optic thin film devices are of two types: a) optical waveguides and b) optical memories and displays.

A great deal of work has been done on making ferroelectric thin film waveguides from $LiNbO_3$ and $Li(Nb,Ta)O_3$. PLZT thin film is even better material for optical waveguide application because of its large electro-optic coefficients [53,54].

1.4 Motivation and aim of the present work

Tungsten-bronze (TB) type structure is an important class of ferroelectric materials which are useful for various device applications because of their excellent properties such as pyroelectric, electro-optic, photorefractive, piezoelectric, etc. There is a lot of scope for substitution by variety of cations without loss of ferroelectricity in this structure because of its open nature and more number of interstitial sites (i.e. A_1, A_2, B_1, B_2 and C) as compared to the perovskite structure where there is only two sites (A and B) that can tailor the physical properties of the compound for various device applications.

In recent times, tungsten-bronze structured $BaO\text{-}R_2O_3\text{-}TiO_2\text{-}Nb_2O_5$ (R=Rare Earth) quaternary system has been found interesting because of their nature of phase-transition [55,56] and as these class of materials are lead free so they are environment friendly in these times of environment consciousness.

After extensive literature survey, it was realized that although some work has been reported for both A- as well as B- site substitutions in this TB- structured quaternary system [57-61] but a comprehensive study of the changes in physical properties due to systematic substitution at A-site in these compounds is lacking. With this background in mind, the structural and electrical behavioural changes due to systematic A (A_1 and A_2) - site substitution in

$Ba_5RTi_3Nb_7O_{30}$ (R=Rare-Earth) tungsten bronze structured material have been investigated. The results and discussions of the studies carried out are discussed in the subsequent chapters of this thesis.

1.5 Crystal structure of $Ba_5RTi_3Nb_7O_{30}$ (R=Rare-Earth)

It consists of a complex array of distorted BO_6 octahedra sharing corners in such a way that three different types of interstices (i.e. A, B and C) are available for cation substitutions in the general formula $[(A_1)_4(A_2)_2(C)_4][(B_1)_2(B_2)_8]O_{30}$ where A_1 and A_2 sites are usually filled by divalent or trivalent cations, B_1 and B_2 sites by tetravalent or pentavalent cations and C site being small, often remains empty giving the general formula $A_6B_{10}O_{30}$. In $Ba_5RTi_3Nb_7O_{30}$, A_1 and A_2 sites are filled by Ba^{2+} and R^{3+}, B_1 and B_2 sites by Ti^{4+} and Nb^{5+} cations and the site C remains empty (Fig. 1.12).

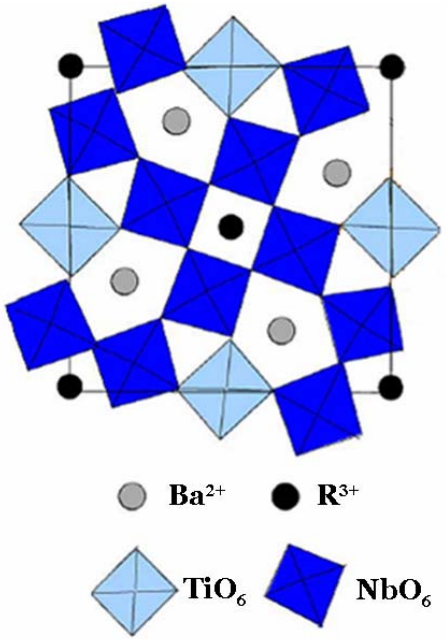

Fig. 1.12 Projection of $Ba_5RTi_3Nb_7O_{30}$ showing site occupancy by the various cations

In the present work, a systematic investigation has been carried out to study the influence of A- site compositional changes on the structural and electrical properties in TB- structured $Ba_5SmTi_3Nb_7O_{30}$ compound which are discussed in the following six chapters of this thesis.

The details of the experimental techniques used in the course of the present work are discussed in detail in **Chapter 2**.

Chapter 3 contains the optimization of the sintering condition for $Ba_5SmTi_3Nb_7O_{30}$ compound for better properties.

In **Chapter 4**, the effect of systematic calcium substitution at the barium site on the structural and electrical properties of $Ba_5SmTi_3Nb_7O_{30}$ compound is presented.

The effect of ionic radii of different rare-earth elements on the physical properties of $Ba_5RTi_3Nb_7O_{30}$ and $CaBa_4RTi_3Nb_7O_{30}$ (R=Rare-Earth) compounds have been discussed in **Chapter 5**.

In **Chapter 6**, the effect of the use of some novel preparation techniques like mechanical activation and microwave sintering on the structural and electrical properties have been discussed.

Chapter 7 contains the inferences from the present study and suggestions for further work are given.

REFERENCES

[1] J. Valasek, Phys. Rev. **17** (1921) 475.

[2] G. H. Haertling, J. Am. Ceram. Soc. **82** (1999) 797.

[3] D. Damjanovic, Rep. Prog. Phys. **61** (1998) 1267.

[4] L. E. Cross and R. E. Newnham, *History of ferroelectrics, ceramics and civilization. High-technology ceramics –past, present and future*, vol. III (American Ceramic Society, Westerville, Ohio,1987) p. 289-305.

[5] B. M. Wul and I. M. Goldman, Dokl. Akad. Nauk. SSSR. **46** (1945) 154.

[6] D. Baker, D. C. Koehler, W. O. Fleckenstein, G. E. Roden and R. Sabia, *Materials Technology*, Vol. II (Prentice-Hall Inc., Englewod Cliffs, New Jersey).

[7] K. Uchino, *Ferroelectric Devices* (Marcel Dekker Inc., New York, 2000).

[8] B. Tareev, *Physics of Dielectric Materials* (Mir Publishers, Moscow, 1979).

[9] R. A. Conclaser and S. D. Nagle, *Materials and Devices for Electrical Engineers and Physicists* (McGraw Hill Co., New York).

[10] S. O. Kasap, *Principles of Electronic Materials and Devices*, 2nd Edition (Tata McGraw-Hill Inc., New York, 2002).

[11] R. C. Buchanan, *Ceramic Materials for Electronics: Processing, Properties & Applications* (Marcel Dekker Inc., New York, 1991).

[12] J. C. Anderson and K. D. Leaver, *Materials Science* (Thomas Nelson and Sons Ltd., London, 1969).

[13] C. Kittel, *Introduction to Solid State Physics* (John Wiley and Sons Inc., New Jersey, 7th Edition, 1996).

[14] R. Waser, U. Böttger and S. Tiedke, *Polar Oxides: Properties, Characterization and Imaging* (Wiley-VCH Verlag GmbH & Co. KGaA, Weinheim, 2005).

[15] R. M. Rose, L. A. Shepard and J. Wulff, *Electronic Properties* (Wiley Eastern Pvt. Ltd., North Dakota, 1965).

[16] I. S. Zheludev, *Physics of Crystalline Dielectrics: Crystallography and Spontaneous Polarization*, Vol. I (Plenum Press, New York, 1971).

[17] W. Känzig, "*Ferroelectrics and Antiferroelectrics*" in Solid State Physics, Vol. 4 (Academic Press, New York, 1957).

[18] M. Lines and A. Glass, *Principles and Applications of Ferroelectrics and Related Materials* (Clarendon Press, Oxford, 1979).

[19] A. J. Dekker, Solid State Physics (Macmillan, New York, 1991).

[20] B. A. Strukov and A. P. Lavanyuk, *Ferroelectric Phenomena in Crystals* (Springer, New York, 1998).

[21] Y. H. Xu, *Ferroelectric Materials* and their Applications (Elsevier Science Publishers, Amsterdam, 1991).

[22] G. Yi, Z. Wu, M. Sayer, C. Jen and J. F. Bussiere, Electron. Lett. **25** (1989) 907.

[23] T. Mitsui, I. Tatsuzaki and E. Nakamura, *An Introduction to the Physics of Ferroelectrics* (Gordon and Breach, London, 1976).

[24] Y. J. Song, H. H. Kim, S. Y. Lee, D. J. Jung, B. J. Koo, J. K. Lee, Y. S. Park, H. J. Cho, S. O. Park and K. Kim, Appl. Phys. Lett. **76** (2000) 451.

[25] J. Y. Nye, *Physical Properties of Crystals* (Clarendon Press, Oxford, 1990).

[26] R. E. Newnham, *Structure – Property Relations* (Springer Verlag, New York, 1975).

[27] A. Safari, R. K. Panda and V. F. Janas, *Ferroelectric Ceramics: Processing, Properties & Applications* (Rutgers University, Piscataway NJ, USA).

[28] S. B. Lang, *Source Book of Pyroelectricity* (Gordon and Breach, New York, 1974).

[29] B. T. Batthais and A. V. Hippel, Phys. Rev. **73** (1948) 1378.

[30] A. V. Hippel, Rev. Modern Phys. **22** (1950) 221.

[31] R. E. Nettleton, Ferroelectrics **1** (1970) 3.

[32] R. E. Nettleton, Ferroelectrics **2** (1971) 5.

[33] B. Jaffe, W. R. Cook Jr. and H. Jaffe, *Piezoelectric Ceramics* (Academic Press, London, 1971).

[34] P. B. Jasmieson, S. C. Abrahams and J. L. Bernstein, J. Chem. Phys. **48** (1965) 5048.

[35] G. Goodman, J. Am. Ceram. Soc. **36** (1953) 368.

[36] M. H. Francombe and B. Lewis, Acta Crystallogr. **11** (1958) 696.

[37] B. Aurivillius, Ark. Kemi. **2** (1950) 519.

[38] B. Aurivillius, Ark. Kemi. **5** (1952) 39.

[39] L. E. Cross, *Ferroelectric Ceramics: Tutorial Reviews, Theory, Processing and Applications* (Birkhauser Verlag, Basel, 1993).

[40] W. G. Cady, *Piezoelectricity* (Dover Publications, New York, 1962).

[41] I. H. Pratt and S. Firestone, J. Vac. Sci. Tech. **8** (1971) 256.

[42] H. J. Hagemann, D. Hennings and R. Wernicke, Phillips Tech. Rev. **41** (1983) 89.

[43] M. Barr and A. Massa, *Programming Embedded Systems* (O'Reilly, Massachusetts, 2006).

[44] M. Okuyama, Bull. Ceram. Soc. Jpn. **30** (1995) 504.

[45] J. F. Scott, L. Kammerdiner, M. Paris, S. Traynor, V. Ottenbacher, A. Shawabkeh and W. F. Oliver, J. Appl. Phys. **64** (1988) 787.

[46] J. F. Scott, C. A. Araujo, H. B. Meadows, L. D. McMillan, A. Shawabkeh and W. F. Oliver, J. Appl. Phys. **65** (1989) 1444.

[47] K. Ijima, Y. Tomita, R. Takayama and I. Ueda, J. Appl. Phys. **60** (1986) 361.

[48] R. Takayama, Y. Tomita, K. Ijima and I. Ueda, J. Appl. Phys. **61** (1987) 411.

[49] A. J. Moulson and J. M. Herbert, *Electroceramics Materials, Properties and Applications* (Chapman and Hall, London, 1990).

[50] B. A. Auld, *Acoustic Fields and Waves in Solids*, Vol. 1, 2nd edition (Krieger Publishing, Melbourne, 1990).

[51] G. S. Kino, Acoustic Waves: Devices Imaging and Analog Signal Processing (Prentice-Hall, Englewood Cliffs, New Jersey, 1987).

[52] C. A. Rosen, Proc. Electronic Component Symp. (1957) 205.

[53] A. Baudrant, H. Vial and J. Daval, J. Cryst. Growth **43** (1978) 197.

[54] S. Miyazawa and N. Uchida, Opt. and Quant. Electron. **7** (1975) 451.

[55] R. N. P. Choudhary, S. R. Shannigrahi and A. K. Singh, Bull. Mater. Sci. **22** (1999) 975.

[56] S. R. Shannigrahi, R. N. P. Choudhary, A. Kumar and H. N. Acharya, J. Phys. Chem. Solids **59** (1998) 737.

[57] Z. Y. Xu and X. M. Chen, J. Mater. Sci.: Mater. Electron. **11** (2000) 219.

[58] J. Li, X. M. Chen and Y. J. Wu, J. Eur. Ceram. Soc. **22** (2002) 87.

[59] T. Kar, R. N. P. Choudhary, S. Sharma, K. S. Singh, Ind. J. Phys. **73A** (1999) 453.

[60] M. R. Ranga Raju and R. N. P. Choudhary, Mater. Chem. Phys. **99** (2006) 135.

[61] A. Panigrahi, N. K. Singh and R. N. P. Choudhary, J. Phys. Chem. Solids **63** (2002) 213.

CHAPTER 2

Chapter 2

Experimental Details

This chapter contains experimental details along with the necessary theoretical background of the various structural and electrical parameters studied in the present work. The experimental techniques including the procedure for sample preparation and characterization are described below.

2.1 Preparation Techniques

This section discusses the method for preparation of the samples.

2.1.1 Solid - state reaction method

The flowchart showing the steps of solid – state reaction method is shown in Fig. 2.1. The key stages in this method of sample preparation are calcination and sintering [1,2].

High purity raw materials (oxides and carbonates) in form of powders are first weighed according to their stoichiometric formula of the composition. The particle size of the powders must be in the submicron range for the solid phase reactions to occur. So the next step in this method is mixing of the powders to eliminate aggregates and grinding of the mixture to reduce the particle size. The powder mixture is then calcined. Calcination process helps in the decomposition of the constituent carbonates resulting in the formation of oxides and removal of carbon dioxide. For example,

$$BaCO_3 \longrightarrow BaO + CO_2 \uparrow$$

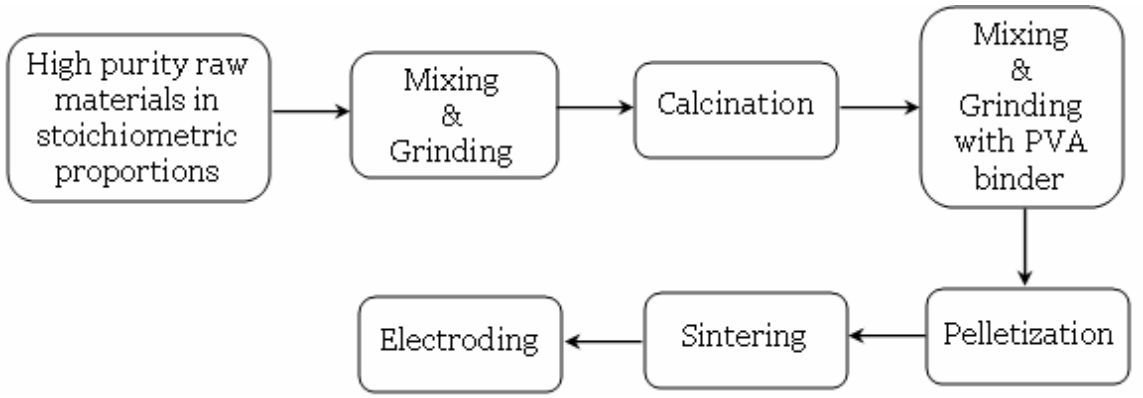

Fig. 2.1 Flowchart diagram representing solid-state reaction method

During the calcinations step, the solid phase reaction takes place between the constituents resulting in the partial phase formation [3-4]. Calcination causes the constituents to interact by interdiffusion of their ions. The calcining temperature is important as it influences the density and hence the final properties of the product. After calcinations, the lumps of the mixture are crushed and thoroughly ground. It is now necessary to add an organic binder material like polyvinyl alcohol (PVA) for sufficient adhesion during pelletization. There are various shaping methods like powder compaction / dry pressing, isostatic pressing, extrusion, slip-casting etc. [5]. The choice of the method depends on the type of material used, desired shape and thickness of the product. After shaping, the pellets are sintered. During sintering, the particles join at the region of contact by growth of neck [6,7]. Therefore, it results in densification and grain growth. The sintering process considerably affects grain boundaries and pores. The various models and mechanisms have explained the sintering process [2,8,9]. From the matter transport mechanism point of view, sintering process can be divided into three stages, viz., initial stage, intermediate stage and final

stage. The initial stage is associated with the growth of neck between the particles by lattice diffusion. In the intermediate stage, particles grow and lose their identity; the pores form continuous channel and all the pores intersect at the grain boundaries. In the final stage, pores either occur as isolated entities on the corner of the grains or totally enclosed within them. The sintering temperature and duration is thus crucial and should be optimized. Also, the surrounding atmosphere influences the properties of the final product. The sintered pellets are then polished so as to give smooth and parallel surfaces. Electroding of the sintered samples is required to provide electrical contacts.

Sample preparation

This section presents the details of the method used for the preparation of the various compositions studied in the present work. The sintering condition was optimized (by preparing the samples under different sintering temperatures and sintering durations) in order to achieve the best properties. The ferroelectric ceramics having the following compositions were prepared by the solid – state reaction technique:

$Ba_{5-x}Ca_xSmTi_3Nb_7O_{30}$; x = 0, 1, 2, 3, 4, 5

$Ba_5RTi_3Nb_7O_{30}$; R = La, Nd, Sm, Eu, Dy

$CaBa_4RTi_3Nb_7O_{30}$; R = La, Nd, Sm, Eu, Dy

The starting chemicals used were barium carbonate ($BaCO_3$), calcium carbonate ($CaCO_3$), titanium oxide (TiO_2), niobium oxide (Nb_2O_5), lanthanum oxide (La_2O_3), neodymium oxide (Nd_2O_3), europium oxide (Eu_2O_3) and dysprosium oxide (Dy_2O_3) (all from Aldrich, USA) and samarium oxide (Sm_2O_3)

(Alfa Aesar, USA) having purity ≥ 99.9 %. The chemicals were weighed in stoichiometric proportions as mentioned above. The weighed powders were mixed and thoroughly ground by agate-mortar and passed through sieve of fine mesh size of 100 μm. This powder mixture was then calcined at 1100 ºC for 20 hours in alumina crucibles. The heating rate was maintained at 5 ºC/min. The calcined powders were ground and admixed with about 5 wt. % PVA (Aldrich, USA) as a binder. Thereafter, the calcined powder was pressed into disk shaped pellets using hydraulic press by applying a uniaxial pressure of 300 MPa. To study the effect of sintering temperature and duration on the structural and electrical behaviour of the studied compositions and to determine the optimum sintering condition for the best properties, the pellets were sintered in air at the following sintering conditions:

(i) 1150 ºC; 20 hours

(ii) 1200 ºC; 20 hours

(iii) 1250 ºC; 20 hours

(iv) 1300 ºC; 2 hours

(v) 1300 ºC; 10 hours

(vi) 1300 ºC; 20 hours

The sintered pellets were then polished to a thickness of nearly 1 mm. High temperature conductive silver paste was applied over the parallel surfaces of the pellets which act as electrodes. Thereafter the pellets were cured at 325 ºC for 1 hour. Calcination, sintering and curing were done in a muffle furnace (Electroheat, India).

2.1.2 Mechanical activation method

In mechanical activation process, the solid state reaction of oxides is activated by high mechanical energy produced by the milling process. This process skips the high energy consuming calcination step, making the preparation process simpler than the conventional solid-state reaction technique as described earlier.

In this process, the stoichiometric mixture of powders was milled in a planetary ball mill (Retsch-PM 100, Germany). To optimize the milling duration the powders were milled for 5 hours, 10 hours and 20 hours at a milling speed of 300 rpm. Milling was carried out in toluene medium with 10 mm zirconium oxide balls in a zirconium oxide vial with a ball-to-powder weight ratio of 10:1. The milling was stopped for 30 minutes after every 1 hour of milling to cool down the system. The mixture was then admixed with 5 wt.% polyvinyl alcohol as a binder and then pressed at 300 MPa into disk shaped pellets. To determine the optimum sintering condition for the best properties, the pellets were sintered in air at the following sintering conditions:

(i) 1100 ºC; 10 hours

(ii) 1200 ºC; 10 hours

(iii) 1300 ºC; 2 hours

(iv) 1300 ºC; 10 hours

The sintered pellets were then polished to a thickness of nearly 1 mm. High temperature conductive silver paste was applied over the parallel surfaces of the samples which act as electrodes and were cured at 325 ºC for 1 hour. The

ferroelectric ceramic having the composition $Ba_5SmTi_3Nb_7O_{30}$ was prepared by this technique.

2.1.3 Microwave sintering

Unlike in conventional sintering where heating takes place by radiation, in microwave sintering the electromagnetic-waves interact with the ceramic materials leading to volumetric heating by dielectric loss. Therefore, in the microwave process of heating, the heat is generated due to the interaction of microwaves with the susceptor (silicon carbide ceramic slabs) inside which the sample is kept. The specimen having composition $Ba_5SmTi_3Nb_7O_{30}$ was microwave sintered by using a microwave furnace (VB Ceramic, India) at 1300 ºC for 2 hours. The rate of heating was maintained at 10 ºC/min.

2.2 Characterization Techniques

This section discusses the instruments / techniques used for structural and electrical characterization of the samples. A brief theoretical description of the characterizing parameters is also given.

2.2.1 Structural Characterization

2.2.1.1 X-ray Diffraction (XRD)

X-ray crystallography is a technique in which the pattern produced by the diffraction of X-rays through the closely spaced atoms in a crystal is recorded and then analyzed to reveal the nature of the lattice (Fig. 2.2). Geometrically, one may imagine that a crystal is made up of families of lattice planes and that the scattering from a given family of planes will only be strong if the X-rays reflected by each plane arrive at the detector in phase. This leads to a relationship between

the order of diffraction pattern n, X-ray wavelength λ, the spacing between lattice planes d and the angle of incidence θ known as Bragg's law [10,11]:

$$n\lambda = 2d\sin\theta \qquad (2.1)$$

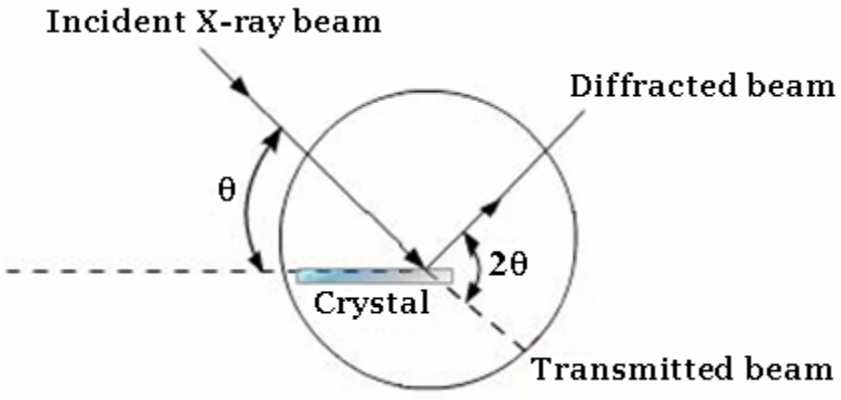

Fig. 2.2 Schematic diagram of X-ray diffraction

X-ray powder diffraction finds frequent use in materials science as it is non-destructive and easy to use.

Utility of the XRD pattern

Phase identification

The most widespread use of this technique is the phase identification of crystalline solids. Each crystalline solid produces its own characteristic diffraction pattern which can be compared to a database of known materials like JCPDS (Joint Committee of Powder Diffraction Standards) database in order to identify the contents of the sample and to determine the presence or absence of any particular phase. Both the positions and the intensity of the lines are characteristic of that particular phase and the pattern thus provides a fingerprint of the material [12].

Crystallinity

In contrast to pattern of a crystalline solid which consists of a series of sharp peaks, amorphous materials (e.g. liquids, glasses etc.) produce a broad background signal. XRD can be used to determine the crystallinity by comparing the integrated intensity of the background pattern to that of the sharp peaks [12].

Crystallite size

From the broadening of the XRD peak, it is possible to determine an average crystallite size by using Debye-Scherrer formula [10]:

$$P_{hkl} = k\lambda / \beta\cos\theta \qquad (2.2)$$

where k = 0.89-1.39, λ = wavelength of the used X-rays, β = FWHM (full width at half maximum, or half-width) and θ = the position (angle) of the peak.

***Structural distortion parameters*:**

Orthorhombic distortion

The strain in a lattice expressed as [2(a-b)/(a+b)] defines the distortion in the a-b plane is termed as orthorhombic distortion or orthorhombicity. From reported literature, it is known that orthorhombic distortion changes with impurity and temperature [13]. It influences the ferroelectric properties of the ceramics [14].

Tetragonal strain

The tetragonal strain is the internal strain in the lattice which is related to the phase transition temperature in these ceramics [15,16]. It is also known as principal strain or tetragonality and is expressed as (c/a) [17].

X-ray diffraction analysis

In the present work, X-ray diffractograms of all the samples were recorded for the structural analysis and for the determination of the various phases present in the samples. A Bruker (Model D8 Advance) diffractometer (Fig. 2.3 (a)) was used with CuK_α radiation of wavelength (λ) 1.5405 Å. The samples were analyzed in the 2θ range from 10° to 70° at a scanning rate of 1° / min with a spin of 30 rpm. The diffractometer was operated using diffraction software which evaluated the inter-planar spacing (d_{hkl}) values corresponding to all the observed peaks using the Bragg's relation.

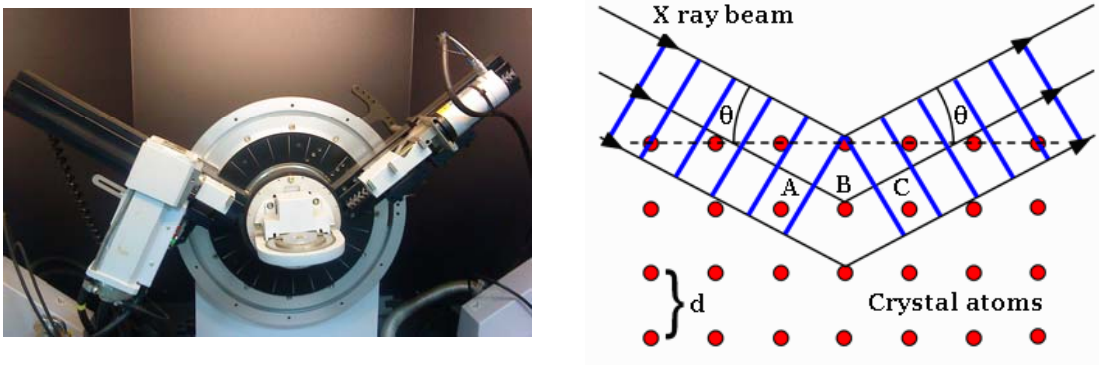

(a) (b)

Fig. 2.3 (a) X-ray diffractometer (b) Bragg's law

Taking the intensity of the highest peak to be 100 %, the relative intensity of other peaks is measured. The lattice parameters a, b, c were calculated from the observed d – values using the formula:

$$d_{hkl} = 1/[(h/a)^2 + (k/b)^2 + (l/c)^2]^{1/2} \qquad (2.3)$$

where h, k, l are the Miller indices corresponding to different planes. The peaks were indexed and the lattice parameters as deduced from the X-ray

diffractograms' data were refined using least square refinement method by a computer program package – PowderX [18]. The structural distortion parameters like tetragonal strain and orthorhombic distortion were calculated using the values of refined lattice parameters and were investigated to observe the influence of cationic substitution in the structure.

High temperature X-ray diffraction analysis

To know the crystal structure in the high-temperature paraelectric phase of the compound high-temperature X-ray diffraction analysis has been done by using Bruker high-temperature stage. The schematic diagram of the heating stage is shown in Fig. 2.4.

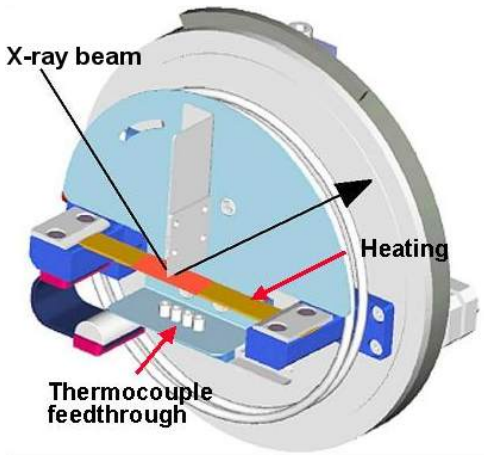

Fig. 2.4 Schematic diagram of high temperature stage of X-ray diffractometer

2.2.1.2 Raman spectroscopy

Raman spectroscopy, based on Raman effect, is a spectroscopic technique used to study vibrational, rotational and other low-frequency modes in a system. It relies on inelastic scattering or Raman scattering of monochromatic light,

usually from a laser in the visible, near infrared or near ultraviolet range. The laser light interacts with phonons or other excitations in the system, resulting in the energy of the laser photons being shifted up or down. The shift in energy gives information about the phonon modes in the system.

In the present study, the room temperature non-resonant Raman measurement has been carried out by a home made Raman spectrometer consisting of a Jobin Yvon-Spex (HR640) monochromator with a notch filter (514.5 nm) and Ar^+ ion laser (Coherent Innova 70, USA).

2.2.1.3 Scanning Electron Microscopy (SEM)

A microscope that uses electrons rather than light for formation of an image is called Electron Microscope. The scanning electron microscope (SEM) is a type of electron microscope that images the sample surface by scanning it with a high-energy beam of electrons in a raster scan pattern. The electrons interact with the atoms that make up the sample producing signals that contain information about the sample's surface topography, composition and other properties such as electrical conductivity. It has a large depth of field, which allows a large amount of the sample to be in focus at one time. The images produced have high resolution, which means that closely spaced features can be examined at a high magnification.

Working principle of SEM

In a typical SEM (Fig. 2.5), an electron beam is thermionically emitted from a tungsten or lanthanum hexaboride (LaB_6) cathode (electron gun) or via field emission guns (FEG) and are accelerated towards an anode. The electron beam, which typically has an energy ranging from 0.5 keV to 40 keV, is focused by one or

two condenser lenses to a spot about 0.4 nm to 5 nm in diameter. The beam passes through pairs of scanning coils or pairs of deflector plates in the electron column, typically in the final lens, which deflect the beam in the x and y axes so that it scans in a raster fashion over a rectangular area of the sample surface. When the primary electron beam interacts with the sample, the electrons lose energy by repeated random scattering and absorption within a teardrop-shaped volume of the specimen known as the interaction volume, which extends from less than 100 nm to around 5 μm into the surface. The size of the interaction volume depends on the electron's landing energy, the atomic number of the specimen and the specimen's density. The energy exchange between the electron beam and the sample results in the reflection of high-energy electrons by elastic scattering, emission of secondary electrons by inelastic scattering and the emission of electromagnetic radiation, each of which can be detected by specialized detectors. The beam current absorbed by the specimen can also be detected and used to create images of the distribution of specimen current. Electronic amplifiers of various types are used to amplify the signals which are displayed as variations in brightness on a cathode ray tube. The raster scanning of the CRT display is synchronized with that of the beam on the specimen in the microscope and the resulting image is therefore a distribution map of the intensity of the signal being emitted from the scanned area of the specimen. The image may be captured by photography from a high resolution cathode ray tube, but in modern machines, is digitally captured and displayed on a computer monitor and saved to the computer's hard disc.

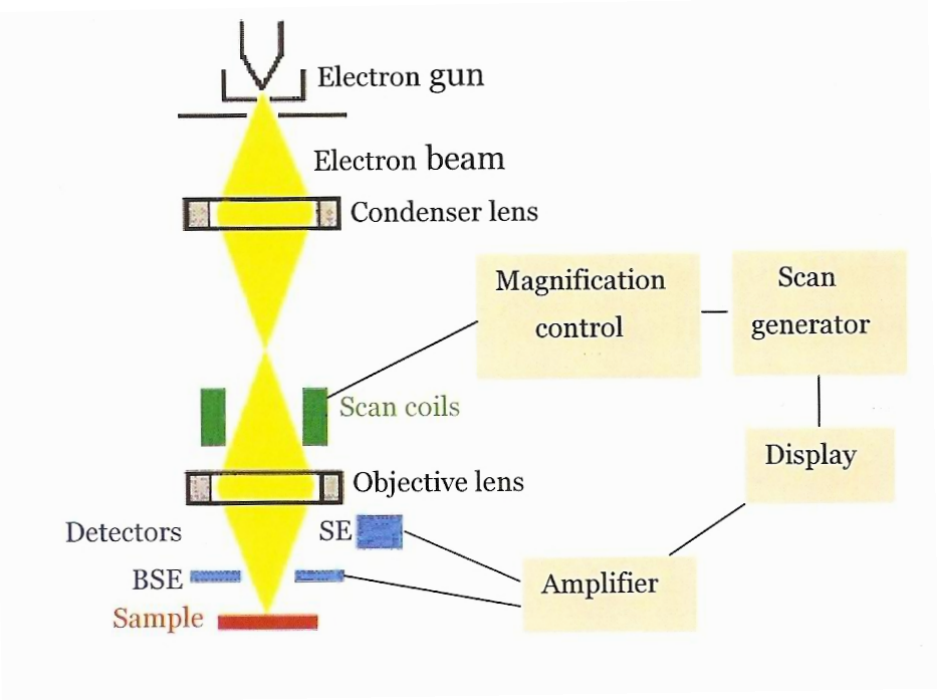

Fig. 2.5 Working principle of SEM

Microstructural studies

In the present study SEM (Model S–3700N, Hitachi, Japan) is used to determine the average grain size and the surface morphology of the samples. The parameters of SEM settings used in the present work are listed in Table 2.1. Average grain size was calculated using the linear intercept method inbuilt in the software.

Table 2.1 Typical SEM parameters used

Accelerating Voltage	**20 kV**
Probe Current	**40 nA**
Working Distance	**10 mm**

2.2.1.4 Transmission Electron Microscopy (TEM)

Transmission electron microscope (Fig. 2.6) is another type of electron microscope whereby a beam of electrons is transmitted through an ultra thin specimen. The electrons interact with the specimen as it passes through. An image is formed from the interaction of the electrons transmitted through the specimen; the image is magnified and focused onto an imaging device, such as a fluorescent screen, on a layer of photographic film or to be detected by a sensor such as a CCD camera. It is capable of imaging at a significantly higher resolution enabling the instrument's user to examine finer details – even as small as a single column of atoms.

In the present study TEM (Model 2100-F, Jeol, Japan) was used to view the nanoparticles of $Ba_5SmTi_3Nb_7O_{30}$ compound prepared by mechanical activation process at a voltage of 200 kV.

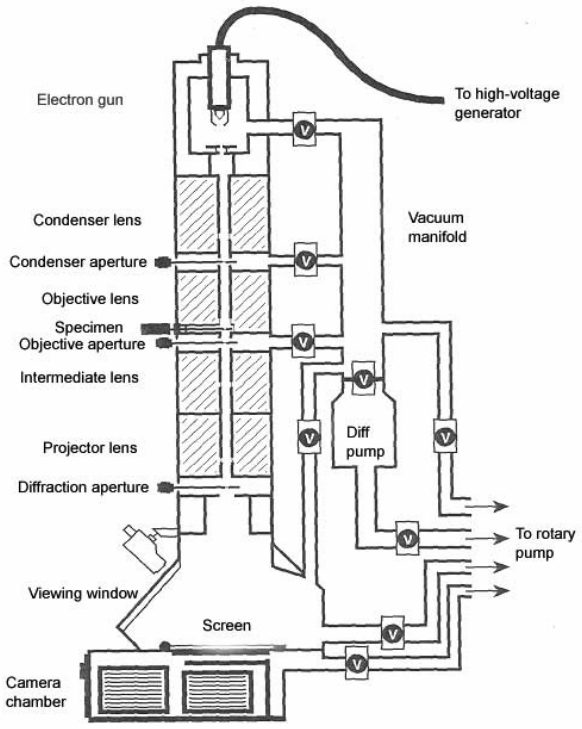

Fig. 2.6 Schematic diagram of TEM

2.2.1.5 Density measurement

The density measurement was performed employing the Archimedes' principle. The Archimedes method is based on hydrostatic weighing and it is the best-known density measurement technique [19]. In this method, the weight of a specimen is measured in two different media, e.g. air and liquid. To calculate the density of the specimen ρ_{exp}, the following equation was used:

$$\rho_{\exp} = \frac{W_{air}\rho_{liq}}{(W_{air} - W_{liq})} \tag{2.4}$$

where ρ_{liq} is the density of the weighing liquid. Weighing in air was done using a precision digital balance (Precisa, Switzerland) with least count of 0.0001 g and the weight in liquid was determined by suspending the sample in ethylene glycol having density 1.112 g/cm^3.

The theoretical density, ρ_{theo} was calculated by dividing the unit cell weight by the unit cell volume, which is estimated from lattice parameters obtained from the XRD data. The relative density was then computed by

$$\rho_{rel} = \frac{\rho_{\exp}}{\rho_{theo}} \tag{2.5}$$

where ρ_{exp} was calculated using Eq. (2.4).

2.2.2 Thermal Characterization

2.2.2.1 Thermogravimetric Analysis (TGA)

Thermogravimetric analysis or thermal gravimetric analysis (TGA) is a type of testing that is performed on samples to determine changes in weight in

relation to its change in temperature. Such analysis relies on a high degree of precision in three measurements: weight, temperature and temperature change.

In the present work, TGA (Model Q – 50, TA Instruments, USA) was used to determine the calcination temperature of $Ba_5SmTi_3Nb_7O_{30}$ compound in the presence of nitrogen with flow rate of 100 ml/min. The rate of heating was 10 ºC/min.

2.2.3 Electrical Characterization

2.2.3.1 Dielectric Studies

In these class of materials the dielectric constant and dielectric loss are the two most important parameters and studies of the dielectric properties provide a great deal of information for understanding the behaviour and the mechanism of electric polarization [20-24]. Dielectric measurements are most commonly used for the identification of phase transitions. Since the ability of these materials to polarize quickly is important for their use in memory applications, it is important to have information on the frequency dependence of the dielectric behaviour [25,26].

Capacitance (*C*) which is the ability of a body to hold electrical charge is expressed for a parallel plate capacitor where two parallel metal electrodes, each of area A, separated by a distance d filled with a dielectric material of permittivity ε as

$$C = \varepsilon \frac{A}{d} \tag{2.6}$$

The permittivity ε which is the intrinsic property of a dielectric mterial is related to the permittivity of free space ε_0 as

$$\varepsilon = \varepsilon_o \varepsilon_r \tag{2.7}$$

where ε_r is the relative permittivity which is simply a number.

Complex Permittivity

The response of normal dielectrics to external fields generally depends on the frequency of the field. This frequency dependence reflects the fact that a material's polarization does not respond instantaneously to an applied field. For this reason permittivity is often treated as a complex function of the angular frequency (ω) of the applied field and is represented as

$$\varepsilon_r^*(\omega) = \varepsilon_r'(\omega) - j\,\varepsilon_r''(\omega)\,; \qquad j = \sqrt{-1} \tag{2.8}$$

where $\varepsilon_r'(\omega)$ is the real part of the permittivity representing the lossless permittivity which is related to the electrical energy stored within the medium and is known as dielectric constant while $\varepsilon_r''(\omega)$ is the imaginary part of the permittivity related to the loss of energy within the medium.

Phasor diagram

For the case of applied voltage (V) being sinusoidal, charge stored in the dielectric can be expressed as:

$$Q = CV_o e^{j\omega t} \tag{2.9}$$

and current flowing through the capacitor is given by

$$\mathrm{I} = j\omega\, \varepsilon_r C_o V \tag{2.10}$$

If the power is not dissipated in the dielectric of the capacitor (ideal dielectric), the phase of current I through the capacitor is ahead of the voltage V by 90°. In real dielectrics, however, the phase angle φ is slightly less than 90°. The total current I through the capacitor can be resolved into two components i.e. $\mathrm{I_c}$

(capacitive current) and I_R (resistive current). This is depicted in the phasor diagram of current and voltage in a capacitor energized by an alternating voltage (Fig. 2.7).

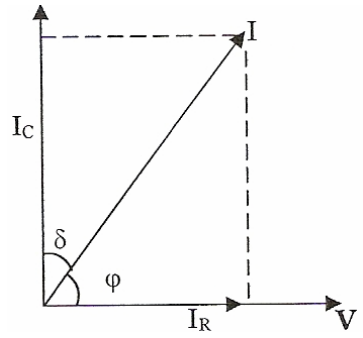

Fig. 2.7 Phasor diagram of I and V in a dielectric

The current I_c is proportional to the charge stored in the capacitor and leads the voltage by 90° and the current I_R is ac conduction current in phase with voltage *V*, which represents the energy loss or power dissipated in the dielectric.

Since the phase angle is very close to 90° in a capacitor with a high quality dielectric, the angle δ is a more descriptive parameter which, when added to the angle φ, becomes equal to 90° [27]:

$$\delta = 90^\circ - \varphi \tag{2.11}$$

where the angle δ is called the dielectric loss angle. The dielectric loss angle is an important parameter for a dielectric material. All other conditions being equal, the dielectric losses grow with this angle [27]. This parameter is usually described by the loss tangent, tan δ.

On choosing the complex form of dielectric constant ε (Eq. 2.8) and using it in Eq. 2.10 we get

$$I = j\omega\varepsilon_r'\varepsilon_o C_o V + \omega\varepsilon_r''\varepsilon_o C_o V \tag{2.12}$$

$$I = I_c + I_R \tag{2.13}$$

From the magnitude of these currents, therefore, the dissipation factor, tan δ can be defined as:

$$D \text{ (dissipation factor)} = \tan \delta = \left| \frac{I_R}{I_C} \right| = \frac{\varepsilon_r''}{\varepsilon_r'} \qquad (2.14)$$

The quality factor Q is defined as the ratio of the energy stored in a component to the energy dissipated by the component per cycle [27] :

$$Q = \frac{Energy\ Stored}{Energy\ Dissipated} = \frac{1}{\tan \delta} = \tan \varphi \qquad (2.15)$$

The value of tan δ for a given material is not strictly constant and depends on various external factors.

Frequency dependence of permittivity

The total polarization ***P***, the total polarizability α and the relative permittivity ε_r of a dielectric in an alternating field, all depend on the ease with which the dipoles can reverse alignment with each reversal of the applied electric field [28,29]. The dependence of ε_r on frequency is known as dielectric dispersion and is shown in Fig. 1.3. As already discussed in section 1.4.2, the different polarization mechanisms dominate in different frequency ranges. Since the relaxation frequencies of all the four polarization processes differ, it is possible to separate their contributions experimentally.

Each polarization component has a characteristic relaxation frequency. The contribution from the slower component drops off as frequency increases. The dielectric loss factor, ε_r'' (ω) correspondingly peaks at each characteristic frequency.

Temperature dependence of permittivity

The effect of temperature on the dielectric constant of ionic and electronic materials is, in general, small at low temperatures, but increases with increasing temperature, primarily because at elevated temperatures, ion mobility becomes appreciable [28].

The total permittivity of normal dielectrics increases with increasing temperature. But, in ferroelectric materials, the permittivity increases with increasing temperature, going through a maximum at the Curie temperature (T_c) and thereafter reduces as temperature is increased further. Above the Curie temperature, the dielectric constant follows Curie-Weiss law [30].

Generally dielectric loss increases appreciably when temperature is raised. In polar dielectrics, apart from dipolar losses, the loss due to electrical conduction also exists, which grows with the increase in temperature [31].

Measurement of dielectric parameters

A precision LCR meter (Agilent 4284A, USA) was used for measuring the dielectric constant and dielectric loss in the present work. The frequency dependence of dielectric permittivity and loss was studied in the frequency range 20 Hz – 1 MHz. The temperature dependence of dielectric properties was measured from room temperature to 400 ºC except for few samples where temperature was lowered below room temperature using liquid nitrogen, to get the Curie temperature, as a function of signal frequency (1 kHz, 10 kHz and 100 kHz) at oscillation amplitude of 1 V with no DC bias. The variations in dielectric constant and loss tangent values with temperature were recorded at

constant heating rate of 2 ºC / minute. The least count of temperature measurement was 1 ºC. For the measurements, the samples were mounted on a laboratory made two probe sample holder. The schematic diagram of the sample holder is shown in Fig. 2.8.

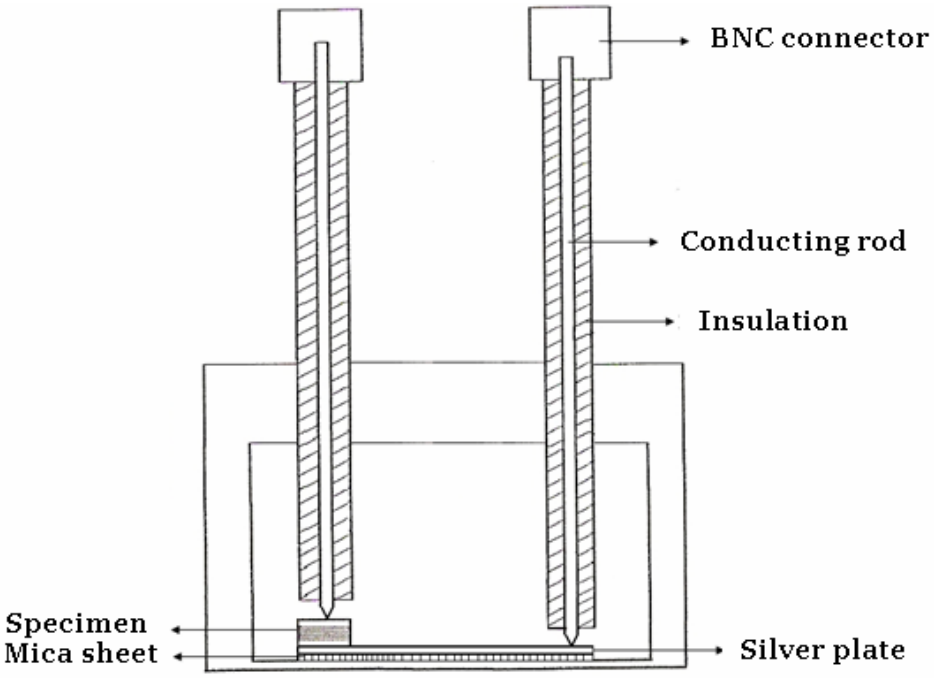

Fig. 2.8 Schematic diagram of the laboratory made sample holder

2.2.3.2 Electrical Conductivity

Electrical conductivity relates the current flow in a material to the electrical field applied across it [27]. Although, dielectrics are the materials that under normal circumstances do not allow current to flow, however, stray charges and defects cause a small conduction through them. In other words, the conductivity σ of the dielectrics is extremely small but it is not zero [32]. In 1926, A. Jaffe [31] put forward the idea that the conduction in ionic crystals, observed even at low temperatures, can be caused by the ions that tear themselves away from the

lattice points as a result of thermal oscillations. This point of view was developed and quantitatively substantiated by Ya Frenkel [33].

The current density in a parallel plate capacitor can be defined in terms of materials properties as [26],

$$J = \omega\varepsilon_o\varepsilon_r''E + j\omega\varepsilon_o\varepsilon_r'E \tag{2.16}$$

where E is the electric field strength. Thus we have,

$$\frac{J}{E} = \sigma + j\omega\varepsilon_o\varepsilon_r' \tag{2.17}$$

which implies that the real part of the ratio J/E is defined as the electrical conductivity σ in the material, i.e.,

$$\sigma(\omega) = \omega\varepsilon_o\varepsilon_r''(\omega) \tag{2.18}$$

The measured loss of material ε_r'' can be expressed as a function of both dipolar loss (ε_d'') and conductivity (σ) as [26] :

$$\varepsilon_r'' = \varepsilon_d'' + \frac{\sigma}{\omega\varepsilon_0} \tag{2.19}$$

Mechanisms of electrical conduction in dielectrics

Electrical conduction in dielectrics can occur by any of the three mentioned processes depending on the type of carriers present in the material [32] :

(i) *Ionic conduction* occurs either through the migration of positive and negative ions in an external field or through the motion of ions in vacancies which reflects the migration of vacancies.

(ii) *Molionic conduction* occurs through the motion of molecular ions (molions) or groups of ionized molecules. This conduction is encountered, especially, in amorphous or liquid dielectrics.

(iii) *Electronic conduction* is due to the motion of free charges (electrons and/or holes) in the solid, though the number of free charges in these materials is extremely small.

Thus, electrical conductivity in these materials can involve both electronic and ionic charge carriers. But in defect-free insulator, the electrons are either tightly bound or located in a filled electron band. Similarly, in a perfect crystal, since there is no mechanism for ions to diffuse, no current can result from the ionic motion.

Ionic Conductivity

The migration of the ionic defects (anion / cation vacancies) in the lattice gives rise to ionic conductivity, because the vacancies move through the lattice under the influence of an applied electric field. The number of these ionic defects increases rapidly at elevated temperatures. If the conductivity is plotted against 1/T, one can usually distinguish between a low-temperature region (**I**) and a high-temperature region (**II**) (Fig. 2.9).

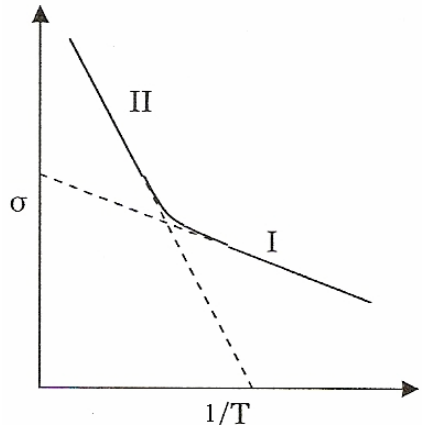

Fig. 2.9 Ionic conductivity σ as a function of 1/T

The low-temperature conduction results from the presence of impurity ions in the lattice and is called the extrinsic region of the conductivity [34]. The high-temperature region involves considerably larger activation energy. It is called the intrinsic region of ionic conductivity and is caused by the movement of the ions in the lattice and / or thermal generation of new defects. The intrinsic conductivity is dominant at high temperatures.

The conductivity can be derived from the Arrhenius equation [32] :

$$\sigma = \sigma_0 \exp\left(\frac{-E}{k_B T}\right) \tag{2.20}$$

and

$$E = \frac{w}{2} + \mu \tag{2.21}$$

where w and μ are the activation energies for defect generation and migration, respectively. For extrinsic conduction $w = 0$ and $E = \mu$; i.e., the ionic mobility becomes the controlling factor in the conduction process of dielectrics.

Electronic Conductivity

The electronic conduction is also known to occur in dielectric materials due to property of an ion to exist in more than one oxidation states which leads to the generation of electrons. This process is a function of temperature and / or compositional fluctuation [32]. If present, then at low temperatures, the electronic conduction is expected to dominate as low thermal energies are sufficient to energize low mass electrons.

Conductivity measurement

The total conductivity (σ_{tot}) of a material is the sum of the dc conductivity (σ_{dc}) and the ac conductivity (σ_{ac}),

$$\sigma_{tot} = \sigma_{dc} + \sigma_{ac}(\omega) \tag{2.22}$$

The dc conductivity was measured using a high precision electrometer (Keithley 6517A, USA). The measurement was performed at 10 V in the temperature range of room temperature to 300 ºC at a heating rate of 2 ºC / minute. Conductivity was calculated using the relation

$$\sigma_{dc} = \frac{d}{AR} \tag{2.23}$$

where d is the thickness of the pellet, A is the area of the conducting surface of the pellet and R is the measured resistance of the sample.

The ac conductivity was calculated using the relation

$$\sigma_{ac}(\omega) = \omega\varepsilon_0\varepsilon_r' \tan\delta \tag{2.24}$$

where dielectric constant (ε_r') and dielctric loss ($\tan\delta$) of the samples were already measured in dielectric measurements.

The Arrhenius plots were drawn between logarithm of conductivity and inverse of temperature (in Kelvin) and activation energy of all the samples were calculated using Eq. (2.20).

2.2.3.3 Impedance Studies

Impedance (Z) is a measure of opposition to the flow of an alternating current (AC) at a given frequency. It is represented as a complex vector quantity (Fig. 2.10). The impedance vector consists of a real part resistance (R) and an imaginary part reactance (X) [35].

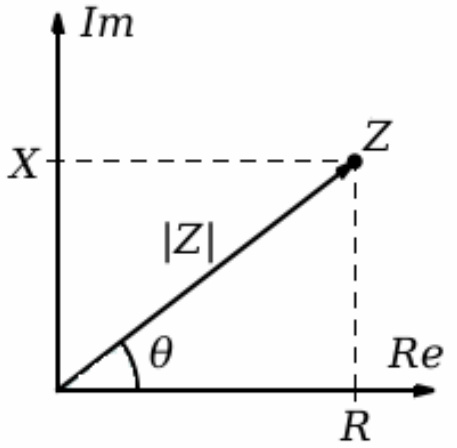

Fig. 2.10 Graphical representation of complex impedance

The electrical properties of a material are often represented in terms of some complex parameters like complex impedance (Z^*), complex admittance (Y^*), complex modulus (M^*), complex permittivity (ε^*) and dielectric loss (tan δ). These frequency dependent parameters are related to each other by the following relations:

$$Z^*(\omega) = Z' - j\,Z'' = R - jX = R_s - \frac{j}{\omega C_s} = \frac{1}{j\omega C_0 \varepsilon^*} \tag{2.25}$$

$$Y^*(\omega) = Y' + j\,Y'' = G + jB = \frac{1}{R_p} + j\omega C_p = j\omega C_o \varepsilon^* = \frac{1}{Z^*} \tag{2.26}$$

$$M^*(\omega) = M' + j\,M'' = \frac{1}{\varepsilon^*} = j\omega C_o Z^* \tag{2.27}$$

$$\varepsilon^*(\omega) = \varepsilon' - j\,\varepsilon'' \tag{2.28}$$

$$\tan\delta = \frac{Z'}{Z''} = \frac{Y'}{Y''} = \frac{M''}{M'} = \frac{\varepsilon''}{\varepsilon'} \tag{2.29}$$

where R_s, C_s are the series resistance and capacitance; R_p, C_p are the parallel resistance and capacitance; C_o is the geometrical capacitance; (Z', Y', M', ε') and

(Z'', Y'', M'', ε'') are the real and imaginary components of impedance, admittance, modulus and permittivity, respectively, G is conductance and B is susceptance.

The complex impedance spectroscopy (CIS) is a useful non-destructive technique for the characterization of electrical behaviour of electroceramic materials [36]. The technique is based on the principle of analyzing the response of a specimen to a sinusoidal electrical signal and subseqeuent calculation of the resulting transfer (impedance) functions with respect to the frequency of the applied signal. The output response, when plotted in a complex plane, appears in the form of a succession of semicircles (known as Nyquist or Cole-Cole plots) in the frequency domain arising as a result of the contribution to the electrical impedance due to various components such as the bulk material, grain boundary effect and interfacial polarization phenomenon (at the material – electrode interface) as can be seen in Fig. 2.11.

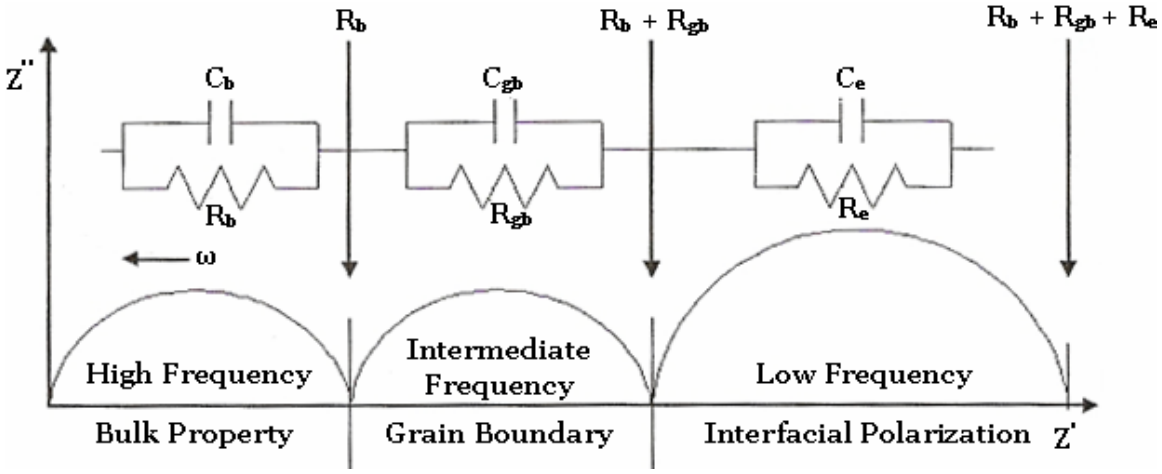

Fig. 2.11 Various components in a complex impedance plane

In view of this speciality, the CIS technique enables us to separate the effects due to each component (bulk, grain boundary and electrode interface) in a

polycrystalline sample because of the different time constants of these phenomena occuring in the specimen [36]. As depicted in Fig. 2.11, the first semicircle in the high frequency region manifests the effect of grain interior, while the second semicircle represents the grain boundary effects. In some cases, a third semicircle appears at very low frequencies due to the electrode – specimen interface effect [37]. Each of these semicircles can be represented by an equivalent circuit consisting of parallel resistance and capacitance (*RC* cicuits) connected in series as shown in Fig. 2.11.

Impedance measurement

Impedance analysis was performed on the specimens using LCR meter (Agilent 4284A, USA) in the frequency range 20 Hz – 1 MHz at oscillation amplitude of 1 V. The studies were performed at temperatures much higher than the Curie temperature of the samples as the semicircles starts manifesting only at the temperatures much higher than the Curie temperature. The various parameters computed from the impedance plots are grain resistance (R_b), grain boundary resistance (R_{gb}), grain capacitance (C_b), grain boundary capcitance (C_{gb}) and the relaxation time. The second intercept of each semicircle on real (Z') - axis gives the respective value of resistance (e.g. R_b and R_{gb}). The semicircles in the impedance spectrum have a characteristic peak occurring at a unique relaxation frequency ($\omega_r = 1/2\pi f_r$). It is expressed as: $\omega_r RC = \omega_r \tau = 1$. Therefore,

$$f_r = \frac{1}{2\pi\tau} = \frac{1}{2\pi RC} \tag{2.30}$$

where τ is relaxation time. The respective capacitances (C_b and C_{gb}) due to the grain and grain boundary effect can be calculated using this relation.

The bulk conductivity (σ_{bulk}) was also calculated from complex-impedance spectroscopy data using the following relation [34] :

$$\sigma_{bulk} = \frac{d}{R_b A} \tag{2.31}$$

where d is the thickness of the pellet and A is the area of the conducting surface of the pellet.

2.2.3.4 Ferroelectric Studies

The observation of hysteresis loop commonly known as Polarization-Electric field (P-E) loop is widely used for the ferroelectric characterization of materials [38]. The P-E loop is obtained using the Sawyer-Tower circuit which is shown in Fig. 2.12.

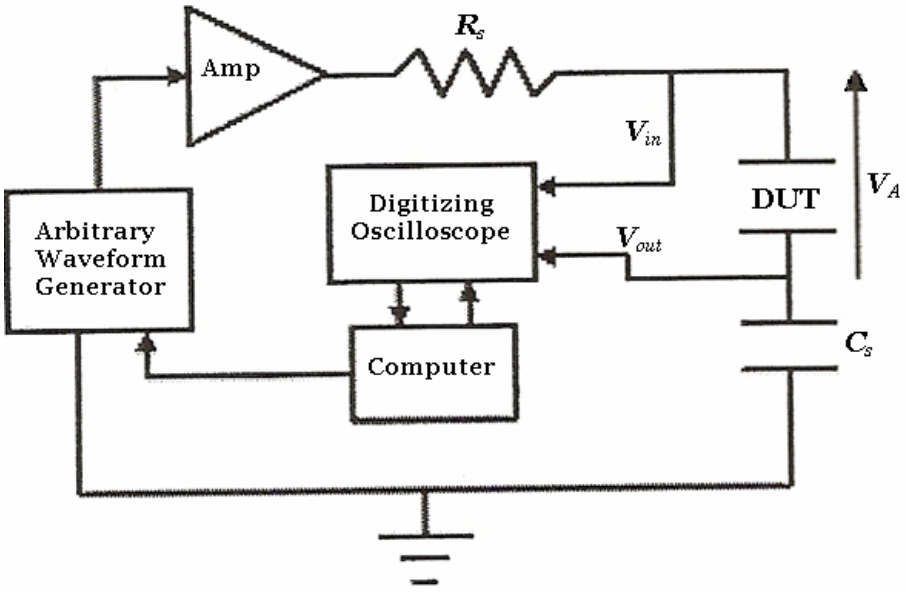

Fig. 2.12 Block diagram of Sawyer-Tower circuit

The ferroelectric device under test (DUT) is placed in series with a sensing capacitor C_s and a resistor R_s. A computer – controlled waveform generator produces an AC signal, which is applied to the DUT. The voltage at the input and

the output of the DUT is measured and is analyzed by the computer (Fig. 2.12). The capacitance of the sensing capacitor must be significantly larger than the capacitance of the device under test to minimize its effect on the measurement. The external charge on the sensing capacitor which is proportional to the external charge on the DUT, is calculated from the value of C_s and the voltage measured across C_s,

$$q = C_s V_{out} \tag{2.32}$$

The voltage applied to the DUT is the difference between the voltage measured at the input and the output of the DUT,

$$V_A = V_{in} - V_{out} \tag{2.33}$$

The polarization (or charge per unit area) is calculated by dividing the total charge by the area of the pellet. The electric field is calculated by dividing the applied voltage by the thickness of the pellet.

The hysteresis loops were recorded at room temperature (except for few samples where temperature has been lowered by using liquid nitrogen as their Curie temperature is below room temperature) using an automatic PE – loop tracer based on Sawyer – Tower circuit at a switching frequency of 100 Hz. The device under test (DUT) i.e., the pellets were placed in silicone oil bath during the measurement. The measurement gives P-E hysteresis loops from which remanent polarization ($2P_r$) and coercive field ($2E_c$) were determined.

2.2.3.5 Poling

The piezoelectric and pyroelectric properties are manifested in a 'poled' specimen [39]. In the poling process, the domains are reoriented and aligned by applying a strong dc electric field, usually at an elevated temperature. An

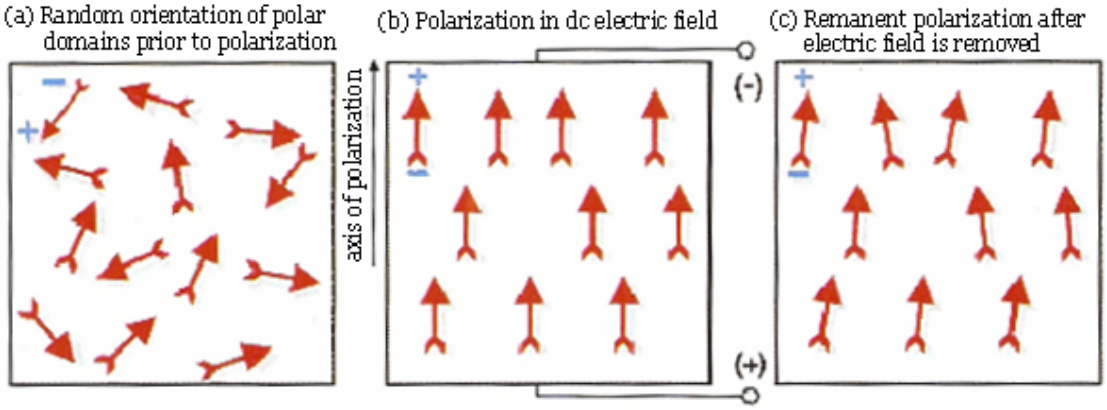

Fig. 2.13 Poling of a ferroelectric ceramic

illustration of this process is shown in Fig. 2.13. In the poling process, almost all the domains are aligned in the direction of electric field. The favourably oriented domains expand at the expense of domains that are not aligned with the field. When the electric field is removed most of the dipoles are locked into a configuration of "near alignment" (Fig. 2.13 c). The specimen now has a permanent polarization called the remanent polarization.

In the present work, the pellets were electrically poled by applying a high d.c. electric field (10 – 20 kV/cm) in silicone oil bath in the temperature range of 100 – 150 ºC for 2 hours.

2.2.3.6 Piezoelectric Studies

The root of the word "piezo" means "pressure" hence the original meaning of the word piezoelectricity implied "pressure electricity". Certain materials produce electric charges on their surfaces as a consequence of applying mechanical stress. The induced charges are proportional to the mechanical stress. This is called the direct piezoelectric effect and was discovered in quartz by Pierre and Jacques

Curie in 1880. Materials showing this phenomenon also conversely have a geometric strain proportional to an applied electric field. This is the converse piezoelectric effect. Mathematically, this can be represented as :

$$D = dT + \varepsilon_r'^{T}E \qquad \text{(Direct)} \qquad (2.34)$$

$$S = s^{E}T + dE \qquad \text{(Converse)} \qquad (2.35)$$

where D is the dielectric displacement (or polarization), T the stress, E the electric field strength, S the strain, d a piezoelectric coefficient, s the material compliance (inverse of stiffness) and ε_r' the dielectric constant. Both of these equations, in matrix form, actually describe a set of equations that relate these properties along different orientations of the material.

The piezoelectric charge coefficient d_{ij} describe the electromechanical parameter of the piezoelectric materials. It is defined as strain developed per unit electric field applied or charge density developed per unit stress [39].

Double subscripts, as in d_{ij}, are used to describe the relationships between electrical and mechanical parameters. The first index indicates the electrical direction (electric field or dielectric displacement) and the second to the mechanical direction (stress or strain). Thus, the parameter d_{33} denotes that the electric field is along the poling axis (direction 3) and the strain also develops along the same axis.

d_{33} measurement: In the present work, the d_{33} measurements of the specimens were done using piezometer system (PiezoTest PM300, UK) at room temperature.

2.2.3.7 Pyroelectric Studies

The pyroelectric effect is the ability of certain materials to generate electrical potential when they are heated. The change in temperature slightly modifies the positions of the atoms within the crystal structure, such that the polarization of the material changes [40]. This polarization change gives rise to an electric potential. Mathematically, this is represented as [17]:

$$J = -\frac{\partial P_S}{\partial t} = -\left(\frac{\partial P_S}{\partial T}\right)\left(\frac{\partial T}{\partial t}\right) = P_T\left(\frac{\partial T}{\partial t}\right) \tag{2.36}$$

or,
$$P_T = \frac{P_I}{A\left(\frac{\partial T}{\partial t}\right)} \tag{2.37}$$

where P_T $\left(=\left|\frac{\partial P_S}{\partial T}\right|\right)$ is denoted as the pyroelectric coefficient, P_I the pyroelectric current, P_s the spontaneous polarization, A the area and $\left(\frac{\partial T}{\partial t}\right)$ the rate of change of temperature.

Pyroelectric measurement: In the present work, poled samples were heated at a constant heating rate of 2 ºC/min. The pyro-current generated in the specimen was measured using a high precision electrometer (Keithley 6517A, USA). From this, the pyroelectric coefficient (P_T) was calculated using Eq. 2.37.

REFERENCES

[1] J. S. Reed, *Introduction to the Principles of Ceramic Processing* (John Wiley & Sons, New York, 1988).

[2] D. W. Richerson, *Modern Ceramic Engineering* (Marcel Dekker, New York, 1982).

[3] J. S. Reed and R. B. Runk, *Ceramic Fabrication Processes, Treatise on Materials Science & Technology*, Vol. 9 (Editor F. F. Y. Wang, Academic Press, New York, 1976).

[4] K. G. Ewsuk and L. W. Harrison, *Ceramic Powder Science III, Ceramic Transactions*, Vol. 12 (The American Ceramic Society, Westerville, Ohio, 1990).

[5] D. Baker, D. C. Koehler, W. O. Fleckenstein, G. E. Roden and R. Sabia, *Materials Technology*, Vol. II (Prentice-Hall Inc., Englewod Cliffs, New Jersey).

[6] W. D. Kingery and B. D. Francois, *Sintering and Related Phenomena* (Gordon Breach Science Publishers, New York, 1965).

[7] K. G. Ewsuk and G. L. Messing, *Hot Isostatic Pressing: Theory and Applications* (ASM International Materials Park, Ohio, 1991).

[8] R. L. Coble and J. E. Burke, *Progress in Ceramic Science*, Vol. 3 (MacMillan, New York, 1963).

[9] N. B. Hannay, *Reactivity of Solids: Treatise on Solid State Chemistry*, Vol. 4 (Plenum Press, New York, 1976).

[10] B. D. Cullity, *Elements of X-ray Diffraction* (Addison-Wesley Publishing Co.

Inc., California, 1978).

[11] S. O. Kasap, *Principles of Electronic Materials and Devices*, 2nd Edition (Tata McGraw-Hill Inc., New York, 2002).

[12] R. K. Puri and V. K. Babbar, Solid State Physics (S. Chand & Co. Ltd., New Delhi, 2001).

[13] H. Nagata, N. Chikushi and T. Takenaka, Jpn. J. Appl. Phy. **38** (1999) 5498.

[14] S. Luo, M. Miyayama and T. Kudo, Mater. Res. Bull. **36** (2001) 531.

[15] B. Su and W. Button, J. Appl. Phys. **95** (2004) 1382.

[16] K. Uchino, *Ferroelectric Devices* (Marcel Dekker Inc., New York, 2000).

[17] V. Shrivastava, A. K. Jha and R. G. Mendiratta, Solid State Comm. **133** (2005) 125.

[18] C. Dong, J. Appl. Cryst. **32** (1999) 838.

[19] H. A. Bowman and R. M. Schoonover, J. Res. Nat. Bur. Stand. **69** C (1965) 217

[20] H. D. Megaw, *Ferroelectricity in crystals* (Methuen & Co. Ltd., London, 1957).

[21] W. Kanzig, *Ferroelectrics and Antiferroelectrics* (Academic Press, New York, 1957).

[22] F. Jona and G. Shirane, Ferroelectric Crystals (Pergamon Press, Oxford, London, 1962).

[23] J. C. Burfoot, *Ferroelectrics* (Van Nostrand, New York, 1967).

[24] J. B. Grindlay, An Introduction to Phenomenological Theory of Ferroelectricity (Pergamon Press, Oxford, London, 1970).

[25] J. C. Anderson and K. D. Leaver, *Materials Science* (Thomas Nelson & Sons Ltd., London, 1969).

[26] Y. H. Xu, *Ferroelectric Materials* (Elsevier Science Publishers, Amsterdam, 1991).

[27] R. C. Buchanan, *Ceramic Materials for Electronics: Processing, Properties & Applications* (Marcel Dekker Inc., New York, 1991).

[28] S. B. Lang, *Source Book of Pyroelectricity* (Gordon & Breach Science Publishers, New York, 1974).

[29] R. M. Rose, L. A. Shepard and J. Wulff, *Electronic Prope*rties (Wiley Eastern Pvt. Ltd., New York, 1965).

[30] C. A. Kittel, *Introduction to Solid State Physics*, 7th edition (John Wiley & Sons Inc., New Jersey, 1996).

[31] B. Tareev, *Physics of Dielectric Materials* (Mir Publishers, Moscow, 1979).

[32] I. Bunget and M. Popenscu, *Physics of Solid Dielectrics* (Elsevier, New York, 1984).

[33] Y. I. Frenkel, Elecktrichestro (Physics of Electrets) **8** (1947) 5.

[34] I. S. Zheludev, *Physics of Crystalline Dielectrics: Crystallography and Spontaneous Polarization*, Vol. I (Plenum Press, New York, 1971).

[35] R. N. P. Choudhary and A. K. Thakur, *Complex Impedance Analysis: A Tool for Ferroelectric Materials* (Proceedings of NSFD – XIII) Nov. 23-25, 2004.

[36] E. Barsoukov and J. R. Macdonald, *Impedance spectroscopy: theory, experiment and applications* (John Wiley & Sons Inc., New Jersey, 2005).

[37] W. P. Mason, *Piezoelectric Crystals and their Application to Ultrasonics* (Van Nostrand, New York, 1950).

[38] C. B. Sawyer and C. H. Tower, Phys. Rev. **35** (1930) 269.

[39] G. H. Haertling, J. Am. Ceram. Soc. **82** (1999) 797.

[40] D. Damjanovic, Rep. Prog. Phys. **61** (1998) 1267.

CHAPTER 3

Chapter 3

$Ba_5SmTi_3Nb_7O_{30}$: Optimization of Preparation Conditions

3.1 INTRODUCTION

Processing of ferroelectric powders play a significant role in determining the microstructural, electrical and optical properties of ferroelectric ceramics [1-7]. Therefore, the calcination and sintering temperatures and durations for preparing a compound by solid –state reaction method is very important and therefore the optimization of the preparation conditions were taken and is presented in this chapter. The samples were sintered under six different sintering conditions as mentioned earlier in Section 2.1.1. The effects of sintering temperature and duration on the microstructure, density, dielectric property, conductivity, ferroelectric, pyroelectric and piezoelectric properties of $Ba_5SmTi_3Nb_7O_{30}$ compound have been investigated with an objective of identifying the optimized sintering condition. The optimized sintering condition is one which results in high dielectric constant, low dielectric loss, good ferroelectric, pyroelectric and piezoelectric properties maintaining the desired tungsten-bronze phase. This optimized calcination and sintering conditions were then used to prepare all the calcium and rare-earths substituted $Ba_5SmTi_3Nb_7O_{30}$ compounds discussed in the following chapters.

3.2 RESULTS AND DISCUSSIONS

3.2.1 Thermal Characterization

3.2.1.1 Thermogravimetric Analysis (TGA)

Thermogravimetric analysis (TGA) of the homogeneous mixture was carried out to determine the calcination temperature and structural stability. Fig. 3.1 shows the TGA analysis of the mixture.

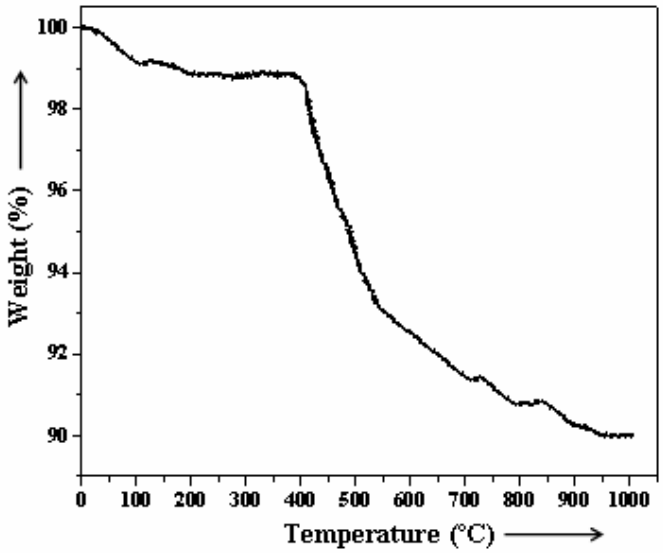

Fig. 3.1 TGA analysis of the homogeneous physical mixture

An initial mass loss of ~ 1 % upto 100 °C can be seen in Fig. 3.1, which is likely due to the evaporation of surface absorbed moisture. Another mass loss of about 8.5 % from 400 °C to 1000 °C is evident in the figure. This mass loss is possibly due to the intermediate reactions and the evolution of CO_2 gas from the precursor materials. Virtually no mass loss beyond 1000 °C suggests that a temperature above 1000 °C is an appropriate calcination temperature. Therefore, the homogeneous mixed powders were calcined at 1100 °C for 20 hours.

3.2.2 Structural Characterization

3.2.2.1 X-ray diffraction

The calcined samples of composition $Ba_5SmTi_3Nb_7O_{30}$ were sintered at various sintering conditions. The room temperature X-ray diffractograms of the samples sintered at various sintering temperatures and sintering durations are shown in Fig. 3.2 (a) and (b) respectively.

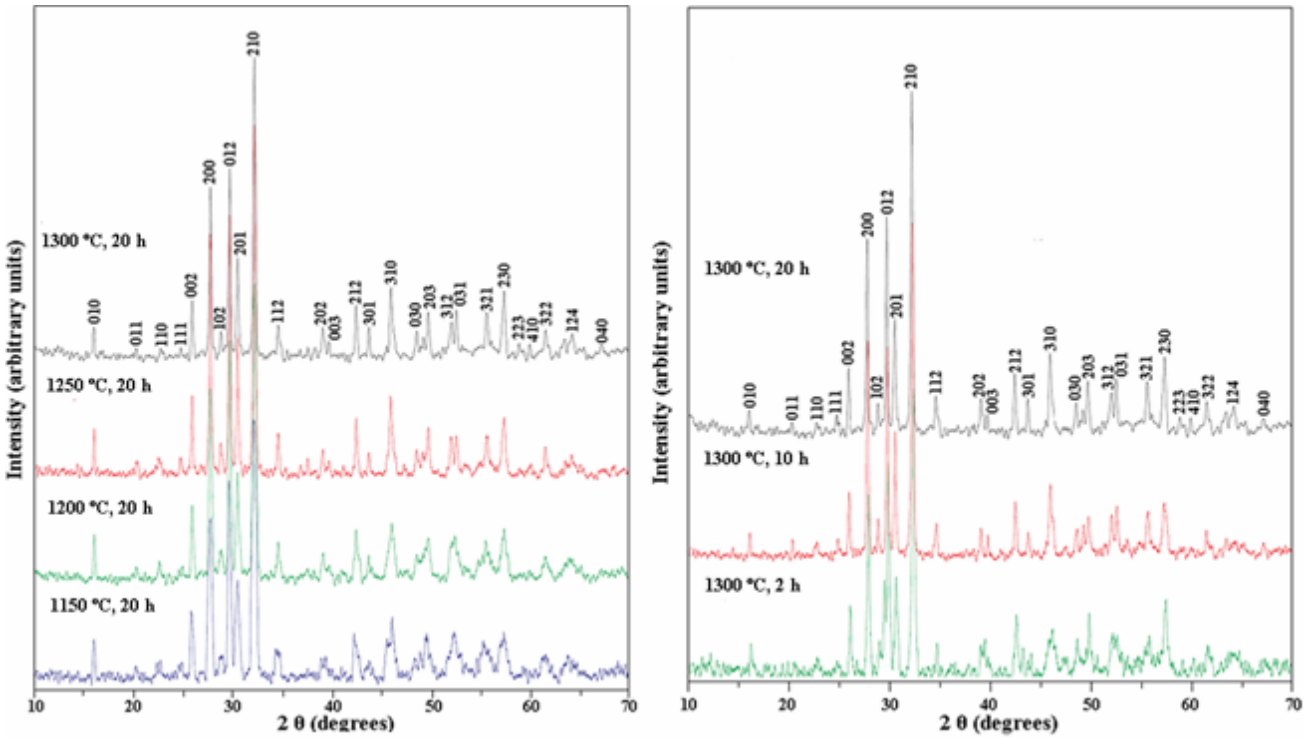

(a) (b)

Fig. 3.2 XRD patterns of $Ba_5SmTi_3Nb_7O_{30}$ sintered at different (a) temperatures and (b) durations

It is observed that single-phase $Ba_5SmTi_3Nb_7O_{30}$ compound is formed in all the sintering conditions. However, some peaks of the samples with lower sintering temperature and duration are merged indicating incomplete growth of the phase. The refined lattice parameters and the unit cell volume for different sintering conditions are tabulated in Table 3.1.

Table 3.1 Variation of lattice parameters and unit cell volume at different sintering conditions

Sintering Conditions	a (Å)	b (Å)	c (Å)	Volume (Å^3)
1150 °C; 20 h	6.5198	5.6101	6.9338	253.62
1200 °C; 20 h	6.5398	5.5728	6.9253	252.39
1250 °C; 20 h	6.5374	5.5397	6.9001	249.89
1300 °C; 20 h	6.4050	5.5566	6.8005	242.03
1300 °C; 10 h	6.4106	5.5595	6.8112	242.75
1300 °C; 2 h	6.3858	5.5435	6.7648	239.47

The lattice parameters and unit cell volume of $Ba_5SmTi_3Nb_7O_{30}$ compound are observed to decrease with increase in sintering temperature. Further, it is observed that $Ba_5SmTi_3Nb_7O_{30}$ samples sintered at above mentioned sintering conditions have orthorhombic crystal with a tungsten-bronze type structure at room temperature.

Temperature variation of X-ray diffraction

To investigate the structural change upon the phase transition from ferroelectric

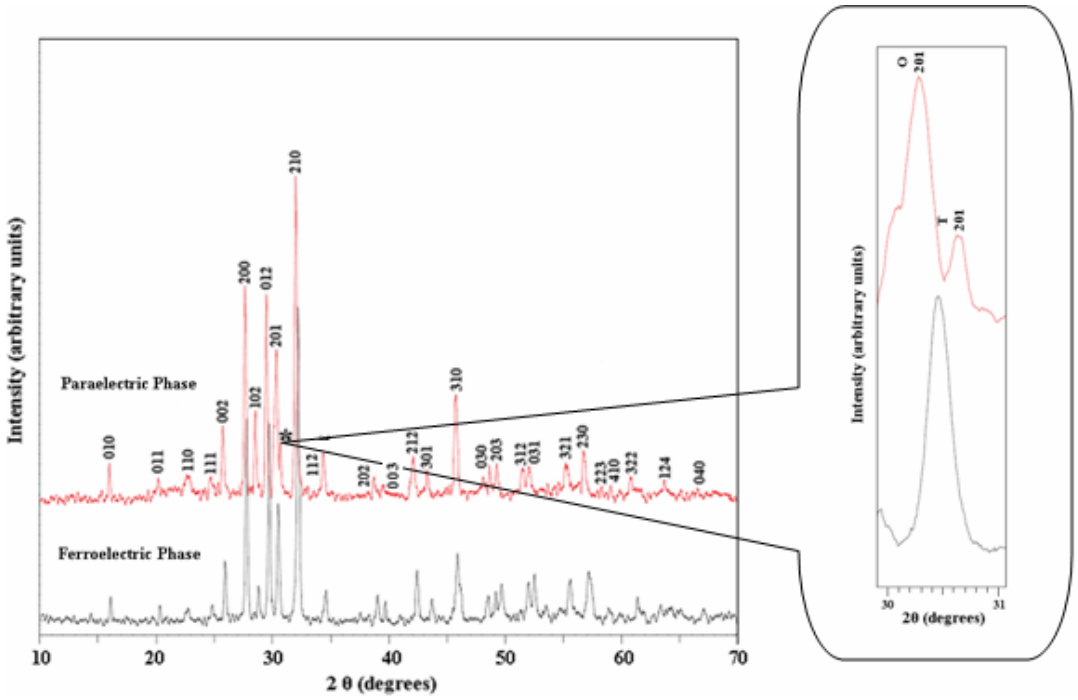

Fig. 3.3 XRD pattern of ferroelectric and parelectric phase in $Ba_5SmTi_3Nb_7O_{30}$ compound

to paraelectric phase (discussed in Section 3.2.3.1), room temperature (ferroelectric phase) as well as high temperature (paraelectric phase) X-ray diffraction analysis was undertaken for $Ba_5SmTi_3Nb_7O_{30}$ sample sintered at 1300 °C for 10 hours (Fig. 3.3). It is observed from the figure that there is tetragonal splitting of (201) peak as we move from ferroelectric to paraelectric phase in $Ba_5SmTi_3Nb_7O_{30}$ compound [8,9]. This indicates that the orthorhombic crystal structure in ferroelectric phase changes to tetragonal crystal structure in paraelectric phase of $Ba_5SmTi_3Nb_7O_{30}$ compound.

3.2.2.2 SEM analysis

Fig. 3.4 (a)-(f) shows the surface morphology of the samples sintered at different sintering conditions using scanning electron microscope.

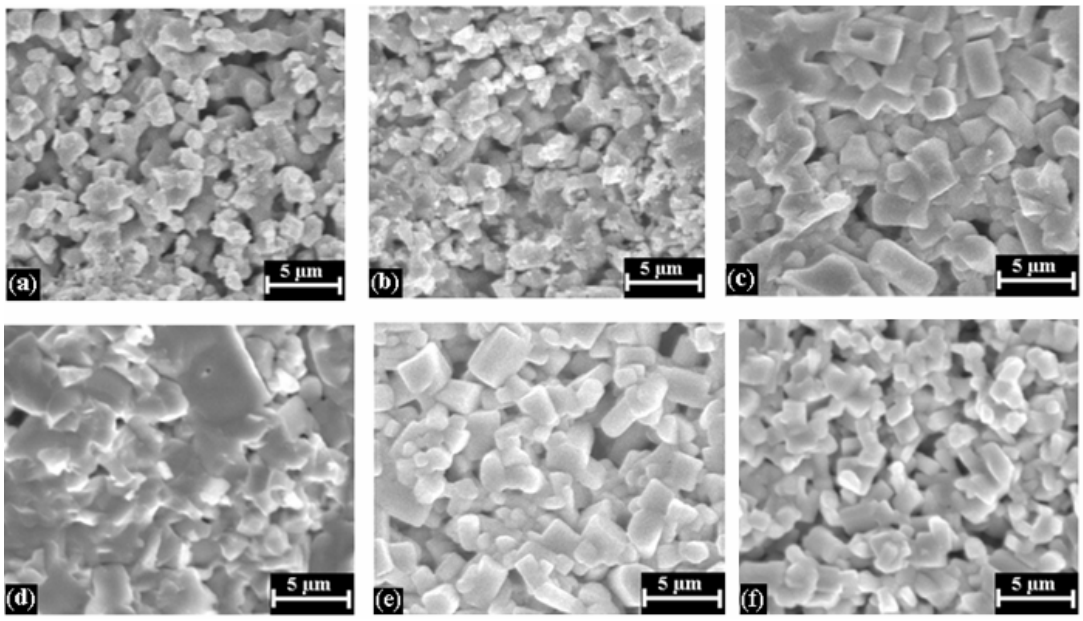

Fig. 3.4 SEM micrographs of the samples sintered at (a) 1150 °C; 20 h (b) 1200 °C; 20 h (c) 1250 °C; 20 h (d) 1300 °C; 20 h (e) 1300 °C; 10 h (f) 1300 °C; 2 h

A careful observation of the micrographs reveals porous and loosely packed grains for the samples sintered at lower sintering temperature and duration. At higher sintering temperature and duration, i.e., 1300 °C for 20 hours it can be seen that the grains diffuse together in the region of contact causing gradual disappearance of grain boundaries [10,11]. However, in the sample sintered at 1300 °C for 10 hours, a microstructure with densely packed grains with sharp and distinct grain boundaries are observed. Also, it is observed that there is an increase in the grain size with increasing sintering temperature and duration. The average grain size increases from nearly 1.4 µm and 1.6 µm in the samples sintered at 1150 °C for 20 hours and 1300 °C for 2 hours respectively to nearly 4.2 µm in the sample sintered at 1300 °C for 20 hours.

3.2.2.3 Relative Density

Fig. 3.5 shows the variation of relative density with sintering temperature and duration of the studied samples.

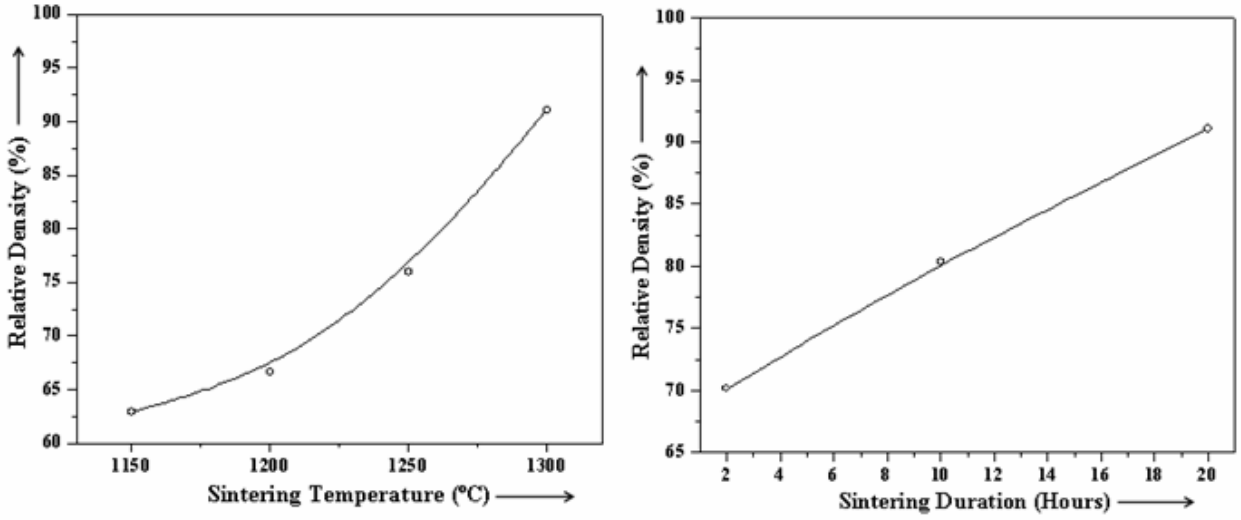

(a) (b)

Fig. 3.5 Variation of relative density with (a) sintering temperature and (b) sintering duration

It is observed that the relative density of the samples increases with the increase in the sintering temperature and duration. This observed variation can be understood in terms of the grain size and porosity observed in SEM micrographs [12,13]. As seen in the SEM micrographs (Fig. 3.4), the samples sintered at lower sintering temperatures and for shorter durations exhibit a poor microstructure with higher porosity causing lower density whereas increase in sintering temperature and duration results in the formation of densely packed grains of larger grain size and highly reduced porosity increasing the density.

3.2.3 Electrical Characterization

3.2.3.1 Dielectric studies

The dielectric properties i.e. dielectric constant (ε_r') and dielectric loss (tan δ) of the studied samples were measured. The variation of ε_r' and tan δ as a function of temperature at 1 kHz, 10 kHz and 100 kHz frequencies and the variation ε_r' and tan δ with frequency at room temperature for different sintering conditions were measured and is presented below.

Variation of ε_r' with temperature: Curie temperature

Fig. 3.6 shows the temperature dependence of dielectric constant (ε_r') at the frequencies 1 kHz, 10 kHz and 100 kHz for the samples sintered at different sintering conditions. For all the sintering conditions, the compound show dielectric anomaly at a temperature called the Curie temperature (T_c) indicating the occurrence of ferroelectric–paraelectric phase transition. The Curie temperature is the same at all the frequencies indicating the non-relaxor behaviour of the compound for all the sintering conditions.

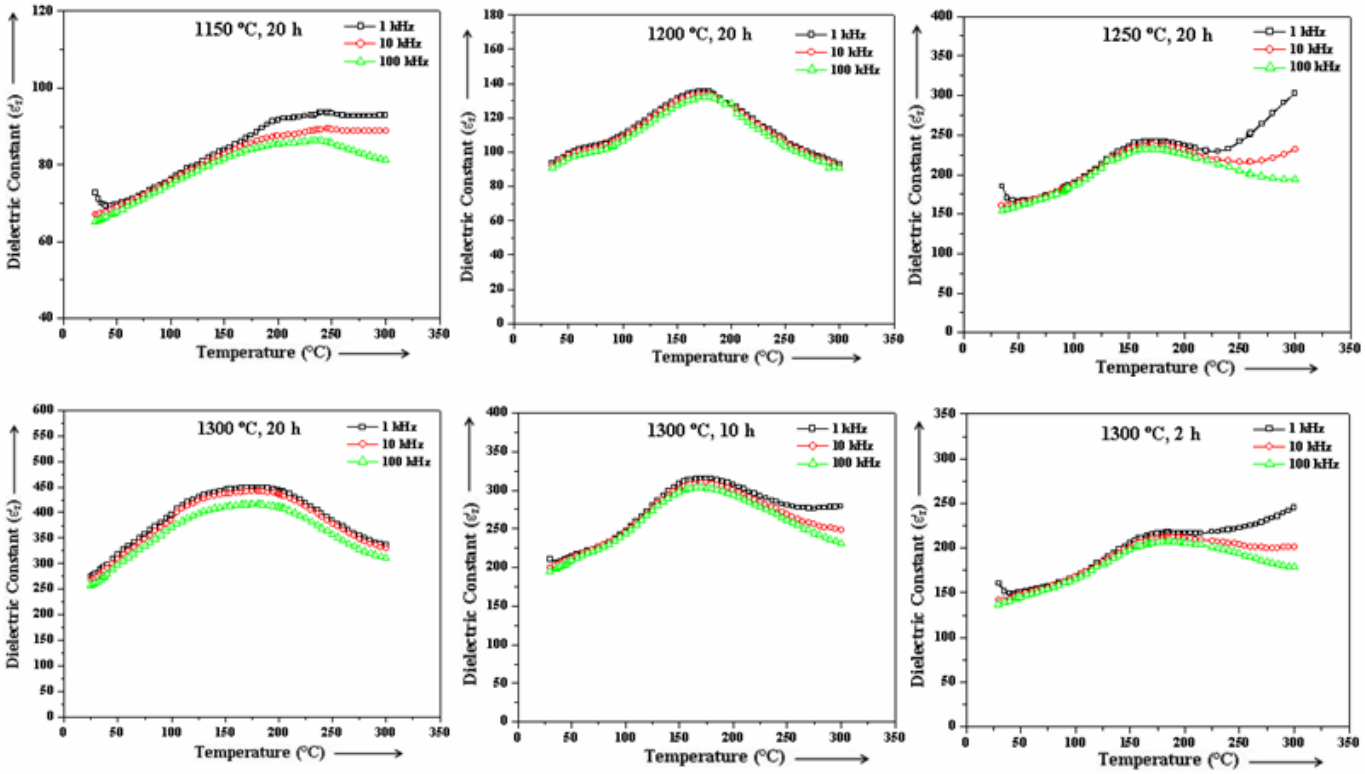

Fig. 3.6 Variation of dielectric constant (ε_r') with temperature at different sintering conditions

To see the effect of sintering temperature and duration on the variation of dielectric constant with temperature, the curves have been plotted in Fig. 3.7 at three different frequencies of 1 kHz, 10 kHz and 100 kHz. Also, the variation of dielectric constant (ε_r') at the Curie temperature (T_c) at these frequencies with sintering temperature and duration is shown in Fig. 3.8. From these figures, it is observed that the dielectric constant increases with increase in sintering temperature and sintering duration. The increase in ε_r' can be understood by the increase in the grain size with increase in sintering temperature and duration. The higher sintering temperature for longer duration increases the average grain size, making the domain wall motion easier resulting in an increased polarization and subsequently increasing the dielectric constant [14]. Also, it is known that these TB structured compounds are expected to

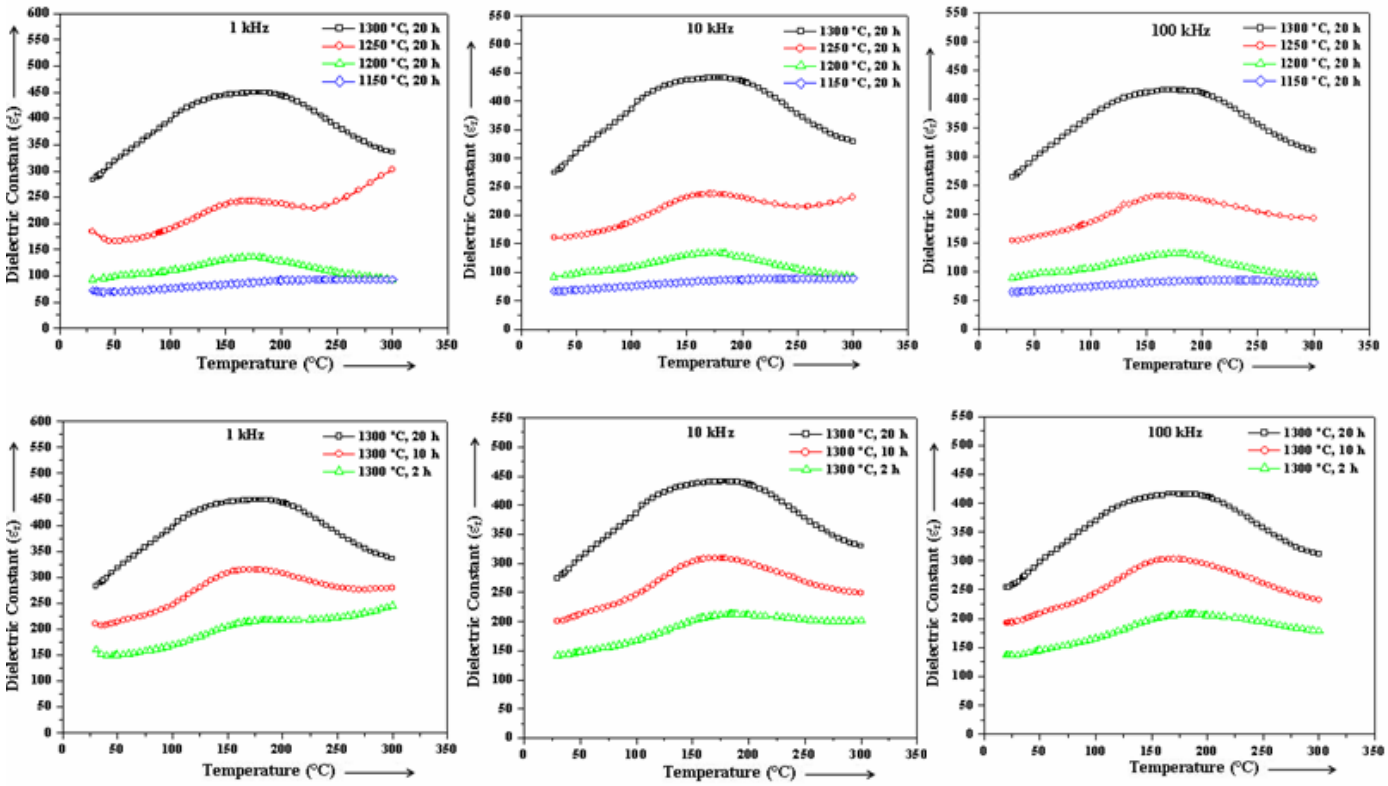

Fig. 3.7 Variation of dielectric constant (ε_r') with temperature of $Ba_5SmTi_3Nb_7O_{30}$ samples at three selected frequencies 1 kHz, 10 kHz and 100 kHz prepared at different sintering conditions

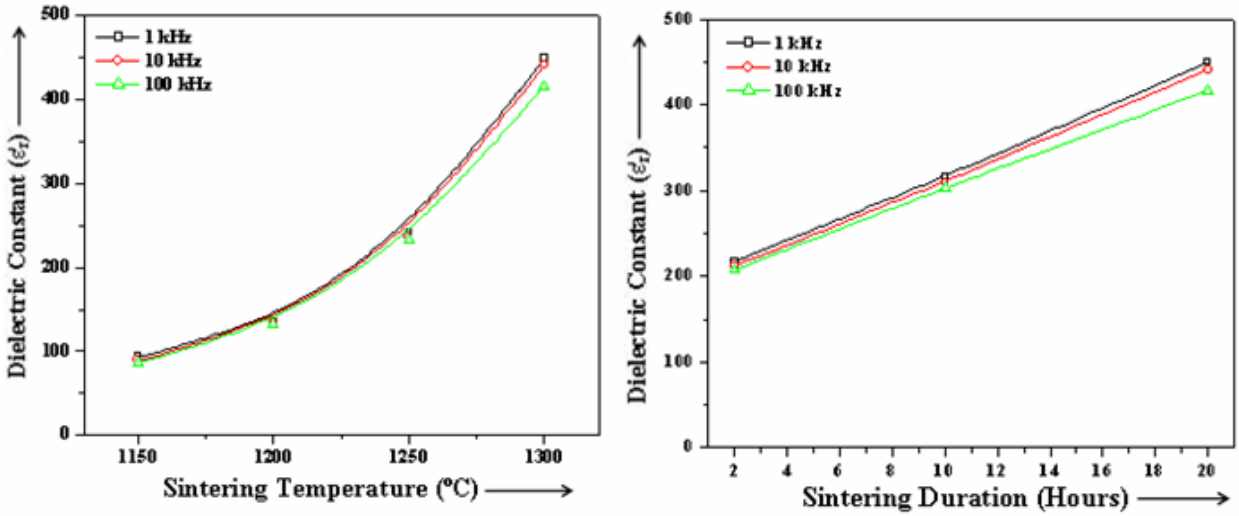

Fig. 3.8 Variation of ε_r' (at T_c) with (a) sintering temperature and (b) sintering duration

lose oxygen during sintering at high temperature [15,16] as per the Kröger and Vink notation can be represented as [17]:

$$O_o \rightarrow \frac{1}{2} O_2 \uparrow + V_o^{\bullet\bullet} + 2e^-$$

where $V_o^{\bullet\bullet}$ denotes oxygen vacancies. The defects such as oxygen vacancies $V_o^{\bullet\bullet}$, act as space charge [18]. Therefore, as the sintering temperature and duration is increased, more and more oxygen vacancies are created. The increase in ε_r' value is known to be related to the oxygen vacancies created during sintering [19]. This could be another possible cause for the increase in ε_r' as sintering temperature and duration of the $Ba_5SmTi_3Nb_7O_{30}$ samples is increased.

In all the samples, the broad dielectric peaks indicate the diffuse nature of the phase transition. The diffusivity constant or degree of disorderness (γ) has been calculated using the formula [20]:

$$\ln\left(\frac{1}{\varepsilon_r'} - \frac{1}{\varepsilon_{r\,\max}'}\right) = \gamma \ln (T\text{-}T_c) + \text{constant} \qquad (3.1)$$

where $\varepsilon'_{r\,max}$ is the maximum value of ε'_r at $T = T_c$. The values of γ have been calculated from the slope of ln ($1/\varepsilon'_r$ - $1/\varepsilon'_{r\,max}$) versus ln (T-T_c) curve (Fig. 3.9) and are given in Table 3.2. For all the samples, γ is found to be between 1 (obeying Curie-Weiss law) and 2 (for completely disordered system) confirming the diffuse phase transition in all the samples. It is found to increase with sintering temperature and duration indicating increase in disorderness in the system with increase in sintering temperature and time. The increased values of γ is possibly due to the defects (here oxygen vacancy) induced disorderness [21,22] which increases with increase in sintering temperature and duration.

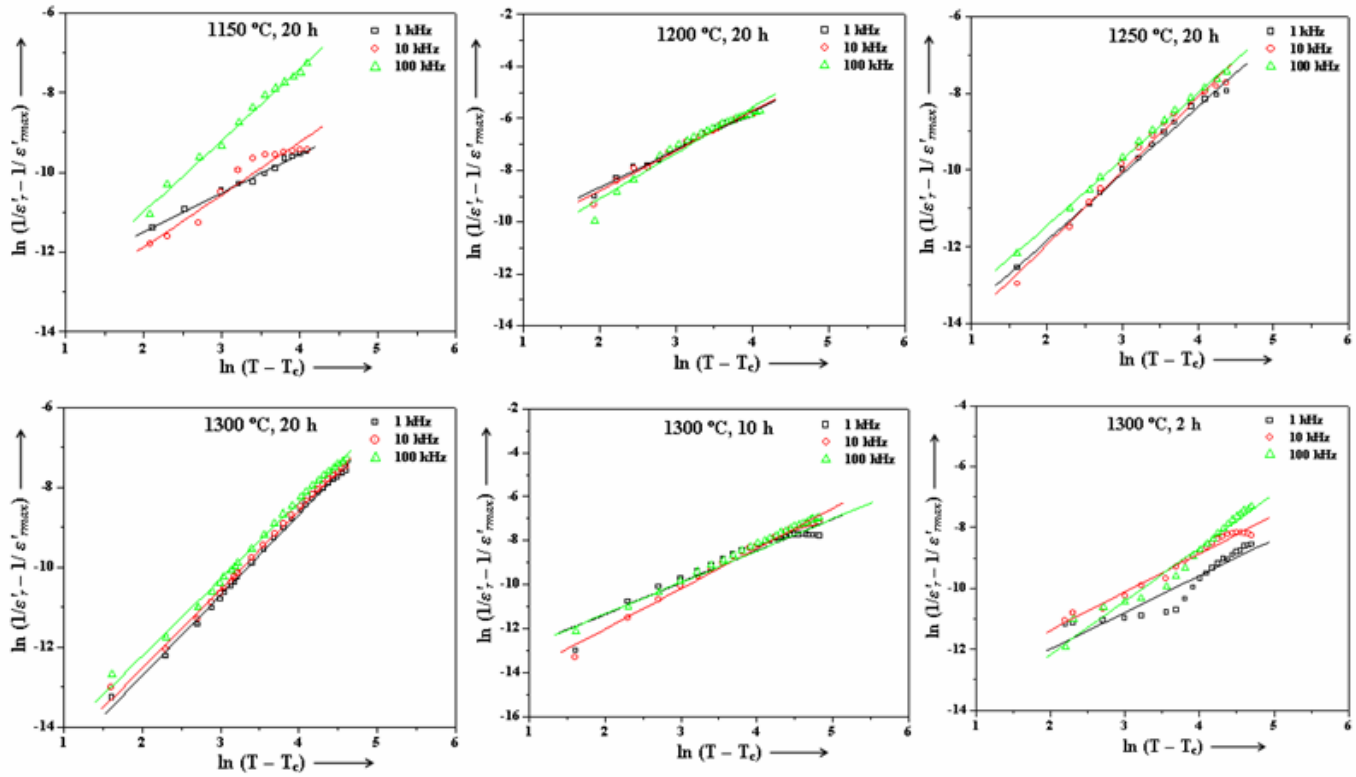

Fig. 3.9 Variation of ln ($1/\varepsilon'_r$ - $1/\varepsilon'_{r\,max}$) with ln (T-T_c) at different sintering conditions

Table 3.2 The calculated values of diffusivity constant (γ) at different sintering conditions

Sintering Conditions	Frequency (kHz)	γ
1150 °C; 20 h	1	1.08
	10	1.19
	100	1.34
1200 °C; 20 h	1	1.16
	10	1.25
	100	1.47
1250 °C; 20 h	1	1.35
	10	1.53
	100	1.73
1300 °C; 20 h	1	1.81
	10	1.89
	100	1.95
1300 °C; 10 h	1	1.28
	10	1.59
	100	1.71
1300 °C; 2 h	1	1.20
	10	1.31
	100	1.45

Variation of tan δ *with temperature*

Fig. 3.10 shows the variation of dielectric loss (tan δ) with temperature at three different frequencies 1 kHz, 10 kHz and 100 kHz for different sintering conditions.

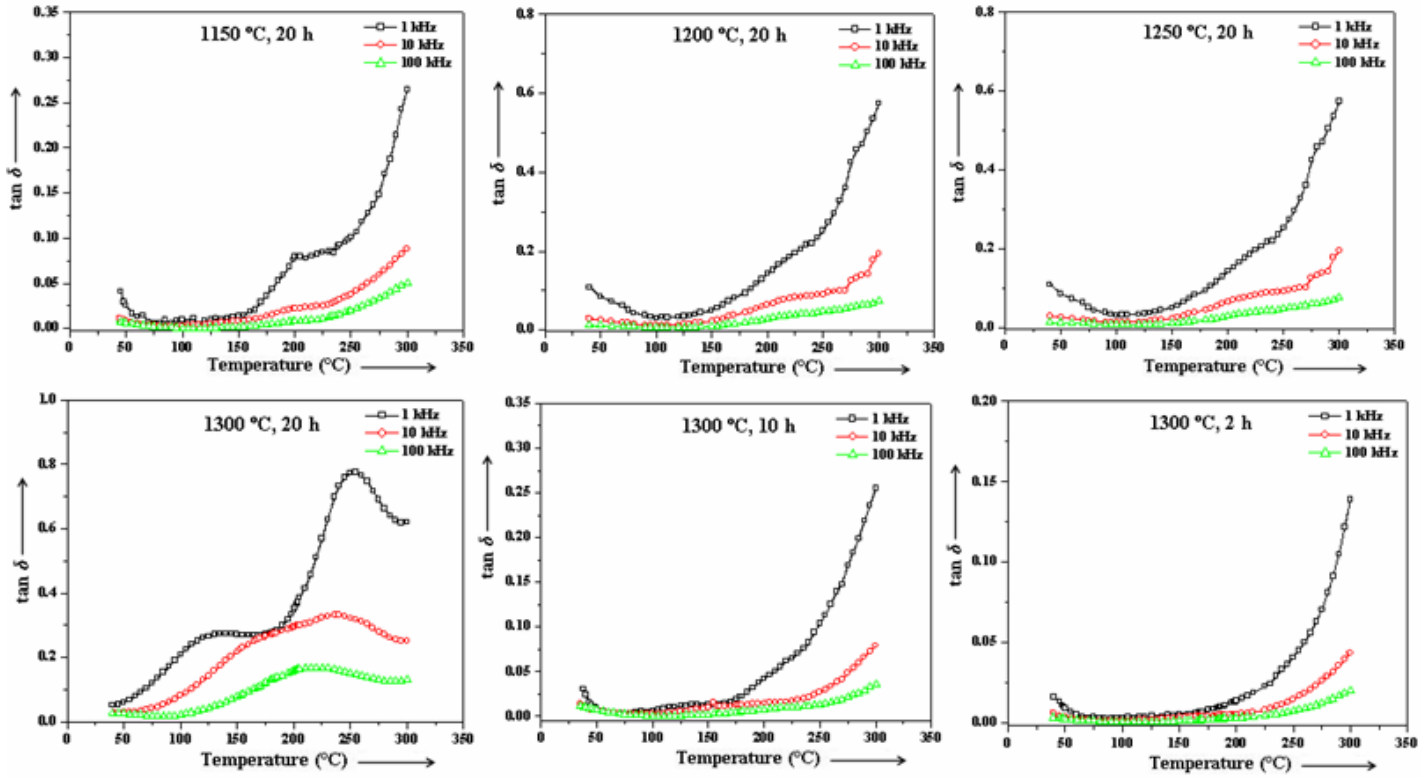

Fig. 3.10 Variation of dielectric loss (tan δ) with temperature at different sintering conditions

The variation of dielectric loss with temperature for the samples sintered at various sintering conditions show that the loss is almost constant at lower temperatures but at higher temperatures it increases sharply particularly at lower frequency. This sharp increase of dielectric loss in high temperature region may be attributed to the increased mobility of space charges arising from the vacancies (like oxygen vacancies) or defects in the sample [18].

To see the effect of sintering temperature and duration on the variation of dielectric loss with temperature, the curves have been plotted in Fig. 3.11 at three different frequencies of 1 kHz, 10 kHz and 100 kHz. It can be seen that the dielectric loss is increasing with increase in the sintering temperature and duration. The increase in the defects (here oxygen vacancy) induced disorderness in the system due to the increase in sintering temperature and duration possibly lead to the increase in the dielectric loss [23]. Unlike other samples, a peak is observed for the specimen

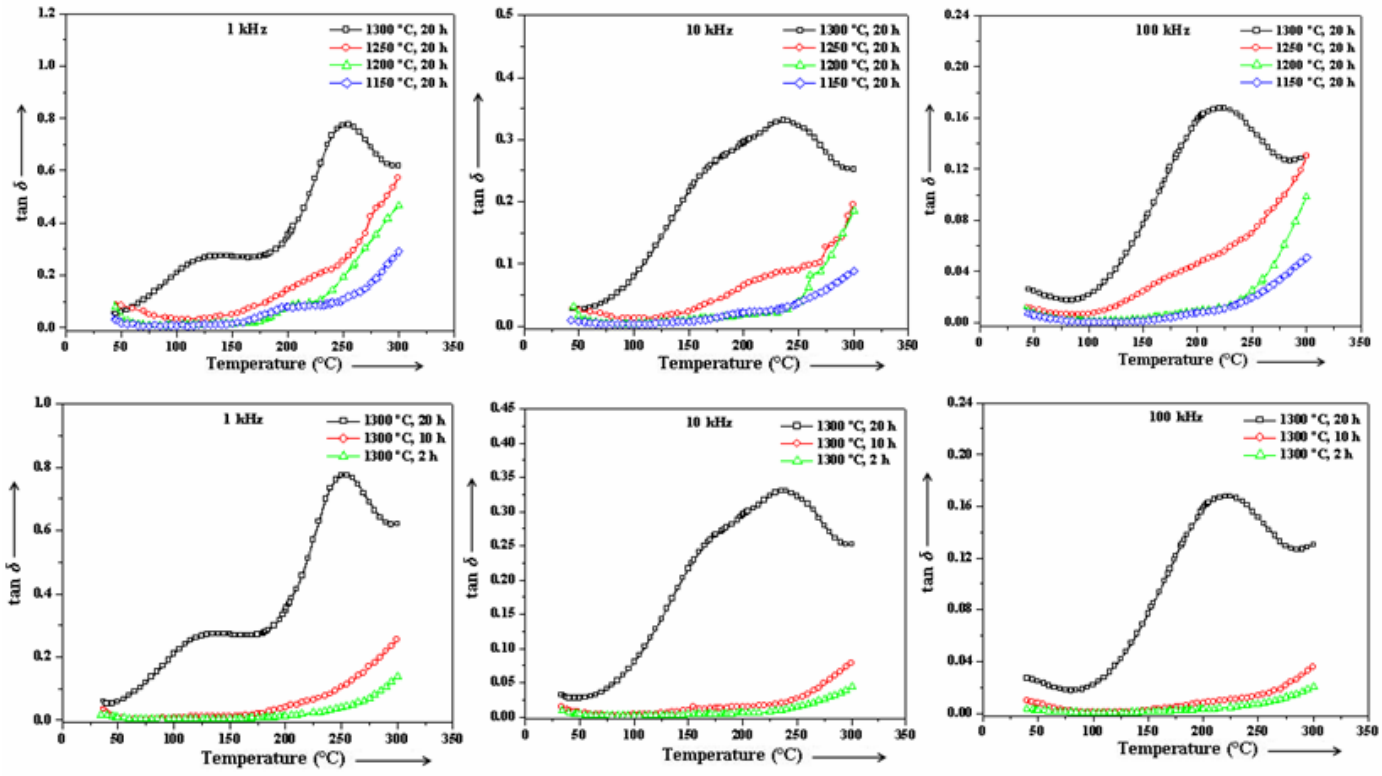

Fig. 3.11 Variation of dielectric loss (tan δ) with temperature of $Ba_5SmTi_3Nb_7O_{30}$ samples (prepared at different sintering conditions) at three selected frequencies (1 kHz, 10 kHz and 100 kHz)

sintered at 1300 °C for 20 hours. This could be the relaxation peak whose formation is attributed to the oxygen vacancies which are present in large concentration in this highly sintered sample of $Ba_5SmTi_3Nb_7O_{30}$ [24,25].

Variation of ε_r' and tan δ *with frequency*

Fig. 3.12 and Fig. 3.13 show the variation of dielectric constant (ε_r') and dielectric loss (tan δ) as a function of frequency in the range from 20 Hz to 500 kHz at room temperature respectively.

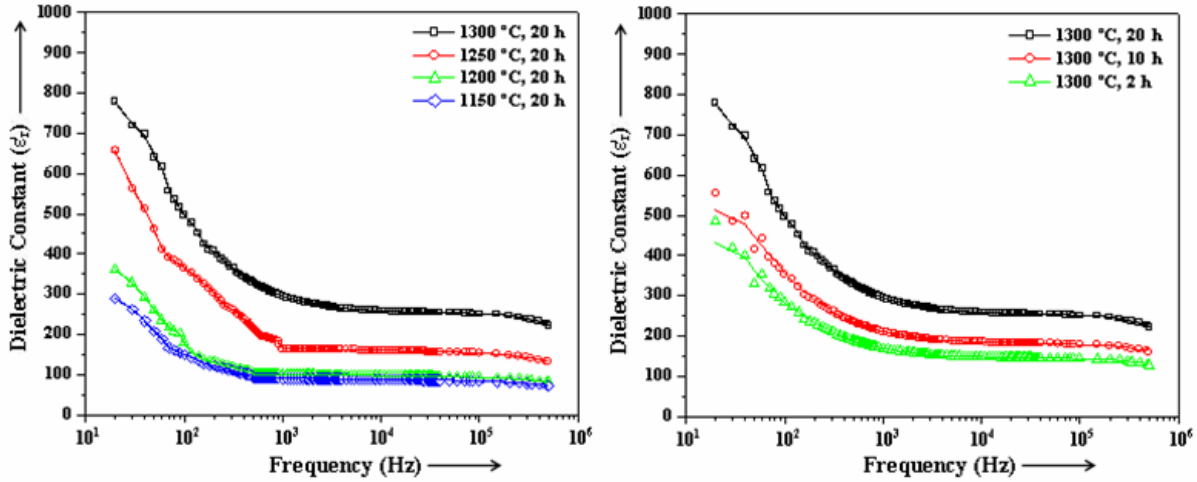

(a) (b)

Fig. 3.12 Variation of dielectric constant (ε_r') with frequency for the samples prepared at different (a) sintering temperatures and (b) sintering durations

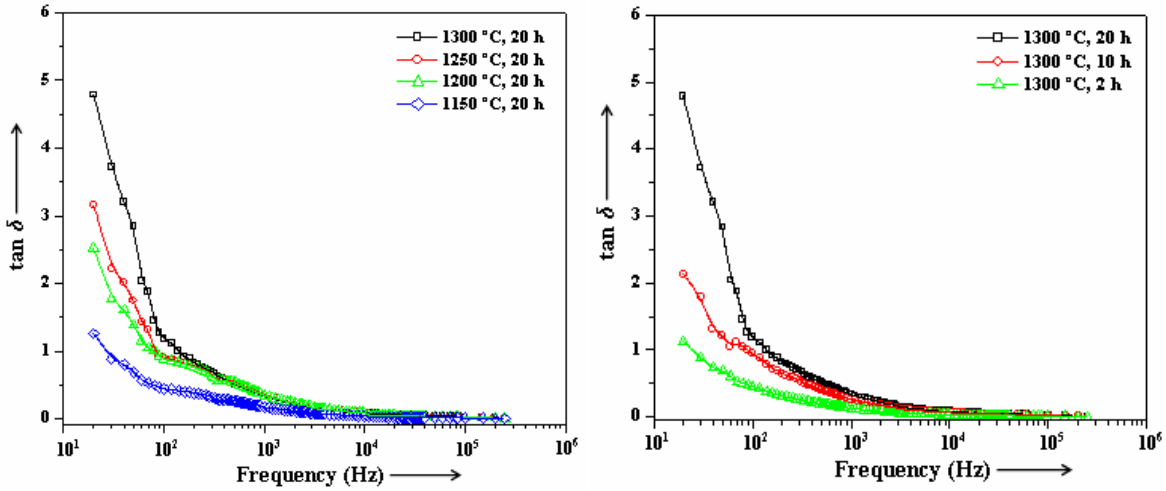

(a) (b)

Fig. 3.13 Variation of dielectric loss (tan δ) with frequency for the samples prepared at different (a) sintering temperatures and (b) sintering durations

It is observed in all the studied samples that both the dielectric constant and dielectric loss decreases upto about 1 kHz and remains nearly constant beyond this frequency. The dielectric constant of a material has polarization contributions from electronic, ionic, dipolar and space charge [26]. Response frequencies for ionic and electronic polarizations are ~ 10^{13} and 10^{15} Hz, respectively; and at frequencies beyond 1 kHz, contribution from space charge polarization is not expected [26]. Thus, the higher values of dielectric constant at lower frequencies can be attributed to the presence of defects such as oxygen vacancies, $V_o^{\bullet\bullet}$. These vacancies act as space charge which plays an important role in the polarization at lower frequencies [27,28]. Moreover, at lower frequencies, the dipoles can follow the field resulting in higher values of dielectric constant while at higher frequencies, the dipoles are unable to follow the rapidly changing field leading to the reduction in the values of dielectric constant.

Similar explanation can be given for the variation of dielectric loss as the source of dielectric loss in insulating ceramics is space charge polarization and/or domain wall relaxation [23].

3.2.3.2 Conductivity studies

DC conductivity

The variation of dc conductivity as a function of temperature for the studied samples is depicted in Fig. 3.14. It can be seen from the figure that for all the samples in the low temperature region the conductivity is almost constant. But at

higher temperatures, it increases with temperature confirming that the compound has negative temperature coefficient of resistance (NTCR) behaviour, a typical characteristic of dielectric materials [29]. The nature of variation of dc conductivity

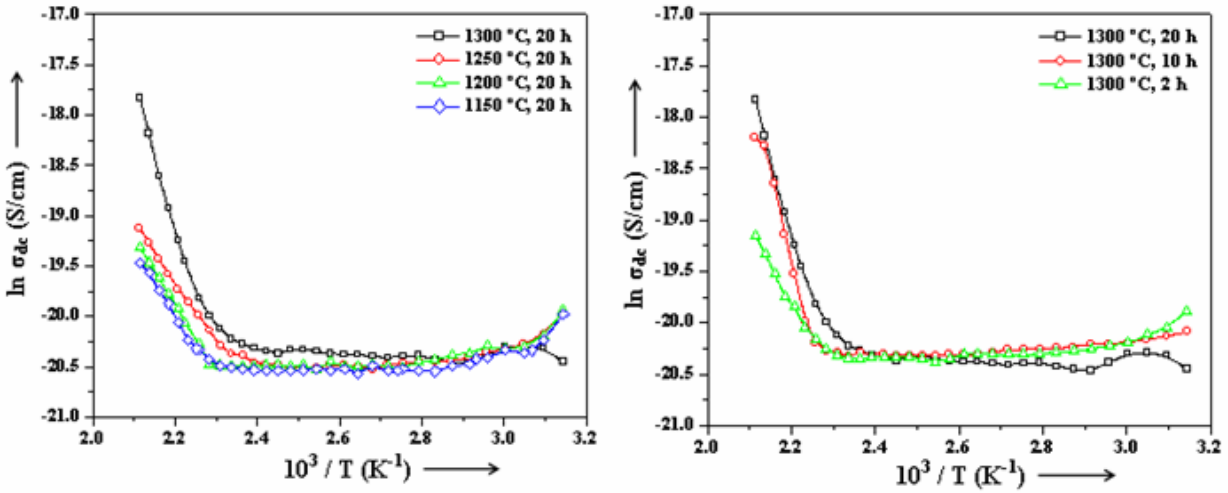

(a) (b)

Fig. 3.14 Variation of dc conductivity with temperature for samples prepared at different (a) sintering temperatures and (b) sintering durations

at higher temperature is linear and follows the Arrhenius relationship:

$$\sigma = \sigma_o \exp\left(\frac{-E_a}{k_B T}\right) \tag{3.2}$$

where σ indicates the conductivity, E_a the activation energy and k_B the Boltzmann constant. The activation energies have been calculated in the higher temperature region using this relation and are given in Table 3.3. The dc conductivity is found to increase with increase in sintering temperature and duration which is consistent with the observed variation of dielectric loss as the contribution of dc conductivity to the measured loss is expressed by Eq. (2.19).

AC conductivity

The temperature variation of ac conductivity at the selected frequencies of 1 kHz, 10 kHz and 100 kHz for $Ba_5SmTi_3Nb_7O_{30}$ samples sintered at different sintering conditions is shown in Fig. 3.15.

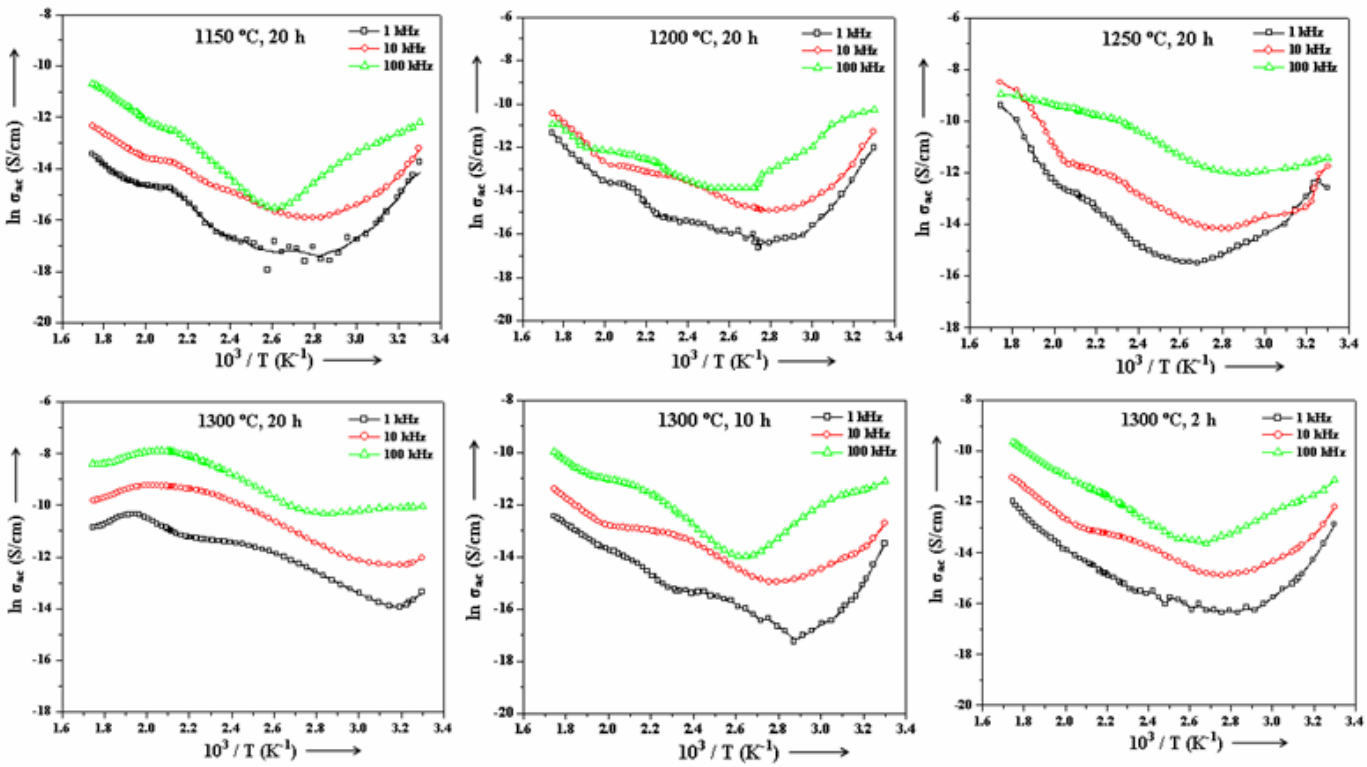

Fig. 3.15 Variation of ac conductivity with temperature at different sintering conditions

For all the samples, there is a change in slope in the curve which can be attributed to the difference in activation energy in the paraelectric and ferroelectric phases. The activation energies, evaluated in the ferroelectric phase (low temperature) and paraelectric phase (high temperature) using Eq. (3.2) are summarized in Table 3.3. To see the effect of sintering temperature and duration on the variation of ac conductivity with temperature, the curves have been plotted in Fig. 3.16 at three different frequencies of 1 kHz, 10 kHz and 100 kHz. It is observed that the ac conductivity increases with increase in sintering temperature and duration which is possibly due to the increased number of oxygen vacancies.

Table 3.3 Activation energies (E_a) as calculated from dc and ac conductivity at different sintering conditions

Sintering Conditions	Frequency (kHz)	E_a (eV) (ac conductivity)		E_a (eV) (dc conductivity)
		Ferroelectric	Paraelectric	
1150 °C; 20 h	1	0.58	0.49	0.52
	10	0.44	0.36	
	100	0.42	0.31	
1200 °C; 20 h	1	0.65	0.40	0.59
	10	0.54	0.34	
	100	0.49	0.26	
1250 °C; 20 h	1	0.56	0.47	0.71
	10	0.46	0.34	
	100	0.27	0.12	
1300 °C; 20 h	1	0.48	0.20	1.03
	10	0.24	0.19	
	100	0.17	0.10	
1300 °C; 10 h	1	0.54	0.37	1.13
	10	0.40	0.34	
	100	0.34	0.26	
1300 °C; 2 h	1	0.42	0.41	0.98
	10	0.39	0.36	
	100	0.31	0.28	

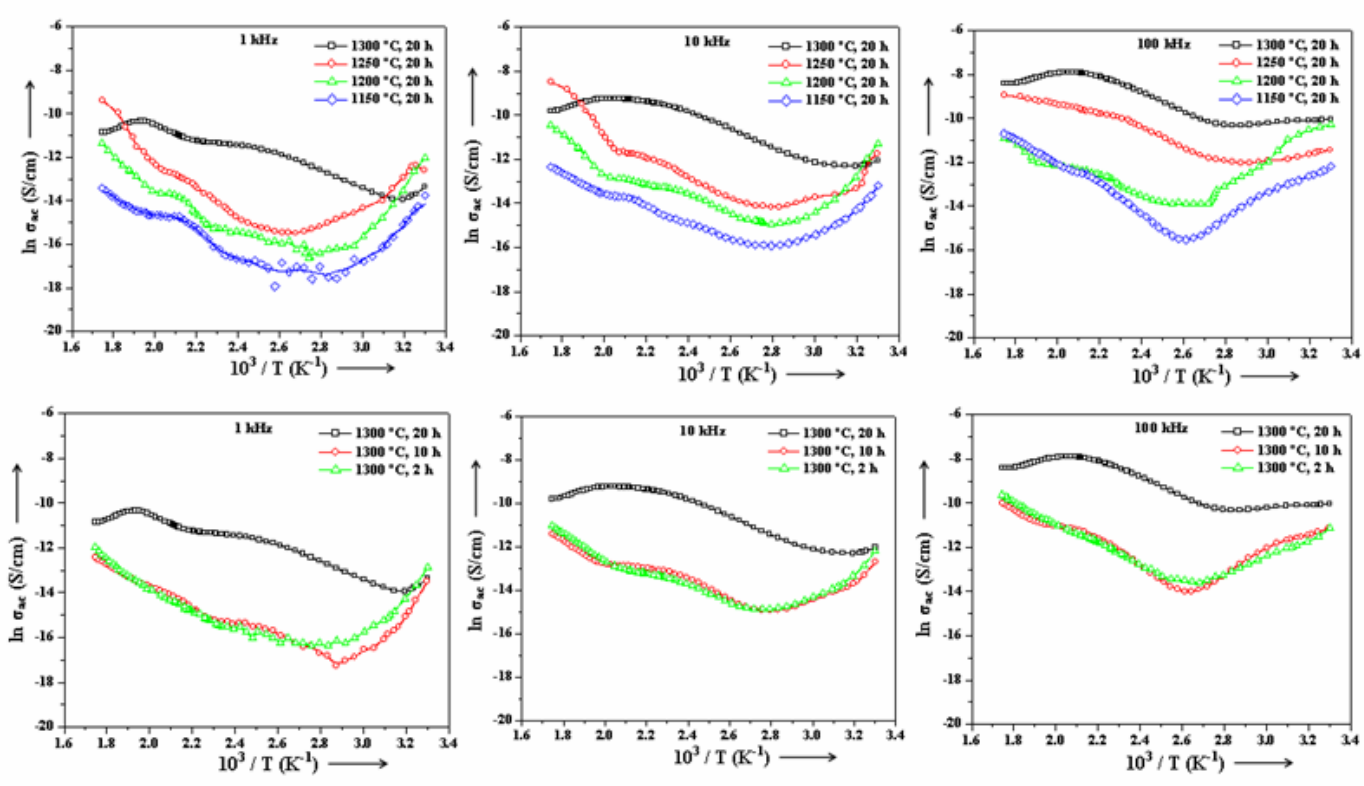

Fig. 3.16 Variation of ac conductivity with temperature at three selected frequencies (1 kHz, 10 kHz and 100 kHz)

Electric transport properties of the polycrystalline ceramics are known to be strongly affected by their microstructures. It is also known that electrical properties are dependent on the inherent defects or charge carriers (like oxygen vacancies) which are produced during sintering [30]. The presence of these oxygen vacancies is corroborated in the dielectric studies also. The oxygen vacancies ($V_o^{\bullet\bullet}$) is effectively doubly positively charged and is considered to be the most mobile intrinsic ionic defect in the ceramic oxides [31,32]. Their motion is manifested by an enhanced conductivity and activation energy nearly 1 eV [33]. As their number increases with the increase in sintering temperature and time, it results in the enhancement of conductivity. Also, the contribution of ac conductivity (σ_{ac}) to the measured dielectric loss (ε_r'') can be understood by the following equation:

$$\sigma_{ac}(\omega) = \omega\varepsilon_o\varepsilon_r''(\omega) \qquad (3.3)$$

at a given frequency ω (= $2\pi f$). Since the dielectric loss in these samples is found to increase with the increase in the sintering temperature and time (Fig. 3.11) so is the ac conductivity as suggested by Eq. (3.3) and observed indeed.

3.2.3.3 Impedance analysis

Fig. 3.17 shows the impedance (Z'-Z'') plots at some selected temperatures of the studied specimens. All the semicircles in the Cole-Cole plots exhibit some depression instead of a semicircle centered on the x-axis. Such behaviour is indicative of non-Debye type of relaxation and it also manifests that there is a distribution of relaxation time instead of a single relaxation time in the material

[34]. It can be noted that unlike all other sintering conditions, there is presence of two semicircles at higher temperature (375 °C) in the sample sintered at 1300 °C for 10 hours. This implies the presence of both grain (bulk property) and grain boundary effects for this particular sintering condition, which can be represented by two parallel RC circuits connected in series as shown in Fig. 3.17. This is consistent with the already observed SEM micrographs (Fig. 3.4) where a microstructure with sharp and distinct grain boundaries is obtained only for this sintering condition. The value of bulk resistances (R_b) at different temperatures for

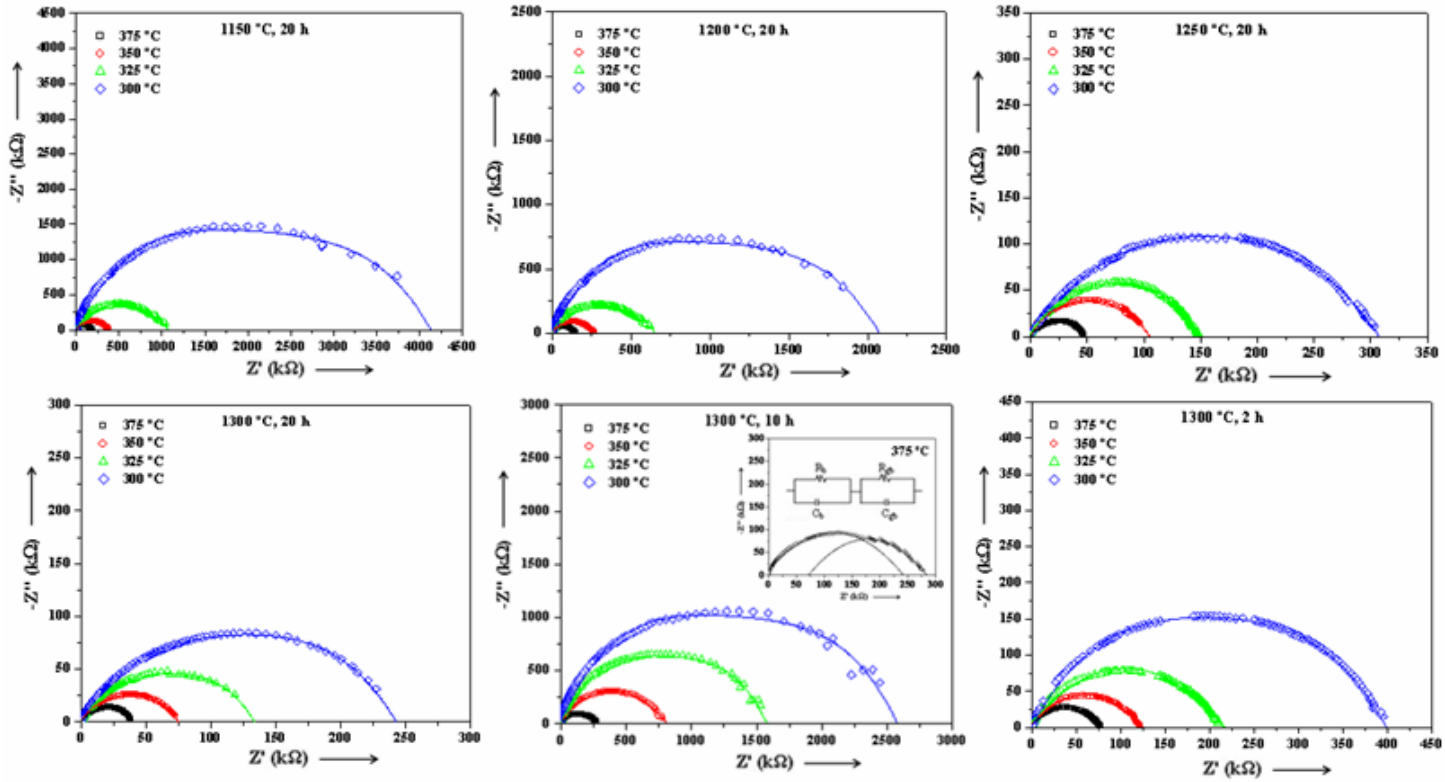

Fig. 3.17 Complex impedance spectrum (Cole-Cole or Nyquist plots) of $Ba_5SmTi_3Nb_7O_{30}$ at different temperatures for all the studied sintering conditions

samples sintered at various sintering conditions have been obtained from the intercept of the semicircular arcs on the real axis (Z') and are given in Table 3.4. It is observed that R_b decreases with rise in the temperature for all the samples. This again confirms the negative temperature coefficient of resistance (NTCR) behaviour of the $Ba_5SmTi_3Nb_7O_{30}$ compound at all the studied sintering conditions. From these values of R_b, the bulk conductivity, σ_{bulk} has been obtained by using Eq. (2.31) and its variation with temperature is shown in Fig. 3.18 for all the studied specimens. The respective capacitances (C_b and C_{gb}) due to the grain and grain boundary effects were calculated

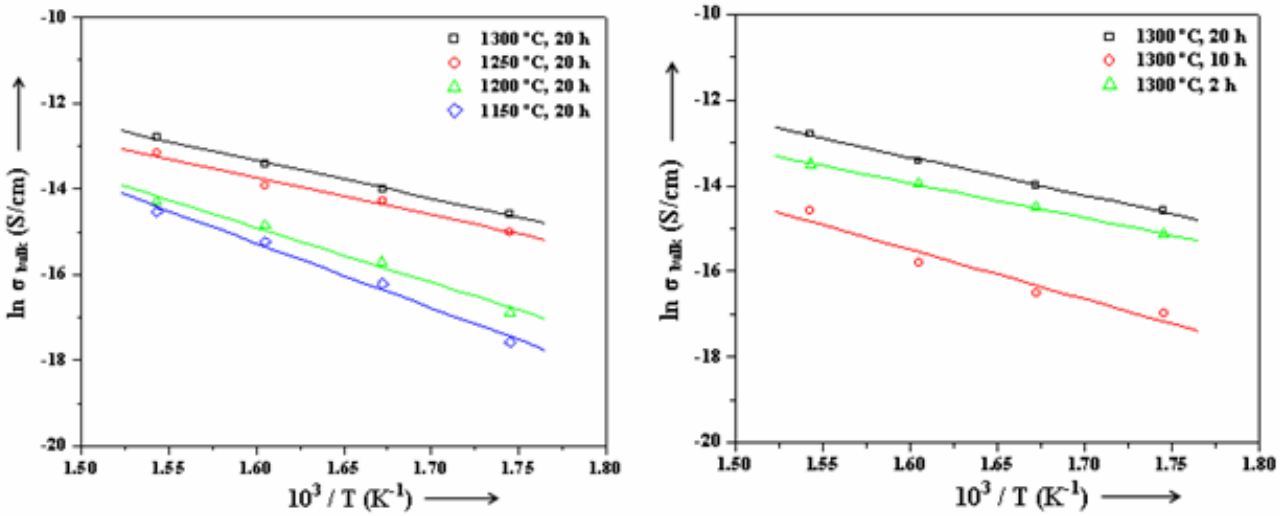

(a) (b)

Fig. 3.18 Variation of bulk conductivity with temperature for the samples prepared at different (a) sintering temperatures and (b) sintering durations

using the Eq. (2.30). The values of R_b, R_{gb}, C_b and C_{gb} obtained from Cole-Cole plots at different temperatures for various sintering conditions are listed in Table 3.4.

The relaxation time due to bulk effect (τ_b) was calculated using Eq. (2.30). Fig. 3.19 shows the temperature variation of τ_b for all the samples sintered at different sintering

Table 3.4 Various parameters obtained from the Cole-Cole plots

Measuring Temperature	300 °C		325 °C		350 °C		375 °C				E_a (eV)
Sintering Conditions	R_b (kΩ)	C_b (nF)	R_b (kΩ)	C_b (nF)	R_b (kΩ)	C_b (nF)	R_b (kΩ)	C_b (nF)	R_{gb} (kΩ)	C_{gb} (nF)	
1150 °C; 20 h	4112	0.24	1060	0.22	390	0.21	190	0.16	-	-	1.30
1200 °C; 20 h	2065	0.55	640	0.37	278	0.32	152	0.23	-	-	1.21
1250 °C; 20 h	307	4.32	150	2.21	105	1.65	47	1.03	-	-	1.11
1300 °C; 20 h	243	8.19	133	5.08	76	3.70	39	2.83	-	-	0.74
1300 °C; 10 h	2590	0.38	1610	0.35	800	0.31	240	0.30	45	3.85	0.95
1300 °C; 2 h	400	0.29	214	0.27	123	0.25	78	0.24	-	-	0.80

conditions. It is observed that the value of τ_b decreases with increase in temperature for all the samples and its temperature dependence follows the Arrhenius relation:

$$\tau_b = \tau_o \exp\left(\frac{-E_a}{k_B T}\right) \tag{3.4}$$

where τ_o is the pre-exponential factor, k_B is Boltzmann constant and E_a the activation energy. The value of activation energy (E_a) calculated using Eq. (3.4) is summarized in Table 3.4.

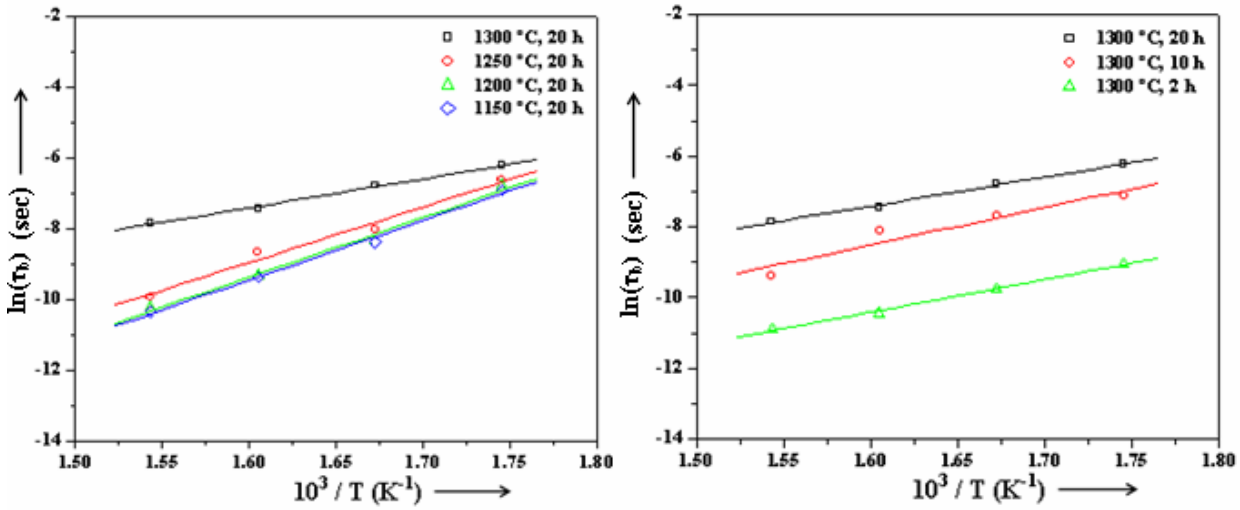

(a) (b)

Fig. 3.19 Variation of relaxation time with temperature for the samples prepared at different (a) sintering temperatures and (b) sintering durations

3.2.3.4 Ferroelectric studies

Fig. 3.20 shows the room temperature P-E hysteresis loops of $Ba_5SmTi_3Nb_7O_{30}$ compound prepared at different sintering conditions. The corresponding values of remanent polarization ($2P_r$) and coercive field ($2E_c$) are tabulated in Table 3.5. On comparing the loops, it is observed that a well-saturated hysteresis loop is obtained

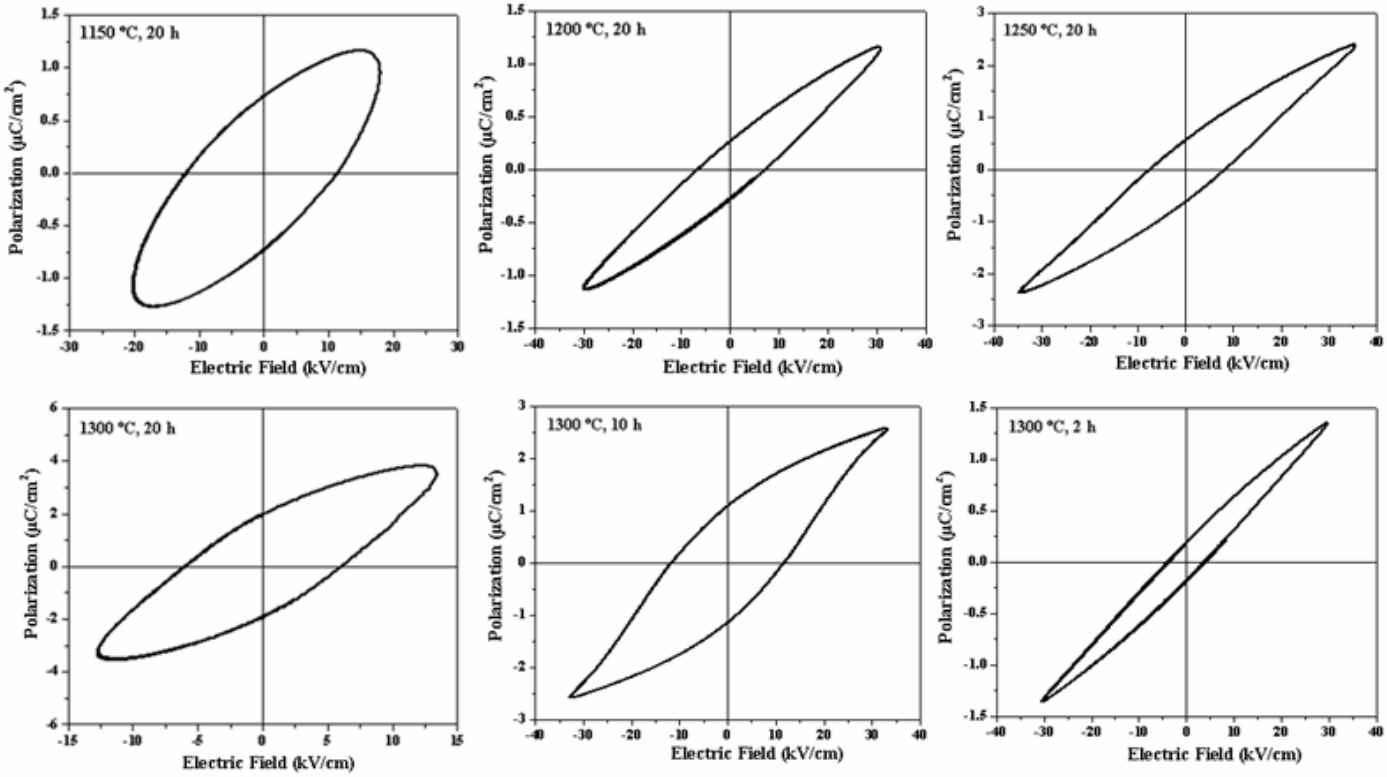

Fig. 3.20 P-E hysteresis loops of the studied samples

for the sample sintered at 1300 °C for 10 hours. It is known that P-E hysteresis loops are microstructure dependent [35]. A densely packed microstructure with uniformly distributed grains and sharp and distinct grain boundaries in the sample results in the formation of the well-defined hysteresis loop. This is indeed the case as seen in Fig. 3.4 (e) for the sample sintered at 1300 °C for 10 hours; for the sample sintered at higher sintering temperature and duration i.e. 1300 °C for 20 hours, a

lossy kind of hysteresis loop is obtained which could be correlated to the higher dielectric loss in the sample sintered at this sintering condition (Fig. 3.11).

Table 3.5 $2P_r$ and $2E_c$ of the samples sintered at different sintering conditions

Sintering Conditions	$2P_r$ ($\mu C/cm^2$)	$2E_c$ (kV/cm)
1150 °C; 20 h	1.4	23.5
1200 °C; 20 h	0.5	14.0
1250 °C; 20 h	1.2	15.5
1300 °C; 20 h	4.2	12
1300 °C; 10 h	2.3	23.3
1300 °C; 2 h	0.4	8.0

Temperature variation of P-E hysteresis loop

Fig. 3.21 shows the temperature variation of the P-E hysteresis loop of

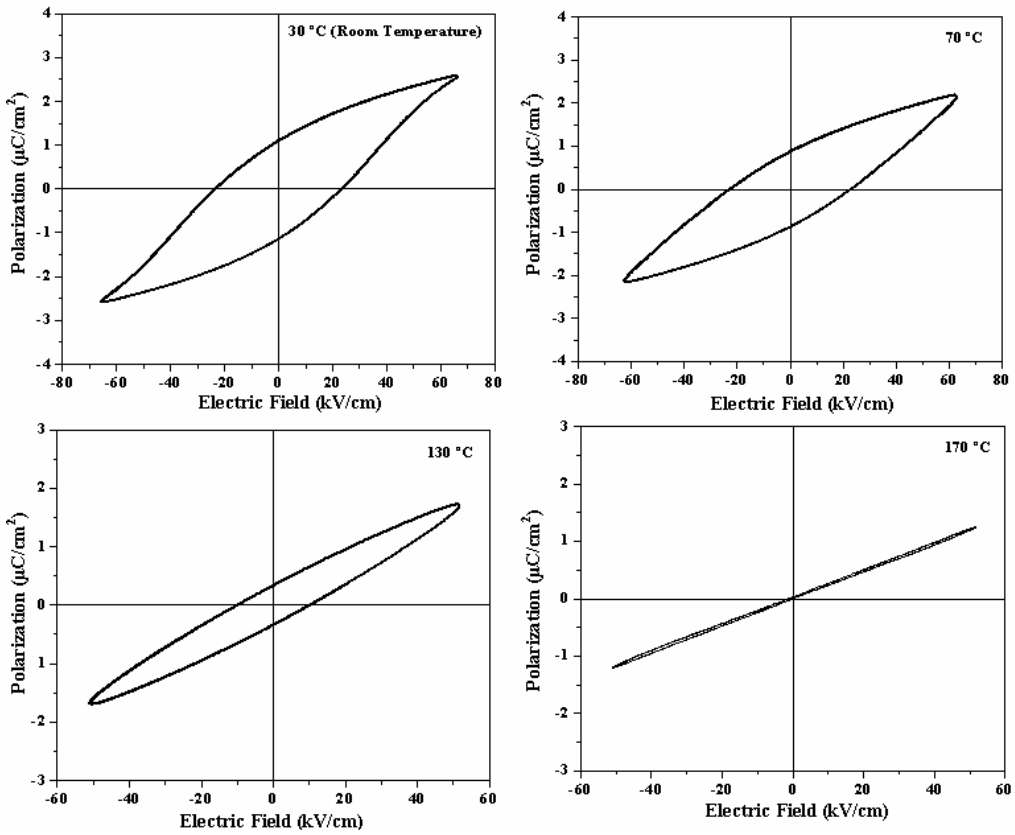

Fig. 3.21 Temperature variation of P-E hysteresis loop of $Ba_5SmTi_3Nb_7O_{30}$ sample sintered at 1300 °C for 10 hours

$Ba_5SmTi_3Nb_7O_{30}$ sample sintered at 1300 °C for 10 hours. It can be seen that the remanent polarization ($2P_r$) value decreases with increasing temperature and finally it becomes zero around the transition temperature ($T_c \approx 170$ °C) of the compound.

3.2.3.5 Pyroelectric studies

The temperature variation of pyroelectric coefficient (P_T) calculated using Eq. (2.37) is shown in Fig. 3.22. For all the samples, the pyroelectric current as

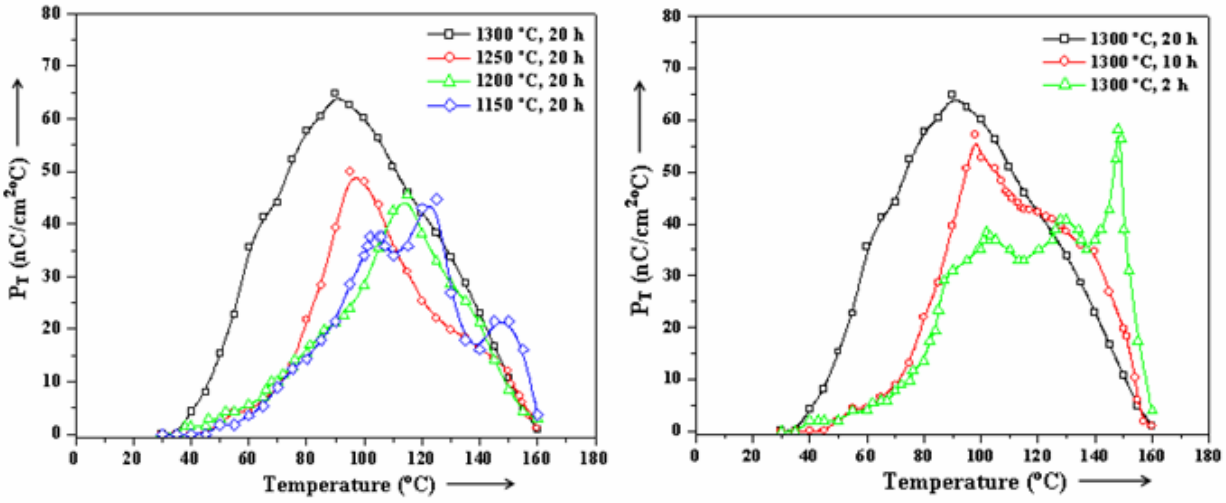

(a) (b)

Fig. 3.22 Temperature variation of pyroelectric coefficient (P_T) for samples prepared at different (a) sintering temperatures and (b) sintering durations

well as the pyroelectric coefficient passes through a peak at a temperature lower than the ferroelectric transition temperature (T_c). The pyroelectric current is generated due to a change in the spontaneous polarization with temperature [36]. It is known that in diffuse kind of phase transition, the rate of change of spontaneous polarization with temperature is maximum at temperature well below T_c [36] which is in conformity with the observations in the present work. The

pyroelectric coefficient is found to increase with increase in sintering temperature and time. At lower sintering temperature and duration, some fluctuations in the peak value of the pyroelectric coefficient can be seen which can be correlated to the porous and loosely packed grains in these samples (Fig. 3.4) [37].

3.2.3.6 Piezoelectric studies

Fig. 3.23 shows the variation of the piezoelectric coefficient, d_{33} with sintering temperature and duration of the prepared $Ba_5SmTi_3Nb_7O_{30}$ samples. It is observed

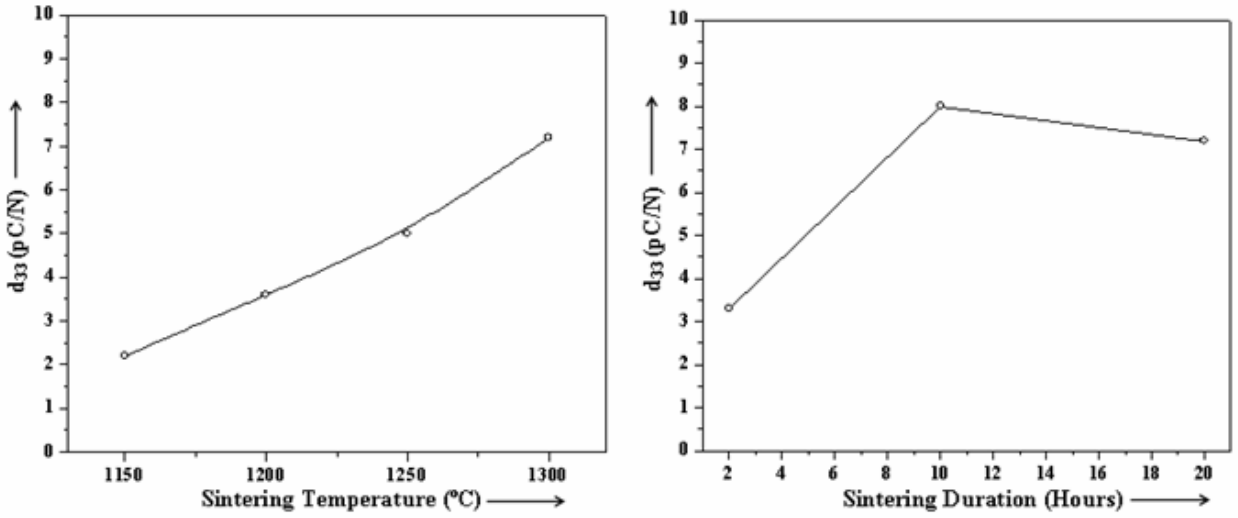

(a) (b)

Fig. 3.23 Temperature variation of piezoelectric coefficient (d_{33}) for samples prepared at different (a) sintering temperatures and (b) sintering durations

that d_{33} value increases with increase in sintering temperature, the maximum value of d_{33} is observed in the sample sintered at 1300 °C for 10 hours which could be ascribed to the sharp and distinct grain boundaries seen in this sample (Fig. 3.4 e) as it would results in the increase of internal electric fields generated by space charge layers at grain boundaries [38]. The maximum d_{33} value obtained at this sintering condition is 8 pC/N. Although, this value is much smaller in comparison to the

values reported for lead based materials (e.g. PZT with d_{33} ~ 400 pC/N) [39] but it is higher than d_{33} (~2 pC/N) of Quartz [40].

3.3 CONCLUSIONS

Based on the above observations and discussions the following conclusions can be drawn:

(i) The optimized calcination condition for the preparation of $Ba_5SmTi_3Nb_7O_{30}$ compound is 1100 °C for 20 hours.

(ii) The optimized sintering condition for the preparation of $Ba_5SmTi_3Nb_7O_{30}$ compound is 1300 °C for 10 hours.

(iii) The synthesized $Ba_5SmTi_3Nb_7O_{30}$ compound at this optimum calcination and sintering condition has orthorhombic crystal structure at room temperature with average grain size of about 2 μm.

(iv) The compound shows a diffuse type of ferroelectric-paraelectric phase transition exhibiting non-relaxor behaviour with a Curie temperature (T_c) of 170 ºC.

(v) The compound has negative temperature coefficient of resistance (NTCR) behaviour.

(vi) The remanent polarization ($2P_r$) value of the sample prepared at the optimum sintering condition is found to be 2.3 μC/cm^2.

(vii) Maximum pyroelectric coefficient (P_T) of the sample prepared at the optimum sintering condition is found to be 57.1 nCcm^{-2} °C^{-1}.

(viii) The piezoelectric coefficient (d_{33} value) at the optimum sintering condition is found to be 8 pC/N.

REFERENCES

[1] J. W. Kim, J. G. Heinrich, J. Eur. Ceram. Soc. **25** (2005) 1637.

[2] H. Kungla and M. J. Hoffmann, J Appl. Phys. **107** (2010) 054111-1.

[3] A. Yang, C. A. Wang, R. Guo, Y. Huang, C. W. Nan, Ceram. Int. **36** (2010) 549.

[4] B. Zhang, D. Q. Xiao, W. J. Wu, J. Li, X. L. Huang, Y. Pei, L. Wu, J. G. Zhu and Z. J. He, IEEE International Symposium on Applications of Ferroelectrics, art. no. 5307593 (2009) 1.

[5] B. Su, J. E. Holmes, B.L. Cheng and T. W. Button, J. Electroceram. **9** (2002) 111.

[6] S. M. Rhim, H. Bak, S. Hong and O. K. Kim, J. Am. Ceram. Soc. **83** (2000) 3009.

[7] P. Kumar and P. Palei, Ceram. Int. (In Press).

[8] X. Zong, Z. Yang, H. Li, M. Yuan, Mater. Res. Bull. **41** (2006) 1447.

[9] T. K. Mandal, Mater. Lett. **61** (2007) 850.

[10] W. F. Hosford, *Materials Science* (Cambridge Univ. Press, New York, 2007) 144.

[11] K. Uchino, *Ferroelectric Devices* (Marcel Dekker Inc., New York, 2000) 70.

[12] A. Chowdhury, M. A. Khan, C. James and S. J. Milne, Mater. Chem. Phys. **113** (2009) 135.

[13] M. A. Brown, J. L. Ding and J. R. Robbins, Ferroelectrics Lett. **34** (2007) 1.

[14] H. T. Martirena and J. C. Burfoot, J. Phys. C: Solid State Phys **7** (1976) 3162.

[15] C. K. Suman, K. Prasad and R. N. P. Choudhary, J. Mat. Sci. **41** (2006) 369.

[16] C. K. Suman, K. Prasad and R. N. P. Choudhary, Mater. Chem. Phys. **82** (2003) 140.

[17] F. A. Kröger and H. J. Vink, Solid State Phys. **3** (1956) 307.

[18] T. Friessnegg, S. Aggarwal, R. Ramesh, B. Nielsen, E. H. Poindexter and D. J. Keeble, Appl. Phys. Lett. **77** (2000) 127.

[19] P. Goel and K. L. Yadav, Mater. Lett. **60** (2006) 3183.

[20] S. M. Pilgrim, A. E. Sutherland and S. R. Winzer, J. Am. Ceram. Soc. **73** (1990) 3122.

[21] V. Raghavan, *Materials Science and Engineering* (Prentice-Hall of India, New Delhi, 2004) 194.

[22] Y. Chen, Y. Y. Zhang, X. L. Dong, G. S. Wang and F. Cao, J. Am. Ceram. Soc. **93** (2010) 161.

[23] I. S. Zheludev, *Physics of Crystalline Dielectrics, Vol I: Crystallography & Spontaneous Polarization* (Plenum Press, New York, 1971).

[24] W. P. Lu, X. Y. Mao and X. B. Chen, J. Appl. Phys. **95** (2004) 1973.

[25] W. P. Lu, J. Zhu, H. Sun, X. B. Chen, J. Mat. Res. **20** (2005) 971.

[26] R. C. Buchanan, *Ceramic Materials for Electronics: Processing, Properties and Applications* (Marcel Dekker Inc., New York, 1986) 38.

[27] Y. Noguchi and M. Miyayama, Appl. Phys. Lett. **78** (2001) 1903.

[28] A. Chen, Y. Zhi and L. E. Cross, Phys. Rev. B **62** (2000) 228.

[29] V. Shrivastava, A. K. Jha, R. G. Mendiratta, Phys. B **371** (2006) 337.

[30] B. Angadi, P. Victor, V. M. Jali, M. T. Lagare, R. Kumar and S. B. Krupanidhi, Mater. Sci. Eng B **100** (2003) 93.

[31] D. M. Symth, Ferroelectrics **117** (1991) 117.

[32] W. L. Warren, K. Vanheusden, D. Dimos, G. E. Pike and B. A. Tuttle, J. Am. Ceram. Soc. **78** (1995) 536.

[33] J. Robertson, C. W. Chen, W. L. Warren and C. D. Gutleben, Appl. Phys. Lett. **69** (1996) 1704.

[34] S. Sen, R. N. P. Choudhary and P. Pramanik, Phys. B **387** (2007) 56.

[35] G. Li, L. Zheng, Q. Yin, B. Jiang and W. Cao, J. Appl. Phys. **98** (2005) 064108-1.

[36] K. Uchino, *Ferroelectric Devices* (Marcel Dekker Inc., New York, 2000).

[37] M. Hosseini and S. J. Moosavi, Ceram. Int. **26** (2000) 541.

[38] Z. Zhang and R. Raj, J. Am. Ceram. Soc. **78** (1995) 3363.

[39] R. Jain, A. K. S. Chauhan, V. Gupta and K. Sreenivas, J. Appl. Phys. **97** (2005) 124101-1.

[40] H. S. Shulman, M. Testorf, D. Damjanovic and N. Setter, J. Am. Ceram. Soc. **79** (1996) 3124.

CHAPTER 4

Chapter 4

$Ba_{5-x}Ca_xSmTi_3Nb_7O_{30}$ (x = 0-5): Effect of Calcium Substitution

4.1 INTRODUCTION

As discussed in Chapter-1 (Sec. 1.3.5), the tungsten-bronze type structure has many interstitial sites (i.e., A_1, A_2, B_1, B_2 and C) for cation occupation. This provides a lot of scope for substitution by variety of cations that can tailor the physical properties of the compound for various device applications. It is found that the physical properties can be improved by different ionic substitution in these interstitial sites [1-10]. Calcium is known to have considerable effect on the structural, dielectric, pyroelectric, conductivity and elastic properties in perovskites and bismuth layer ceramics [11-18]. Infact, it is known to be a good substituent for lead in some lead based compounds which makes them environment friendly [19-24]. Xu et. al. [25] have reported that calcium substitution in $Ba_3Sm_3Ti_5Ta_5O_{30}$ results in considerable decrease in dielectric loss which makes them more suitable for microwave applications. To find the effect of calcium substitution in the presently studied compound $Ba_5SmTi_3Nb_7O_{30}$, samples replacing barium by calcium were prepared and studied. Compositions $Ba_{5-x}Ca_xSmTi_3Nb_7O_{30}$ (x = 0-5) were prepared and studied for their microstructure, density, dielectric property, conductivity and ferroelectric properties.

4.2 RESULTS AND DISCUSSIONS

4.2.1 Structural Characterization

4.2.1.1 X-ray diffraction

The observed XRD patterns of the studied samples having different concentrations of calcium are shown in Fig. 4.1. It is observed in the diffractogram that the specimen remains single phase upto x = 1. For the samples with x ≥ 2, additional peaks are observed which indicates the formation of secondary phase. As the calcium concentration increases, the splitting as well as the intensity of

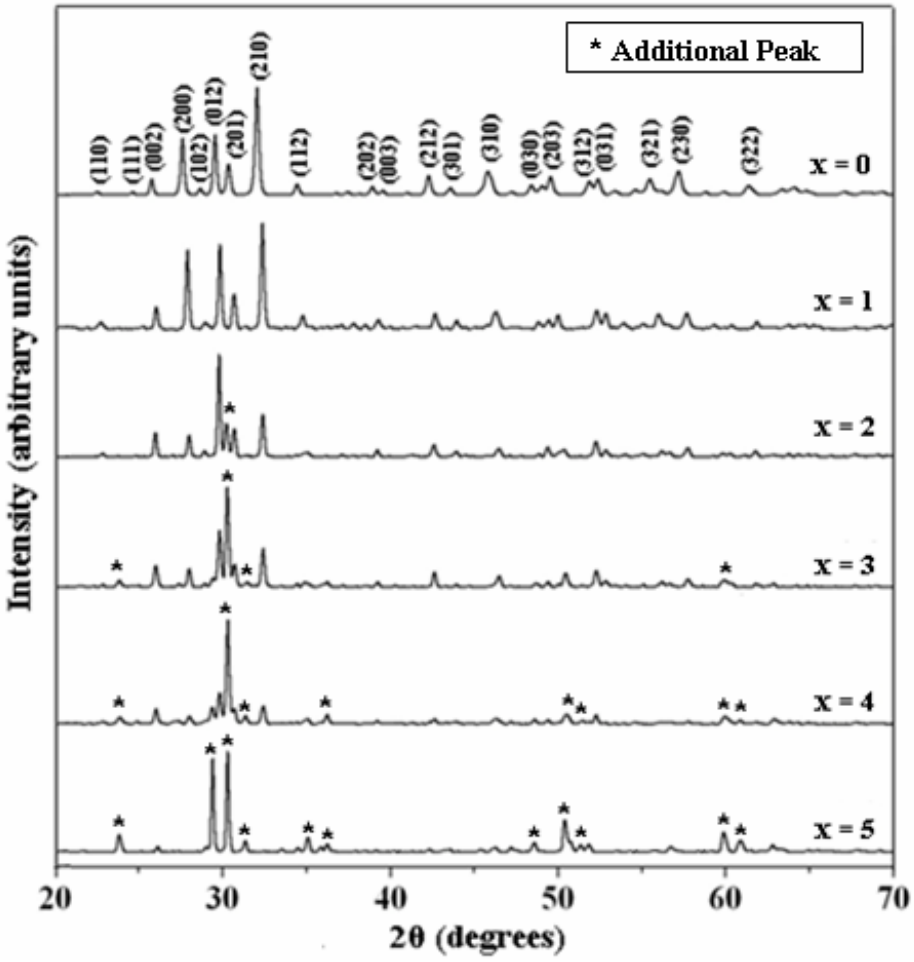

Fig. 4.1 XRD pattern of $Ba_{5-x}Ca_xSmTi_3Nb_7O_{30}$ (x = 0-5) compounds

additional peaks increase. A comparison of the additional peaks with standard XRD patterns (JCPDS file No. 30-0270) shows the formation of $Ca_3Nb_2Ti_3O_{14}$ as secondary phase. The refined lattice parameters and the unit cell volume at different calcium concentrations are summarized in Table 4.1. All the $Ba_{5-x}Ca_xSmTi_3Nb_7O_{30}$ (x = 0-5) compounds are found to have orthorhombic crystal with tungsten-bronze type structure at room temperature. A decrease in

Table 4.1 Lattice parameters and unit cell volume at different calcium concentrations

x	a (Å)	b (Å)	c (Å)	Volume (Å^3)
0	6.4106	5.5595	6.8112	242.75
1	6.3078	5.5914	6.8250	240.71
2	6.2608	5.7506	6.8111	245.22
3	6.2629	5.7556	6.8139	245.62
4	6.2480	5.7650	6.8244	245.81
5	6.1924	5.7484	6.7915	241.75

the unit cell volume from x = 0 to x = 1 is observed which can be understood to be due to the smaller ionic radius of Ca^{2+} as compared to Ba^{2+} (Table 4.2). However, for higher concentration of calcium (i.e. x ≥ 2), unit cell volume increases.

Table 4.2 Ionic Radii and Ionic Polarizability of ions

Ions	Coordination Number	Ionic Radii (Å)	Ionic Polarizability (α_I) (Å^3)
Ca^{2+}	6	1.000	3.17
Ba^{2+}	6	1.360	6.40
Sm^{3+}	6	0.964	4.74
Ti^{4+}	6	0.605	2.94
Nb^{5+}	6	0.640	3.98

The crystal structural distortion parameters, namely, orthorhombicity [2(a-b)/(a+b)] and tetragonal strain (c/a) have been calculated and plotted as a function of calcium concentration (Fig. 4.2). It is observed that the tetragonality increases while orthorhombicity decreases as calcium content is increased.

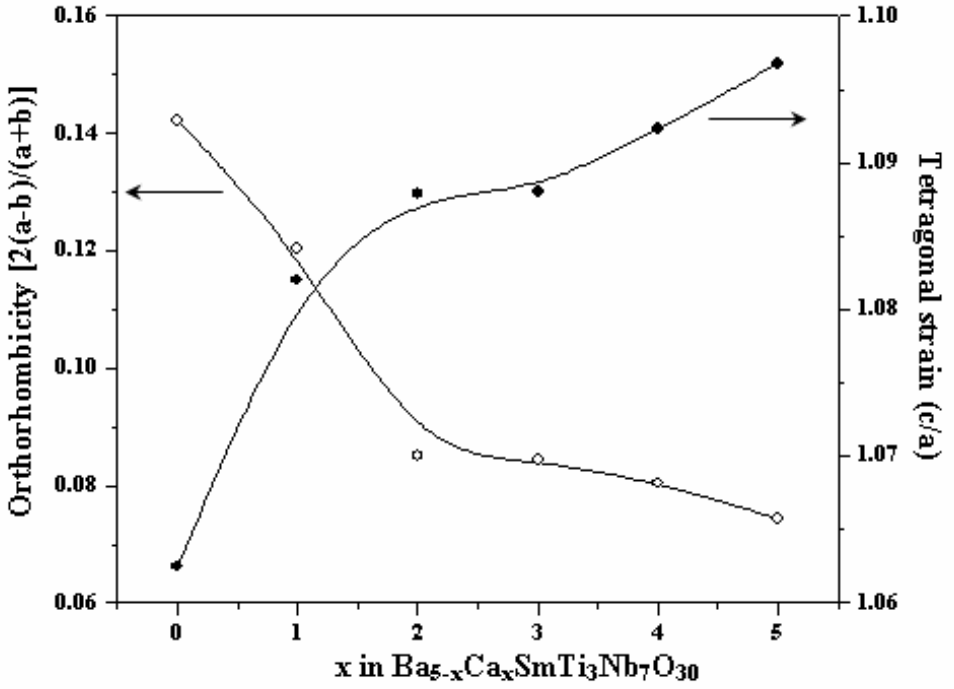

Fig. 4.2 Compositional variation of orthorhombicity and tetragonal strain

4.2.1.2 SEM analysis

The SEM micrographs of the Ca free and Ca-substituted samples are shown in Fig. 4.3 which shows considerable increase in grain size with increasing Ca content. The average grain size in the sample with x = 0 is ~ 2 μm while in the sample with $1 \leq x \leq 5$ the size is found to be in the range of ~10-17 μm. The shape of grains changes from oval to rod like structure with increase in calcium content. Similar shape change of grains on addition of calcium has been reported earlier

also [17]. However, it can be seen that the size of rod like structure reduces in the barium free sample.

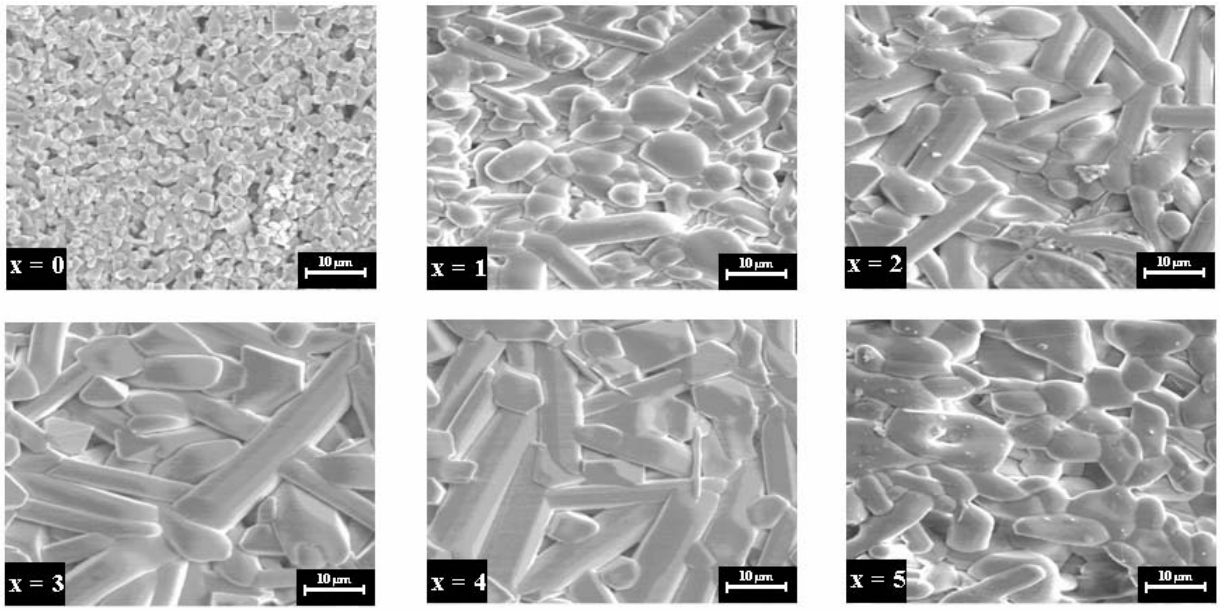

Fig. 4.3 SEM micrographs of $Ba_{5-x}Ca_xSmTi_3Nb_7O_{30}$ (x = 0-5) samples

4.2.1.3 Relative Density

Fig. 4.4 shows the variation of relative density with calcium content in $Ba_{5-x}Ca_xSmTi_3Nb_7O_{30}$ (x = 0-5) compounds.

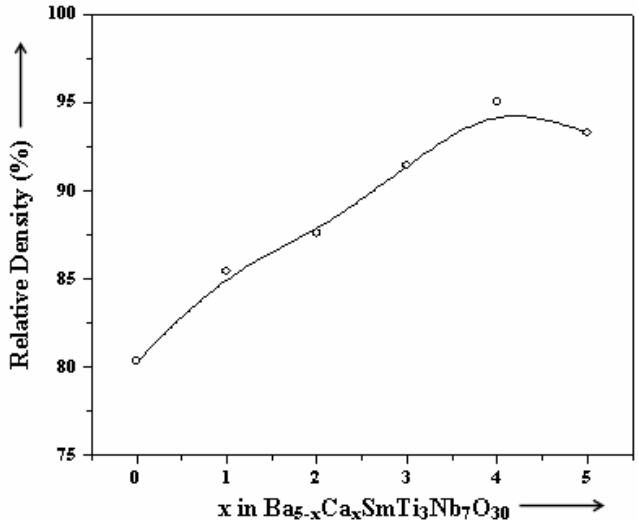

Fig. 4.4 Variation of relative density with calcium concentration in $Ba_{5-x}Ca_xSmTi_3Nb_7O_{30}$ (x = 0-5)

It is observed that the relative density of the samples increases with the increase in the calcium concentration which can be correlated to the increase in the grain size and the decreased porosity (Fig. 4.3). However, a small decrease in the density in barium free sample is due to the reduction of the grain size and increase in the porosity in this sample (Fig. 4.3).

4.2.2 Electrical Characterization

4.2.2.1 Dielectric studies

It is well known that the dielectric constant (ε_r') and dielectric loss (tan δ) of ferroelectric materials in most cases depend upon the composition, grain size, secondary phases, etc. [17]. In this section, the influence of calcium substitution in $Ba_{5-x}Ca_xSmTi_3Nb_7O_{30}$ (x = 0-5) compounds on dielectric properties is presented.

Variation of ε_r' with temperature: Curie temperature

Fig. 4.5 shows the temperature dependence of dielectric constant (ε'_r) for all the $Ba_{5-x}Ca_xSmTi_3Nb_7O_{30}$ (x = 0-5) compounds at different frequencies (1 kHz, 10 kHz, 100 kHz). It is observed that the compounds with x = 0-4 undergo ferroelectric-paraelectric phase transition of diffuse type at the Curie temperature (T_c), whereas the compound with x = 5 does not show any dielectric anomaly in the measured temperature range. It is also observed that all the compounds have the same T_c at all the above mentioned frequencies, suggesting that the compounds do not show any relaxor behaviour. Further, the dielectric constant

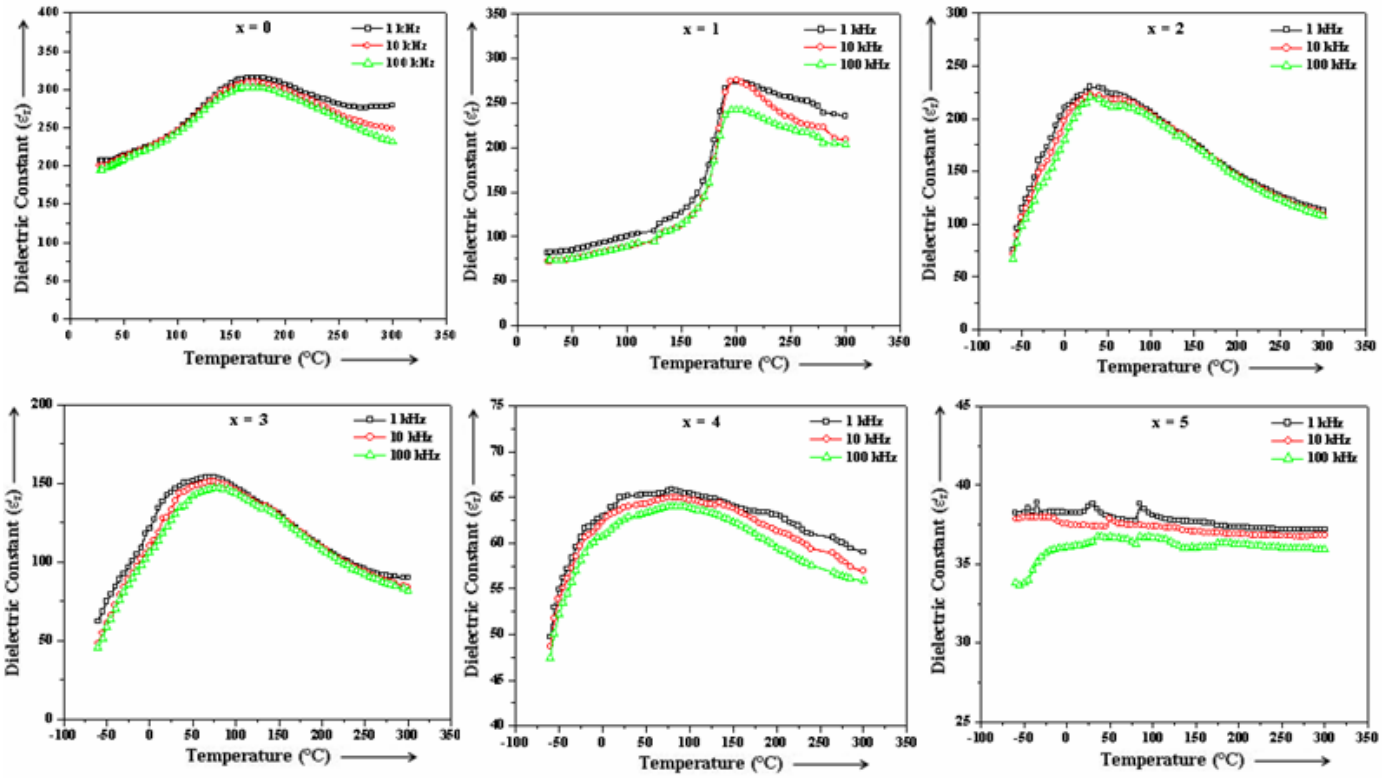

Fig. 4.5 Variation of dielectric constant (ε'_r) with temperature at 1 kHz, 10 kHz and 100 kHz frequencies of $Ba_{5-x}Ca_xSmTi_3Nb_7O_{30}$ (x = 0-5) compounds

decreases as the calcium content increases (Table 4.2). This is possibly due to the decrease in the net polarization of the compounds with increase in calcium content as the ionic polarizability α_I of Ca is lower than that of Ba (Table 4.2). However, T_c increases from 170 °C (in Ca free specimen) to 200 °C in calcium (x = 1) containing specimen. This can be understood in terms of the increased tetragonal strain (c/a) of the specimen. Larger value of tetragonal strain (c/a) on adding Ca (Fig. 4.2) indicates that a larger amount of thermal energy is required for the phase transition resulting in an increase in T_c. However, for higher concentration of calcium (i.e. x ≥ 2), T_c decreases sharply (Table 4.3). This is likely due to the formation of the secondary phase in the compound.

Table 4.3 Dielectric constant at T_c ($\varepsilon'_{r\,max}$), Curie temperature (T_c) and diffusivity (γ) of $Ba_{5-x}Ca_xSmTi_3Nb_7O_{30}$ (x = 0-5) compounds at 1 kHz, 10 kHz and 100 kHz

x	**Frequency (kHz)**	$\varepsilon'_{r\,max}$	T_c (°C)	γ
0	1 10 100	315 309 303	170	1.28 1.59 1.71
1	1 10 100	274 276 243	200	1.14 1.20 1.28
2	1 10 100	230 223 220	30	1.22 1.35 1.50
3	1 10 100	153 151 147	80	1.28 1.37 1.52
4	1 10 100	66 65 64	85	1.25 1.48 1.60
5	1 10 100	- - -	-	- - -

At all the frequencies, the dielectric peak is found to be broadened indicating the diffuse nature of phase transitions. The diffusivity constant or degree of disorderness (γ) has been calculated using the formula [26]:

$$\ln\left(\frac{1}{\varepsilon'_r}-\frac{1}{\varepsilon'_{r\,\max}}\right)=\gamma\ln(T-T_c)+\text{constant} \qquad (4.1)$$

where $\varepsilon'_{r\,max}$ is the maximum value of ε'_r at $T = T_c$. The values of γ have been calculated from the slope of ln ($1/\varepsilon'_r$ - $1/\varepsilon'_{r\,max}$) versus ln (T-T_c) curve (Fig. 4.6) and are given in Table 4.3. For all the studied compositions except x = 5, γ is found to be between 1 (obeying Curie-Weiss law) and 2 (for completely disordered system) confirming the observed diffuse nature of phase transitions in all the samples. The value of γ is found to decrease from calcium free to x = 1 compound but it

increases as concentration of calcium is further increased. It suggests that the composition with x = 1 is more ordered than other compositions [27].

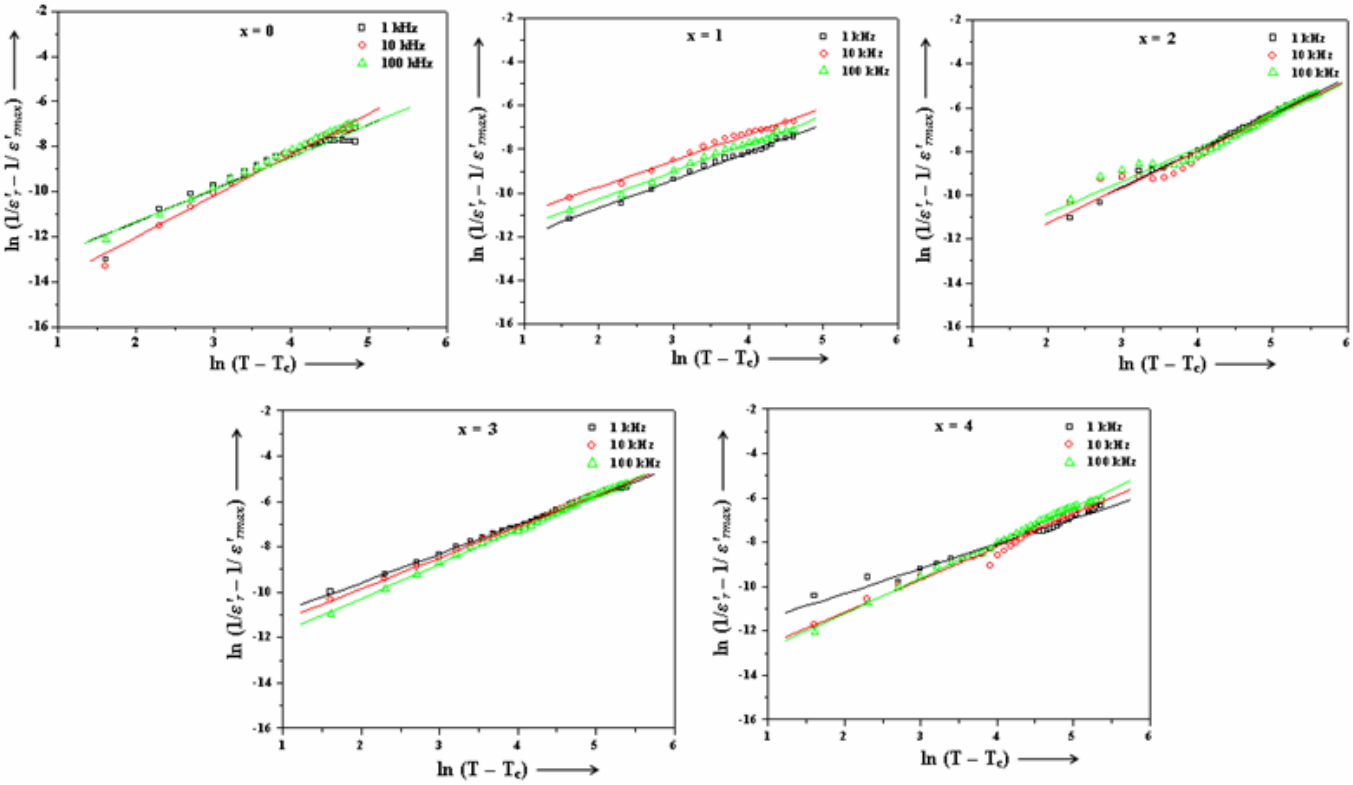

Fig. 4.6 Variation of ln ($1/\varepsilon'_r$ - $1/\varepsilon'_{r\,max}$) with ln (T-T_c) at different calcium concentration

Variation of tan δ *with temperature*

For all $Ba_{5-x}Ca_xSmTi_3Nb_7O_{30}$ (x = 0-5) compounds, at the selected frequencies i.e. 1 kHz, 10 kHz, 100 kHz, the variation of dielectric loss with temperature (Fig. 4.7) shows that the loss is almost constant initially but at higher temperatures it increases sharply. This sharp increase of dielectric loss in high temperature region may be attributed to the increased mobility of space charges arising from the defects or vacancies (like oxygen vacancies) in the sample [28].

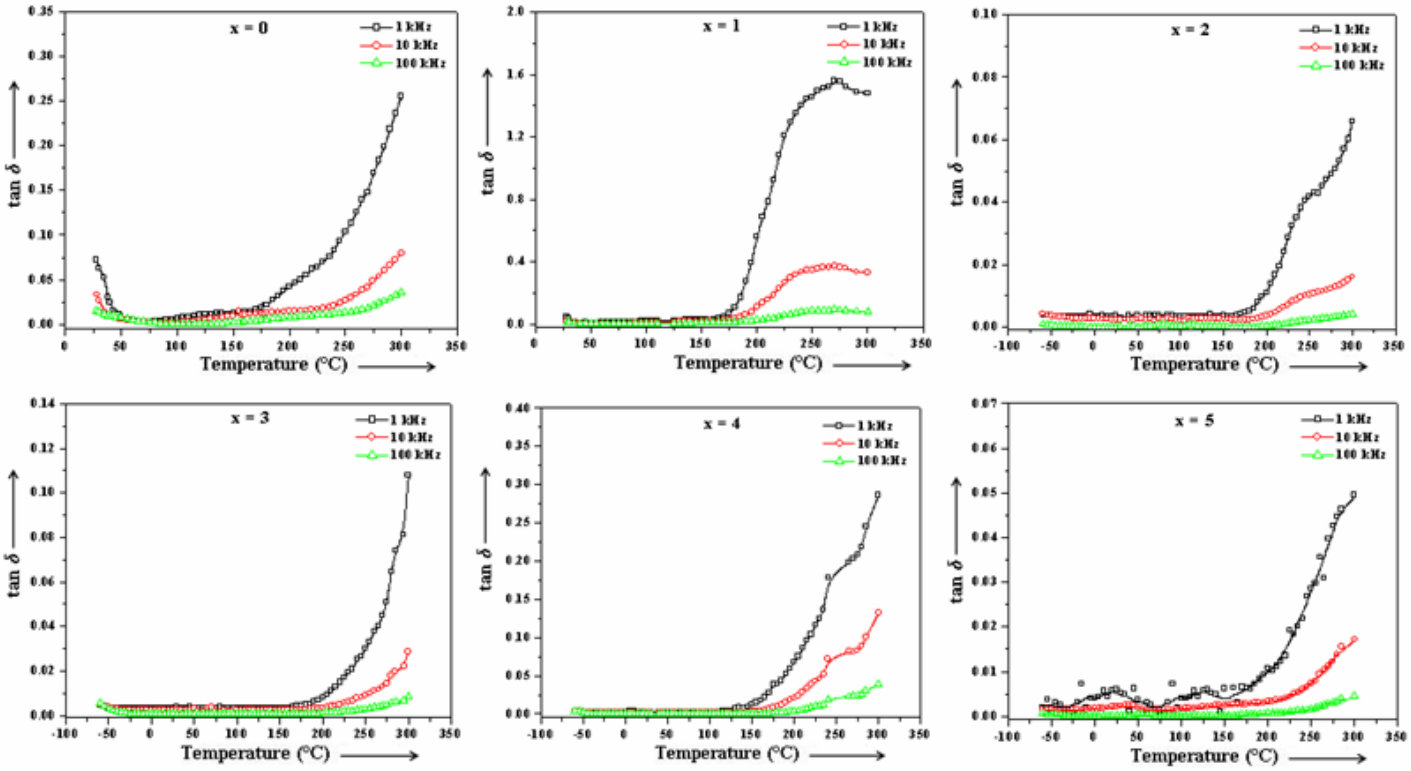

Fig. 4.7 Variation of dielectric loss (tan δ) with temperature at 1 kHz, 10 kHz and 100 kHz frequencies of $Ba_{5-x}Ca_xSmTi_3Nb_7O_{30}$ (x = 0-5) compounds

Variation of ε_r' and tan δ *with frequency*

Fig. 4.8 (a) and (b) shows the variation of dielectric constant (ε_r') and dielectric

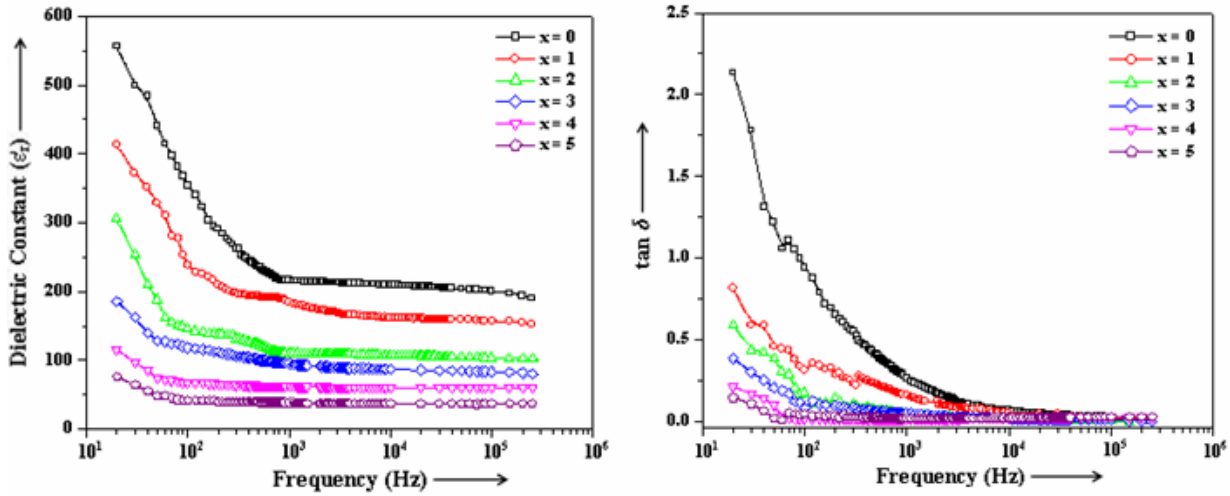

Fig. 4.8 Variation of (a) dielectric constant (ε_r') and (b) dielectric loss (tan δ) with frequency

loss (tan δ) as a function of frequency in the range 20 Hz to 500 kHz at room temperature respectively. For all the compositions, the dielectric constant and dielectric loss decreases upto about 1 kHz and remains nearly constant beyond this frequency. However, the dependency of dielectric constant and loss on frequency decreases with the increase in the calcium content. The dielectric constant of a material has polarization contributions from electronic, ionic, dipolar and space charge [29]. Response frequencies for ionic and electronic polarizations are ~ 10^{13} and 10^{15} Hz, respectively; and at frequencies beyond 1 kHz, contribution from space charge polarization is not expected [29]. Thus, the higher values of dielectric constant at lower frequencies can be attributed to the presence of space charges in the structure which exist as defects such as oxygen vacancies [30,31]. Moreover, at lower frequencies, the dipoles can follow the applied alternating electric field resulting in higher values of dielectric constant while at higher frequencies the dipoles are unable to follow the rapidly changing field leading to the reduction in the values of dielectric constant. The same reasons also hold for the variation of dielectric loss as the source of dielectric loss in insulating ceramics is space charge polarization and/or domain wall relaxation [32]. It can also be seen that the dielectric constant and dielectric loss at room temperature decreases with increase in calcium concentration.

4.2.2.2 Conductivity studies

DC conductivity

Fig. 4.9 shows the variation of dc conductivity ($\sigma_{dc} = 1/\rho$) with inverse of temperature (10^3/T) for all the compositions. It can be seen from the figure that at low temperatures the conductivity is constant while at higher temperatures it increases

with temperature indicating negative temperature coefficient of resistance (NTCR) – type behaviour in all the studied compounds. The nature of variation of dc conductivity at higher temperature is linear and follows the Arrhenius relationship:

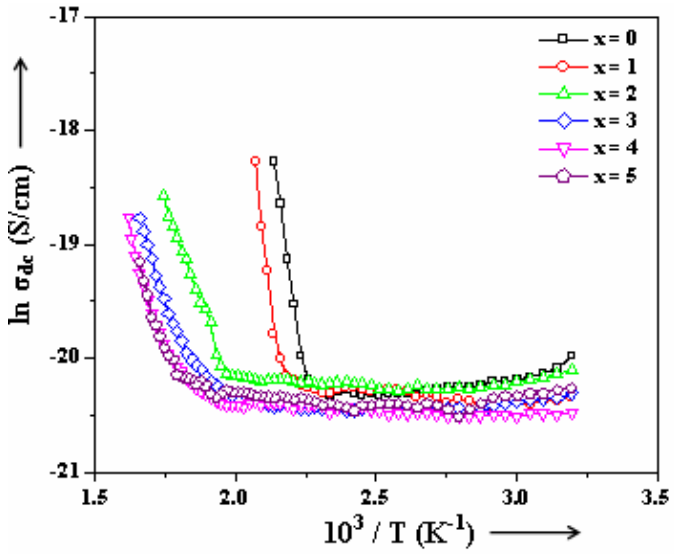

Fig. 4.9 Variation of dc conductivity (ln σ_{dc}) with inverse of temperature (10^3/T) in $Ba_{5-x}Ca_xSmTi_3Nb_7O_{30}$ (x = 0-5) compounds

$$\sigma = \sigma_o \exp\left(\frac{-E_a}{k_B T}\right) \tag{4.2}$$

where σ indicates the conductivity, E_a the activation energy and k_B the Boltzmann constant. The activation energies have been calculated in the higher temperature region using this relation and are given in Table 4.4.

AC conductivity

The temperature variation of ac conductivity at the selected frequencies of 1 kHz, 10 kHz and 100 kHz for $Ba_{5-x}Ca_xSmTi_3Nb_7O_{30}$ (x=0-5) samples is shown in Fig. 4.10.

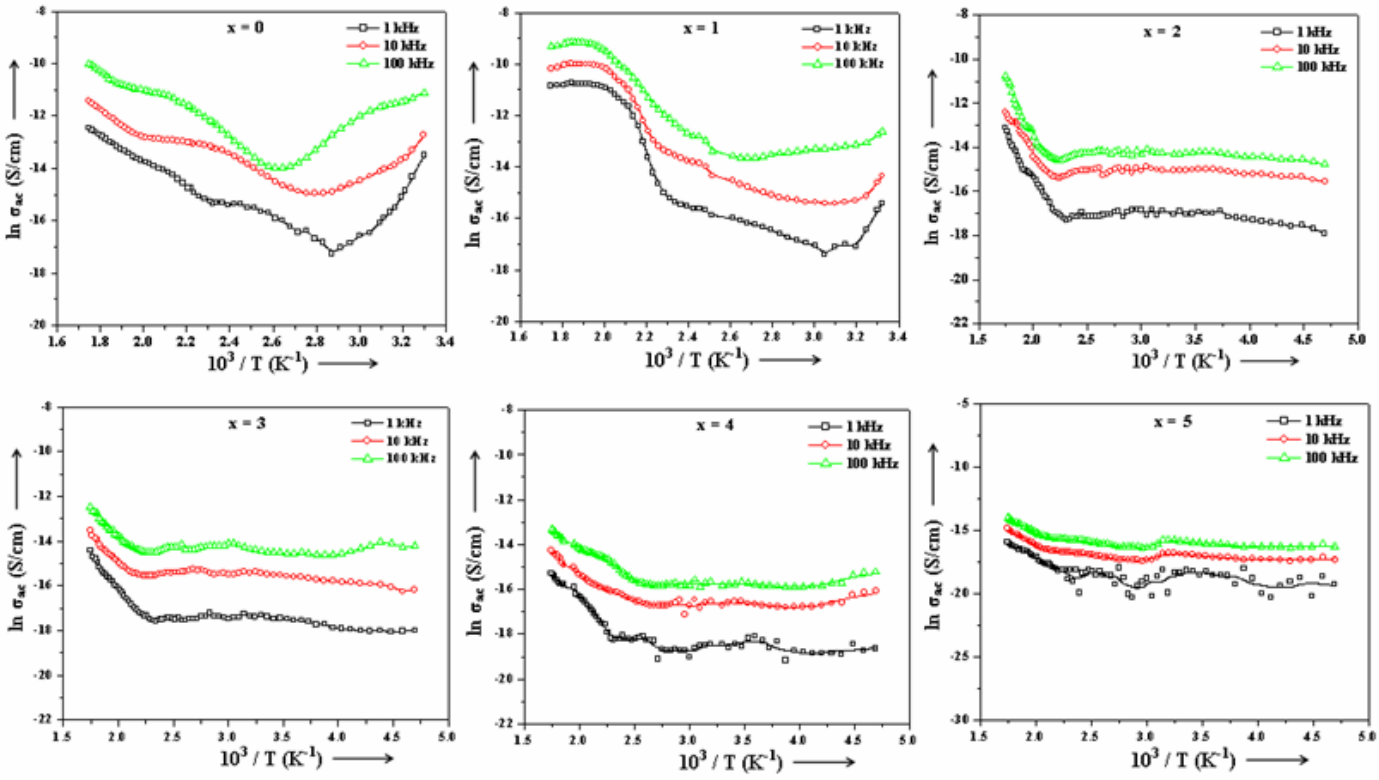

Fig. 4.10 Variation of ac conductivity (ln σ_{dc}) with inverse of temperature (10^3/T) of $Ba_{5-x}Ca_xSmTi_3Nb_7O_{30}$ (x = 0-5) compounds at 1 kHz, 10 kHz and 100 kHz

It is observed that the conductivity of the compounds at higher temperature is higher, which is a common behaviour in these ceramics [33,34]. The nature of variation of σ_{ac} over a wide temperature range indicates the thermally activated conduction process in these materials. This is due to the presence of defects like oxygen vacancies whose mobility increases at higher temperatures [28]. The activation energies, evaluated in the high temperature region using Eq. (4.2) are summarized in Table 4.4. To see the effect of calcium concentration on the variation of ac conductivity with temperature, the curves have been plotted in Fig. 4.11 at three different frequencies of 1 kHz, 10 kHz and 100 kHz. It is observed that the ac conductivity increases with calcium substitution upto x = 1

Table 4.4 Activation energies (E_a) as calculated from dc and ac conductivity at different calcium concentration

x	Frequency (kHz)	E_a (eV) (ac conductivity)	E_a (eV) (dc conductivity)
0	1 10 100	0.37 0.34 0.26	1.13
1	1 10 100	0.55 0.52 0.47	1.27
2	1 10 100	0.73 0.63 0.60	0.60
3	1 10 100	0.47 0.35 0.34	0.56
4	1 10 100	0.42 0.24 0.23	0.63
5	1 10 100	0.40 0.17 0.16	0.69

and decreases for higher concentration of calcium (i.e. x ≥ 2) which could be ascribed to the increase in dielectric loss in the x = 1 specimen (Fig. 4.7).

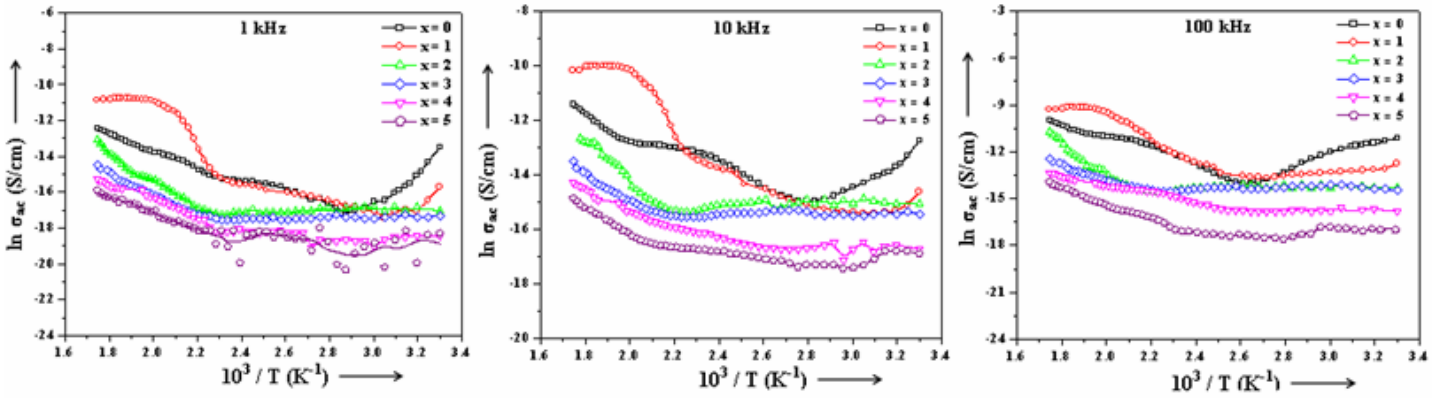

Fig. 4.11 Variation of ac conductivity with temperature at three selected frequencies (1 kHz, 10 kHz and 100 kHz)

4.2.2.3 Impedance analysis

Fig. 4.12 shows the impedance (Z'-Z'') plots at different temperatures for $Ba_{5-x}Ca_xSmTi_3Nb_7O_{30}$ (x = 0-5) samples. All the semicircles in the Cole-Cole plots exhibit some depression instead of a semicircle centered on the x-axis. This is indicative of non-Debye type of relaxation and it also manifests that there is a distribution of relaxation time instead of a single relaxation time in the material [35]. For all the samples, there is a presence of two semicircles at higher temperature

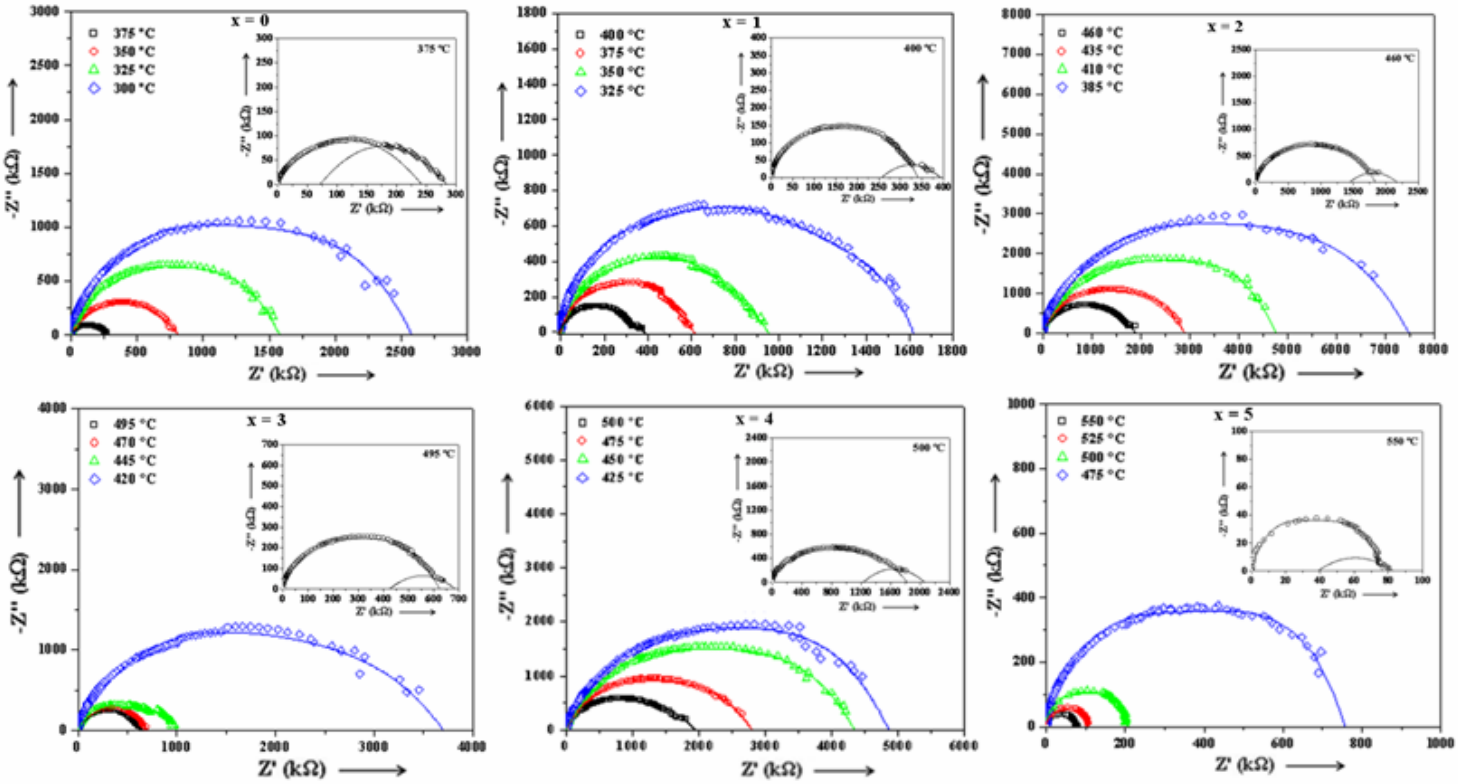

Fig. 4.12 Complex impedance spectrum (Cole-Cole or Nyquist plots) of $Ba_{5-x}Ca_xSmTi_3Nb_7O_{30}$ (x = 0-5) compounds at different temperatures

(Fig. 4.12 inset) which exhibit the presence of both grain (bulk property) and grain boundary effects. The value of bulk resistances (R_b) at different temperatures for samples sintered at various sintering conditions have been obtained from the

intercept of the semicircular arcs on the real axis (Z') and are given in Table 4.5. It is observed that R_b decreases with rise in the temperature for all the samples. This again confirms the negative temperature coefficient of resistance (NTCR) behaviour of the $Ba_{5-x}Ca_xSmTi_3Nb_7O_{30}$ (x = 0-5) compounds. From these values of R_b, the bulk conductivity, σ_{bulk} has been obtained by using Eq. (2.31) and its variation with temperature is shown in Fig. 4.13 for all the samples. The respective capacitances (C_b and C_{gb}) due to the grain and grain boundary effect can be calculated using the Eq. (2.30). The values of R_b, R_{gb}, C_b and C_{gb} obtained from Cole-Cole plots at different temperatures for various calcium concentrations in $Ba_{5-x}Ca_xSmTi_3Nb_7O_{30}$ (x = 0-5) compounds are listed in Table 4.5.

Table 4.5 Various parameters obtained from the Cole-Cole plots

x	Temperature (°C)	R_b (kΩ)	C_b (nF)	R_{gb} (kΩ)	C_{gb} (nF)	E_a (eV)
0	300	2590	0.38	-	-	
	325	1610	0.35	-	-	0.99
	350	800	0.31	-	-	
	375	240	0.30	45	3.85	
1	325	1621	0.23	-	-	
	350	951	0.22	-	-	0.67
	375	619	0.21	-	-	
	400	340	0.18	53	18.78	
2	385	7474	0.15	-	-	
	410	4745	0.13	-	-	0.78
	435	2899	0.10	-	-	
	460	1832	0.09	345	7.69	
3	420	3692	0.27	-	-	
	445	1003	0.26	-	-	1.06
	470	704	0.25	-	-	
	495	622	0.17	62	11.68	
4	425	4834	0.15	-	-	
	450	4319	0.12	-	-	0.62
	475	2777	0.11	-	-	
	500	1822	0.10	241	9.44	
5	475	757	1.82	-	-	
	500	208	1.17	-	-	1.22
	525	107	0.93	-	-	
	500	76	0.62	7	26.39	

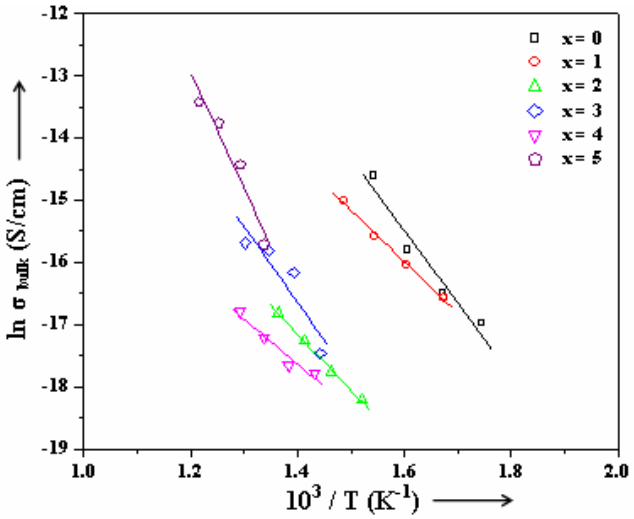

Fig. 4.13 Variation of bulk conductivity with temperature

The relaxation time due to bulk effect (τ_b) has been calculated using Eq. (2.30). Fig. 4.14 shows the temperature variation of τ_b for all the samples. It is observed that the value of τ_b decreases with increase in temperature for all the samples and its temperature dependence follows the Arrhenius relation:

$$\tau_b = \tau_o \exp\left(\frac{-E_a}{k_B T}\right) \tag{4.3}$$

where τ_o is the pre-exponential factor, k_B is Boltzmann constant and E_a the activation energy. The value of activation energy (E_a) using Eq. (4.3) is summarized in Table 3.4.

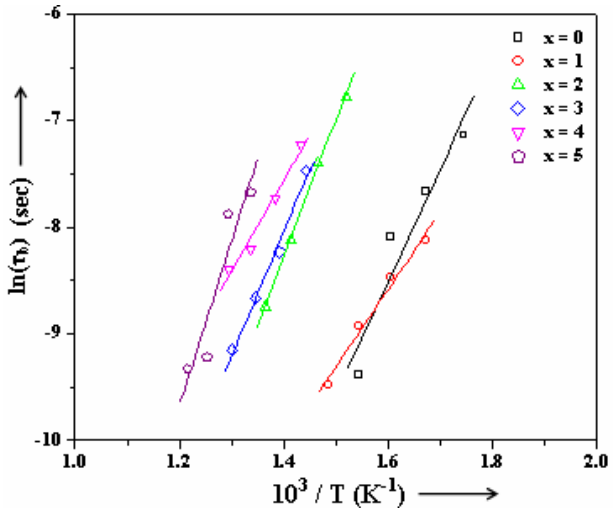

Fig. 4.14 Variation of relaxation time with temperature

4.2.2.4 Ferroelectric studies

Fig. 4.15 shows the variation of polarization as a function of electric field for all the compounds. The observed values of remanent polarization ($2P_r$) and the coercive field ($2E_c$) for all the compounds are given in Table 4.6. The remanent polarization ($2P_r$) is found to increase on Ca substitution i.e., for the specimen with x = 1. The increase in remanent polarization can be correlated to the

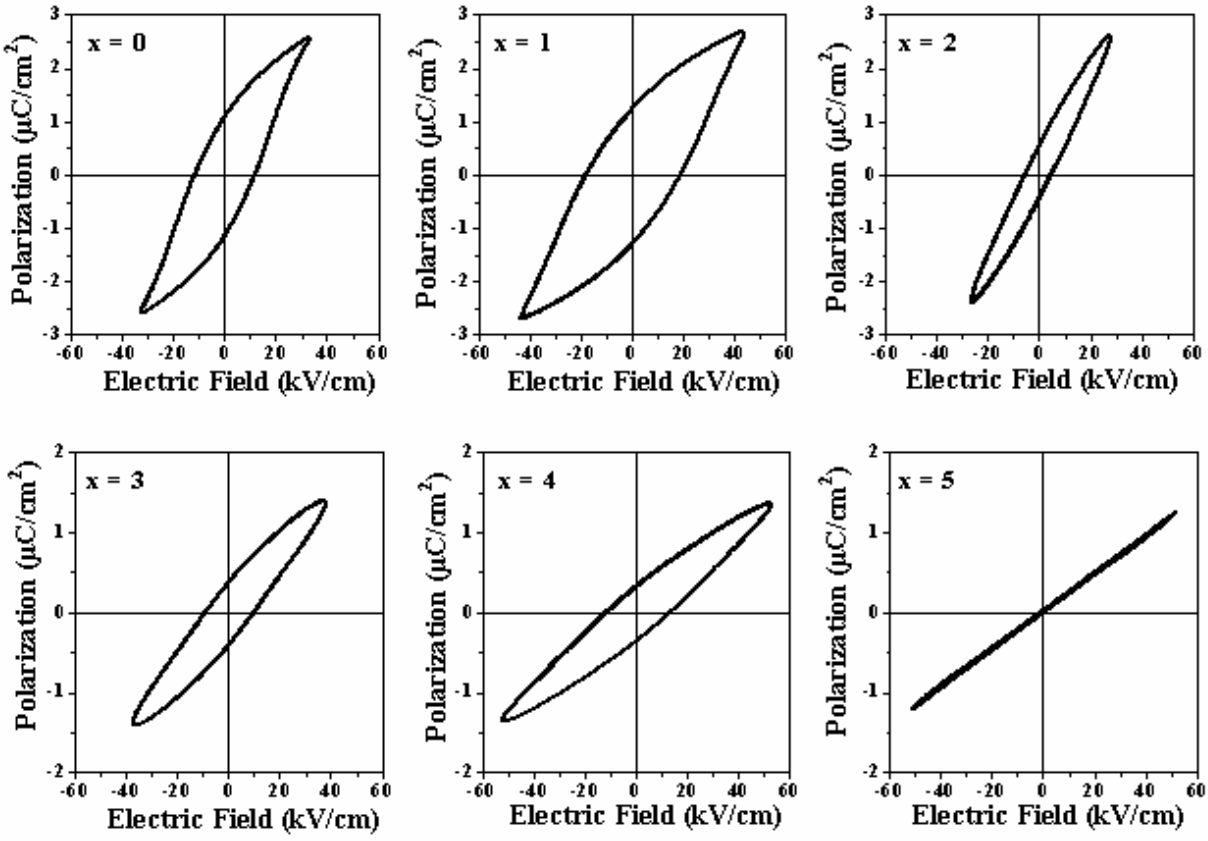

Fig. 4.15 *P-E* hysteresis loops of $Ba_{5-x}Ca_xSmTi_3Nb_7O_{30}$ (x = 0-5) compounds at room temperature

pronounced structural distortion arising due to the partial substitution of smaller size cation Ca at Ba-site [17]. But for higher concentration of calcium, $2P_r$ decreases and finally the loop becomes a straight line for x = 5 confirming that

the compound is no longer ferroelectric on completely replacing barium by calcium, which is in conformity with dielectric observations.

Table 4.6 $2P_r$ and $2E_c$ of $Ba_{5-x}Ca_xSmTi_3Nb_7O_{30}$ (x = 0-5) samples

x	$2P_r$ ($\mu C/cm^2$)	$2E_c$ (kV/cm)
0	2.3	23.3
1	2.5	36.7
2	1.0	10.3
3	0.8	18.4
4	0.7	22.9
5	-	-

4.3 CONCLUSIONS

Based on the above observations and discussions the following conclusions can be drawn from this chapter:

(i) Orthorhombic TB-structure is formed in all $Ba_{5-x}Ca_xSmTi_3Nb_7O_{30}$ (x = 0-5) compounds.

(ii) Single phase is maintained for x = 1 beyond which increasing presence of $Ca_3Nb_2Ti_3O_{14}$ as secondary phase is observed.

(iii) A decrease in the lattice parameters is observed with calcium substitution.

(iv) Tetragonality increases while orthorhombicity decreases with increasing calcium substitution.

(v) Average grain size increases with increase in calcium content of the specimen.

(vi) Dielectric constant decreases with increase in calcium concentration in the specimen.

(vii) All the compounds exhibit non-relaxor type ferroelectric-paraelectric diffuse phase transition with least diffusivity in x = 1 composition except for x = 5

where the compound does not show any phase transition.

(viii) The Curie temperature (T_c) increases from 170 ^{o}C for the specimen x = 0 to 200 ^{o}C for the x = 1 specimen.

(xi) Negative temperature coefficient of resistance (NTCR) behaviour is observed in all the compounds.

(x) Remanent polarization ($2P_r$) is found to be maximum for the specimen with x = 1.

REFERENCES

[1] M. R. Ranga Raju and R. N. P. Choudhary, Mater. Chem. Phys. **99** (2006) 135.

[2] Y. Yang, Y. Liu, J. Meng, Y. Huan and Y. Wu, J. Alloys Compd. **453** (2008) 401.

[3] C. D. Oh, M. S. Kim, J. H. Lee, J. J. Kim, H. Y. Lee and S. H. Cho, Integ. Ferroelectrics **74** (2005) 61.

[4] Y. K. Hwang and Y. U. Kwon, Mater. Res. Bull. **32** (1997) 1495.

[5] C. M. Cho, J. R. Kim, J. H. Noh and K. S. Hong, J. Eur. Ceram. Soc. **27** (2007) 2927.

[6] J. H. Ko, D. H. Kim, S. G. Lushnikov, R. S. Katiyar and S. Kojima, Ferroelectrics **286** (2003) 61.

[7] A. K. Singh and R. N. P. Choudhary, Ferroelectrics **308** (2004) 23.

[8] N. K. Singh, R. N. P. Choudhary and A. Panigrahi, J. Mater. Sci. Lett. **20** (2001) 707.

[9] A. K. Singh and R. N. P. Choudhary, J. Mater. Sci: Mater. Electron. **15** (2004) 379.

[10] M. R. Ranga Raju and R. N. P. Choudhary, J. Mater. Sci. **39** (2004) 1765.

[11] R. K. Zheng, J. Wang, X. G. Tang, Y. Wang, H. L. W. Chan and C. L. Choy, J. Appl. Phys. 98 (2005) 084108-1.

[12] M. A. Mohiddon and K. L. Yadav, IEEE Trans. Dielect. Elect. Insul. **15** (2008) 1236.

[13] S. Sen and R. N. P. Choudhary, J. Mater. Sci: Mater. Electron. **15** (2004) 671.

[14] S. Sen and R. N. P. Choudhary, Mater. Lett. **58** (2004) 661.

[15] F. S. Barnes, H. D. Wu, R. Benton, S. Chumchuensuk, A. Muthitacharoen and B. Y. Xu, Integ. Ferroelectrics **24** (1999) 327.

[16] V. Shrivastava, A. K. Jha and R. G. Mendiratta, Ferroelectrics **356** (2007) 54.

[17] R. R. Das, P. Bhattacharya, W. Pérez and R. S. Katiyar, Ceram. Inter. **30** (2004) 1175.

[18] A. Ando, M. Kimura and Y. Sakabe, Jpn. J. Appl. Phys. **42** (2003) 520.

[19] T. Wei, Y.Wang, C. Zhu, X.W. Dong, Y.D. Xia, J. S. Zhu and J. M. Liu, Appl. Phys. A **90** (2008) 185.

[20] T. D. Hadnagy and T. Davenport, Integ. Ferroelectrics **22** (1998) 183.

[21] H. Huang, L. M. Zhou and L. B. Kong, J. Electroceram. **16** (2006) 343.

[22] L. Zheng, P. Yang, W. P. Xu, C. Lin, W. Wu and M. Okuyama, Integ. Ferroelectrics **20** (1998) 73.

[23] S. H. Kim, J. Ha, C. S. Hwang and A. I. Kingon, Thin Solid Films **394** (2001) 131.

[24] W. R. Xue and P. W. Lu, IEEE International Symposium on Applications of Ferroelectrics (1994) 101.

[25] Z. Y. Xu and X. M. Chen, J. Mater. Sci: Mater. Electron. **11** (2000) 219.

[26] S. M. Pilgrim, A. E. Sutherland and S. R. Winzer, J. Amer. Ceram. Soc. **73** (1990) 3122.

[27] T. Badapanda, S. K. Rout, S. Panigrahi and T. P. Sinha, Curr. Appl. Phys. **9** (2009) 727.

[28] T. Friessnegg, S. Aggarwal, R. Ramesh, B. Nielsen, E. H. Poindexter and D. J. Keeble, Appl. Phys. Lett. **77** (2000) 127.

[29] R. C. Buchanan, *Ceramic Materials for Electronics: Processing, Properties & Applications* (Marcel Dekker Inc., New York, 1991).

[30] Y. Noguchi and M. Miyayama, Appl. Phys. Lett. **78** (2001) 1903.

[31] A. Chen, Y. Zhi and L. E. Cross, Phys. Rev. B **62** (2000) 228.

[32] I. S. Zheludev, *Physics of Crystalline Dielectrics, Vol I: Crystallography & Spontaneous Polarization* (Plenum Press, New York, 1971).

[33] K. S. Singh, R. Sati and R. N. P. Choudhary, Pramana **38** (1992) 161.

[34] K. S. Rao, T. N. V. K. V. Prasad, A. S. V. Subrahmanyam, J. H. Lee, J. J. Kim and S. H. Cho, Mater. Sci. Engg. B. **98** (2003) 279.

[35] S. Sen, R. N. P. Choudhary and P. Pramanik, Phys. B **387** (2007) 56.

CHAPTER 5

Chapter 5

$Ba_5RTi_3Nb_7O_{30}$ and $CaBa_4RTi_3Nb_7O_{30}$ (R = Rare Earth): Effect of Ionic Radii of Rare Earths

5.1 INTRODUCTION

The significance of tungsten-bronze (TB) family is the possibilities to tailor the material properties by substituting suitable cations with different ionic radii and valences among many available interstitial sites. Rare-earths are important additives which are added to control the temperature coefficient of capacitance (TCC), grain growth, electrical resistance and reliability [1-5]. In many materials they are known to influence the crystal structure, ferroelectric, piezoelectric and magnetic properties [6-20]. So, the main focus of this chapter is to study the effects of ionic radii of rare-earth elements on the structural and electrical properties of both $Ba_5RTi_3Nb_7O_{30}$ and $CaBa_4RTi_3Nb_7O_{30}$ (R = La, Nd, Sm, Eu, Dy) compounds. The ionic radii and the ionic polarizability of the various rare-earth elements used in the present study are given in Table 5.1.

Table 5.1 Ionic Radii and Ionic Polarizability of different rare-earth ions

Ions	Coordination Number	Ionic Radii (Å)	Ionic Polarizability (α_i) ($Å^3$)
La^{3+}	6	1.061	6.03
Nd^{3+}	6	0.995	5.01
Sm^{3+}	6	0.964	4.74
Eu^{3+}	6	0.950	4.53
Dy^{3+}	6	0.908	4.10

5.2 RESULTS AND DISCUSSIONS

5.2.1 Structural Characterization

5.2.1.1 X-ray diffraction

X-ray diffractograms of the $Ba_5RTi_3Nb_7O_{30}$ and $CaBa_4RTi_3Nb_7O_{30}$ (R = La, Nd, Sm, Eu, Dy) samples are shown in Fig. 5.1 (a) and Fig. 5.1 (b) respectively.

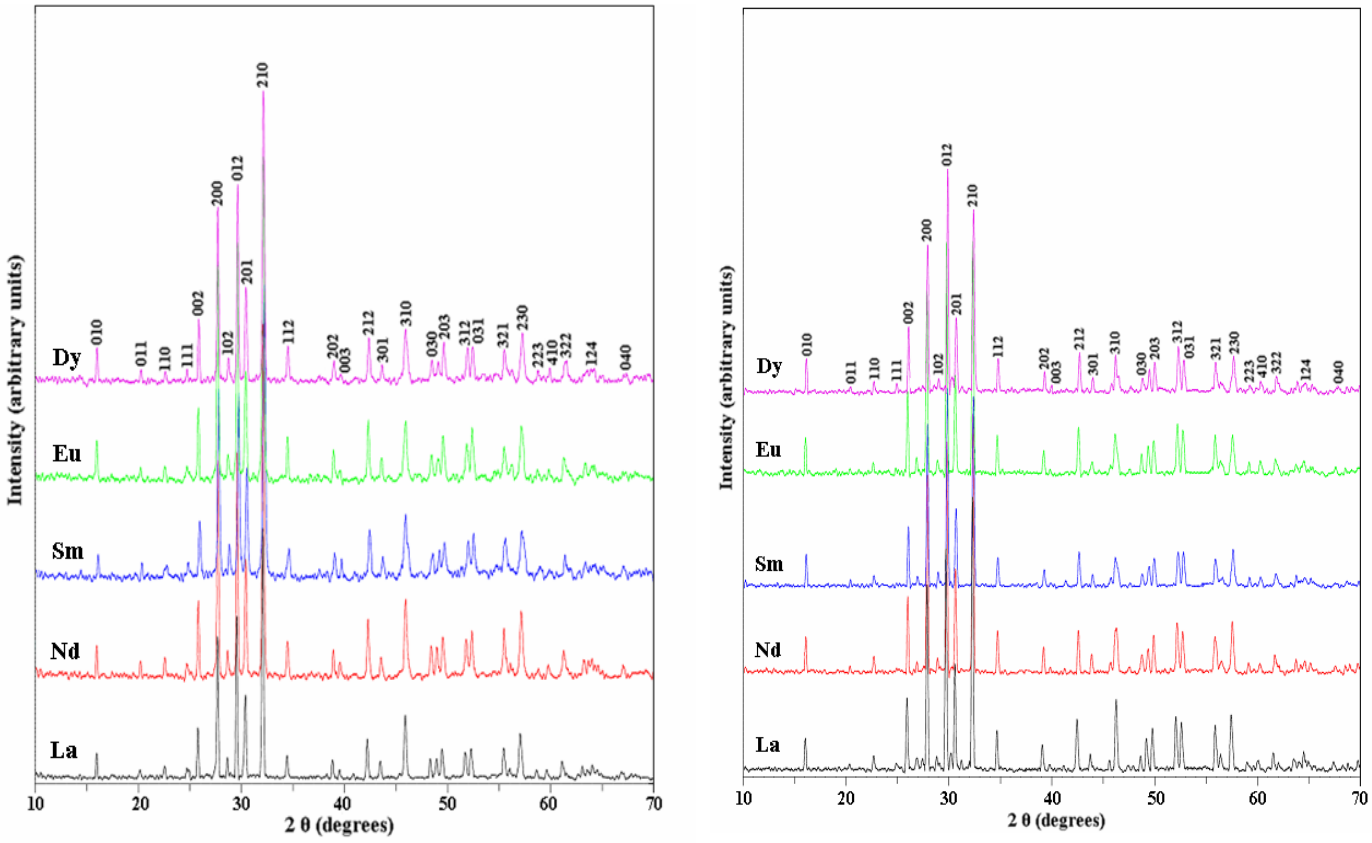

(a) (b)

Fig. 5.1 XRD patterns of (a) $Ba_5RTi_3Nb_7O_{30}$ and (b) $CaBa_4RTi_3Nb_7O_{30}$ compounds

It is observed that single-phase compound is formed in all the rare-earths containing compounds. The refined lattice parameters and the unit cell volume of $Ba_5RTi_3Nb_7O_{30}$ and $CaBa_4RTi_3Nb_7O_{30}$ compounds are given in Table 5.2 (a) and (b) respectively. The lattice parameters and unit cell volume of $Ba_5RTi_3Nb_7O_{30}$ and

Table 5.2 Lattice parameters, unit cell volume and average grain size of various rare-earths containing:

(a) $Ba_5RTi_3Nb_7O_{30}$ compounds

Sample	a (Å)	b (Å)	c (Å)	c/a	Volume (Å^3)	Average Grain Size (μm)
$Ba_5LaTi_3Nb_7O_{30}$	6.4544	5.5791	6.8204	1.0567	245.60	1.0
$Ba_5NdTi_3Nb_7O_{30}$	6.4483	5.5642	6.8198	1.0576	244.69	1.3
$Ba_5SmTi_3Nb_7O_{30}$	6.4106	5.5595	6.8112	1.0625	242.75	1.5
$Ba_5EuTi_3Nb_7O_{30}$	6.4045	5.5504	6.8106	1.0634	242.10	1.8
$Ba_5DyTi_3Nb_7O_{30}$	6.3912	5.5474	6.8003	1.0640	241.37	2.5

(b) $CaBa_4RTi_3Nb_7O_{30}$ compounds

Sample	a (Å)	b (Å)	c (Å)	c/a	Volume (Å^3)	Average Grain Size (μm)
$CaBa_4LaTi_3Nb_7O_{30}$	6.3562	5.6087	6.8348	1.0753	243.66	3.5
$CaBa_4NdTi_3Nb_7O_{30}$	6.3424	5.6036	6.8336	1.0774	242.87	3.7
$CaBa_4SmTi_3Nb_7O_{30}$	6.3078	5.5914	6.8250	1.0820	240.71	4.1
$CaBa_4EuTi_3Nb_7O_{30}$	6.3009	5.5823	6.8241	1.0830	240.08	6.6
$CaBa_4DyTi_3Nb_7O_{30}$	6.2908	5.5791	6.8138	1.0831	239.30	7.5

$CaBa_4RTi_3Nb_7O_{30}$ compounds are observed to decrease with decrease in the ionic radii of the rare-earths. However, the lattice parameters and unit cell volume of calcium containing $CaBa_4RTi_3Nb_7O_{30}$ compounds are smaller than their corresponding rare-earth containing but calcium free $Ba_5RTi_3Nb_7O_{30}$ compounds. All the compounds have orthorhombic crystal with a tungsten-bronze type structure.

5.2.1.2 Raman studies

Fig. 5.2 (a) and (b) show the Raman spectra recorded at room temperature of the $Ba_5RTi_3Nb_7O_{30}$ and $CaBa_4RTi_3Nb_7O_{30}$ compounds respectively. Although the defects in the ceramics make the Raman vibrational modes broaden and overlap with each other, there are four obvious Raman bands observed around 270, 525, 615, 840 cm^{-1}. According to the earlier reports of the Raman spectra for tungsten bronze compounds [21-24], the Raman bands around 270, 615 and 840 cm^{-1} are considered

as the three characteristic Raman peaks associated with the internal modes of the oxygen octahedron BO_6, namely the O-B-O bending, O-B-O stretching and B-O stretching vibrational modes. The Raman band around 525 cm^{-1} can be associated with the external modes and affected by cations in the pentagonal and square tunnels. The observation of softening of this mode with the increase in the ionic radii of rare-earths indicates the decrease in the compressive stress as the ionic-radii of the rare-earths increases.

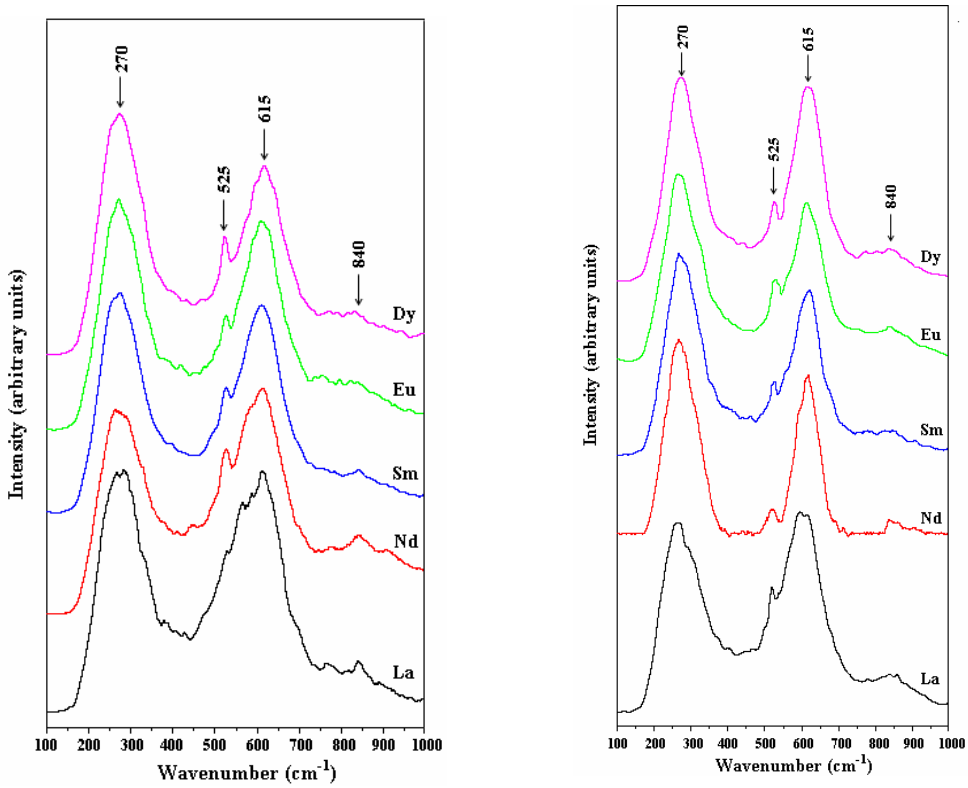

Fig. 5.2 Room temperature Raman spectra of (a) $Ba_5RTi_3Nb_7O_{30}$ and (b) $CaBa_4RTi_3Nb_7O_{30}$ compounds

5.2.1.3 SEM analysis

Fig. 5.3 (a) and (b) show the SEM micrographs of the $Ba_5RTi_3Nb_7O_{30}$ and $CaBa_4RTi_3Nb_7O_{30}$ compounds respectively. It can be seen that the average grain size increases with decrease in the ionic radii of the rare-earths in both calcium free as well as calcium containing compounds (Table 5.2). However, it is found that with

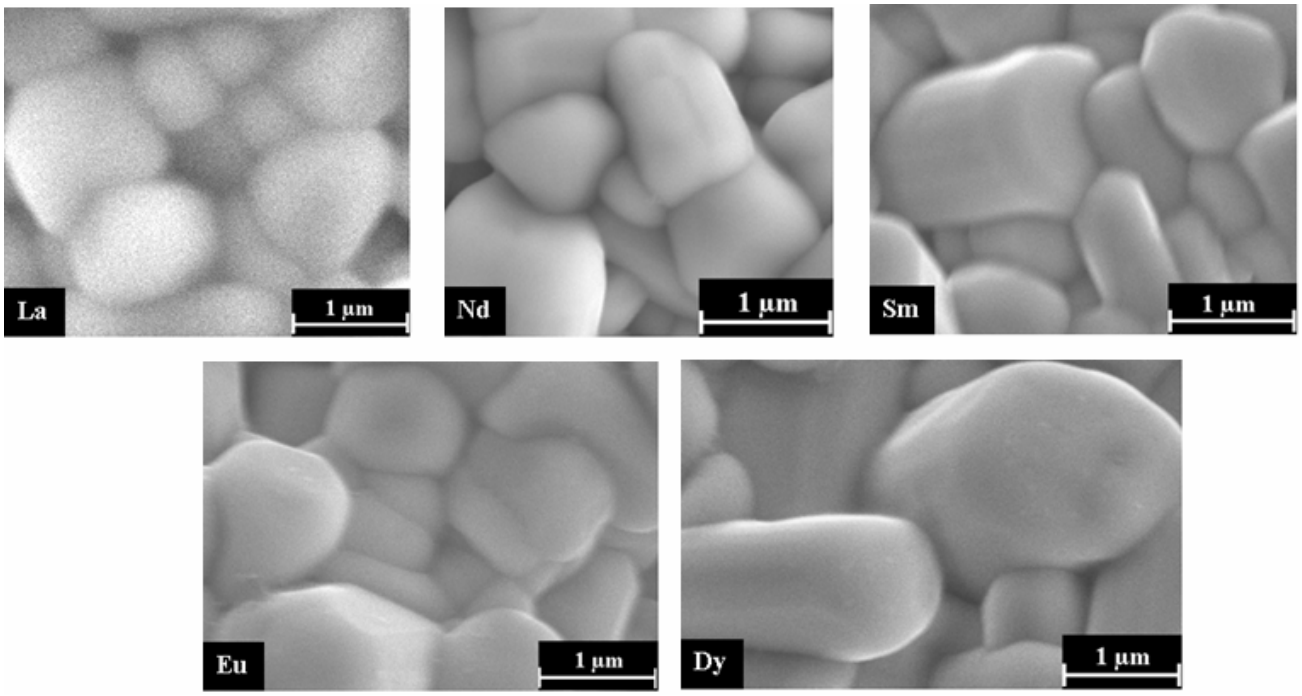

(a)

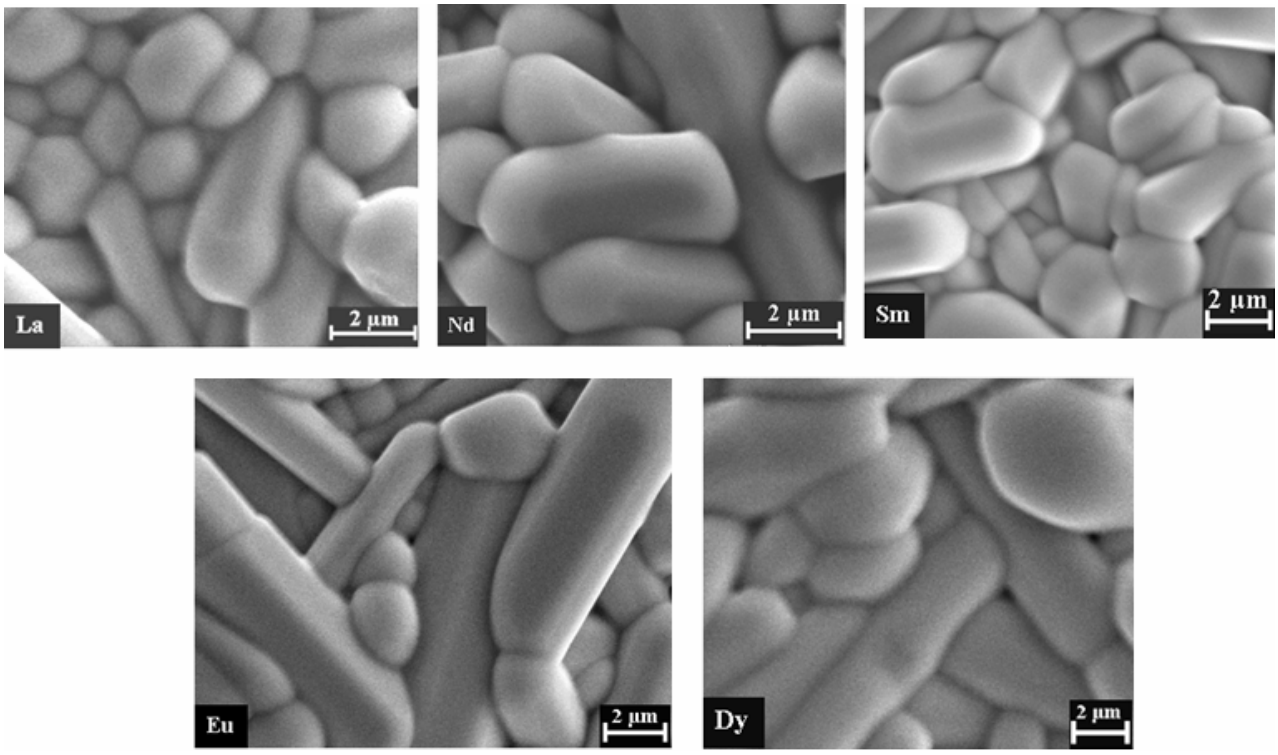

(b)

Fig. 5.3 SEM micrographs of (a) $Ba_5RTi_3Nb_7O_{30}$ and (b) $CaBa_4RTi_3Nb_7O_{30}$ compounds

calcium addition the average grain size increases and the shape of the grains changes from spherical to cylindrical in each of the rare-earth containing $Ba_5RTi_3Nb_7O_{30}$ compounds.

5.2.2 Electrical Characterization

5.2.2.1 Dielectric studies

To see the effect of ionic radii of the rare-earths on the dielectric properties (a) the variation of ε_r' and tan δ as a function of temperature at 1 kHz, 10 kHz and 100 kHz frequencies and (b) the variation ε_r' and tan δ with frequency at room temperature of $Ba_5RTi_3Nb_7O_{30}$ and $CaBa_4RTi_3Nb_7O_{30}$ compounds was investigated and is presented below.

Variation of ε_r' with temperature: Curie temperature

Fig. 5.4 (a) and (b) show the temperature dependence of dielectric constant (ε_r') at frequencies namely 1 kHz, 10 kHz and 100 kHz of $Ba_5RTi_3Nb_7O_{30}$ and $CaBa_4RTi_3Nb_7O_{30}$ respectively. It is observed that the compounds show ferroelectric-paraelectric phase transition of diffuse type at the Curie temperature (T_c). Except lanthanum (La) containing compounds i.e. $Ba_5LaTi_3Nb_7O_{30}$ and $CaBa_4LaTi_3Nb_7O_{30}$, the T_c is to be found same for all the measured frequencies in all the rare-earths containing $Ba_5RTi_3Nb_7O_{30}$ and $CaBa_4RTi_3Nb_7O_{30}$ compounds indicating the non-relaxor behaviour of the compounds. However, $Ba_5LaTi_3Nb_7O_{30}$ and $CaBa_4LaTi_3Nb_7O_{30}$ compounds have ferroelectric to paraelectric phase transition at the transition temperature (T_m) which is found to shift towards higher temperature at higher frequencies (Fig. 5.4), which is typical

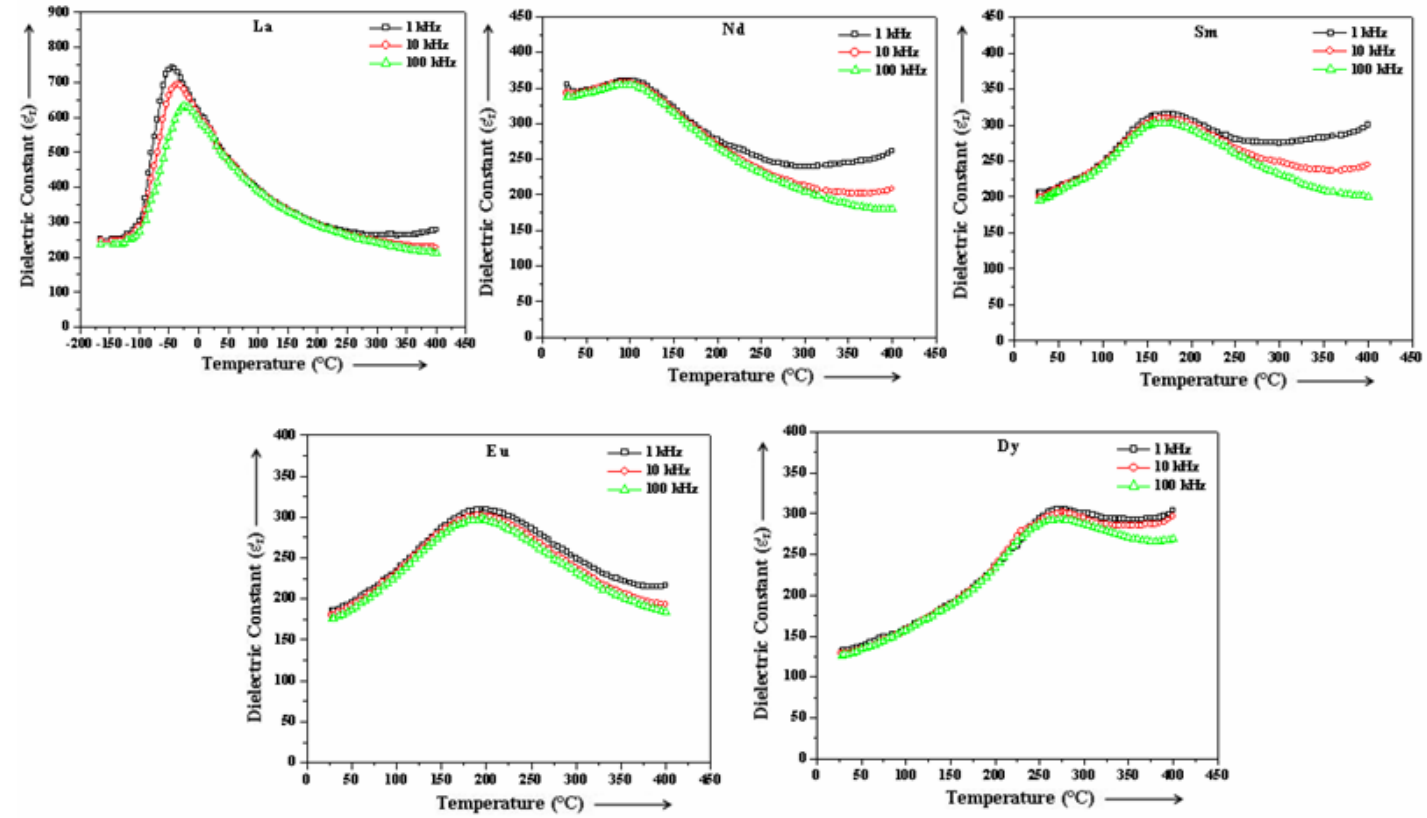

(a)

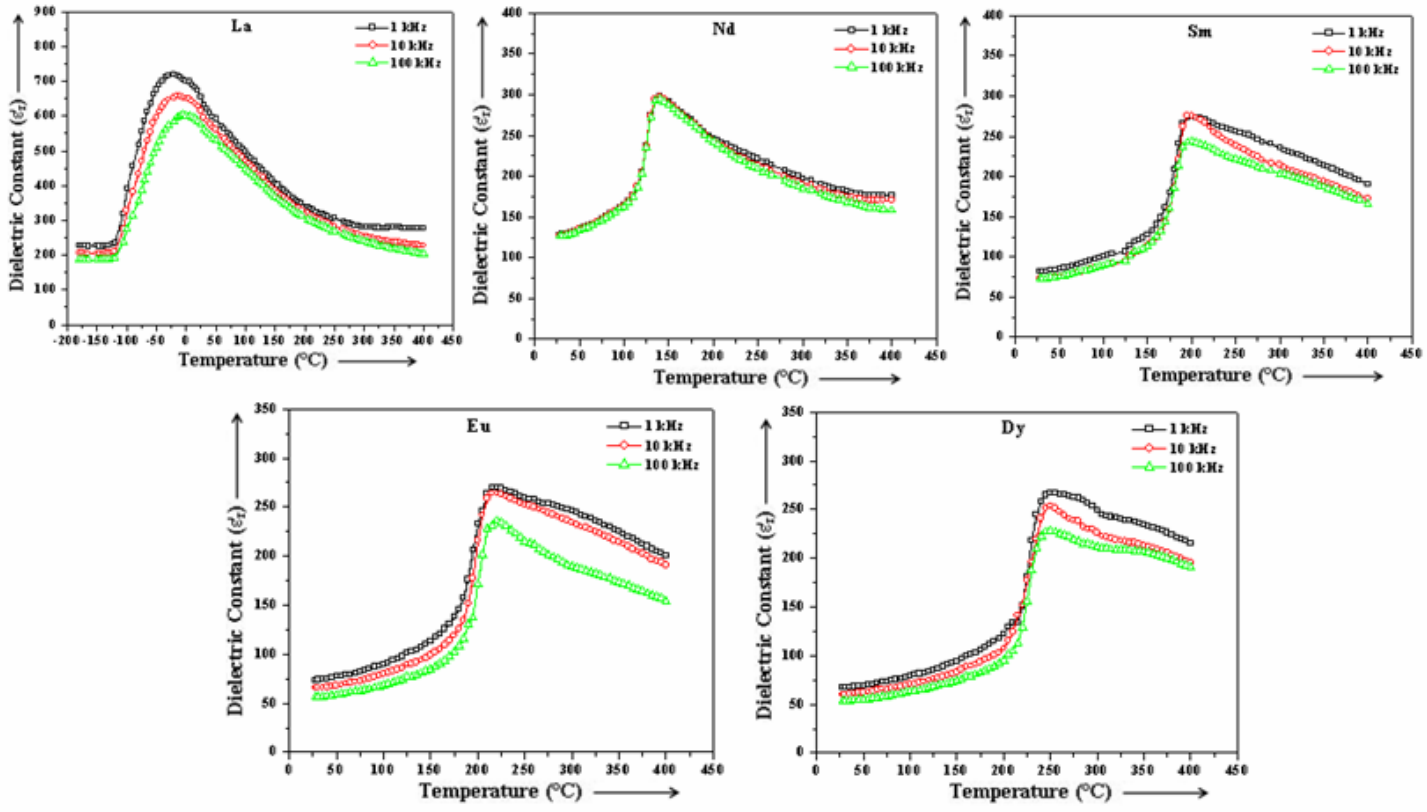

(b)

Fig. 5.4 Variation of ε'_r with temperature in (a) $Ba_5RTi_3Nb_7O_{30}$ and (b) $CaBa_4RTi_3Nb_7O_{30}$ compounds

relaxor behavior [25]. The dielectric relaxation in relaxor ferroelectrics can be expressed by Vogel–Fulcher (VF) relationship as [25]:

$$\omega = f_o \exp\left[\frac{E_a}{k_B(T_m - T_f)}\right] \tag{5.1}$$

where $\omega = 2\pi f$ is the angular frequency, f_o is the Debye frequency, E_a is the activation energy, k_B is the Boltzmann constant, T_m is the temperature at which dielectric constant is maximum and T_f is the static freezing temperature. The plots of ln $(1/\omega)$ versus T_m for $Ba_5LaTi_3Nb_7O_{30}$ and $CaBa_4LaTi_3Nb_7O_{30}$ ceramics are shown in Fig. 5.5 (a) and (b) respectively. It can be seen that data fit well with the VF relationship, which confirms the relaxor behavior of $Ba_5LaTi_3Nb_7O_{30}$ and $CaBa_4LaTi_3Nb_7O_{30}$ compounds. The estimated values of f_o, E_a and T_f are given in the inset of the figures.

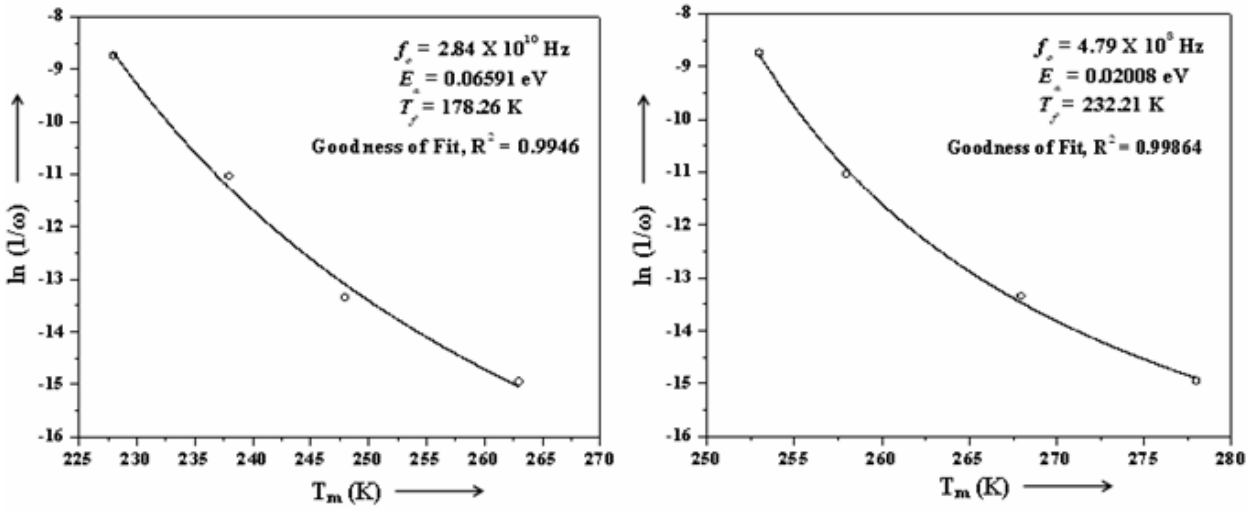

Fig. 5.5 Variation of ln $(1/\omega)$ versus T_m for (a) $Ba_5RTi_3Nb_7O_{30}$ and (b) $CaBa_4RTi_3Nb_7O_{30}$ compounds

To see the effect of ionic radii of the rare-earths on the variation of dielectric constant with temperature, the curves have been plotted in Fig. 5.6 (a) and (b) for

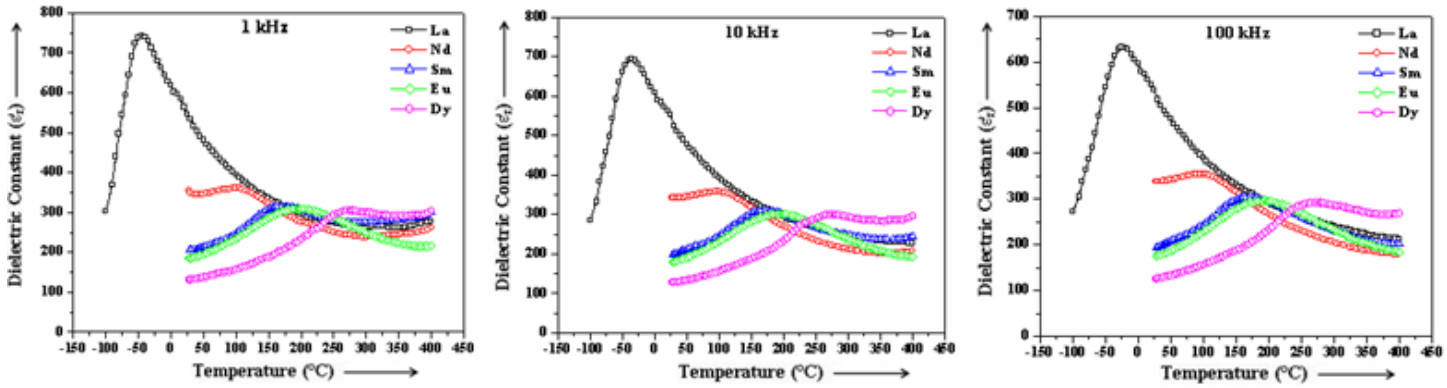

(a)

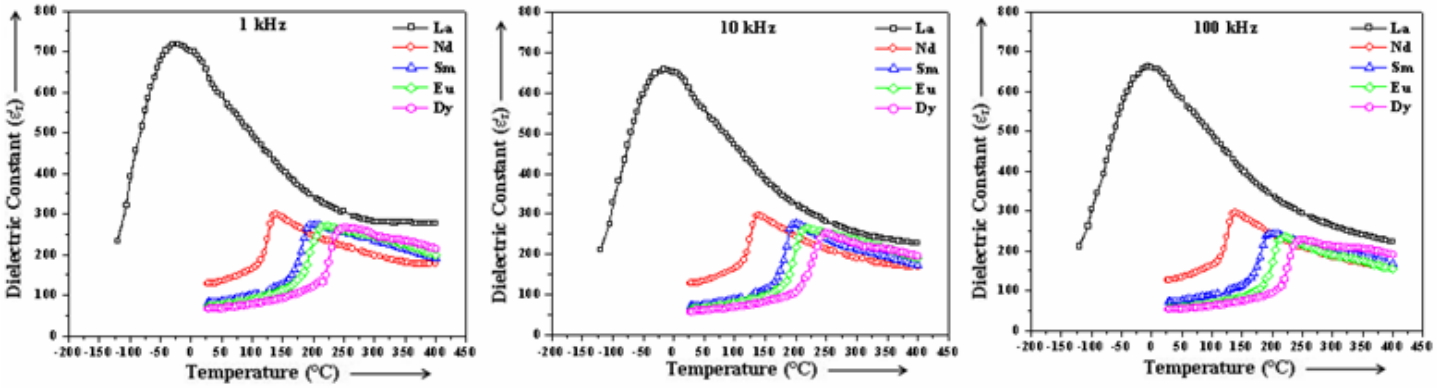

(b)

Fig. 5.6 Comparison of the variation of dielectric constant (ε_r') with temperature of (a) $Ba_5RTi_3Nb_7O_{30}$ and (b) $CaBa_4RTi_3Nb_7O_{30}$ samples at three selected frequencies (1 kHz, 10 kHz and 100 kHz)

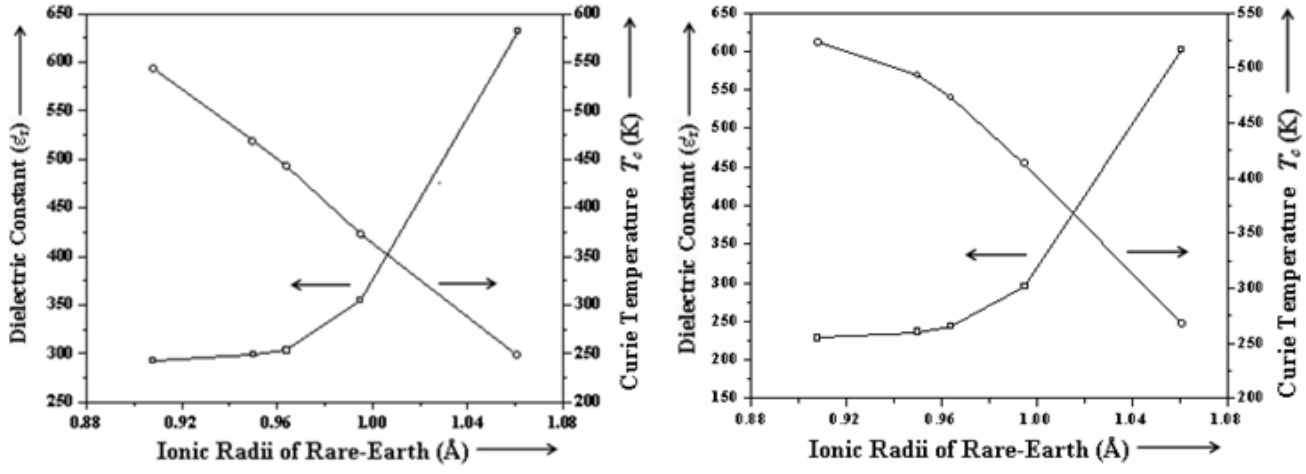

(a) (b)

Fig. 5.7 Variation of ε_r' and T_c of (a) $Ba_5RTi_3Nb_7O_{30}$ and (b) $CaBa_4RTi_3Nb_7O_{30}$ compounds with ionic radii of the rare-earths

$Ba_5RTi_3Nb_7O_{30}$ and $CaBa_4RTi_3Nb_7O_{30}$ compounds respectively at three different frequencies of 1 kHz, 10 kHz and 100 kHz and also the variation of dielectric constant (ε_r') at Curie temperature (T_c) and T_c at 100 kHz with the ionic radii of the rare-earths is shown in Fig. 5.7 (a) and (b) for $Ba_5RTi_3Nb_7O_{30}$ and $CaBa_4RTi_3Nb_7O_{30}$ compounds respectively. From these figures, it is observed that the dielectric constant increases and Curie temperature decreases with the increase in the ionic radii of the rare-earths. From Clausius-Mossotti relation, the dielectric constant of a material can be expressed as:

$$\varepsilon'_r = \left(\frac{3V_m + 8\pi\alpha}{3V_m - 4\pi\alpha}\right) = 1 + \left(\frac{12\pi(\alpha / V_m)}{3 - 4\pi(\alpha / V_m)}\right) \qquad (5.2)$$

where V_m (= $V_{\text{unit cell}}/Z$) is the molar volume and α is the net dielectric polarizability. The increase of the ionic polarizability (α_i) with the increase in ionic radii of the rare- earths (Table 5.1) possibly increase the dielectric constant as manifested by Eq. (5.2). The structural distortion parameter, tetragonal strain (c/a) has been reported to be related to the ferroelectric Curie temperature [26,27]. The variation in T_c, thus, can also be related to the observed tetragonal strain variation (Table 5.2). Larger value of strain indicates that a larger amount of thermal energy is required for the phase transition and therefore an increase in T_c is expected with an increase in the strain. As the tetragonal strain decreases with the increase in the ionic radii of the rare-earths (Table 5.1), so is the Curie temperature.

All the $Ba_5RTi_3Nb_7O_{30}$ and $CaBa_4RTi_3Nb_7O_{30}$ compounds show broad dielectric peaks indicating the diffuse nature of the phase transition. The

diffusivity constant or degree of disorderness (γ) has been calculated using the formula:

$$\ln\left(\frac{1}{\varepsilon'_r}-\frac{1}{\varepsilon'_{r\max}}\right)=\gamma\ln(T-T_c)+\text{constant} \qquad (5.3)$$

where $\varepsilon'_{r\ max}$ is the maximum value of ε'_r at $T = T_c$. The values of γ have been calculated from the slope of ln $(1/\varepsilon'_r - 1/\varepsilon'_{r\ max})$ versus ln $(T-T_c)$ curve (Fig. 5.8) and are given in Table 5.3. It is found to increase with the decrease in ionic radii of the rare-earths. However, the diffusivity constant of calcium containing $CaBa_4RTi_3Nb_7O_{30}$ compounds are smaller than their corresponding rare-earth containing but calcium free $Ba_5RTi_3Nb_7O_{30}$ compounds.

Table 5.3 Variation of diffusivity constant (γ) of (a) $Ba_5RTi_3Nb_7O_{30}$ and (b) $CaBa_4RTi_3Nb_7O_{30}$ compounds

(a)

Sample	Frequency (kHz)	γ
$Ba_5LaTi_3Nb_7O_{30}$	1	1.17
	10	1.18
	100	1.35
$Ba_5NdTi_3Nb_7O_{30}$	1	1.19
	10	1.30
	100	1.44
$Ba_5SmTi_3Nb_7O_{30}$	1	1.28
	10	1.59
	100	1.71
$Ba_5EuTi_3Nb_7O_{30}$	1	1.30
	10	1.60
	100	1.73
$Ba_5DyTi_3Nb_7O_{30}$	1	1.31
	10	1.63
	100	1.76

(b)

Sample	Frequency (kHz)	γ
$CaBa_4LaTi_3Nb_7O_{30}$	1	1.07
	10	1.10
	100	1.14
$CaBa_4NdTi_3Nb_7O_{30}$	1	1.12
	10	1.19
	100	1.25
$CaBa_4SmTi_3Nb_7O_{30}$	1	1.14
	10	1.21
	100	1.28
$CaBa_4EuTi_3Nb_7O_{30}$	1	1.17
	10	1.22
	100	1.33
$CaBa_4DyTi_3Nb_7O_{30}$	1	1.21
	10	1.23
	100	1.35

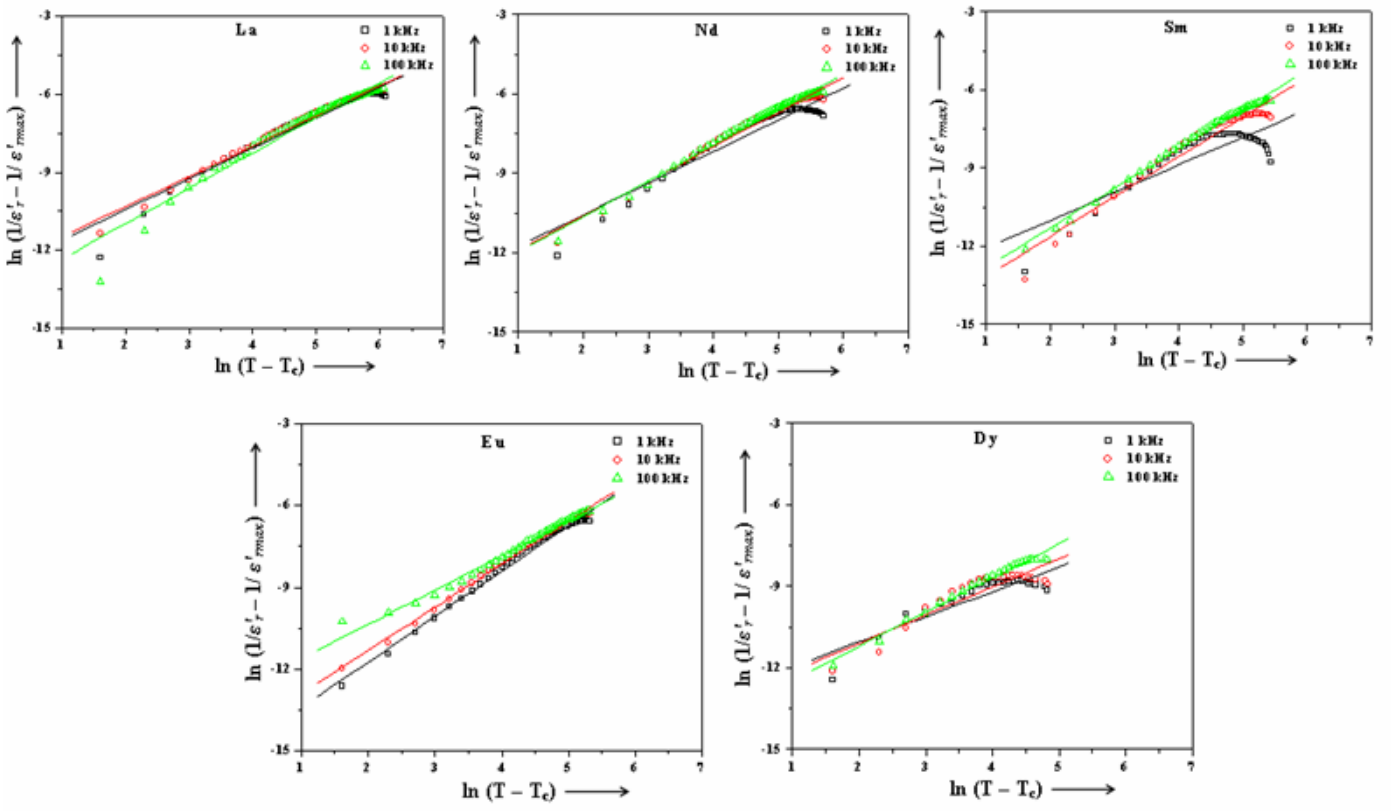

(a)

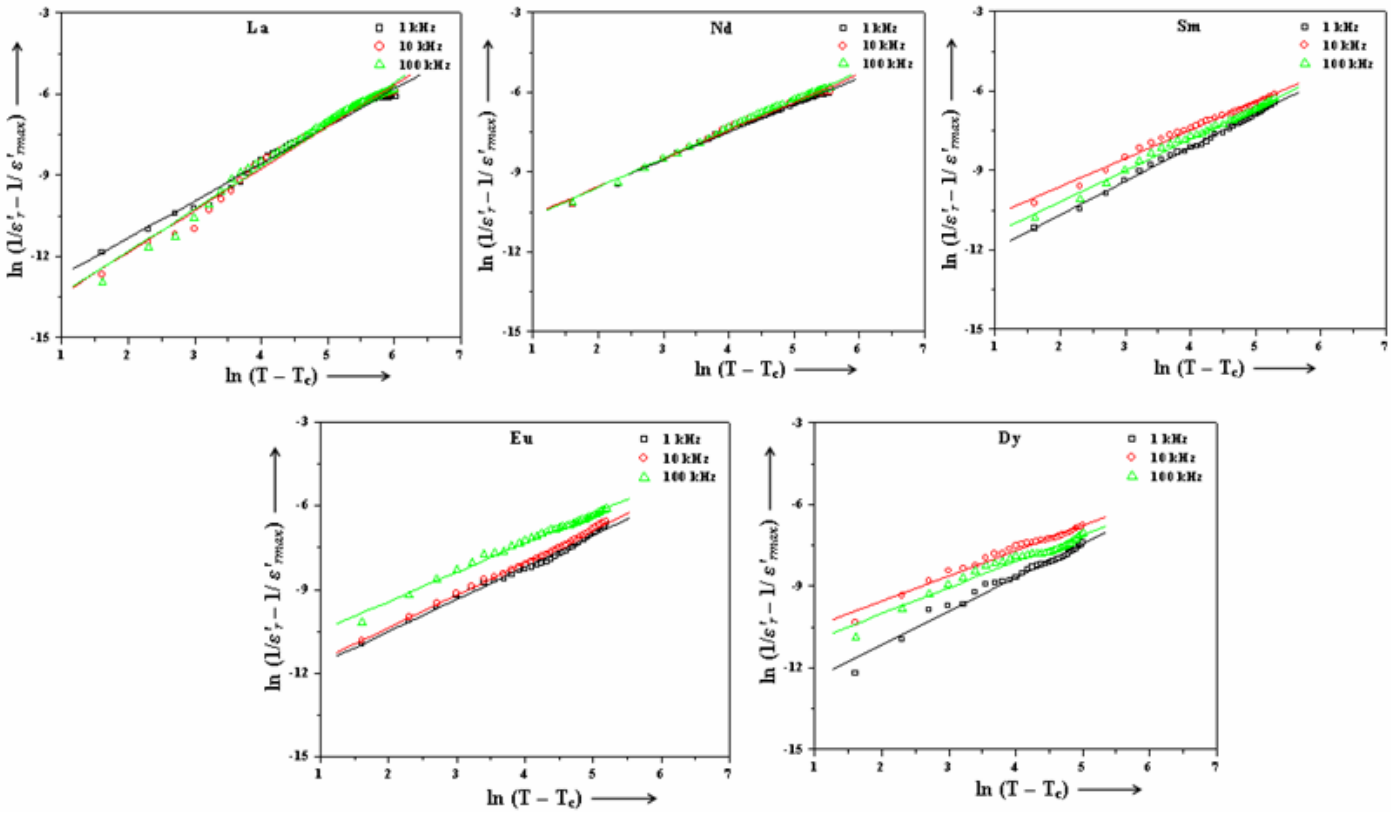

(b)

Fig. 5.8 Variation of ln ($1/\varepsilon'_r$ - $1/\varepsilon'_{r\,max}$) with ln (T-T_c) of (a) $Ba_5RTi_3Nb_7O_{30}$ and (b) $CaBa_4RTi_3Nb_7O_{30}$

Variation of tan δ *with temperature*

Fig. 5.9 shows the variation of dielectric loss (tan δ) with temperature at the selected frequencies of 1 kHz, 10 kHz and 100 kHz.

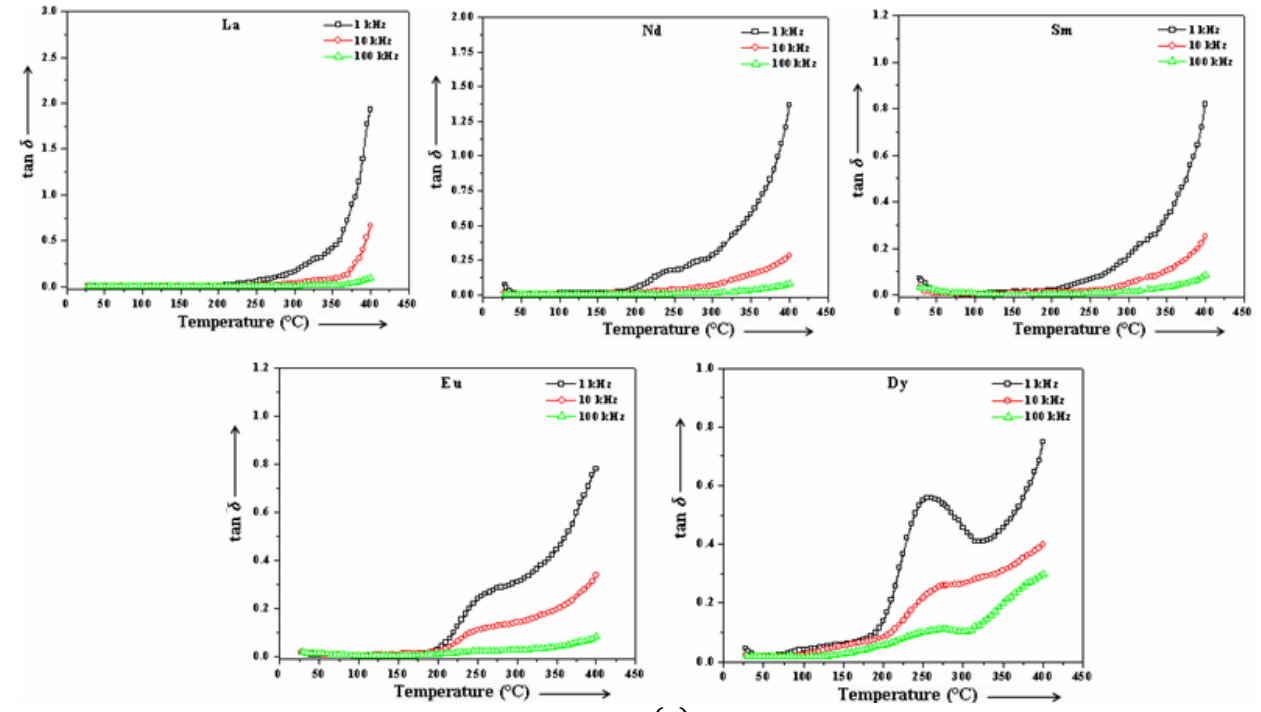

(a)

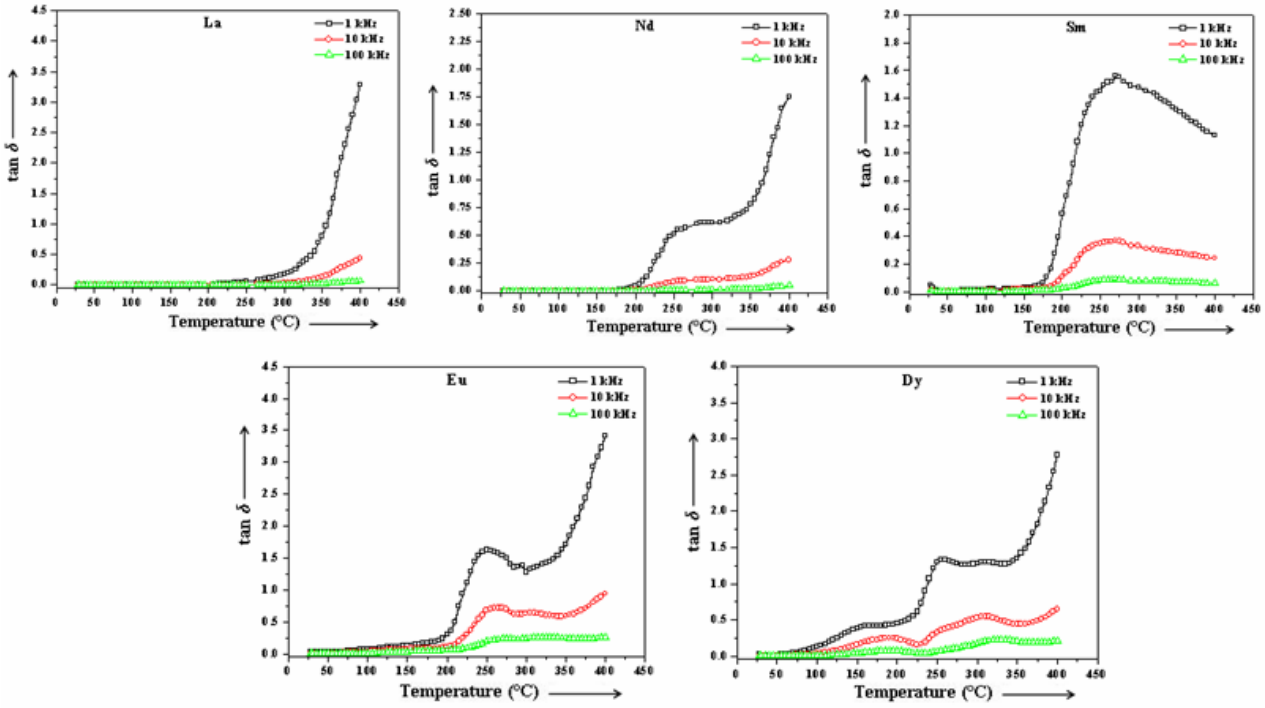

(b)

Fig. 5.9 Variation of tan δ with temperature in (a) $Ba_5RTi_3Nb_7O_{30}$ and (b) $CaBa_4RTi_3Nb_7O_{30}$ compounds

The temperature variation of dielectric loss of all the $Ba_5RTi_3Nb_7O_{30}$ and $CaBa_4RTi_3Nb_7O_{30}$ samples show that the loss is almost constant at lower temperatures but at higher temperatures it increases sharply particularly at lower frequency. This sharp increase of dielectric loss in high temperature region may be attributed to the increased mobility of space charges arising from the defects or vacancies (like oxygen vacancies) in the specimens [28]. To see the effect of ionic radii of the rare-earths on the variation of dielectric loss with temperature, the curves have been plotted in Fig. 5.10 (a) and (b) for $Ba_5RTi_3Nb_7O_{30}$ and $CaBa_4RTi_3Nb_7O_{30}$ compounds respectively at three different frequencies of 1 kHz, 10 kHz and 100 kHz. It can be seen that the dielectric loss increases with decrease in the ionic radii of the rare-earths. Also, relaxation peaks are observed with the

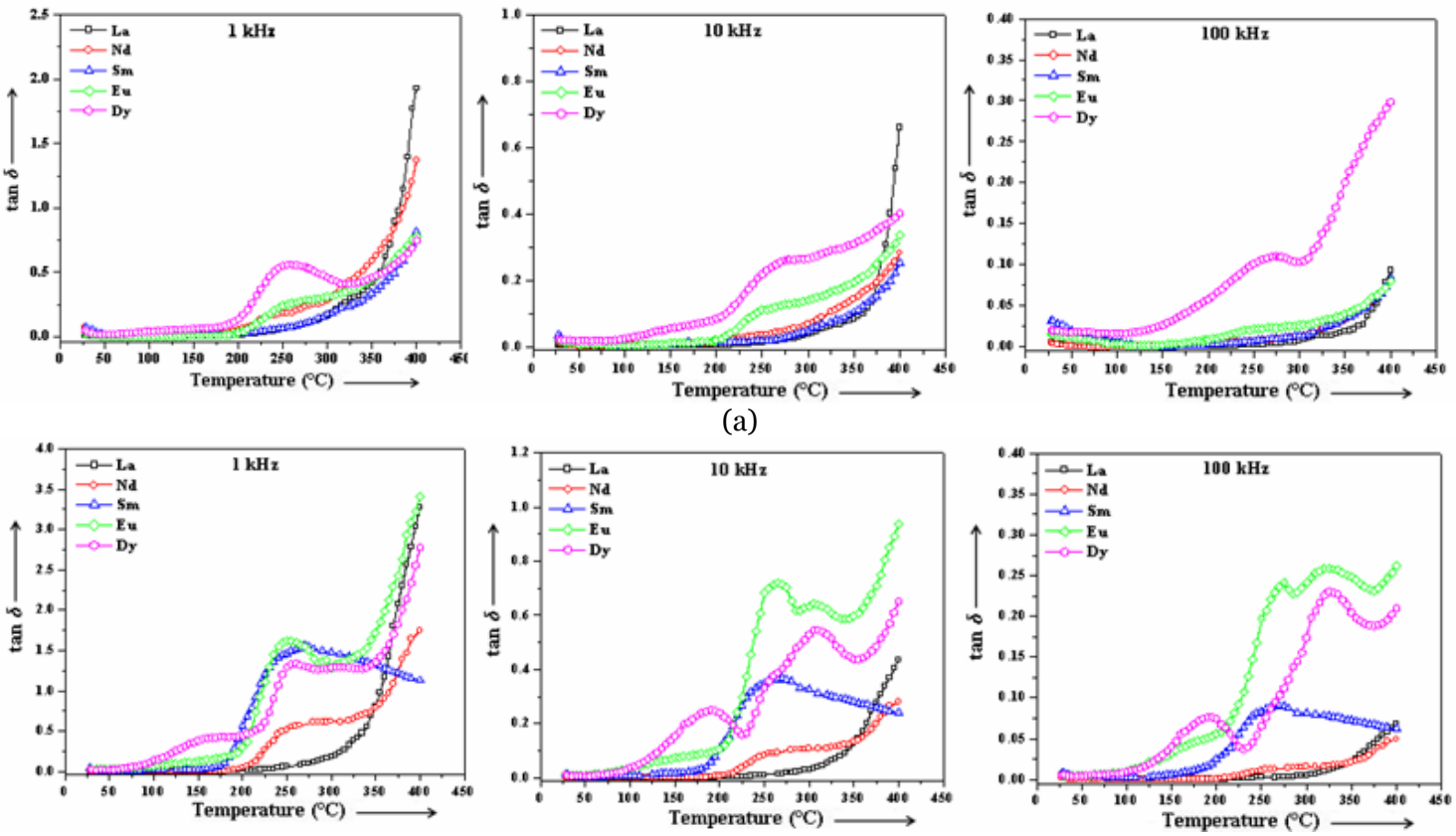

Fig. 5.10 Comparison of temperature variation of tan δ of (a) $Ba_5RTi_3Nb_7O_{30}$ and (b) $CaBa_4RTi_3Nb_7O_{30}$ compounds

lowering of the ionic radii of the rare-earths in both calcium free as well as calcium substituted compounds at all the selected frequencies within the measured temperature range which can be attributed to the thermal-excitation of structural defects [29].

Variation of ε_r' and tan *δ with frequency*

Fig. 5.11 and Fig. 5.12 show the variation of dielectric constant (ε_r') and

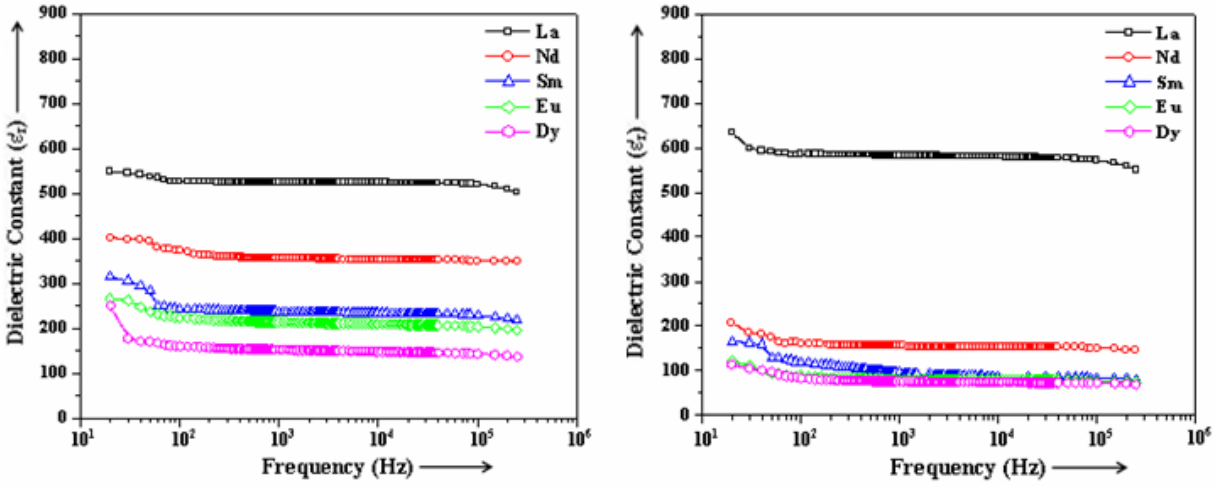

(a) (b)

Fig. 5.11 Variation of ε_r' with frequency in (a) $Ba_5RTi_3Nb_7O_{30}$ and (b) $CaBa_4RTi_3Nb_7O_{30}$ compounds

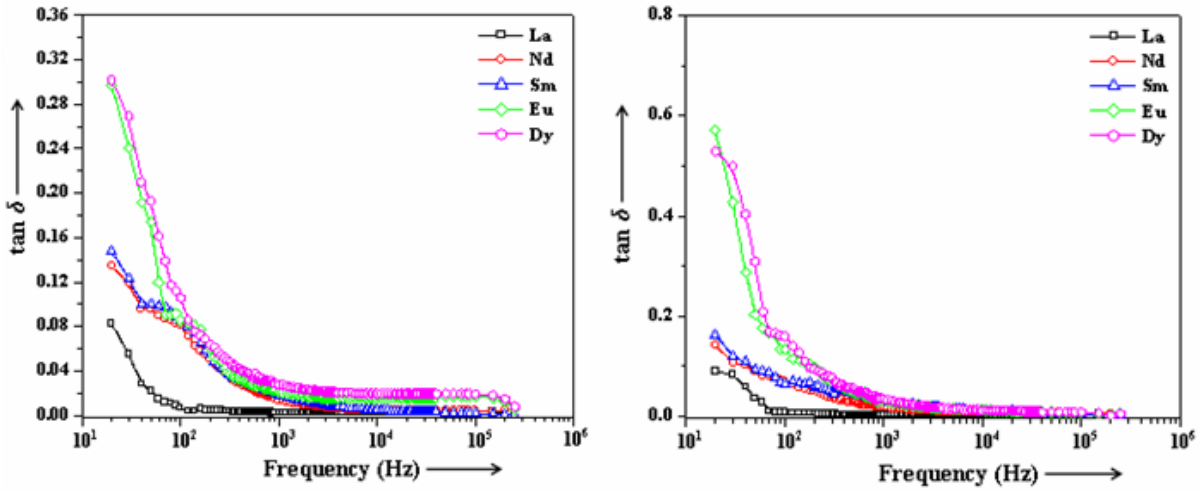

(a) (b)

Fig. 5.12 Variation of ε_r' with frequency in (a) $Ba_5RTi_3Nb_7O_{30}$ and (b) $CaBa_4RTi_3Nb_7O_{30}$ compounds

dielectric loss (tan δ) as a function of frequency at room temperature respectively for $Ba_5RTi_3Nb_7O_{30}$ and $CaBa_4RTi_3Nb_7O_{30}$ compounds. It is observed for all $Ba_5RTi_3Nb_7O_{30}$ and $CaBa_4RTi_3Nb_7O_{30}$ specimens both the dielectric constant and dielectric loss decreases upto about 1 kHz and remains nearly constant thereafter. The dielectric constant of a material has polarization contributions from electronic, ionic, dipolar and space charge [30]. Response frequencies for ionic and electronic polarizations are ~ 10^{13} and 10^{15} Hz, respectively; and at frequencies beyond 1 kHz, contribution from space charge polarization is not expected [30]. Thus, the higher values of dielectric constant at lower frequencies can be attributed to the presence of space charges in the structure which exist as defects such as oxygen vacancies [31,32]. Moreover, at lower frequencies, the dipoles can follow the field resulting in higher values of dielectric constant while at higher frequencies the dipoles are unable to follow the rapidly changing field leading to the reduction in the values of dielectric constant.

The same behaviour is also responsible for the observed variation of dielectric loss as the source of dielectric loss in insulating ceramics is space charge polarization and/or domain wall relaxation [33]. It can also be seen from the figures that the room temperature dielectric constant decreases while the room temperature dielectric loss increases with the reduction of the ionic radii of the rare-earths in both calcium free and calcium substituted compounds in the measured frequency range.

5.2.2.2 Conductivity studies

DC conductivity

The variation of dc conductivity as a function of temperature for $Ba_5RTi_3Nb_7O_{30}$ and $CaBa_4RTi_3Nb_7O_{30}$ compounds are shown in Fig. 5.13 (a) and (b) respectively. For both calcium free as well as calcium containing compounds, it is

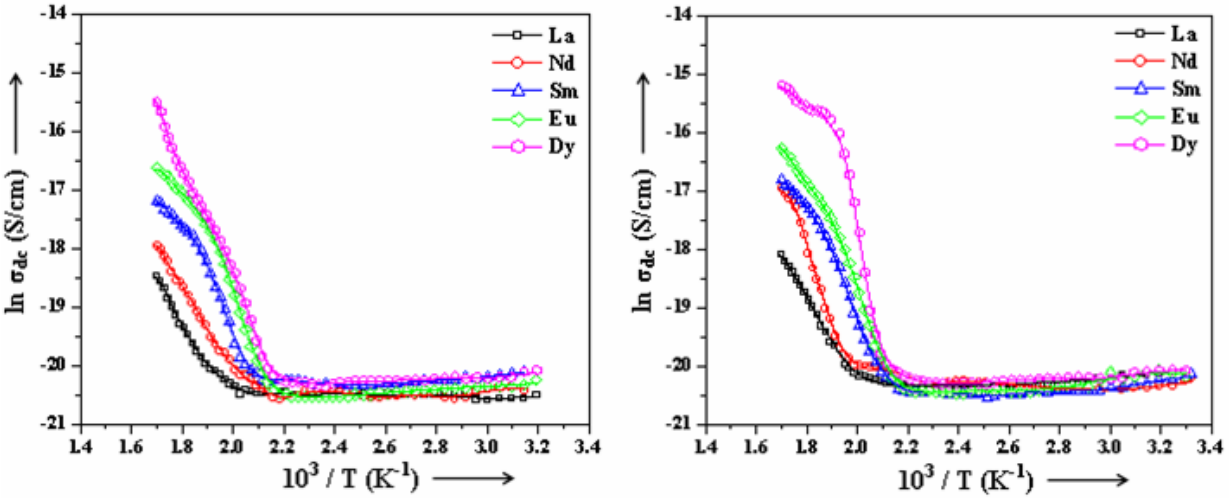

Fig. 5.13 Temperature variation of dc conductivity in (a) $Ba_5RTi_3Nb_7O_{30}$ and (b) $CaBa_4RTi_3Nb_7O_{30}$ compounds

observed that at low temperatures the conductivity is constant. But at higher temperatures, it increases with temperature confirming that all the compounds have negative temperature coefficient of resistance (NTCR) behaviour, a typical characteristic of dielectric materials [34]. The nature of variation of dc conductivity at higher temperature is linear and follows the Arrhenius relationship:

$$\sigma = \sigma_o \exp\left(\frac{-E_a}{k_B T}\right) \tag{5.4}$$

where σ indicates the conductivity, E_a the activation energy and k_B is the Boltzmann constant. The activation energies have been calculated in the higher temperature region using Eq. (5.4) and are given in Table 5.4. The dc conductivity is found to increase while activation energy decreases with decrease in the ionic radii of the

rare earths in both calcium free and calcium substituted compounds. This observed variation of dc conductivity with ionic radii of the rare earths is consistent with dielectric loss, which also increases with decrease in the ionic radii of the rare earths as dielectric loss is related to dc conductivity by the Eq. (2.19).

AC conductivity

Figs. 5.14 (a) and (b) show the temperature variation of ac conductivity at the selected frequencies of 1 kHz, 10 kHz and 100 kHz for $Ba_5RTi_3Nb_7O_{30}$ and $CaBa_4RTi_3Nb_7O_{30}$ compounds respectively. For all the specimens, a change in slope in the curve is seen which can be attributed to the difference in activation energy in the paraelectric and ferroelectric phases. The activation energies at the above mentioned frequencies, evaluated in the high temperature paraelectric phase using Eq. (5.4) are summarized in Table 5.4. It is observed that the activation energy decreases with decrease in the ionic radii of the rare-earths in both calcium free and calcium substituted compounds. However, the activation energy of calcium containing $CaBa_4RTi_3Nb_7O_{30}$ compounds is higher than their corresponding rare-earth containing but calcium free $Ba_5RTi_3Nb_7O_{30}$ compounds. This is likely due to the reduction of the degree of disorderness (γ) in the calcium containing specimens (Table 5.3). To see the effect of ionic radii of rare-earths on the temperature variation of ac conductivity, the curves have been plotted in Fig. 5.15 at three different frequencies of 1 kHz, 10 kHz and 100 kHz. It is observed that the ac conductivity increases with the decrease in the ionic radii of the rare-earths in both calcium free and calcium containing compounds which can be related to the increase in the dielectric loss (Fig. 5.8).

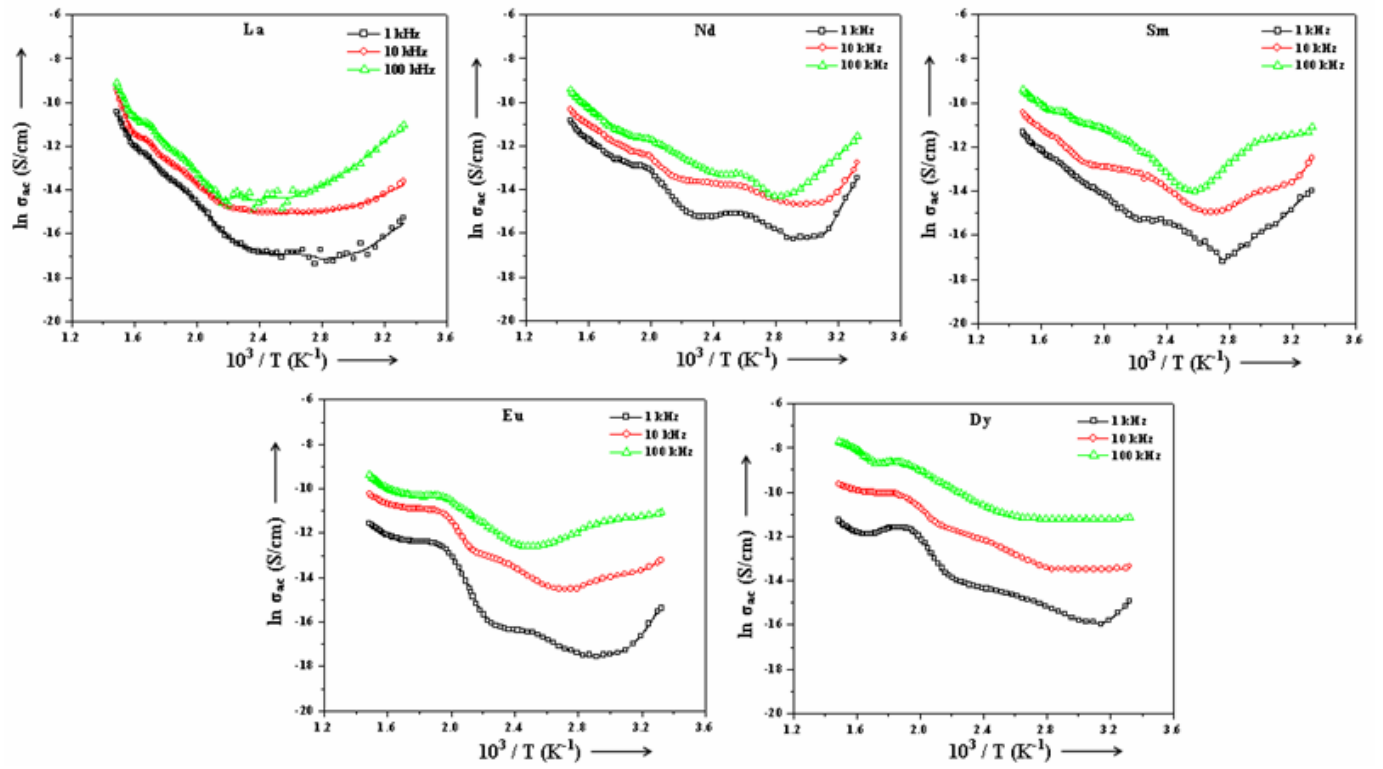

(a)

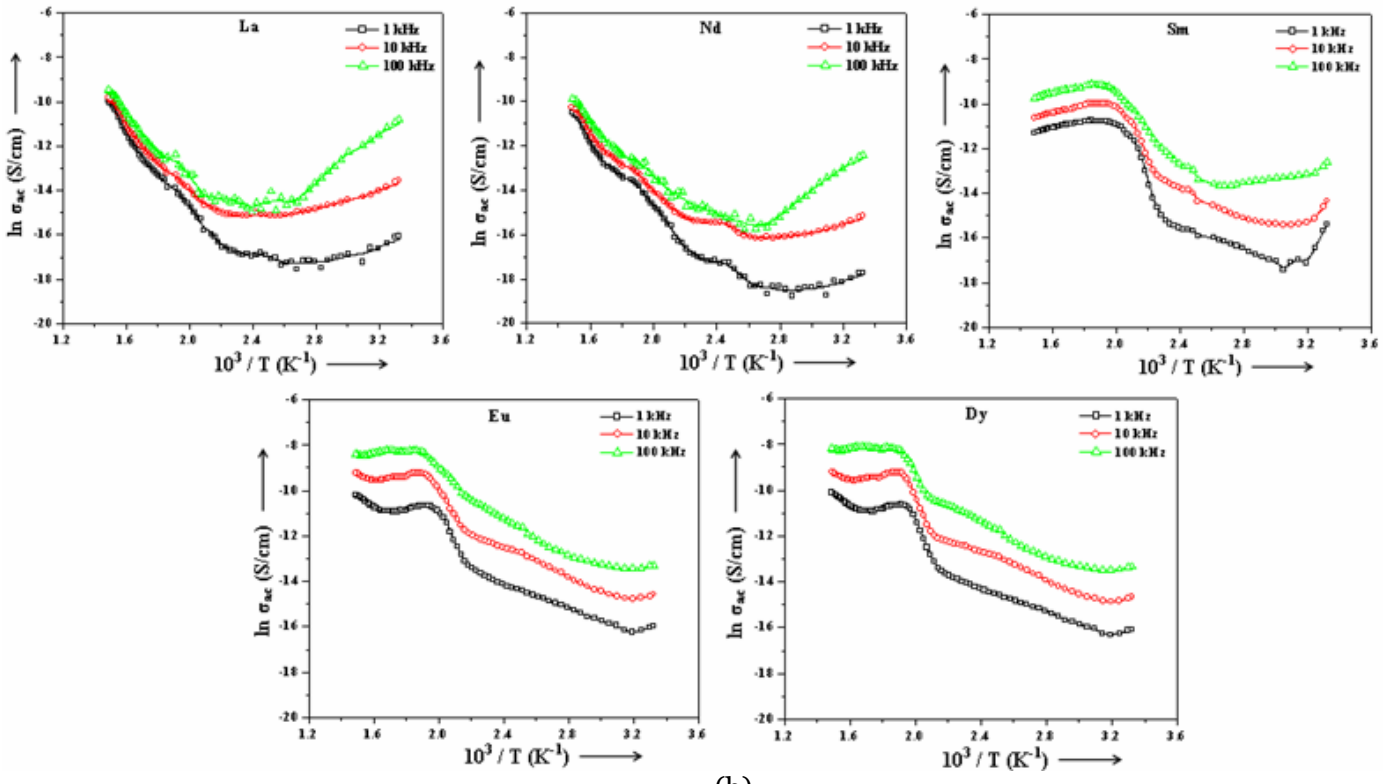

(b)

Fig. 5.14 Temperature variation of ac conductivity in (a) $Ba_5RTi_3Nb_7O_{30}$ and (b) $CaBa_4RTi_3Nb_7O_{30}$ compounds at 1 kHz, 10 kHz and 100 kHz

Table 5.4 Activation energies (E_a) as calculated from dc and ac conductivity for:

(a) $Ba_5RTi_3Nb_7O_{30}$ compounds

Sample	Frequency (kHz)	E_a (eV) (ac conductivity)	E_a (eV) (dc conductivity)
$Ba_5LaTi_3Nb_7O_{30}$	1 10 100	0.62 0.60 0.47	1.31
$Ba_5NdTi_3Nb_7O_{30}$	1 10 100	0.42 0.29 0.26	1.25
$Ba_5SmTi_3Nb_7O_{30}$	1 10 100	0.37 0.34 0.26	1.13
$Ba_5EuTi_3Nb_7O_{30}$	1 10 100	0.35 0.33 0.25	0.89
$Ba_5DyTi_3Nb_7O_{30}$	1 10 100	0.27 0.25 0.22	0.59

(b) $CaBa_4RTi_3Nb_7O_{30}$ compounds

Sample	Frequency (kHz)	E_a (eV) (ac conductivity)	E_a (eV) (dc conductivity)
$CaBa_4LaTi_3Nb_7O_{30}$	1 10 100	0.65 0.64 0.49	1.47
$CaBa_4NdTi_3Nb_7O_{30}$	1 10 100	0.60 0.56 0.48	1.35
$CaBa_4SmTi_3Nb_7O_{30}$	1 10 100	0.55 0.52 0.47	1.27
$CaBa_4EuTi_3Nb_7O_{30}$	1 10 100	0.46 0.42 0.38	1.06
$CaBa_4DyTi_3Nb_7O_{30}$	1 10 100	0.37 0.32 0.27	0.79

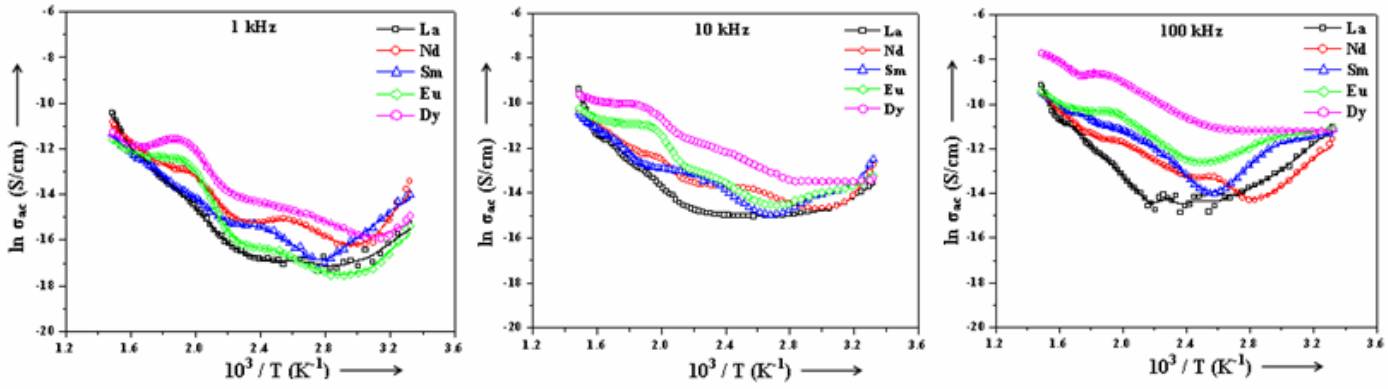

(a)

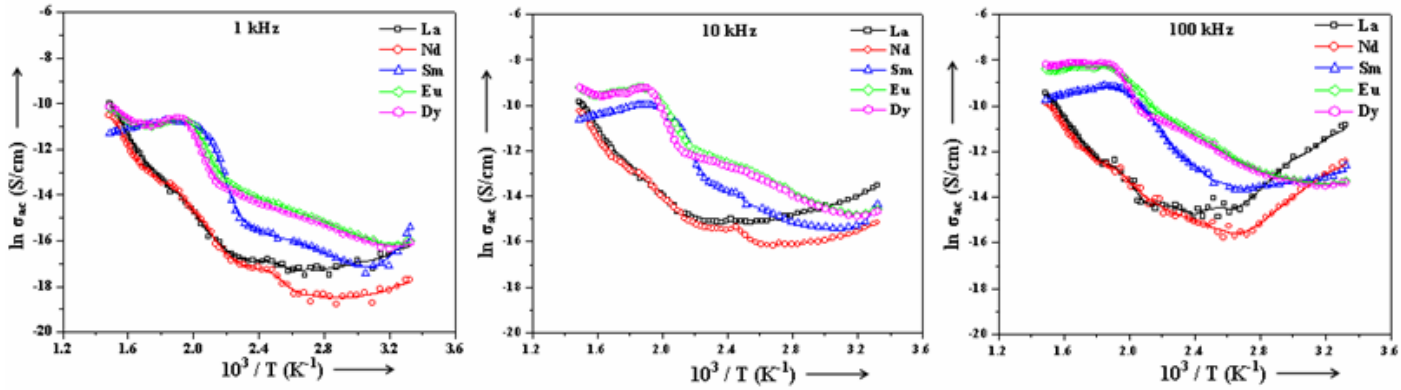

(b)

Fig. 5.15 Comparison of temperature variation of ac conductivity in (a) $Ba_5RTi_3Nb_7O_{30}$ and (b) $CaBa_4RTi_3Nb_7O_{30}$ compounds at 1 kHz, 10 kHz and 100 kHz

Total conductivity

The total electrical conductivity can be represented by an equation proposed by Jonscher [35],

$$\sigma_{tot} = \sigma_{dc} + \sigma_{ac}(\omega) = \sigma_o + A\omega^n \qquad (5.5)$$

where σ_{dc} (or σ_o) is the dc conductivity due to excitation of electron from a localized state to the conduction band, and $A\omega^n$ is the ac conductivity due to the dispersion phenomena occurring in the material. A is a temperature dependent constant and n is the power law exponent which generally varies between 0 and 1 depending on temperature. The exponent n represents the degree of interaction between mobile ions with the lattice around them and the prefactor A determines

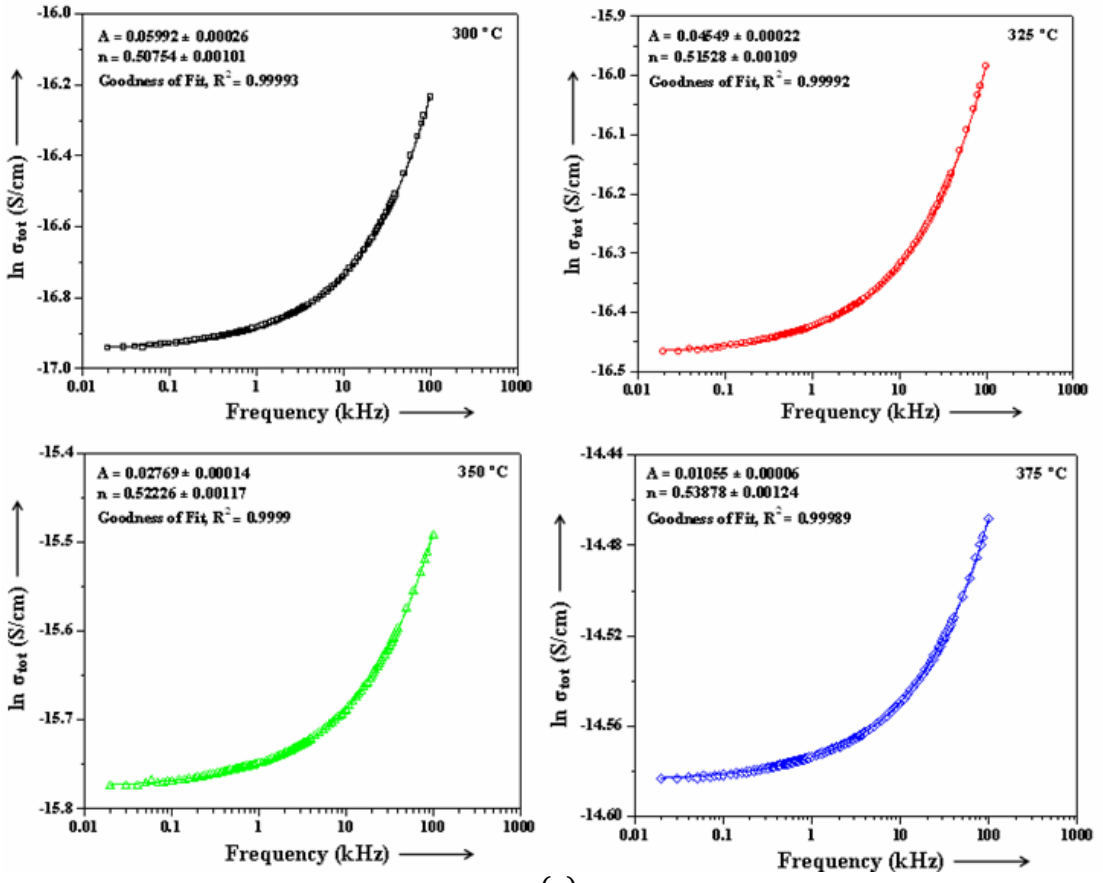

(a)

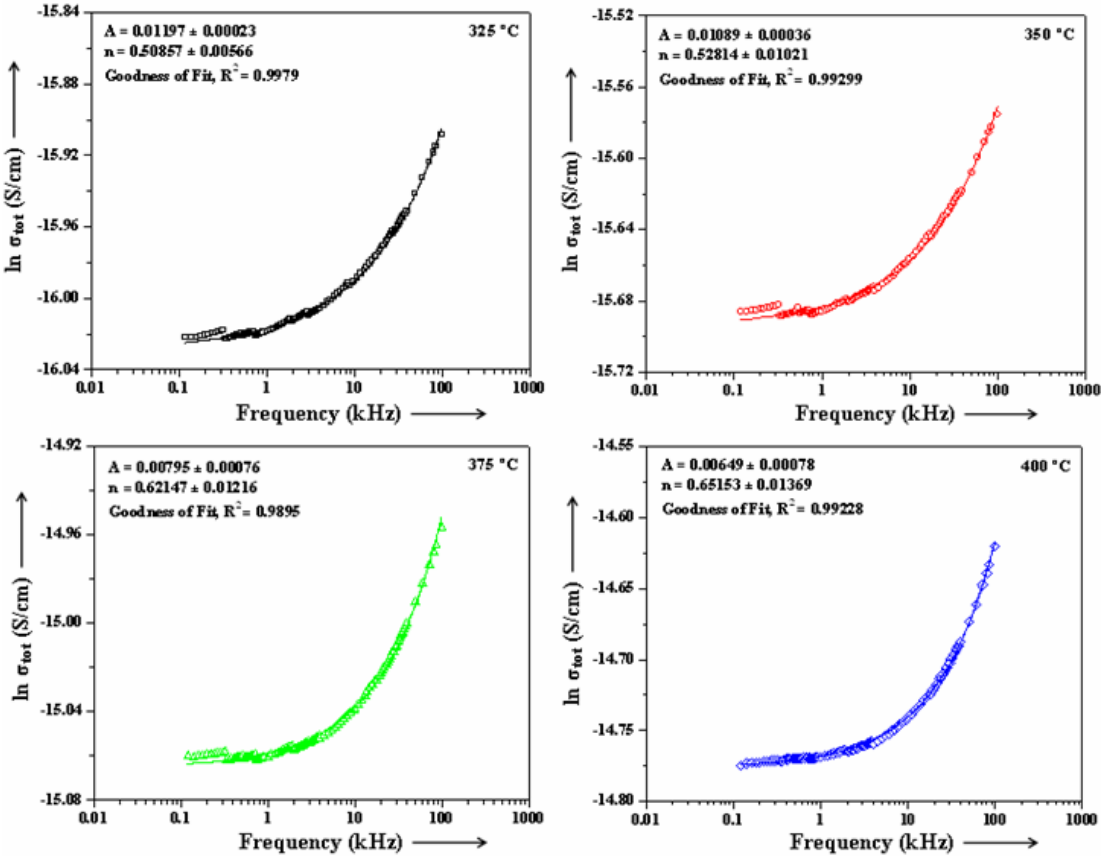

(b)

Fig. 5.16 Frequency variation of σ_{tot} of (a) $Ba_5SmTi_3Nb_7O_{30}$ and (b) $CaBa_4SmTi_3Nb_7O_{30}$ at different temperatures

the strength of polarizability [36]. All the compounds are found to obey the Jonscher's equation (Eq. 5.5), for example as shown in Fig. 5.16 (a) and (b) for $Ba_5SmTi_3Nb_7O_{30}$ and $CaBa_4SmTi_3Nb_7O_{30}$ compounds respectively and the Jonscher's fitting results i.e. A and n are summarized in Table 5.5 for each measuring temperature. For each of the compound, parameter A decreases while n increases with the increase in the measuring temperature which suggests that the strength of the polarizability reduces while the ions-lattice interaction increases with temperature in this class of compounds.

Table 5.5 Jonscher's fitting parameters, prefactor A and exponent n for:

(a) $Ba_5RTi_3Nb_7O_{30}$

Sample	Temperature (°C)	A	n
$Ba_5LaTi_3Nb_7O_{30}$	340	0.03730	0.46771
	365	0.01331	0.57042
	390	0.00770	0.65836
	415	0.00399	0.69174
$Ba_5NdTi_3Nb_7O_{30}$	350	0.09380	0.37768
	375	0.08782	0.39311
	400	0.06730	0.43148
	425	0.04757	0.43348
$Ba_5SmTi_3Nb_7O_{30}$	300	0.05992	0.50754
	325	0.04549	0.51528
	350	0.02769	0.52226
	375	0.01055	0.53878
$Ba_5EuTi_3Nb_7O_{30}$	325	0.06342	0.46384
	350	0.05131	0.48060
	375	0.04262	0.54205
	400	0.01249	0.67190
$Ba_5DyTi_3Nb_7O_{30}$	350	0.28195	0.38129
	375	0.17648	0.41830
	400	0.09905	0.42223
	425	0.06473	0.43390

(b) $CaBa_4RTi_3Nb_7O_{30}$

Sample	Temperature (°C)	A	n
$CaBa_4LaTi_3Nb_7O_{30}$	340	0.00846	0.24224
	365	0.00771	0.62951
	390	0.00526	0.65067
	415	0.00424	0.69993
$CaBa_4NdTi_3Nb_7O_{30}$	330	0.05511	0.39601
	355	0.04318	0.43550
	380	0.04178	0.44183
	405	0.00926	0.61404
$CaBa_4SmTi_3Nb_7O_{30}$	325	0.01197	0.50857
	350	0.01089	0.52814
	375	0.00795	0.62147
	400	0.00649	0.65153
$CaBa_4EuTi_3Nb_7O_{30}$	325	0.01501	0.55013
	350	0.01470	0.56044
	375	0.01257	0.58428
	400	0.00748	0.71381
$CaBa_4DyTi_3Nb_7O_{30}$	325	0.03957	0.45384
	350	0.03842	0.48419
	375	0.02901	0.48993
	400	0.01144	0.54341

5.2.2.3 Impedance analysis

Fig. 5.17 (a) and (b) show the impedance (Z'-Z'') plots at different measuring temperatures of $Ba_5SmTi_3Nb_7O_{30}$ and $CaBa_4SmTi_3Nb_7O_{30}$ compounds respectively.

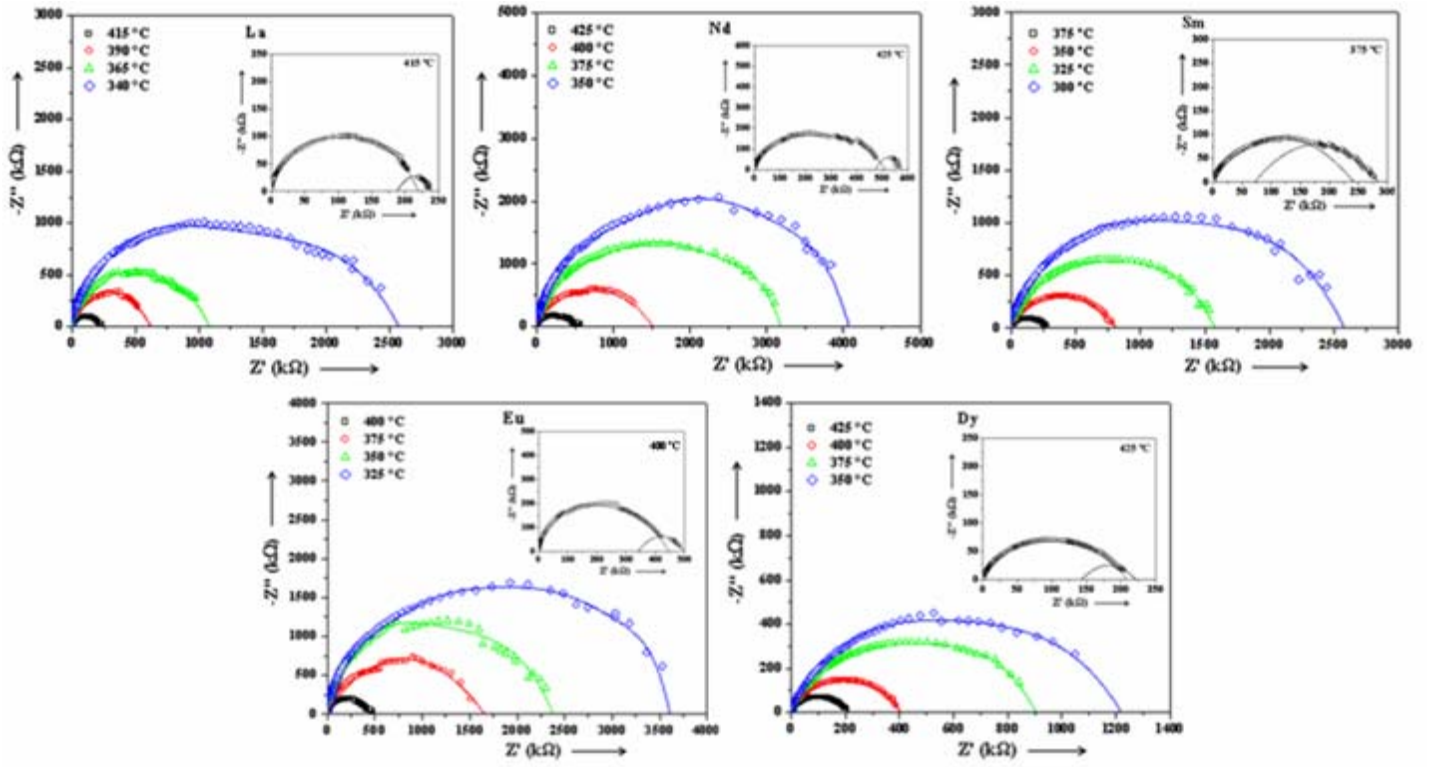

(a)

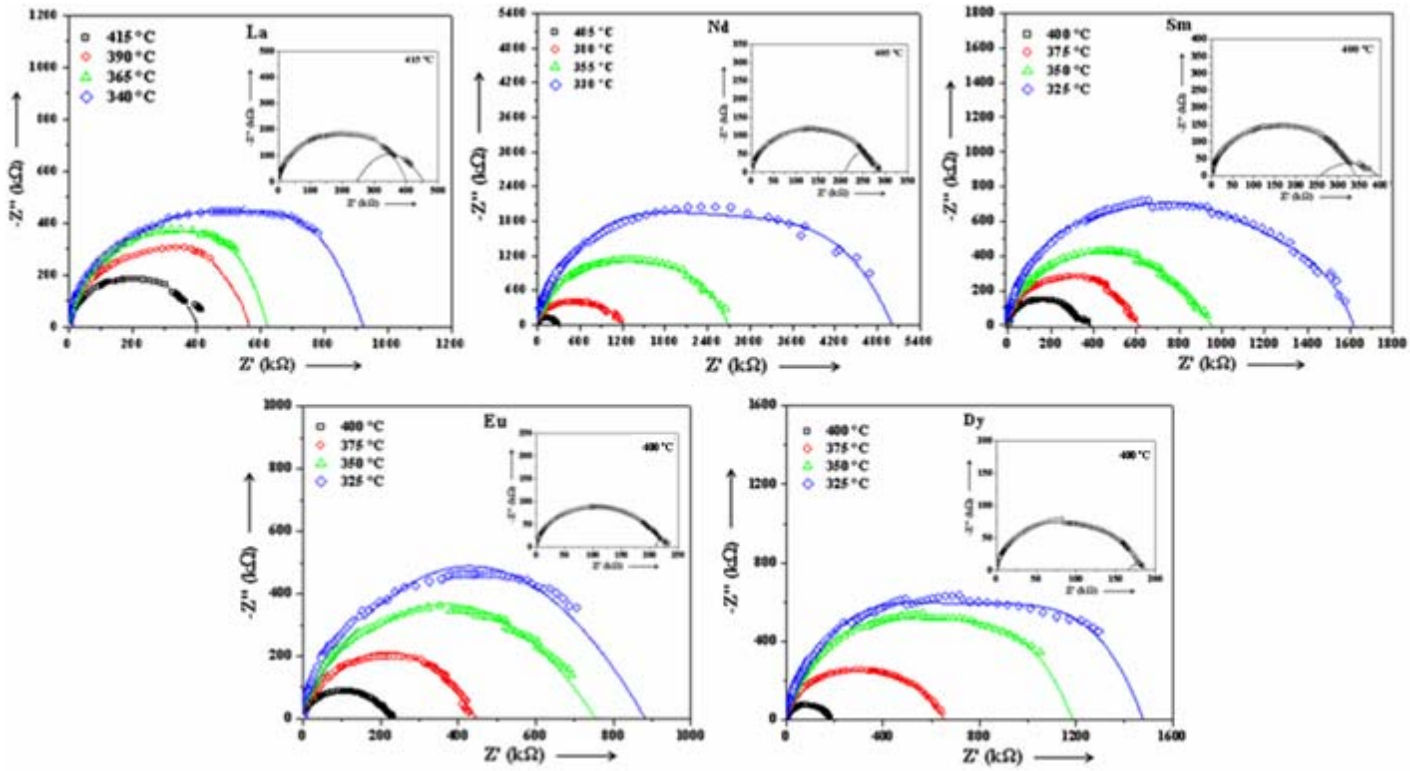

(b)

Fig. 5.17 Cole-Cole plots of (a) $Ba_5SmTi_3Nb_7O_{30}$ and (b) $CaBa_4SmTi_3Nb_7O_{30}$ compounds at different temperatures

Table 5.6 Various parameters obtained from the Cole-Cole plots for:

(a) $Ba_5SmTi_3Nb_7O_{30}$

Sample	Temperature (°C)	R_b (kΩ)	C_b (nF)	R_{gb} (kΩ)	C_{gb} (nF)	E_a (eV)
$Ba_5LaTi_3Nb_7O_{30}$	340	2573	0.26	-	-	
	365	1076	0.20	-	-	1.15
	390	617	0.18	-	-	
	415	219	0.17	20	15.29	
$Ba_5NdTi_3Nb_7O_{30}$	350	4066	0.28	-	-	
	375	3181	0.21	-	-	1.03
	400	1538	0.20	-	-	
	425	514	0.17	61	21.75	
$Ba_5SmTi_3Nb_7O_{30}$	300	2590	0.38	-	-	
	325	1610	0.35	-	-	0.99
	350	800	0.31	-	-	
	375	240	0.30	45	3.85	
$Ba_5EuTi_3Nb_7O_{30}$	325	3610	0.41	-	-	
	350	2372	0.32	-	-	0.92
	375	1650	0.31	-	-	
	400	444	0.30	56	20.32	
$Ba_5DyTi_3Nb_7O_{30}$	350	1216	0.93	-	-	
	375	904	0.88	-	-	0.90
	400	403	0.66	-	-	
	425	207	0.55	14	126.38	

(b) $CaBa_4SmTi_3Nb_7O_{30}$

Sample	Temperature (°C)	R_b (kΩ)	C_b (nF)	R_{gb} (kΩ)	C_{gb} (nF)	E_a (eV)
$CaBa_4LaTi_3Nb_7O_{30}$	340	911	0.73	-	-	
	365	623	0.35	-	-	1.08
	390	551	0.26	-	-	
	415	401	0.20	54	4.76	
$CaBa_4NdTi_3Nb_7O_{30}$	330	5003	0.20	-	-	
	355	2692	0.19	-	-	0.94
	380	1203	0.17	-	-	
	405	279	0.15	10	28.45	
$CaBa_4SmTi_3Nb_7O_{30}$	325	1621	0.23	-	-	
	350	951	0.22	-	-	0.67
	375	619	0.21	-	-	
	400	340	0.18	53	18.78	
$CaBa_4EuTi_3Nb_7O_{30}$	325	881	0.24	-	-	
	350	753	0.23	-	-	0.63
	375	446	0.22	-	-	
	400	227	0.21	4	284.49	
$CaBa_4DyTi_3Nb_7O_{30}$	325	1480	0.32	-	-	
	350	1187	0.25	-	-	0.54
	375	652	0.22	-	-	
	400	183	0.21	6	221.16	

All the semicircles in the Cole-Cole plots exhibit some depression instead of a semicircle centered on the x-axis. Such behaviour is indicative of non-Debye type of relaxation and it also manifests that there is a distribution of relaxation time instead of a single relaxation time in the material [37]. For all the samples, there is a presence of two semicircles at higher temperature (Fig. 5.17 inset) which exhibits the presence of both grain (bulk property) and grain boundary effects. The value of bulk resistances (R_b) at different temperatures for all the samples have been obtained from the intercept of the semicircular arcs on the real axis (Z') and are given in Table 5.6. It is observed that R_b decreases with rise in the temperature for all the samples. This again confirms the negative temperature coefficient of resistance (NTCR) behaviour of all the calcium free and calcium substituted rare-earths containing compounds. From these values of R_b, the bulk conductivity, σ_{bulk} has been obtained by using Eq. (2.31) and its variation with temperature is shown in Fig. 5.18 for all the samples. The respective capacitances (C_b and C_{gb}) due to the grain and grain boundary effect have been calculated using Eq. (2.30). The values of R_b, R_{gb}, C_b and C_{gb} obtained from Cole-Cole plots at different temperatures for $Ba_5SmTi_3Nb_7O_{30}$ and $CaBa_4SmTi_3Nb_7O_{30}$ compounds are listed in Table 5.6.

The relaxation time due to bulk effect (τ_b) has been calculated using Eq. (2.30). Fig. 5.19 shows the temperature variation of τ_b for all the samples. It is observed that the value of τ_b decreases with increase in temperature for all the samples and its temperature dependence follows the Arrhenius relation:

$$\tau_b = \tau_o \exp\left(\frac{-E_a}{k_B T}\right) \tag{5.6}$$

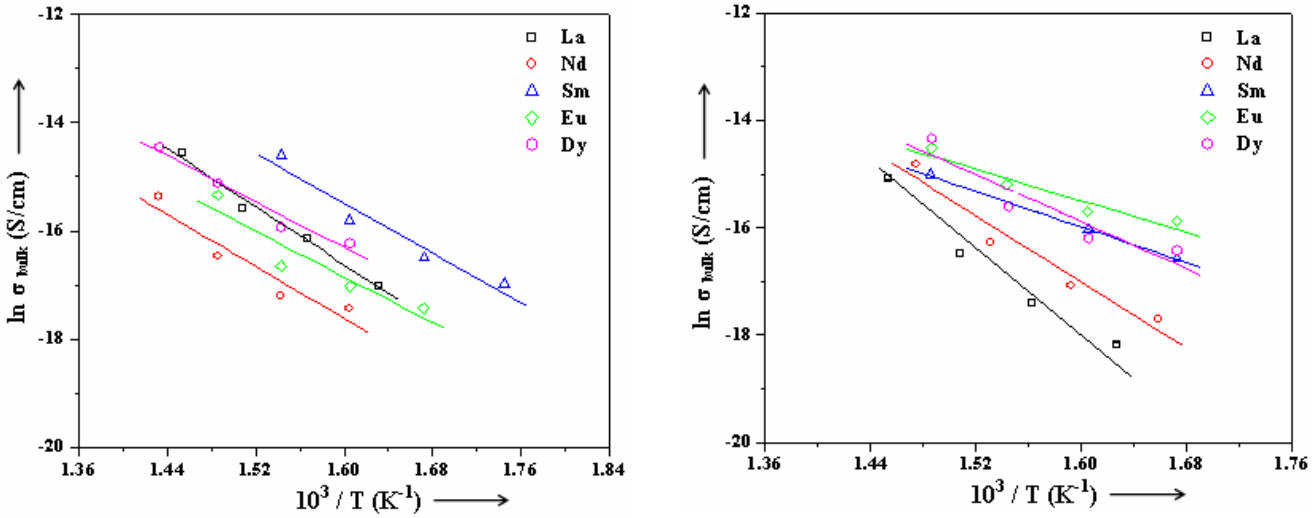

(a) (b)

Fig. 5.18 Temperature variation of bulk conductivity in (a) $Ba_5RTi_3Nb_7O_{30}$ and (b) $CaBa_4RTi_3Nb_7O_{30}$ compounds

where τ_o is the pre-exponential factor, k_B is Boltzmann constant and E_a the activation energy. The value of activation energy (E_a) using Eq. (5.6) is summarized in Table 3.4. It can again be noted that the activation energy decreases with decrease in the ionic radii of the rare-earths in both calcium free as well as calcium substituted compounds.

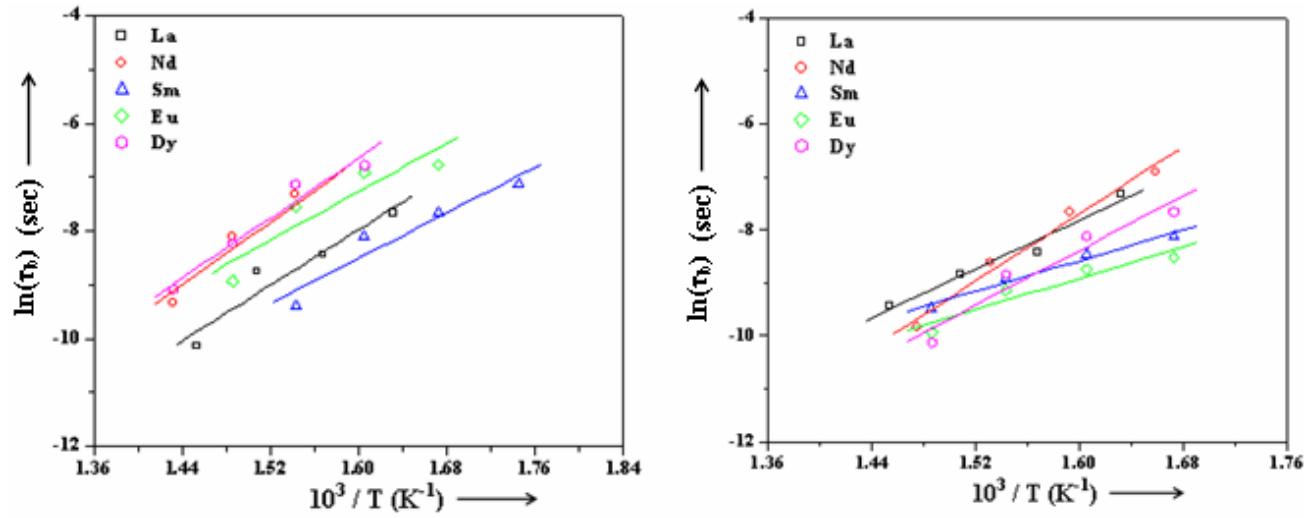

(a) (b)

Fig. 5.19 Temperature variation of relaxation time in (a) $Ba_5RTi_3Nb_7O_{30}$ and (b) $CaBa_4RTi_3Nb_7O_{30}$ compounds

5.2.2.4 Ferroelectric studies

Figs. 5.20 (a) and (b) show the P-E hysteresis loops of $Ba_5RTi_3Nb_7O_{30}$ and $CaBa_4RTi_3Nb_7O_{30}$ compounds respectively. The corresponding values of remanent polarization ($2P_r$) and coercive field ($2E_c$) are summarized in Table 5.7. On comparing

Table 5.7 Values of $2P_r$ and $2E_c$ of (a) $Ba_5RTi_3Nb_7O_{30}$ and (b) $CaBa_4RTi_3Nb_7O_{30}$ compounds

(a)

Sample	$2P_r$ ($\mu C/cm^2$)	$2E_c$ (kV/cm)
$Ba_5LaTi_3Nb_7O_{30}$	0.5	6.0
$Ba_5NdTi_3Nb_7O_{30}$	0.7	10.0
$Ba_5SmTi_3Nb_7O_{30}$	2.3	23.3
$Ba_5EuTi_3Nb_7O_{30}$	2.4	30.5
$Ba_5DyTi_3Nb_7O_{30}$	2.6	33.0

(b)

Sample	$2P_r$ ($\mu C/cm^2$)	$2E_c$ (kV/cm)
$CaBa_4LaTi_3Nb_7O_{30}$	0.7	6.2
$CaBa_4NdTi_3Nb_7O_{30}$	1.0	12.5
$CaBa_4SmTi_3Nb_7O_{30}$	2.5	36.7
$CaBa_4EuTi_3Nb_7O_{30}$	3.4	52.7
$CaBa_4DyTi_3Nb_7O_{30}$	3.6	63.0

the loops (Fig. 5.21 (a) and (b) and Table 5.7), it is observed that remanent polarization ($2P_r$) and coercive field ($2E_c$) values are found to increase with decrease in the ionic radii of the rare-earths in both calcium free as well as calcium containing compounds. However, it is found that for each rare-earth containing compounds, the remanent polarization ($2P_r$) and coercive field ($2E_c$) values increases with addition of calcium which is possibly due to the pronounced structural distortion arising due to the partial substitution of smaller cation calcium at barium-site [38].

5.2.2.5 Pyroelectric studies

The temperature variation of pyroelectric coefficient (P_T) for $Ba_5RTi_3Nb_7O_{30}$ and $CaBa_4RTi_3Nb_7O_{30}$ compounds calculated using Eq. (2.37) is shown in Fig. 5.22 (a) and (b) respectively. For all the specimens, the pyroelectric current as well as the

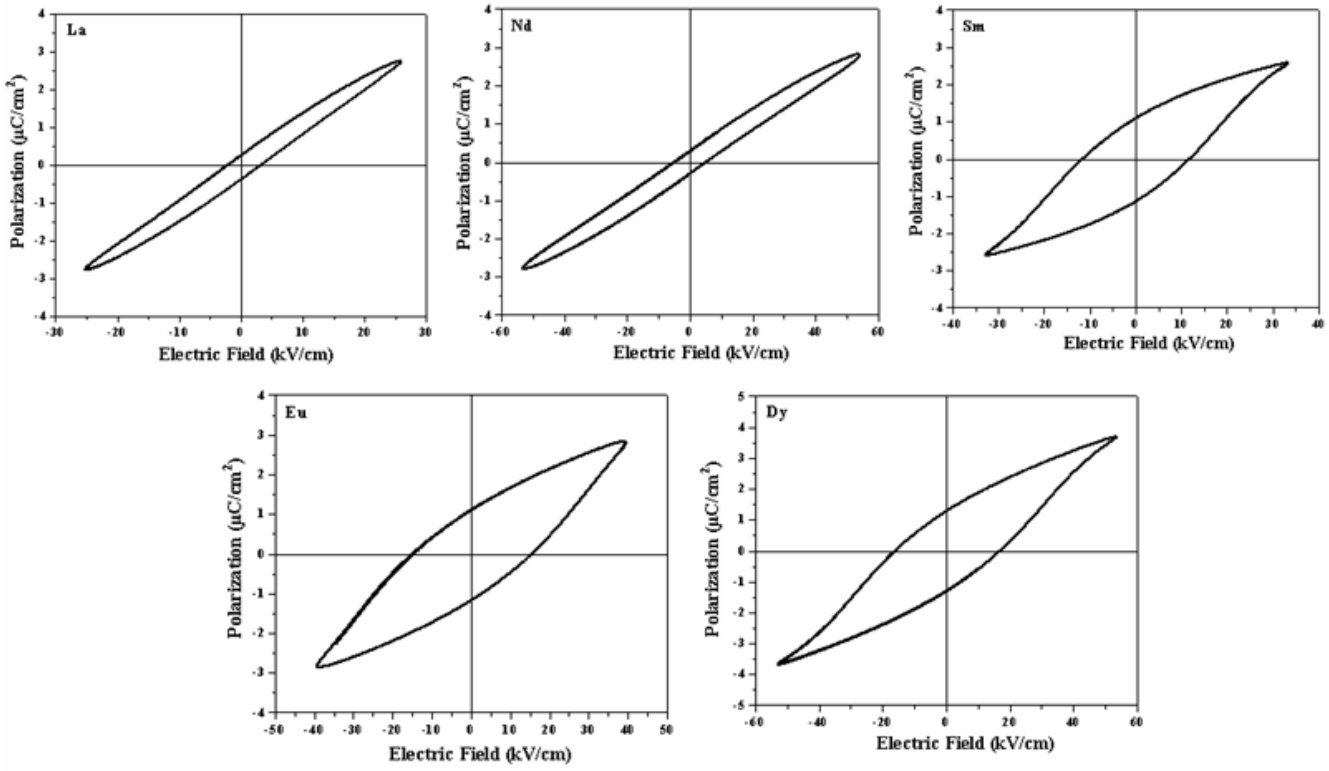

(a)

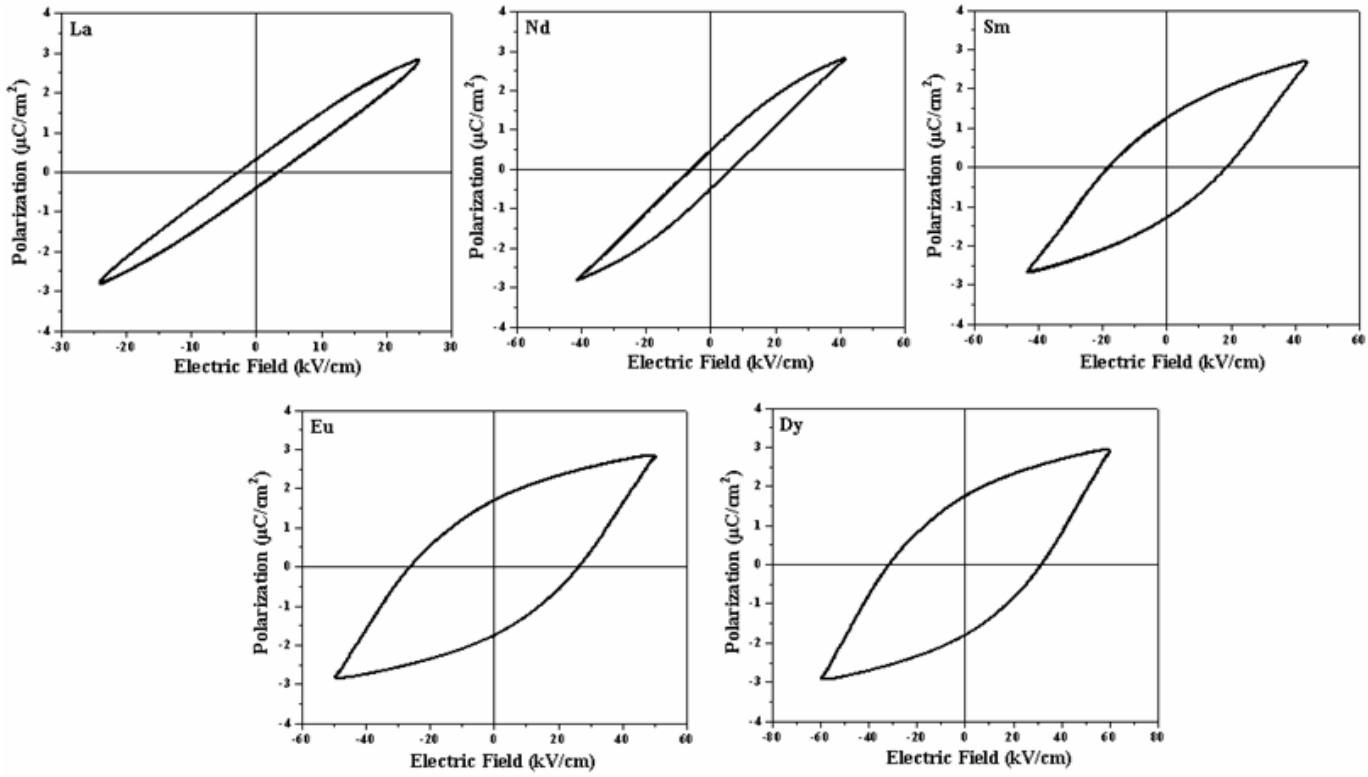

(b)

Fig. 5.20 *P-E* hysteresis loops of (a) $Ba_5RTi_3Nb_7O_{30}$ and (b) $CaBa_4RTi_3Nb_7O_{30}$ compounds

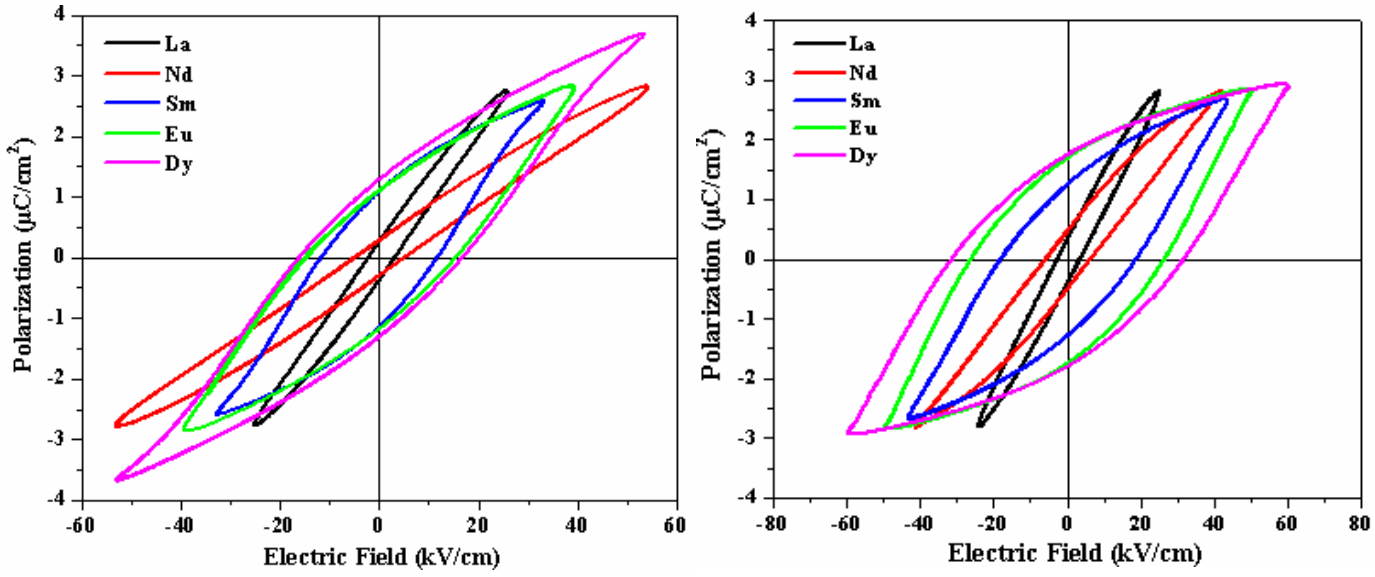

(a) (b)

Fig. 5.21 Comparison of *P-E* hysteresis loops of (a) $Ba_5RTi_3Nb_7O_{30}$ and (b) $CaBa_4RTi_3Nb_7O_{30}$ compounds

pyroelectric coefficient passes through a peak at a temperature lower than the ferroelectric transition temperature (T_c). The pyroelectric current is generated due to the spontaneous polarization change with temperature [39]. It is known that in diffuse kind of phase transition, the rate of change of spontaneous polarization with

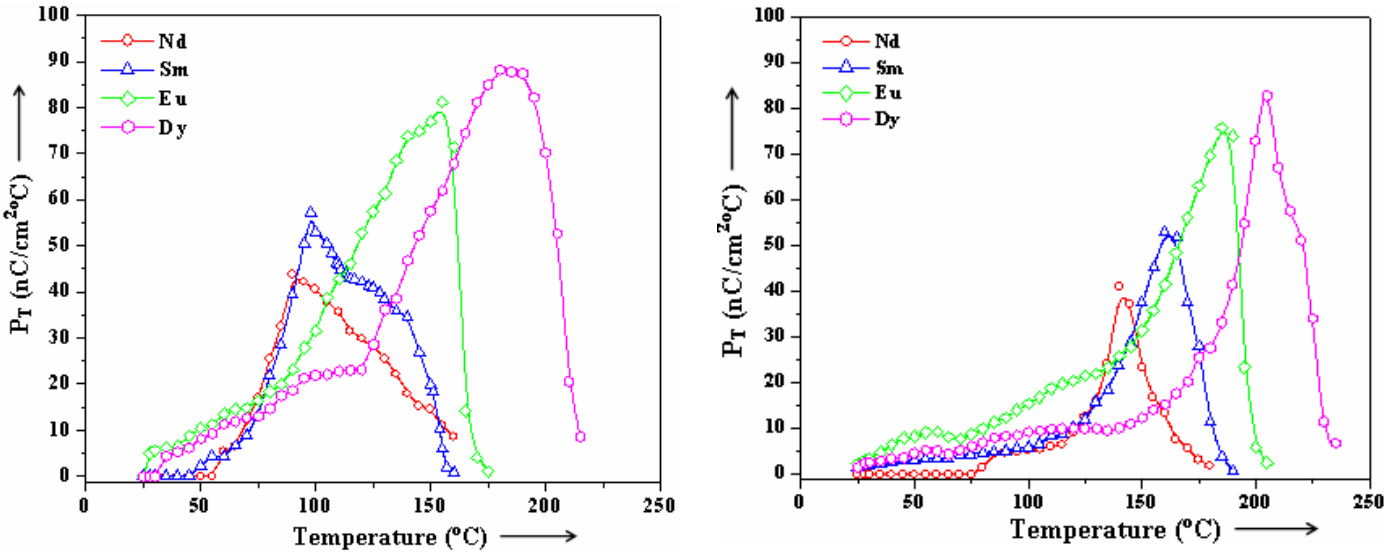

(a) (b)

Fig. 5.22 Variation of pyroelectric coefficient (P_T) with temperature of (a) $Ba_5RTi_3Nb_7O_{30}$ and (b) $CaBa_4RTi_3Nb_7O_{30}$ compounds

temperature is maximum at temperature well below T_c [39] which is in conformity with the observed diffuse phase transition. However, the diffuseness of the phase transition in the calcium substituted rare-earth containing compounds is lesser than that in calcium free compounds. The pyroelectric coefficient is found to increase with decrease in the ionic radii of the rare-earths in both calcium free and calcium substituted compounds which likely due to the increase of the spontaneous polarization as observed in Fig. 5.21.

5.2.2.6 Piezoelectric studies

Fig. 5.23 (a) and (b) show the variation of the piezoelectric coefficient (d_{33}) with the ionic radii of the rare-earths in $Ba_5RTi_3Nb_7O_{30}$ and $CaBa_4RTi_3Nb_7O_{30}$ samples respectively. It is observed that d_{33} value decreases with increase in the ionic radii of the rare-earths in both calcium free and calcium substituted compounds.

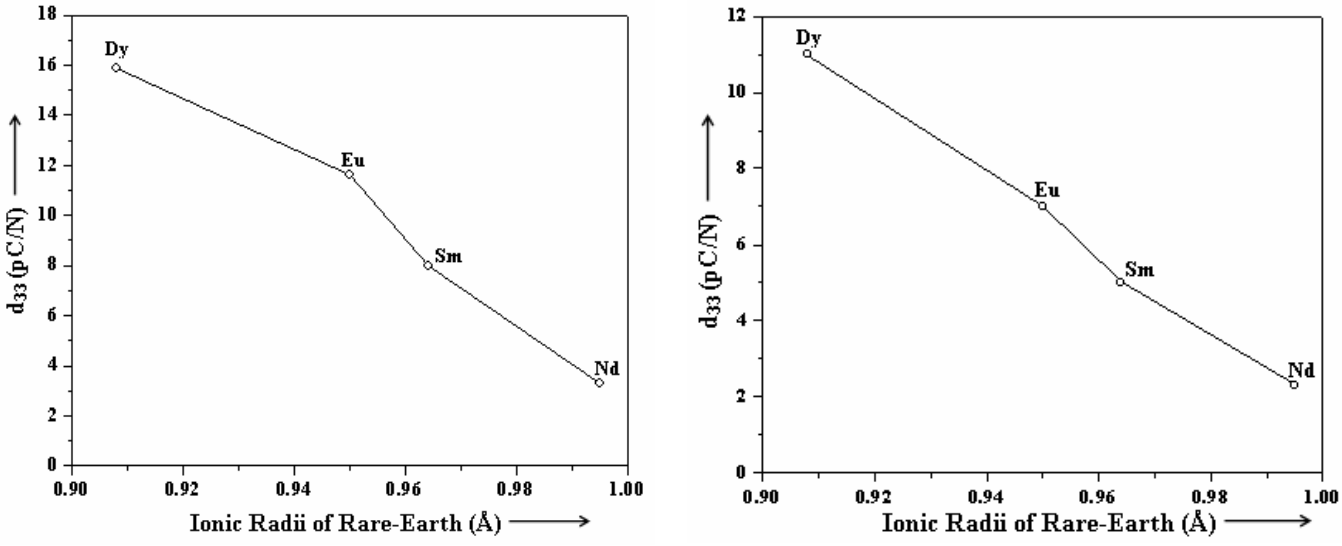

(a) (b)

Fig. 5.23 Variation of piezoelectric coefficient (d_{33}) with temperature in (a) $Ba_5RTi_3Nb_7O_{30}$ and (b) $CaBa_4RTi_3Nb_7O_{30}$ compounds

5.3 CONCLUSIONS

Based on the above observations and discussions the following conclusions can be drawn.

(i) Single phase compound is formed in all the rare-earth containing specimen.

(ii) Lattice parameters and unit cell volume decrease with decrease in the ionic radii of the rare-earths.

(iii) Average grain size increases with decrease in the ionic radii of the rare-earths.

(iv) All compounds exhibit non-relaxor type ferroelectric-paraelectric diffuse phase transition with increasing diffusivity as ionic radii of the rare-earths decreases except in La- containing compounds (i.e. $Ba_5LaTi_3Nb_7O_{30}$ and $CaBa_4RTi_3Nb_7O_{30}$) where the nature of the compounds is observed to be relaxor.

(v) Dielectric constant (ε'_r) decreases while Curie temperature (T_c) increases with decrease in the ionic radii of the rare-earths.

(vi) Conductivity of the specimen increase with the decrease in the ionic radii of the rare-earths.

(vii) Remanent polarization ($2P_r$) increases with decrease in the ionic radii of the rare - earths. However, its value is higher in calcium substituted compounds as compared to calcium free compounds.

(viii) Pyroelectric coefficient (P_T) of the specimen increases with the decrease in the ionic radii of the rare-earths.

(ix) Piezoelectric coefficient (d_{33} value) of the specimen increases with the decrease in the ionic radii of the rare-earths.

REFERENCES

[1] H. Kishi, Y. Mizuno and H. Chazono, Jpn. J. Appl. Phys. **42** (2003) 1.

[2] J. H. Hwang, Y. H. Han, Jpn. J. Appl. Phys. **40** (2001) 676.

[3] Y. Tsur, T. D. Dunbar, C. A. Randall, J. Electroceram. 7 (2001) 25.

[4] Y. Sakabe, Y. Hamaji, H. Sano and N. Wada, Jpn. J. Appl. Phys. **41** (2002) 5668.

[5] D. M. Smyth, *The Defect Chemistry of Metal Oxides* (Oxford, New York, 2000).

[6] H. Nakaki, H. Uchida, K. Nishida, M. Osada, H. Funakubo, T. Katoda and S. Koda, Jpn. J. Appl. Phys. **44** (2005) 6905.

[7] M. Miyayama and Y. Noguchi, J. Eur. Ceram. Soc. **25** (2005) 2477.

[8] R. Khazanchi, S. Sharma and T. C. Goel, J. Electroceram. **14** (2005) 113.

[9] X. Chou, J. Zhai, H. Jiang and Xi Yao, J. Appl. Phys. **102** (2007) 084106.

[10] N. Udomkan, P. Limsuwan and T. Tunkasiri, Int. J. Mod. Phys. B **21** (2007) 4549.

[11] C. Ostos, L. Mestres, M. L. Martinez-Sarrion, J. E. Garcia, A. Albareda and R. Perez, Solid State Sciences 11 (2009) 1016.

[12] Y. J. Yu, H. L.W. Chan, F. P. Wang and L. C. Zhao, Microelectron. Eng. **66** (2003) 726.

[13] S. K. Jo, J. S. Park and Y. H. Han, J. Alloys Compd. **501** (2010) 259.

[14] N. Wakiya, J. K. Wang, A. Saiki, K. Shinozaki and N. Mizutani, J. Eur. Ceram. Soc. **19** (1999) 1071.

[15] Y. Yao, C. L. Mak and K. H. Wong, Int. J. Appl. Ceram. Technol. **6** (2009) 671.

[16] C. Ostos, M. L. Martinez-Sarrion, L. Mestres, E. Delgado and P. Prieto, J. Solid State Chem. **182** (2009) 2620.

[17] C. Y. Ren, Phys. Rev. B **79** (2009) 125113.

[18] A. Lahmar, S. Habouti, M. Dietze, C. H. Solterbeck and M. Es-Souni, Appl. Phys. Lett. **94** (2009) 012903.

[19] M. R. Rangaraju, R. N. P. Choudhary and H. R. Rukmini, Ferroelectrics, **325** (2005) 25.

[20] C. W. Ahn, H. J. Lee, S. H. Kang, I. W. Kim, M. S. Choi, J. S. Lee, H. W. Kim and B. M. Jin, J Electroceram. **21** (2008) 847.

[21] V. Hornebecq, C. Elissalde, V. Porokhonskyy, V. Bovtun, J. Petzelt, I. Gregora, M. Maglione and J. Ravez, J. Phys. Chem. Solids **64** (2003) 471.

[22] H. R. Xia, H. Yu, H. Yang, K. X. Wang, B. Y. Zhao, J. Q. Wei, J. W. Wang and Y. G. Liu, Phys. Rev. B **55** (1997) 14892.

[23] C. David, A. Tunyagi, K. Betzler, and M. Wöhlecke, Phys. Status Solidi B **244** (2007) 2127.

[24] X. L. Zhu, X. M. Chen, X. Q. Liu and X. G. Li, J. Appl. Phys. **105** (2009) 124110.

[25] M. Verma, K. Sreenivas and V. Gupta, J. Appl. Phys. **105** (2009) 024511.

[26] I. Coondoo, A. K. Jha and S. K. Agarwal, J. Eur. Ceram. Soc. **27** (2007) 253.

[27] A. Onodera, K. Yoshio, C. C. Myint, S. Kojima, H. Yamashita and T. Takama, Jpn. J. Appl. Phys. **38** (1999) 5683.

[28] T. Friessnegg, S. Aggarwal, R. Ramesh, B. Nielsen, E. H. Poindexter and D. J. Keeble, Appl. Phys. Lett. **77** (2000) 127.

[29] M. S. Cao, Z. L. Hou, J. Yuan, L. T. Xiong and X. L. Shi, J. Appl. Phys. **105** (2009) 106102.

[30] R. C. Buchanan, *Ceramic Materials for Electronics: Processing, Properties & Applications* (Marcel Dekker Inc., New York, 1991).

[31] Y. Noguchi and M. Miyayama, Appl. Phys. Lett. **78** (2001) 1903.

[32] A. Chen, Y. Zhi and L. E. Cross, Phys. Rev. B **62** (2000) 228.

[33] I. S. Zheludev, *Physics of Crystalline Dielectrics, Vol I: Crystallography & Spontaneous Polarization* (Plenum Press, New York, 1971).

[34] V. Shrivastava, A. K. Jha and R. G. Mendiratta, Phys. B **371** (2006) 337.

[35] A. K. Jonscher, Nature **267** (1977) 673.

[36] C. Karthik and K. B.R. Varma, J. Phys. Chem. Solids **67** (2006) 2437.

[37] S. Sen, R. N. P. Choudhary and P. Pramanik, Phys. B **387** (2007) 56.

[38] R. R. Das, P. Bhattacharya, W. Pérez and R. S. Katiyar, Ceram. Inter. **30** (2004) 1175.

[39] K. Uchino, Ferroelectric Devices (Marcel Dekker Inc., New York, 2000).

CHAPTER 6

Chapter 6

Synthesis by Some Novel Techniques

6.1 INTRODUCTION

It is well known that materials' performances are dependent on their processing. Method of synthesis of ferroelectric materials have played a significant role in determining the microstructural, electrical and optical properties of ferroelectric ceramics [1-3]. As in earlier chapters, ferroelectric powders were synthesized via a solid-state reaction process, using constituent oxides as the starting materials. Due to their relatively rough grains, these powders require relatively high sintering temperature to obtain ferroelectric ceramics with desired compositions and performances [1-3]. To reduce the sintering temperature, it is necessary to use powders with small particle size and narrow size distribution. For this purpose, submicron or even nanosized ferroelectric powders have been synthesized by various wet-chemistry methods in the last decades, including chemical coprecipitation [4-7], sol-gel process [8-11], hydrothermal synthesis [12-18], microemulsion, combustion [19], thermal pyrolysis spray, molten salt [20,21], etc. Although significant progresses have been achieved, there are problems. For example, sol-gel process uses metal alkoxides as the starting materials, which are very expensive and extremely sensitive to the environmental conditions such as moisture, light and heat.

Moisture sensitivity makes it necessary to conduct the experiment in dry boxes or clean rooms. Co-precipitation processes involve repeated washing in order to eliminate the anions coming from the precursor salts used, making the process complicated and very time consuming. Furthermore, it is difficult to produce large batches by using most of the chemical solution processing routes. Therefore, exploring alternative methods for the preparation of ferroelectric ceramics is still of technological as well as scientific significances. Recently, a novel technique called mechanical activation method (high energy ball-milling) has been successfully employed to synthesize a wide range of nano-sized ceramic powders, such as ZrO_2 [22,23], Fe_2O_3 [24,25], YBCO superconductor [26], ferrite [27-29], as well as various ferroelectrics [30-41]. The most significant characteristic of this technique is that the formation of the designed compounds is due to the reactions of oxide precursors which are activated by mechanical energy, instead of the heat energy required in the conventional solid-state reaction process. In view of this, $Ba_5SmTi_3Nb_7O_{30}$, a member of tungsten-bronze family was prepared by this novel synthesis route and the same is discussed in this chapter. The chapter also compares the properties of the compound prepared by this technique with that prepared by the conventional solid-state reaction method.

Microwave sintering is a novel technique of sintering due to its unique characteristics, such as rapid heating, enhanced densification rate and improved microstructures [42-44]. Later part of this chapter discusses the properties of $Ba_5SmTi_3Nb_7O_{30}$ compound prepared by microwave sintering and compares them with that prepared by conventional sintering.

6.2 RESULTS AND DISCUSSIONS

I. Mechanical Activation Method

(i) Optimization of Milling Duration

6.2.1 Structural and Micro-structural Characterization

Fig. 6.1 compares the XRD pattern of the stoichiometric $Ba_5SmTi_3Nb_7O_{30}$ powders milled for different durations i.e. 5 hours, 10 hours and 20 hours. The XRD peaks were indexed using the observed d-values and a software package, PowderX [45]. It can be seen that phase development starts from 5 hours and improves with the duration of milling.

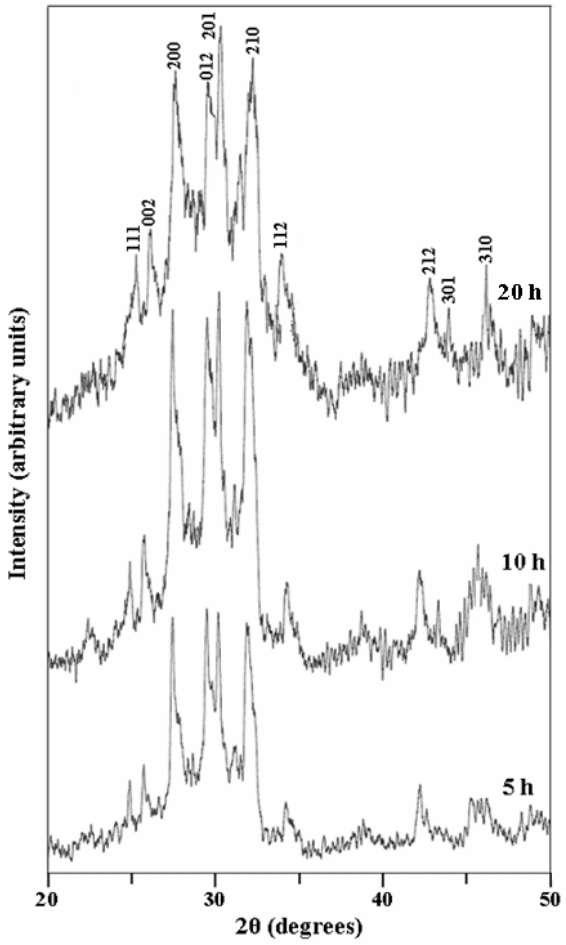

Fig. 6.1 XRD patterns of $Ba_5SmTi_3Nb_7O_{30}$ powders milled for different durations

Fig. 6.2 shows the SEM images of the specimens milled for different durations. The size of the particles can be seen to be getting reduced with increasing milling time.

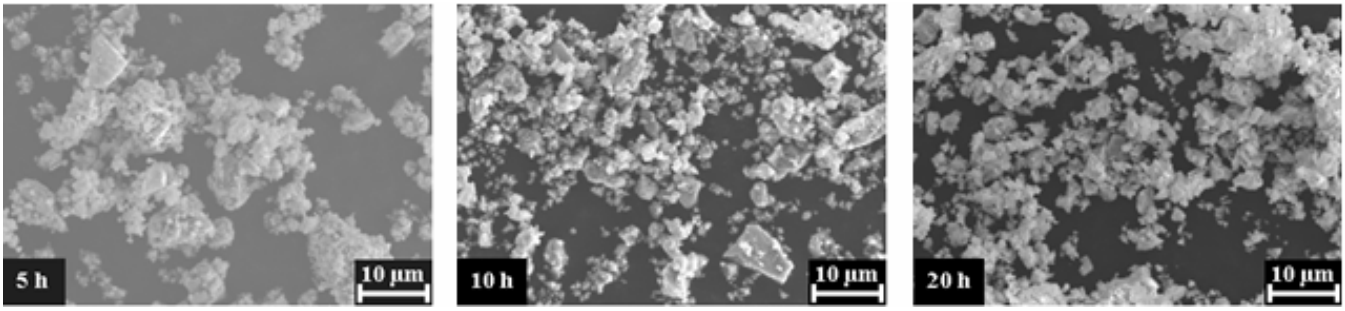

Fig. 6.2 SEM micrographs of $Ba_5SmTi_3Nb_7O_{30}$ powders prepared at different milling time

TEM image of 20 hours milled sample (Fig. 6.3) shows that there is agglomeration of particles due to the reduction in their sizes. A detailed study at high magnification shows that agglomerate consists of particles, mostly rounded shapes, in the range of 20-40 nm. Nanoparticles are observed clearly, although they have aggregated together to form irregularly shaped agglomerates.

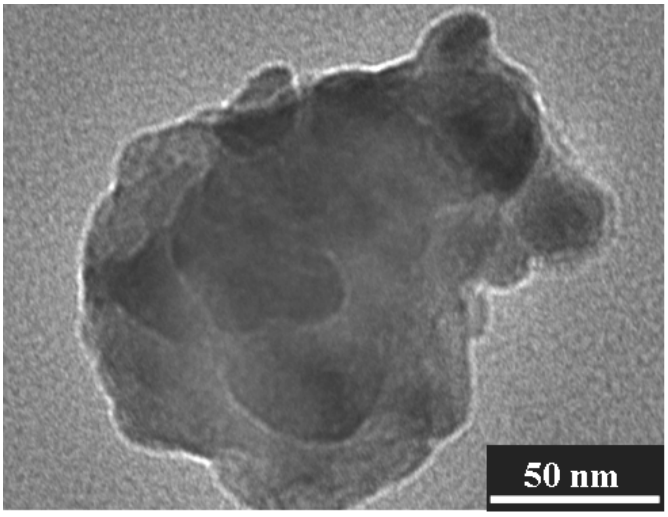

Fig. 6.3 TEM micrograph of 20 hours milled $Ba_5SmTi_3Nb_7O_{30}$ powder

Fig. 6.4 shows the XRD patterns of the samples sintered at 1300 ºC for 10 hours milled for different durations which reveal the formation of single phase $Ba_5SmTi_3Nb_7O_{30}$ compound. The peaks become well defined and shifts slightly to higher angles with increasing milling durations suggesting a decrease in the lattice parameters and unit cell volume (Table 6.1). It is observed that the compound prepared by mechanical activation process has an orthorhombic TB-type structure. The crystallite size calculated from the broadening of XRD peaks using the Scherrer's formula (Eq. 2.2) [46] of milled $Ba_5SmTi_3Nb_7O_{30}$ decreases with increasing milling time (Table 6.1).

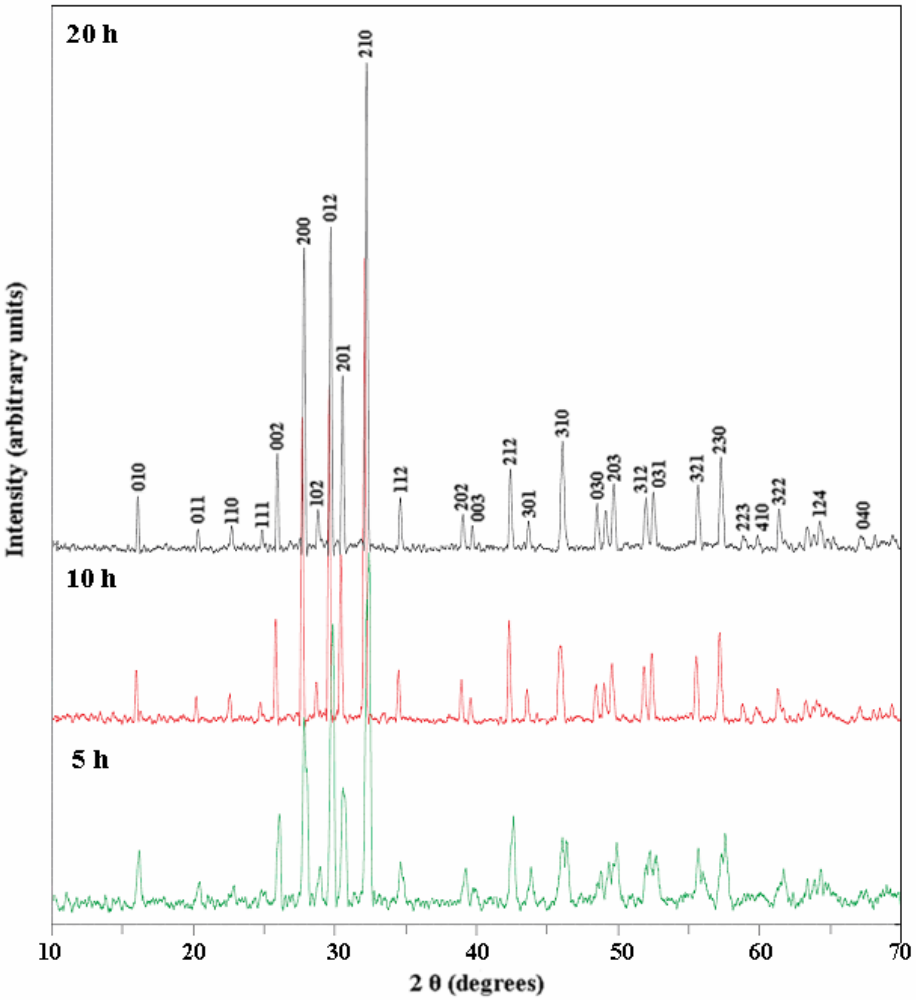

Fig. 6.4 XRD patterns of $Ba_5SmTi_3Nb_7O_{30}$ sintered samples milled at different durations

The corresponding SEM micrographs of the sintered samples prepared at different milling time are shown in Fig. 6.5. The average grain size of the compound decreases from 1-2 μm in the samples milled for 5 hours and 10 hours to less than 1 μm in the sample milled for 20 hours (Table 6.1).

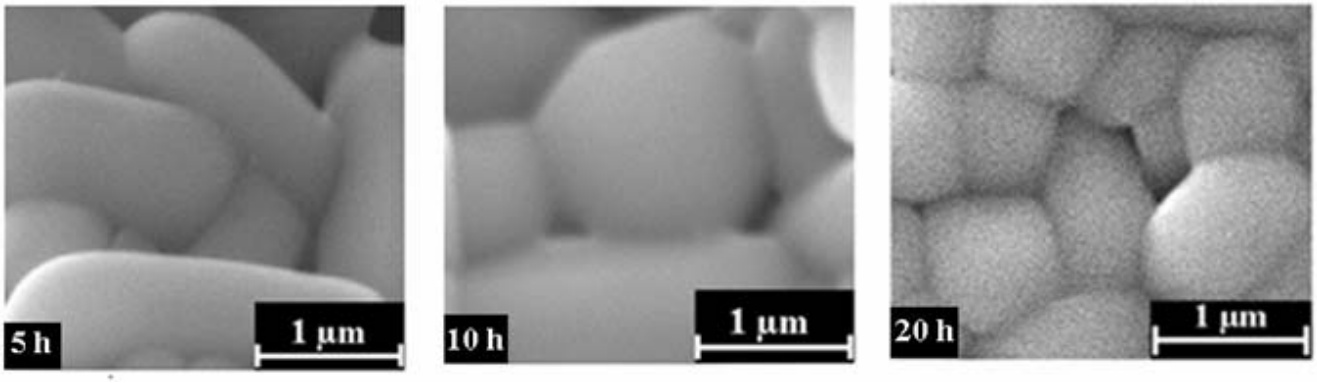

Fig. 6.5 SEM micrographs of $Ba_5SmTi_3Nb_7O_{30}$ sintered samples milled for different durations

Table 6.1 Lattice parameters, unit cell volume and average grain size of $Ba_5SmTi_3Nb_7O_{30}$ sintered samples milled at different durations

Milling Duration (Hours)	a (Å)	b (Å)	c (Å)	c/a	Volume (Å^3)	Crystallite Size (nm)	Average Grain Size (μm)
5	6.4098	5.5423	6.8037	1.0615	241.70	30	2
10	6.4074	5.5402	6.7975	1.0609	241.30	19	1.5
20	6.4058	5.5386	6.7925	1.0604	240.99	15	0.5

6.2.2 Electrical Characterization

6.2.2.1 Dielectric studies

To see the effect of milling duration on the dielectric properties (a) the variation of ε_r' and tan δ as a function of temperature at 1 kHz, 10 kHz and 100 kHz frequencies and (b) the variation ε_r' and tan δ with frequency at room temperature of $Ba_5SmTi_3Nb_7O_{30}$ compound prepared by milling for different durations is presented in this section.

Variation of ε_r' with temperature: Curie temperature

The temperature dependence of dielectric constant (ε'_r) measured at 1 kHz, 10 kHz and 100 kHz are shown in Fig. 6.6. For all the milling durations, the compound show dielectric anomaly at a temperature called the Curie temperature (T_c) indicating the occurrence of ferroelectric–paraelectric phase transition. The T_c is same at all the measured frequencies at a given milling time indicating the non-relaxor behaviour of the compound prepared for all the milling durations.

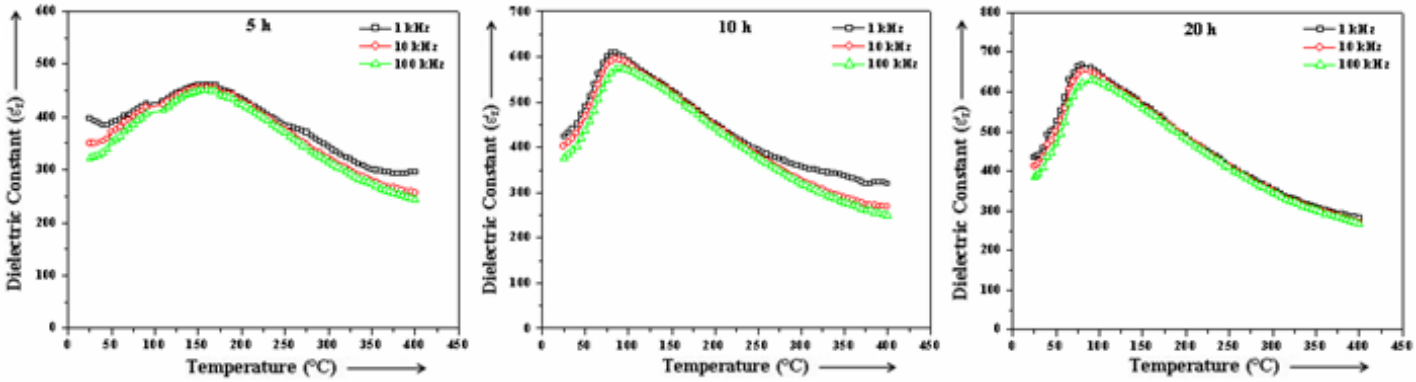

Fig. 6.6 Variation of dielectric constant (ε_r') with temperature at different milling time

Fig. 6.7 shows the comparison of the variation of dielectric constant (ε_r') with temperature for different milling duration at three different frequencies of 1 kHz, 10 kHz and 100 kHz. It is observed that the dielectric constant value increases with increase in milling time and is maximum in the sample milled for 20 hours (Table 6.2). It is known that in the fine-grained ferroelectric ceramics, ε_r' increases due to an increase in residual internal stress [47-50]. Thus the increase in ε'_r value is due to the decrease in the average grain size with increase in milling

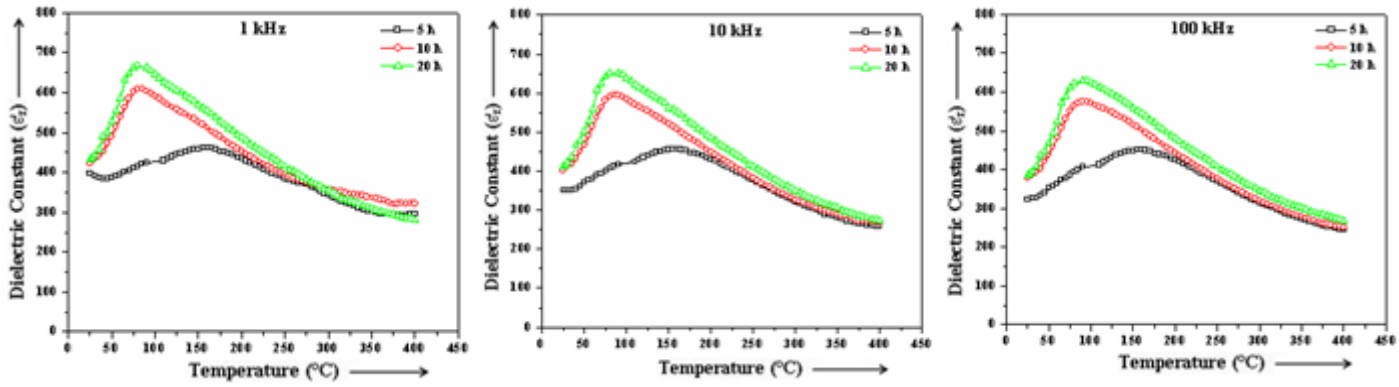

Fig. 6.7 Comparison of the variation of dielectric constant (ε_r') with temperature of $Ba_5SmTi_3Nb_7O_{30}$ samples (prepared at different milling time) at three selected frequencies (1 kHz, 10 kHz and 100 kHz)

time (Fig. 6.5). The small observed reduction of the unit cell volume (Table 6.1) with increase in milling duration may additionally be increasing the observed dielectric constant as can be followed from Clausius-Mossotti relation:

$$\varepsilon'_r = \left(\frac{3V_m + 8\pi\alpha_D}{3V_m - 4\pi\alpha_D}\right) = 1 + \left(\frac{12\pi(\alpha_D / V_m)}{3 - 4\pi(\alpha_D / V_m)}\right) \qquad (6.1)$$

where V_m (= $V_{\text{unit cell}}/Z$) is the molar volume and α_D is the net dielectric polarizability.

However, the Curie temperature (T_c) is found to decrease with increase in the milling time (Table 6.2). This possibly is due to the decrease in crystallite size with increase in milling time as it is known that T_c is strongly dependent on the crystallite size and it decreases significantly even when the crystallite size decreases by a marginal value [51-52]. Moreover, specimen with smaller grains has more interfacial or grain boundary energy as it contains larger number of grain boundaries (Fig. 6.5) which results in the requirement of smaller amount of thermal energy to undergo the phase transition [53].

Table 6.2 Dielectric parameters of $Ba_5SmTi_3Nb_7O_{30}$ compound prepared at different milling time

Milling Duration (Hours)	Frequency (kHz)	$\varepsilon'_{r\,max}$	T_c (°C)	γ
5	1	461	140	1.26
	10	456		1.52
	100	451		1.70
10	1	610	100	1.19
	10	596		1.36
	100	575		1.51
20	1	668	90	1.15
	10	651		1.32
	100	630		1.47

The dielectric peak in all the samples is found to be broadened indicating the diffuse nature of the phase transition. The diffusivity constant (γ) has been calculated using the empirical relation,

$$\ln\left(\frac{1}{\varepsilon'_r}-\frac{1}{\varepsilon'_{r\,\max}}\right)=\gamma\ln(T-T_c)+\text{constant} \qquad (6.2)$$

where $\varepsilon'_{r\ max}$ is the maximum value of ε'_r at $T = T_c$. The value of γ for all the samples was obtained from the slope of ln $(1/\varepsilon'_r - 1/\varepsilon'_{r\,max})$ versus ln $(T-T_c)$ curve (Fig. 6.8) and are listed in Table 6.2. The values of γ is found to be between 1 (obeying Curie-Weiss law) and 2 (for completely disordered system) confirming the diffuse phase transition in all the samples. The value of γ is found to be lowest for the 20 hours milled sample.

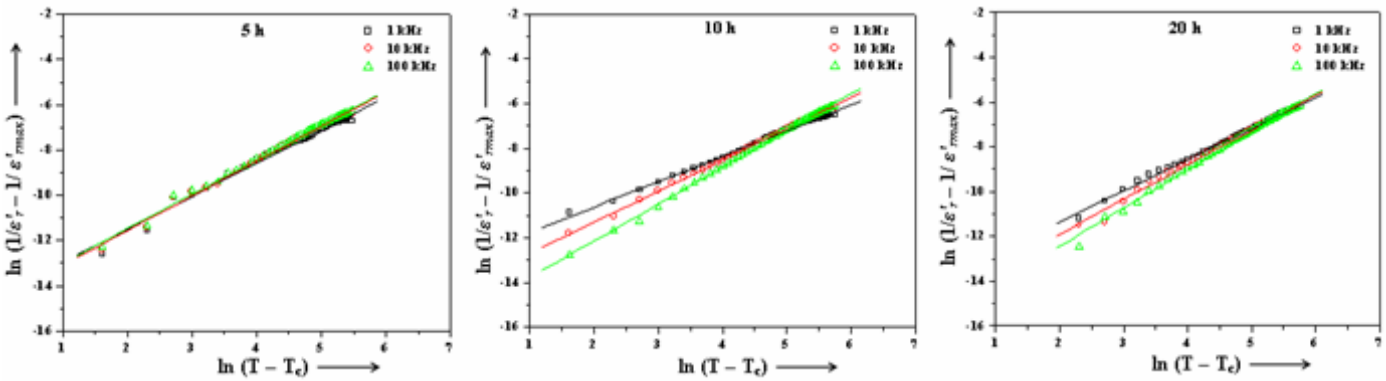

Fig. 6.8 Variation of ln $(1/\varepsilon'_r - 1/\varepsilon'_{r\,max})$ with ln $(T-T_c)$ for different milling durations

Variation of tan *δ with temperature*

Fig. 6.9 shows the temperature variation of dielectric loss (tan δ) at three different frequencies of 1 kHz, 10 kHz and 100 kHz for different milling durations.

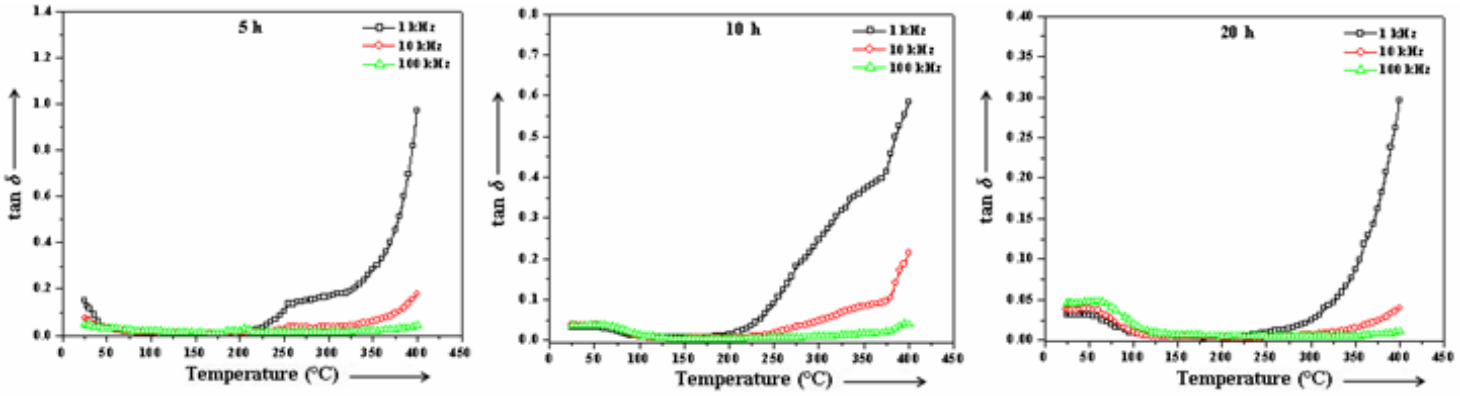

Fig. 6.9 Variation of dielectric loss (tan δ) with temperature

In all the samples, the dielectric loss (tan δ) has smaller values at lower temperatures and at higher temperatures it increases sharply. This sharp increase of tan δ in high temperature region may be attributed to the increased mobility of space charges arising from the defects or vacancies (like oxygen vacancies) in the samples [54]. To see the effect of milling duration on the temperature variation of dielectric loss, the curves have been plotted in Fig. 6.10 at three different frequencies of 1 kHz, 10 kHz and 100 kHz. It can be seen that the dielectric loss is lowest in 20 hours milled sample as compared to

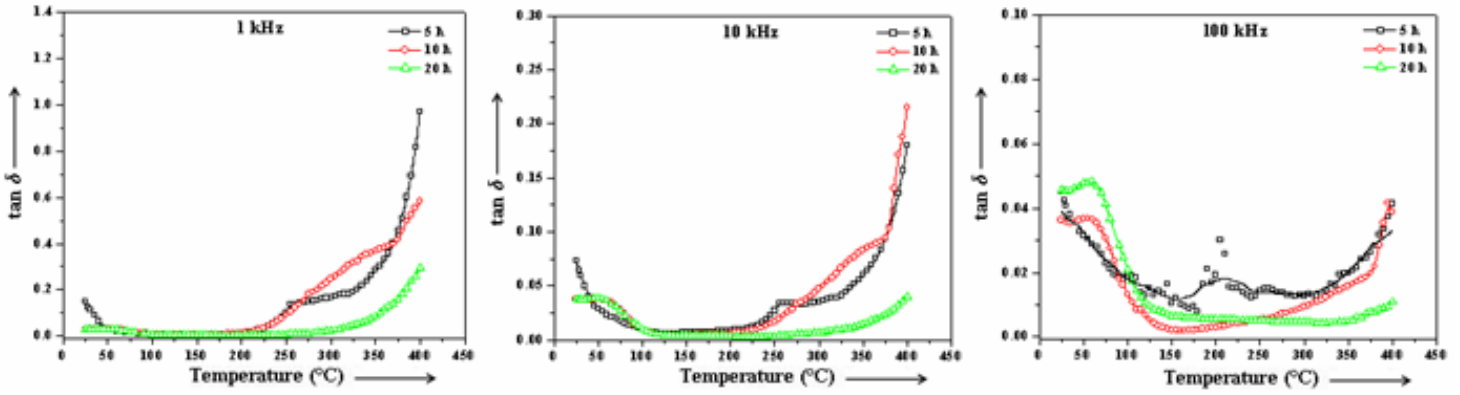

Fig. 6.10 Temperature variation of dielectric loss (tan δ) (prepared at different milling time) at three selected frequencies (1 kHz, 10 kHz and 100 kHz)

5 hours and 10 hours milled samples at all the selected frequencies.

Variation of ε_r' and tan δ *with frequency*

Fig. 6.11 (a) and (b) shows the variation of dielectric constant (ε_r') and dielectric loss (tan δ) as a function of frequency in the range from 20 Hz to 500 kHz at room temperature respectively for $Ba_5SmTi_3Nb_7O_{30}$ samples prepared at different milling time. For all the samples, both dielectric constant and dielectric loss decrease upto about 1 kHz and remains nearly constant beyond this frequency. At lower frequencies, the dipoles are able to follow the alternating field resulting in higher values of dielectric constant and dielectric loss while at higher frequencies the dipoles are unable to follow the rapidly changing field leading to the reduction in the values of dielectric constant and loss. It is worth noting that the room temperature dielectric constant value is highest and room temperature dielectric loss is lowest for the 20 hours milled sample compared to 5 hours and 10 hours milled samples.

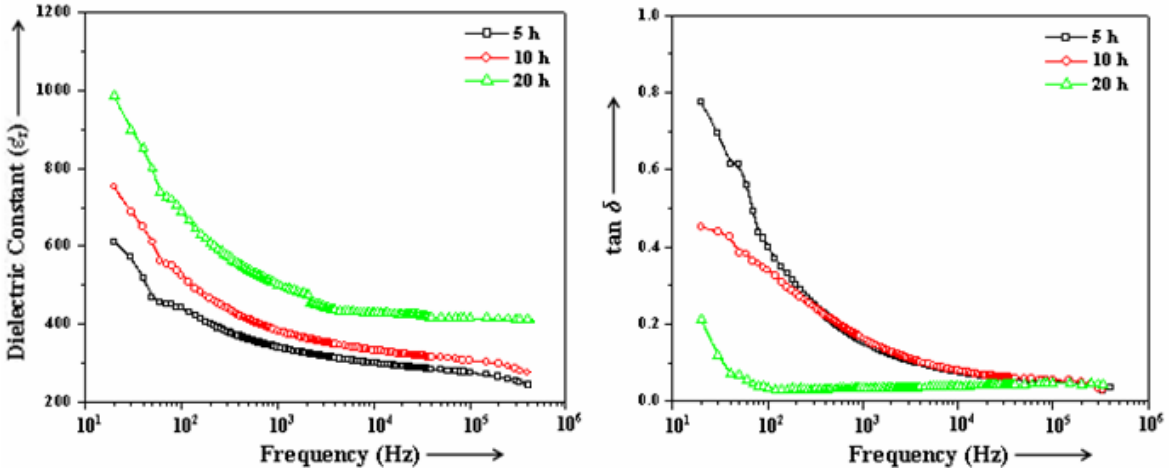

(a) (b)

Fig. 6.11 Variation of (a) dielectric constant (ε_r') and (b) dielectric loss (tan δ) with frequency at room temperature

6.2.2.2 Conductivity studies

DC conductivity

The temperature variation of dc conductivity for $Ba_5SmTi_3Nb_7O_{30}$ compound prepared at different milling durations are shown in Fig. 6.12. The conductivity is constant at lower temperatures but at higher temperatures, it increases with temperature in all the samples. This indicates negative temperature coefficient of resistance (NTCR) – type behaviour of $Ba_5SmTi_3Nb_7O_{30}$ compound prepared by this process. The dc conductivity is found to be lowest in 20 hours milled specimen. The nature of variation of dc conductivity at higher temperature is linear and follows the Arrhenius relationship:

$$\sigma = \sigma_o \exp\left(\frac{-E_a}{k_B T}\right) \tag{6.3}$$

where σ indicates the conductivity, E_a the activation energy and k_B the Boltzmann constant. The activation energies have been calculated in the higher temperature region using Eq. (6.3) and are given in Table 6.3.

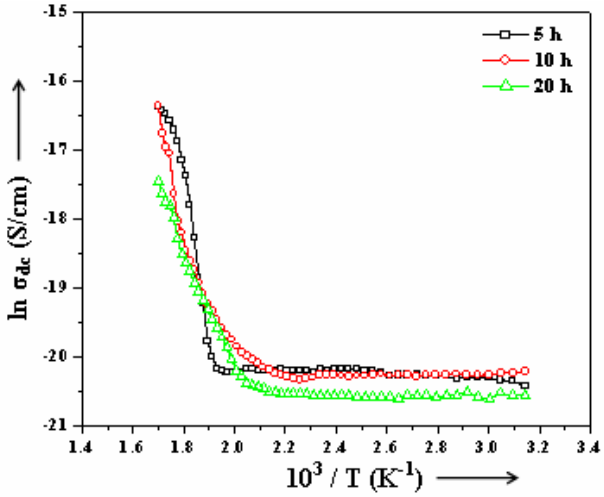

Fig. 6.12 Temperature variation of dc conductivity (ln σ_{dc})

AC conductivity

The temperature variation of ac conductivity at the selected frequencies of 1 kHz, 10 kHz and 100 kHz for $Ba_5SmTi_3Nb_7O_{30}$ samples prepared at different milling time is shown in Fig. 6.13.

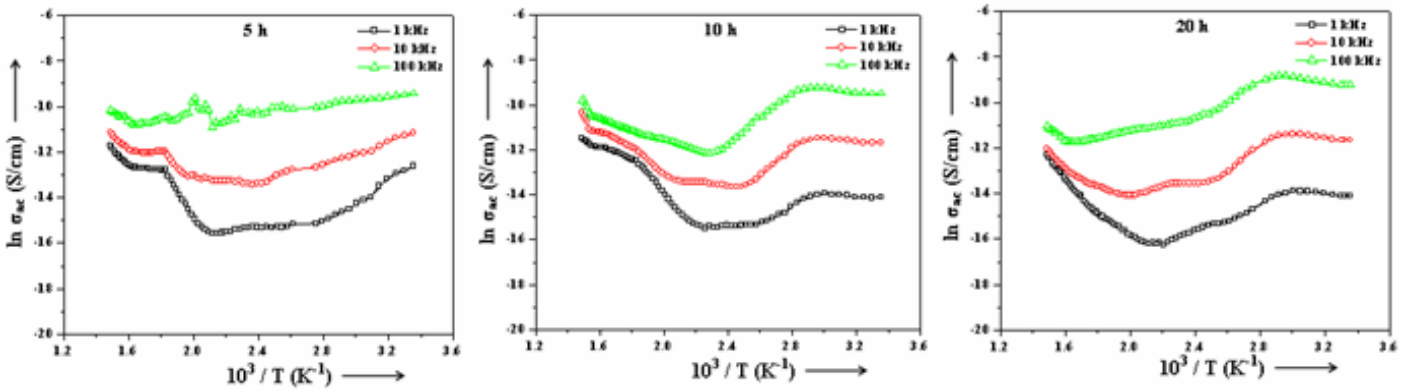

Fig. 6.13 Temperature variation of ac conductivity (ln σ_{ac})

For all the samples, there is a change in slope in the curve which can be attributed to the difference in activation energy in the paraelectric and ferroelectric phases. The activation energies (E_a), evaluated in the high temperature region using Eq. (6.3) are summarized in Table 6.3. It is found that

Table 6.3 Activation energies (E_a) as calculated using dc and ac conductivity curves for $Ba_5SmTi_3Nb_7O_{30}$ samples prepared at different milling time

Milling Duration (Hours)	Frequency (kHz)	E_a (eV) (ac conductivity)	E_a (eV) (dc conductivity)
5	1	0.49	0.75
	10	0.23	
	100	0.16	
10	1	0.52	0.82
	10	0.38	
	100	0.23	
20	1	0.56	1.15
	10	0.43	
	100	0.36	

E_a increases with increase in milling time. Reduction of the crystallite size with increase in milling time can be attributed for this increase in E_a [51]. To see the effect of milling time on the temperature variation of ac conductivity, the curves have been plotted in Fig. 6.14 at three different frequencies of 1 kHz, 10 kHz and 100 kHz. It is observed that the ac conductivity decreases with increase in the milling time which can be correlated to the observed decrease in the dielectric loss (Fig. 6.10).

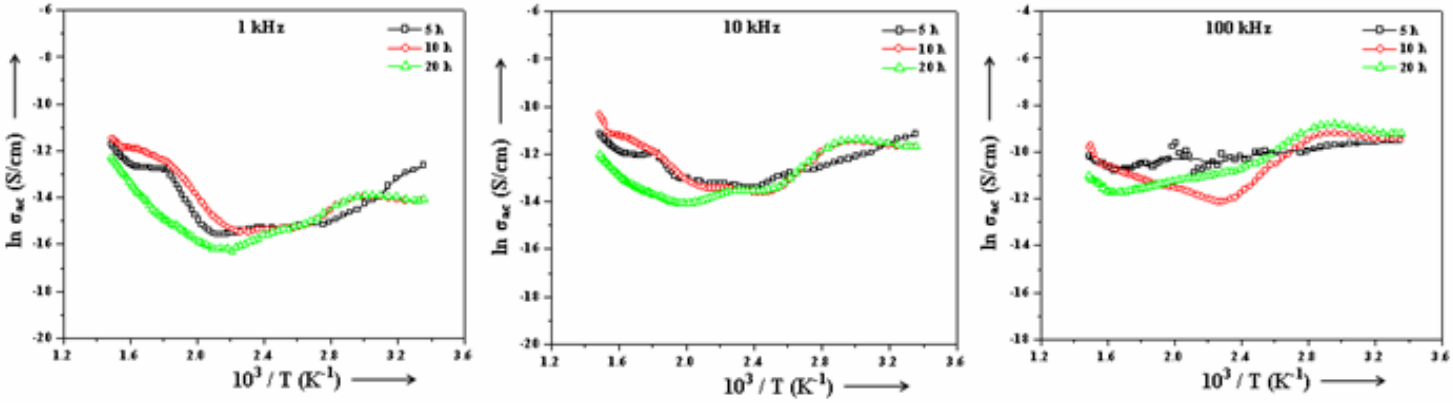

Fig. 6.14 Temperature variation of ac conductivity of $Ba_5SmTi_3Nb_7O_{30}$ compound (prepared at different milling time) at three selected frequencies (1 kHz, 10 kHz and 100 kHz)

(ii) Optimization of Sintering Condition

In order to optimize the sintering condition, the pellets formed out of the powder milled for 20 hours, the optimized milling duration, were sintered in air at the different sintering conditions namely 1100 ºC; 10 hours, 1200 ºC; 10 hours, 1300 ºC; 2 hours and 1300 ºC; 10 hours.

6.2.3 Structural Characterization

6.2.3.1 X-ray diffraction

The room temperature X-ray diffractograms of the samples sintered at various sintering temperatures and sintering durations are shown in Fig. 6.15 (a) and (b) respectively.

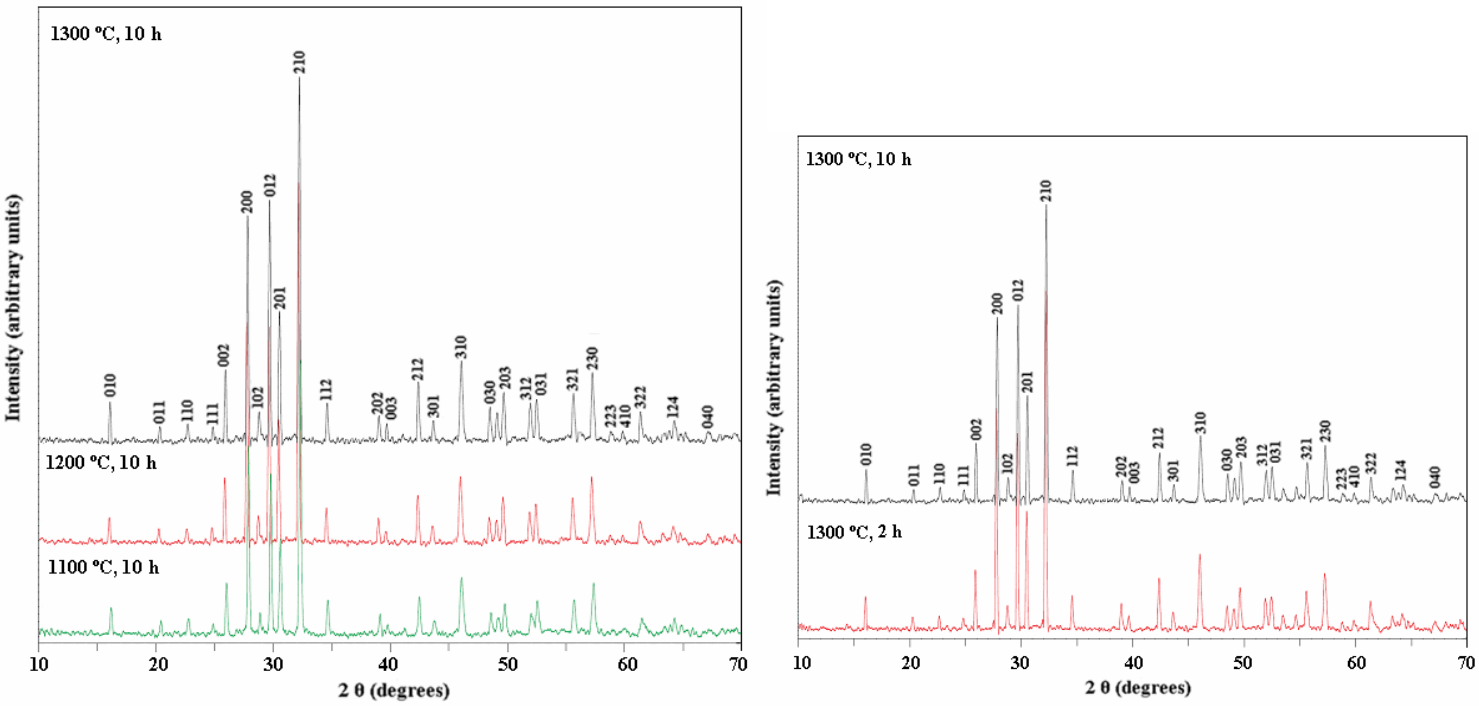

(a) (b)

Fig. 6.15 XRD patterns of ball milled $Ba_5SmTi_3Nb_7O_{30}$ samples sintered at different (a) temperatures and (b) durations

It is observed that single-phase $Ba_5SmTi_3Nb_7O_{30}$ compound is forming in all the sintering conditions. The refined lattice parameters and the unit cell volume at different sintering conditions are tabulated in Table 6.4. The lattice parameters

Table 6.4 Variation of lattice parameters and unit cell volume at different sintering conditions

Sintering Conditions	a (Å)	b (Å)	c (Å)	Volume (Å^3)
1100 °C; 10 h	6.4324	5.5517	6.8127	243.29
1200 °C; 10 h	6.4206	5.5496	6.8032	242.41
1300 °C; 10 h	6.4058	5.5386	6.7925	240.99
1300 °C; 2 h	6.4108	5.5426	6.7869	241.16

and unit cell volume of $Ba_5SmTi_3Nb_7O_{30}$ compound are observed to decrease with increase in sintering temperature and time. From these results, it is found that $Ba_5SmTi_3Nb_7O_{30}$ samples sintered at the above mentioned sintering conditions

prepared by mechanical activation process have an orthorhombic crystal with a tungsten-bronze type structure at room temperature.

6.2.4 Electrical Characterization

6.2.4.1 Dielectric studies

In this section, with an objective to find an optimized sintering condition, the dielectric properties of $Ba_5SmTi_3Nb_7O_{30}$ compound prepared by mechanical activation method at different sintering conditions is presented.

Variation of ε_r' with temperature: Curie temperature

Fig. 6.16 shows the temperature variation of dielectric constant (ε_r') of $Ba_5SmTi_3Nb_7O_{30}$ compound prepared by mechanical activation method at different

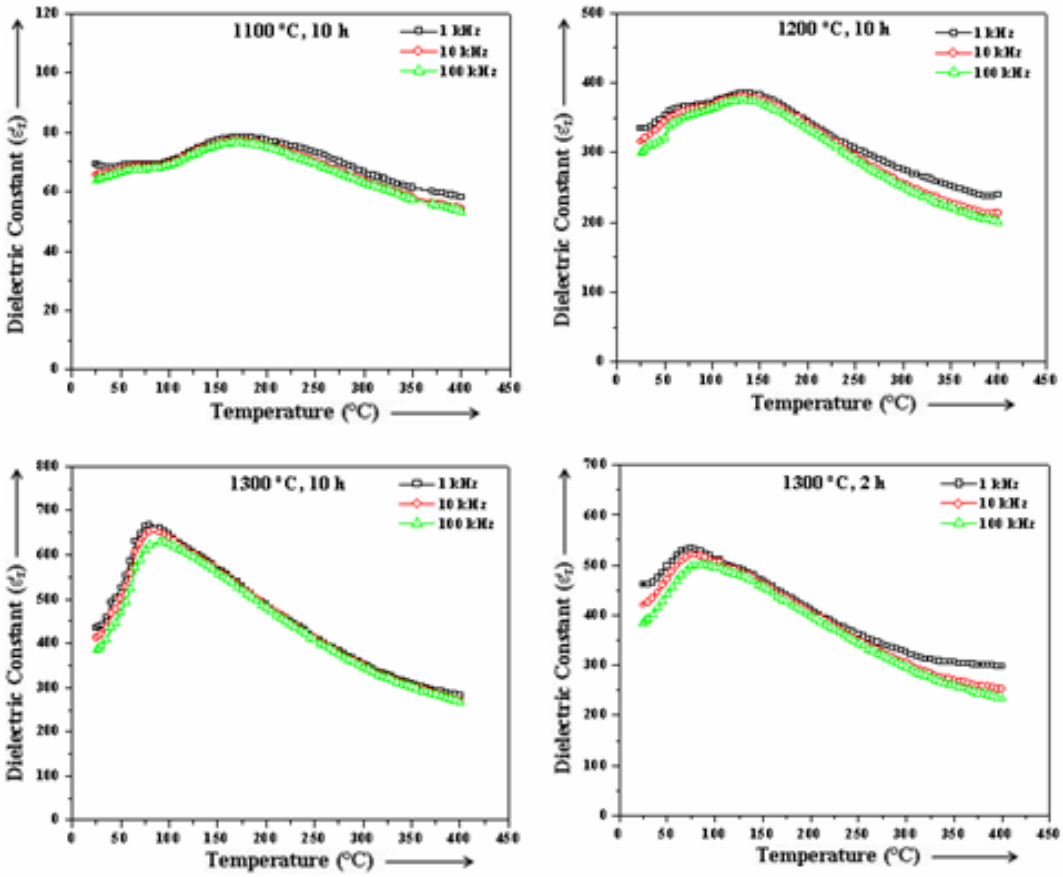

Fig. 6.16 Temperature variation of dielectric constant (ε_r') at different sintering conditions

sintering conditions. For all the sintering conditions, the compound show dielectric anomaly at a temperature called the Curie temperature (T_c) indicating the occurrence of ferroelectric–paraelectric phase transition. The T_c is the same at all the measured frequencies for a given sintering condition indicating the non-relaxor behaviour of the compound at all the sintering conditions. To see the effect of sintering temperature and duration on the variation of dielectric constant with temperature, the curves have been plotted in Fig. 6.17 at three different frequencies of 1 kHz, 10 kHz and 100 kHz. It is observed that the dielectric constant value increases with increase in sintering temperature and duration (Table 6.5) and is highest in the sample sintered at 1300 ºC for 10 hours.

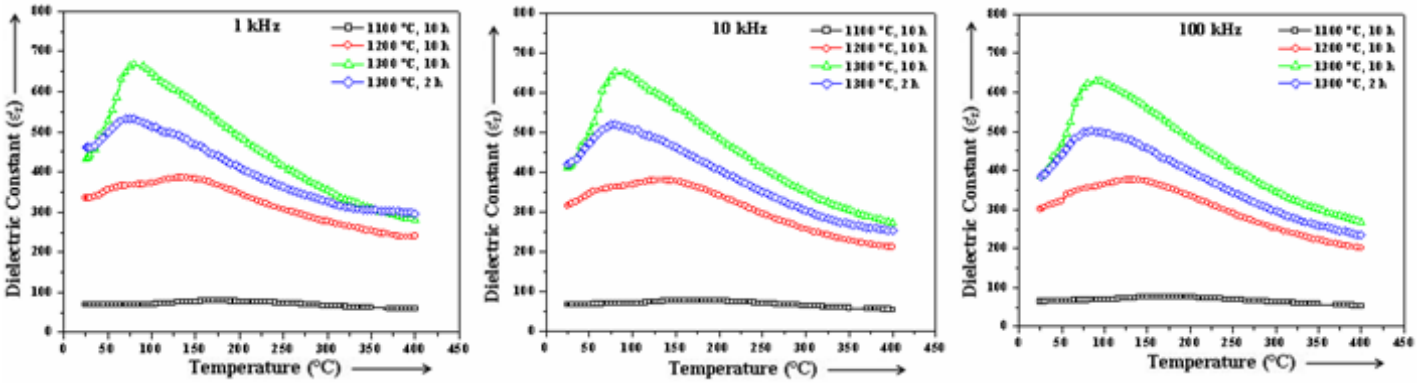

Fig. 6.17 Temperature variation of dielectric constant (ε_r') of the studied samples prepared at different sintering conditions at 1 kHz, 10 kHz and 100 kHz

All the samples prepared at different sintering conditions show diffuse kind of phase transition and the diffusivity constant (γ) has been calculated using the Eq. (6.2). The value of γ for all the samples are obtained from the slope of ln ($1/\varepsilon'_r$ - $1/\varepsilon'_{r\ max}$) versus ln (T-T_c) curve (Fig. 6.18) and are listed in Table 6.5. It is found to be between 1 (obeying Curie-Weiss law) and 2 (for completely disordered system) confirming the diffuse phase transition in all the samples. The value of γ is observed to decrease with the increase in sintering temperature and duration.

Table 6.5 Dielectric parameters of $Ba_5SmTi_3Nb_7O_{30}$ compound prepared at different sintering conditions

Sintering Conditions	Frequency (kHz)	$\varepsilon'_{r\,max}$	γ
1100 °C; 10 h	1	78	1.64
	10	77	1.71
	100	76	1.78
1200 °C; 10 h	1	386	1.35
	10	380	1.56
	100	376	1.71
1300 °C; 10 h	1	668	1.15
	10	651	1.32
	100	630	1.47
1300 °C; 2 h	1	533	1.18
	10	520	1.35
	100	501	1.54

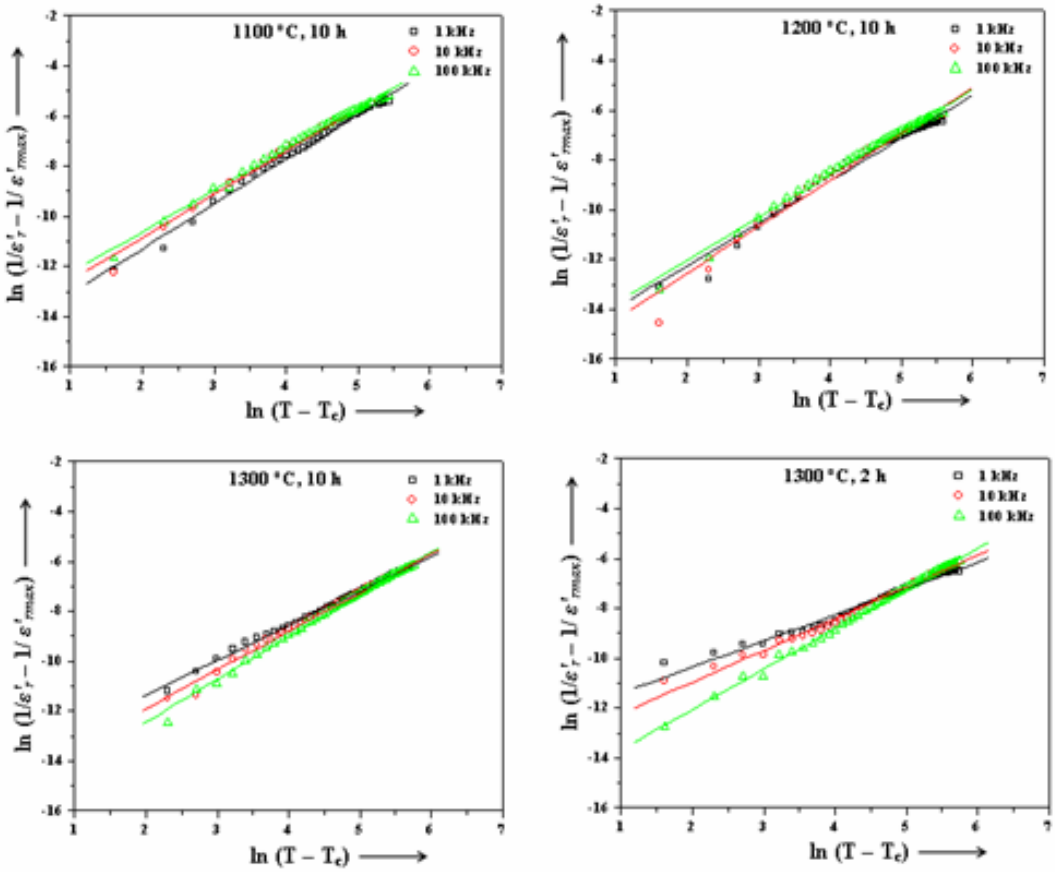

Fig. 6.18 Variation of ln ($1/\varepsilon'_r$ - $1/\varepsilon'_{r\,max}$) with ln (T-T_c) at different sintering conditions

Variation of tan *δ with temperature*

The temperature variations of dielectric loss (tan δ) at the selected frequencies of 1 kHz, 10 kHz and 100 kHz for different sintering conditions are shown in Fig. 6.19. The temperature variation of dielectric loss for the samples

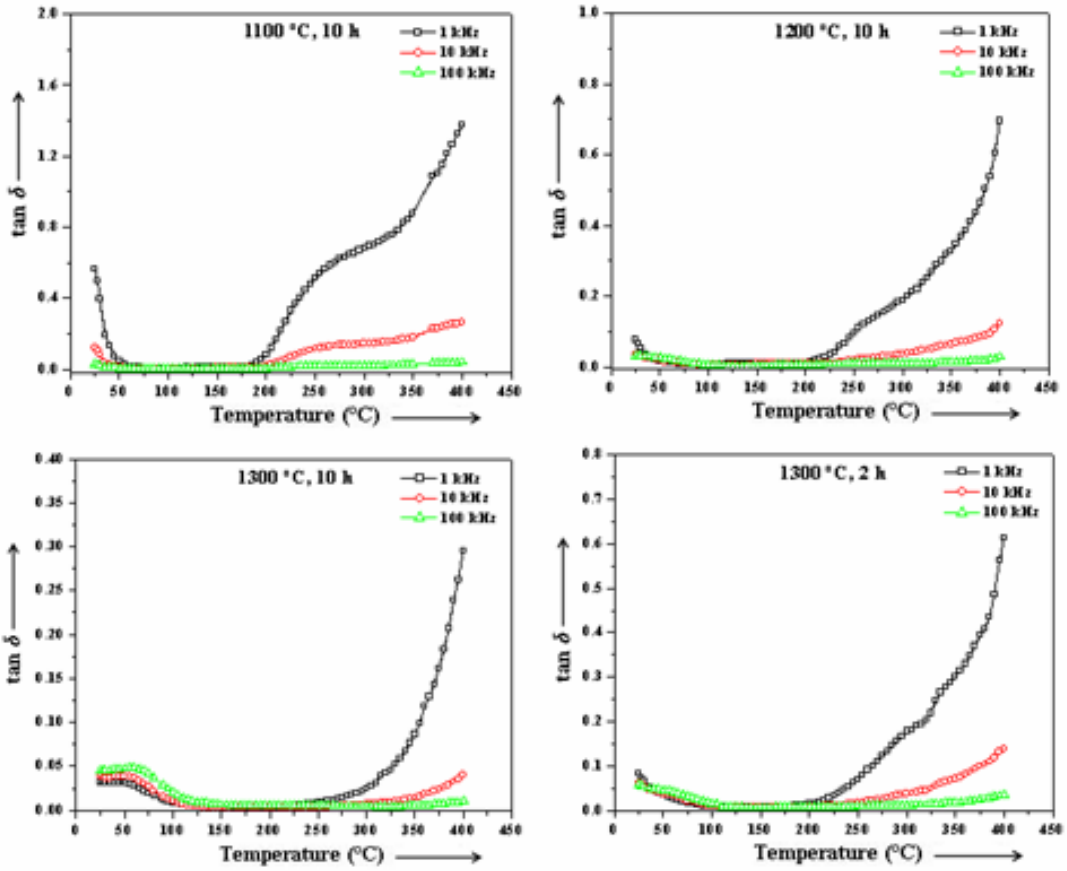

Fig. 6.19 Temperature variation of dielectric loss (tan δ) at different sintering conditions

sintered at various sintering conditions show that the loss is almost constant at lower temperatures but at higher temperatures it increases sharply particularly at lower frequency. This sharp increase of dielectric loss in high temperature region may be attributed to the increased mobility of space charges arising from the defects or vacancies (like oxygen vacancies) in the sample [54]. To see the effect of sintering temperature and duration on the variation of dielectric loss with temperature,

curves have been plotted in Fig. 6.20 at three different frequencies of 1 kHz, 10 kHz and 100 kHz. It can be seen that the dielectric loss decreases with the increase in the sintering temperature and duration and is least in the sample sintered at 1300 ºC for 10 hours.

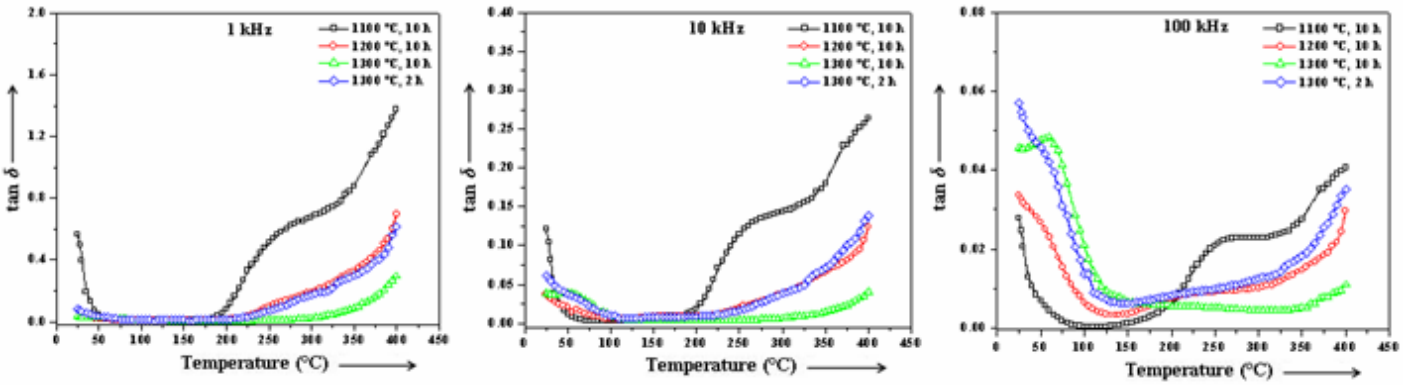

Fig. 6.20 Temperature variation of dielectric loss (tan δ) of the studied specimens prepared at different sintering conditions at 1 kHz, 10 kHz and 100 kHz

Variation of ε_r' and tan δ *with frequency*

Figs. 6.21 (a) and (b) show the variation of dielectric constant (ε_r') and dielectric loss (tan δ) as a function of frequency in the range from 20 Hz to 500 kHz at room temperature respectively of $Ba_5SmTi_3Nb_7O_{30}$ samples prepared at different

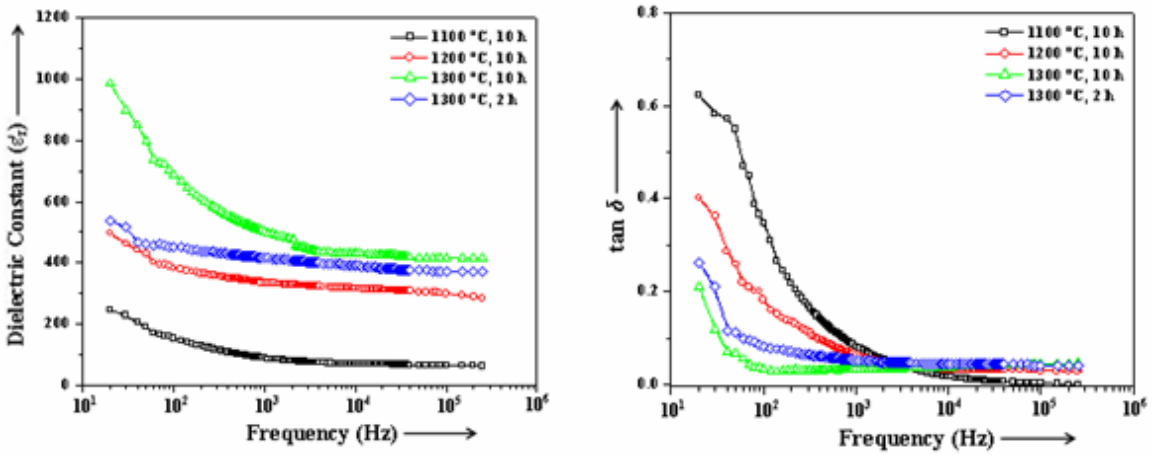

(a) (b)

Fig. 6.21 Variation of (a) ε_r' and (b) tan δ with frequency for the samples sintered at different sintering conditions

sintering conditions. For all the samples, both dielectric constant and dielectric loss decrease upto about 1 kHz and remain nearly constant beyond this frequency. At lower frequencies, the dipoles are able to follow the alternating field resulting in higher values of dielectric constant and dielectric loss while at higher frequencies the dipoles are unable to follow the rapidly changing field leading to the reduction in the values of dielectric constant and loss.

6.2.4.2 Conductivity studies

AC conductivity

Fig. 6.22 shows the temperature variation of ac conductivity at the selected frequencies of 1 kHz, 10 kHz and 100 kHz for $Ba_5SmTi_3Nb_7O_{30}$ samples sintered at different sintering conditions. For all the samples, there is a change in slope in

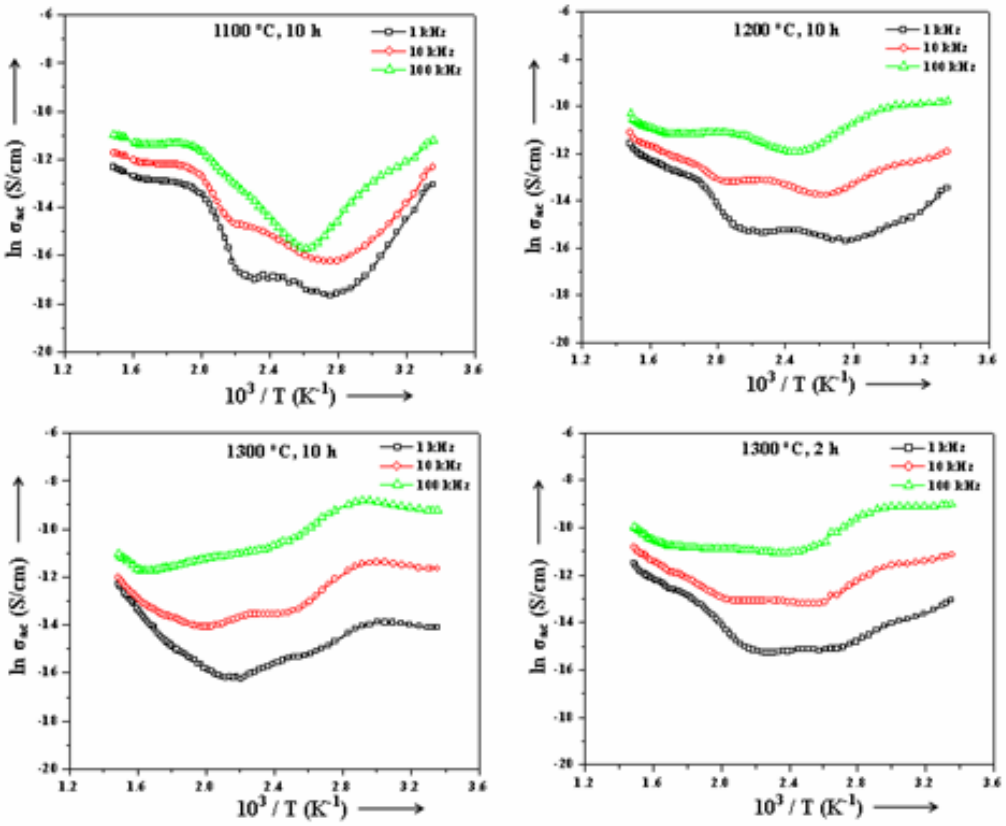

Fig. 6.22 Temperature variation of ac conductivity of the specimens sintered at different sintering conditions

the curve which can be attributed to the difference in activation energy in the paraelectric and ferroelectric phases. The activation energies, evaluated in the ferroelectric phase (low temperature) and paraelectric phase (high temperature) using Eq. (6.3) are summarized in Table 6.6.

Table 6.6 Activation energies (E_a) as calculated from ac conductivity at different sintering conditions

Sintering Conditions	Frequency (kHz)	E_a (eV) (ac conductivity)	
		Ferroelectric	Paraelectric
1100 °C; 10 h	1	0.73	0.44
	10	0.60	0.29
	100	0.54	0.18
1200 °C; 10 h	1	0.23	0.50
	10	0.22	0.36
	100	0.11	0.25
1300 °C; 10 h	1	0.28	0.56
	10	0.23	0.43
	100	0.17	0.36
1300 °C; 2 h	1	0.21	0.48
	10	0.19	0.33
	100	0.16	0.29

To see the effect of sintering temperature and duration on the variation of ac conductivity with temperature, the curves have been plotted in Fig. 6.23 at three different frequencies of 1 kHz, 10 kHz and 100 kHz.

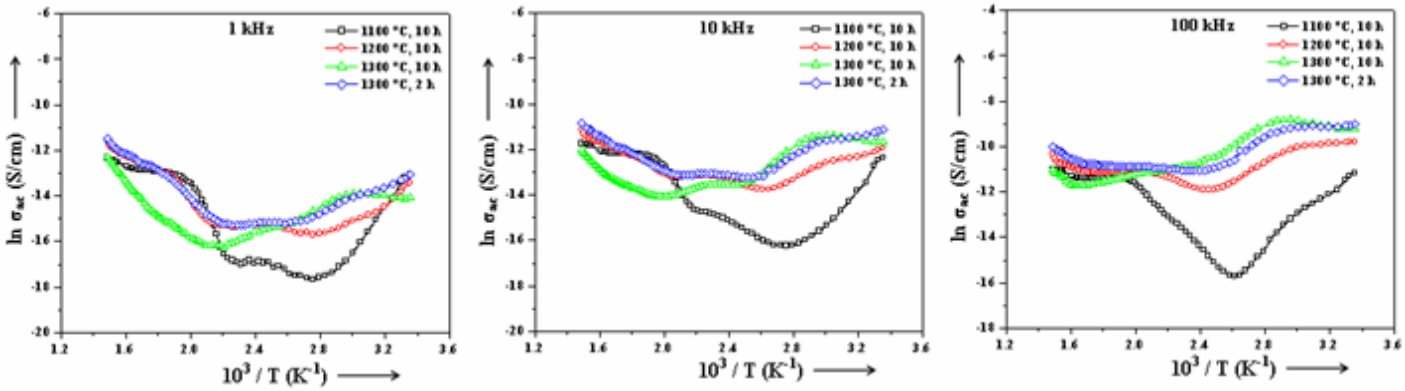

Fig. 6.23 Temperature variation of ac conductivity of $Ba_5SmTi_3Nb_7O_{30}$ compound prepared at different sintering conditions at 1 kHz, 10 kHz and 100 kHz

6.2.4.3 Impedance analysis

Fig. 6.24 shows the impedance (Z'-Z'') plots at different measuring temperatures of $Ba_5SmTi_3Nb_7O_{30}$ samples prepared by mechanical activation method sintered at different sintering conditions. All the semicircles in the Cole-Cole plots exhibit some depression instead of a semicircle centered on the x-axis. Such behaviour is indicative of non-Debye type of relaxation and it also manifests that there is a distribution of relaxation time instead of a single relaxation time in the material [55]. For all the samples, there is a presence of two semicircles at higher temperature (Fig. 6.23 inset) which exhibits the presence of both grain (bulk property) and grain boundary effects. The value of bulk resistances (R_b) at

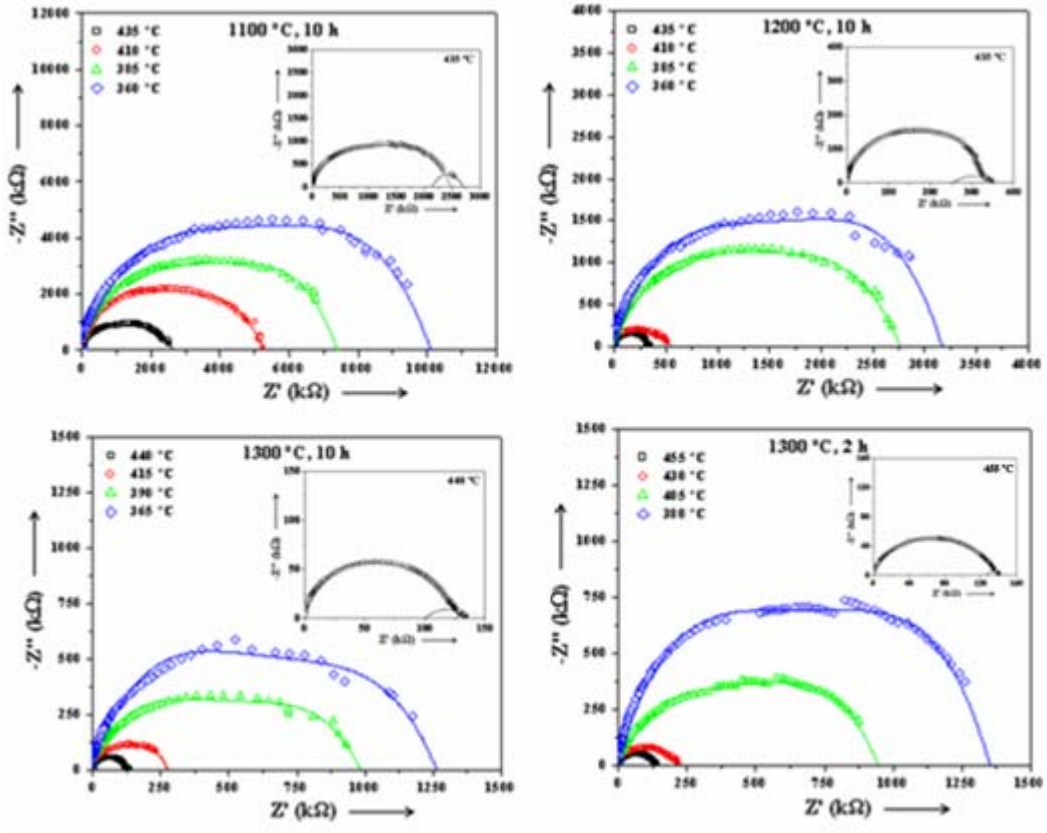

Fig. 6.24 Complex impedance spectrum (Cole-Cole or Nyquist plots) at different temperatures for all the studied sintering conditions

different temperatures for samples sintered at various sintering conditions have been obtained from the intercept of the semicircular arcs on the real axis (Z') and are given in Table 6.7. It is observed that R_b decreases with rise in the temperature for all the samples. This again confirms the negative temperature coefficient of resistance (NTCR) behaviour of the $Ba_5SmTi_3Nb_7O_{30}$ compound at all the studied sintering conditions. From these values of R_b, the bulk conductivity, σ_{bulk} has been obtained by using Eq. (2.31) and its variation with temperature is shown in Fig. 6.25 for all the samples. The respective capacitances (C_b and C_{gb}) due to the grain and grain boundary effect have been calculated using Eq. (2.30). The values of R_b, R_{gb}, C_b and C_{gb} obtained from Cole-Cole plots at different temperatures for various sintering conditions are listed in Table 6.7. The relaxation time due to bulk effect (τ_b) has been calculated using Eq. (2.30). Fig. 6.26 shows the temperature variation of τ_b for all the samples sintered at different sintering conditions. It is observed that the value of τ_b decreases with the increase in temperature for all the samples and its temperature

Table 6.7 Various parameters obtained from the Cole-Cole plots

Sintering Conditions	**Temperature (°C)**	**R_b (kΩ)**	**C_b (nF)**	**R_{gb} (kΩ)**	**C_{gb} (nF)**	**E_a (eV)**
1100 °C; 10 h	360	10116	0.079	-	-	
	385	7411	0.073	-	-	0.80
	410	5288	0.063	-	-	
	435	2478	0.060	223	5.95	
1200 °C; 10 h	360	3162	0.25	-	-	
	385	2753	0.21	-	-	1.29
	410	548	0.16	-	-	
	435	331	0.15	25	10.62	
1300 °C; 10 h	365	1265	0.90	-	-	
	390	979	0.41	-	-	1.35
	415	275	0.20	-	-	
	440	129	0.19	7	30.71	
1300 °C; 2 h	380	1354	0.29	-	-	
	405	940	0.25	-	-	1.27
	430	219	0.24	-	-	
	455	139	0.23	4	180.99	

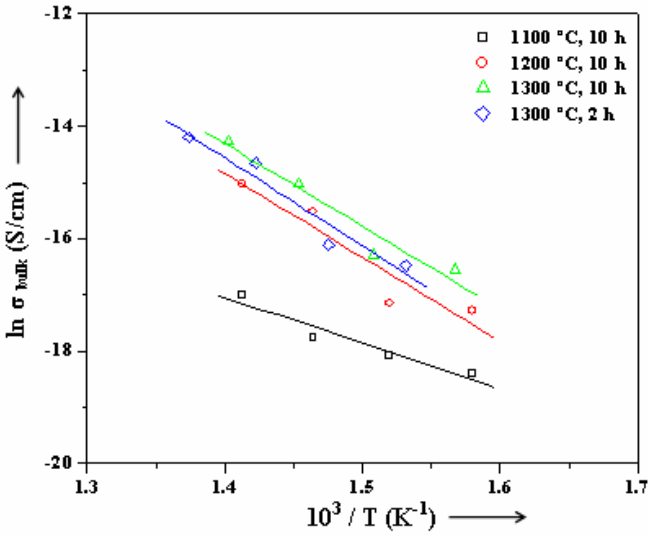

Fig. 6.25 Temperature variation of bulk conductivity

dependence follows the Arrhenius relation:

$$\tau_b = \tau_o \exp\left(\frac{-E_a}{k_B T}\right) \tag{6.4}$$

where τ_o is the pre-exponential factor, k_B is Boltzmann constant and E_a the activation energy. The value of activation energy (E_a) calculated using Eq. (6.4) is summarized in Table 6.7.

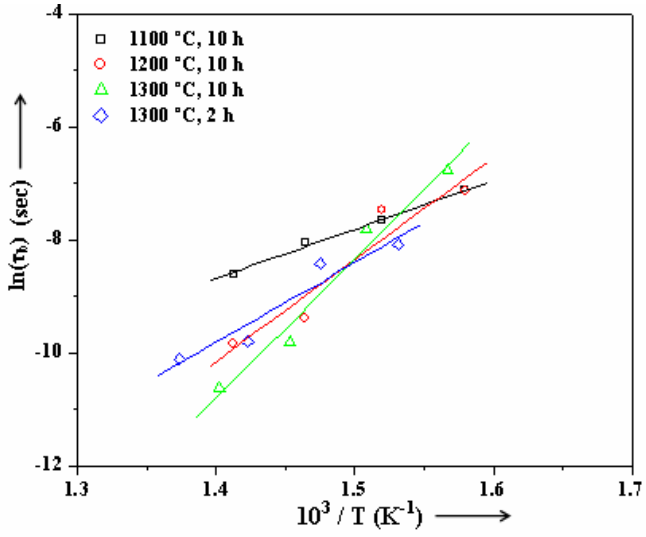

Fig. 6.26 Temperature variation of relaxation time

(iii) Comparison between Conventional and Mechanical Activation Processes

In this section, various properties obtained in $Ba_5SmTi_3Nb_7O_{30}$ compound prepared by conventional solid-state reaction process have been compared with that obtained by mechanical activation method.

6.2.5 Structural studies

6.2.5.1 X-ray diffraction

Room temperature X-ray diffraction patterns of the studied samples are shown in Fig. 6.27, which reveal the formation of single phase compound by both the processes. The peaks are comparatively well defined and shifts slightly to higher angles in the specimen prepared by the mechanical activation process as

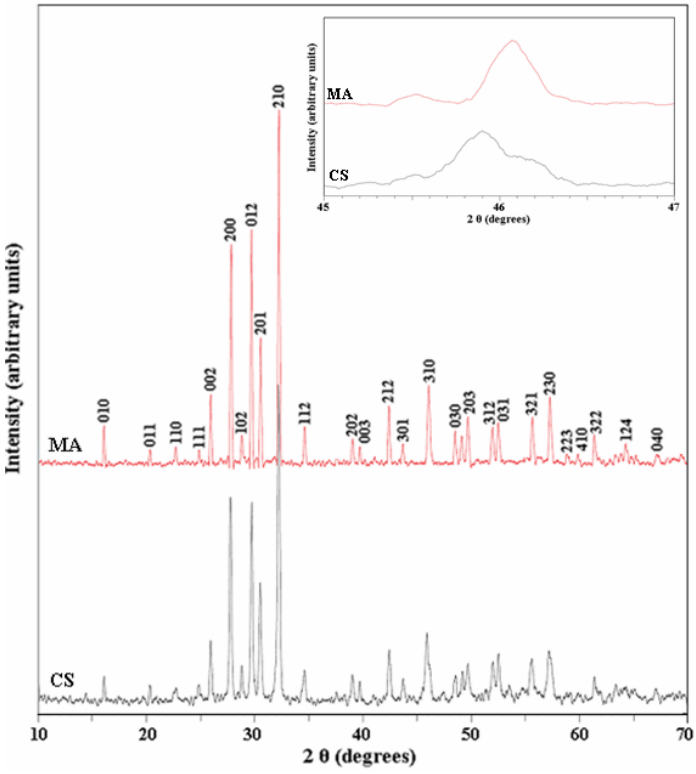

Fig. 6.27 XRD patterns of $Ba_5SmTi_3Nb_7O_{30}$ compound prepared by conventional (CS) and mechanical activation (MA) processes

compared to that by conventional technique, as can be seen in Fig. 6.26 (inset) for (310) peak. The refined lattice parameters for both the cases are listed in the Table 6.8. It is observed that the values of lattice parameters are slightly lower in the sample prepared by mechanical activation process as compared to that by conventional solid-state reaction method. However, it is found that the specimens prepared by both the processes have an orthorhombic TB-type structure.

Table 6.8 Comparison of different parameters in $Ba_5SmTi_3Nb_7O_{30}$ compound prepared by conventional solid-state reaction and mechanical activation processes

Parameters	**Sample Preparation Method**	
	Conventional Solid-State Reaction	**Mechanical Activation**
a (Å)	6.4106	6.4058
b (Å)	5.5595	5.5386
c (Å)	6.8112	6.7925
V (Å^3)	242.75	240.99
$\varepsilon'_{r\,max}$ at 100 kHz	303	630
γ	1.71	1.47
$2P_r$ (μC/cm^2)	2.3	5.2
$2E_c$ (kV/cm)	23.3	27.8
d_{33} (pC/N)	8	11

6.2.5.2 SEM analysis

The SEM micrographs of the specimens prepared by both the processes are shown in Fig. 6.28. It can be seen that the average grain size in the specimen prepared by the mechanical activation technique is much lower (≤ 1 μm) as compared to that prepared by the conventional solid-state reaction method (~2-3 μm).

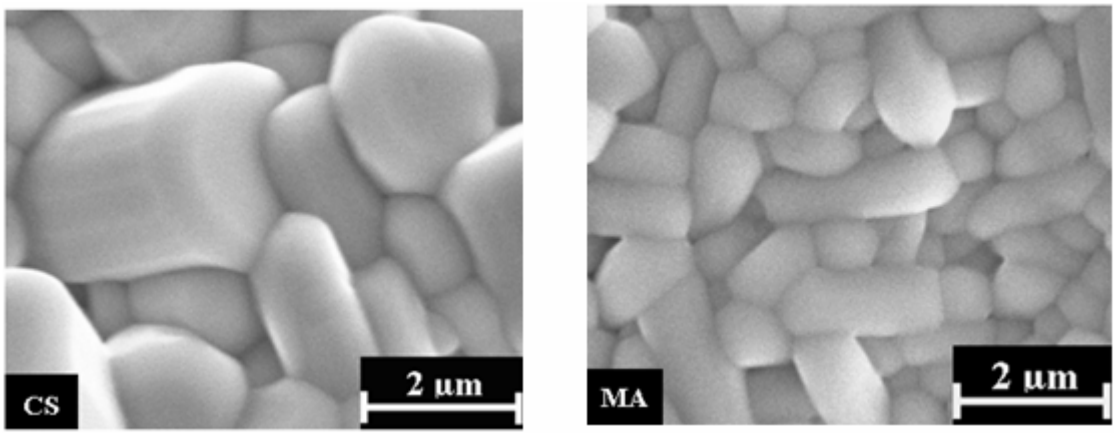

Fig. 6.28 SEM micrographs of $Ba_5SmTi_3Nb_7O_{30}$ compound prepared by conventional (CS) and mechanical activation (MA) processes

6.2.6 Electrical studies

6.2.6.1 Dielectric properties

The temperature dependence of dielectric constant (ε'_r) at 100 kHz is shown in Fig. 6.29 for both the samples. It is observed that ε'_r value of the sample prepared by mechanical activation process is much higher compared to that of the sample synthesized by conventional solid-state reaction process (Table 6.8). It is known that in the fine-grained ferroelectric ceramics the dielectric constant increases due to an increase in residual internal stress [47-50]. Thus the higher ε'_r value in the sample prepared by mechanical activation process can be attributed

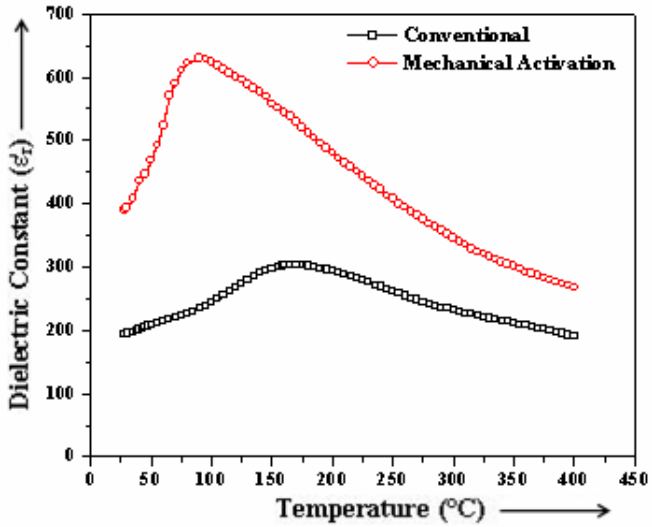

Fig. 6.29 Temperature variation of dielectric constant (ε'_r) at 100 kHz for $Ba_5SmTi_3Nb_7O_{30}$ compounds prepared by conventional and mechanical activation processes

to its smaller grain size (Fig. 6.28). The reduction of the unit cell volume (Table 6.8) is another possible reason for the observed increase in dielectric constant in mechanically activated sample as follows from Clausius-Mossotti relation (Eq. 6.1). However, the Curie temperature (T_c) is found to be lower in this sample (90 °C) compared to that in the sample prepared by the conventional process (170 °C) which can be understood in terms of the smaller crystallite size in the ball-milled sample as it is known that T_c is strongly dependent on the crystallite size and it decreases with decrease in the crystallite size [51,52]. Moreover, the mechanically activated sample, due to smaller grains, has more interfacial or grain boundary energy as it contains larger number of grain boundaries (Fig. 6.28) which results in the requirement of smaller amount of thermal energy to undergo the phase transition [53].

The dielectric peak in both the cases is found to be broadened indicating the diffuse nature of the phase transition. The value of γ at 100 kHz for both the samples was obtained from the slope of ln ($1/\varepsilon'_r - 1/\varepsilon'_{r\,max}$) versus ln ($T$-$T_c$) curve

(Fig. 6.30) and are listed in Table 6.8. The values of γ is found to be between 1 (obeying Curie-Weiss law) and 2 (for completely disordered system) confirming the diffuse nature of phase transition in both the samples. It is found to be lower for the sample prepared by the mechanical activation process, confirming the observations in Fig. 6.29.

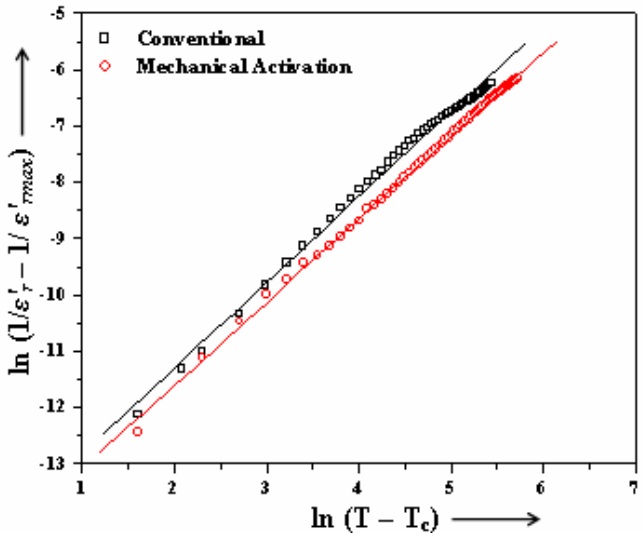

Fig. 6.30 Comparison of variation of ln ($1/\varepsilon'_r$ - $1/\varepsilon'_{r\,max}$) with ln (T-T_c) for the samples prepared by conventional and mechanical activation processes

Fig. 6.31 shows the temperature variation of dielectric loss (tan δ) at 100 kHz of the studied specimens. In both the cases, the loss has smaller values at lower temperatures but at higher temperatures it increases sharply. This sharp increase of dielectric loss in high temperature region may be attributed to the increased mobility of space charges arising from the defects or vacancies (like oxygen vacancies) in the samples [54]. However, the dielectric loss in the sample prepared by mechanical activation process is lesser compared to that of the sample synthesized by conventional solid-state reaction method.

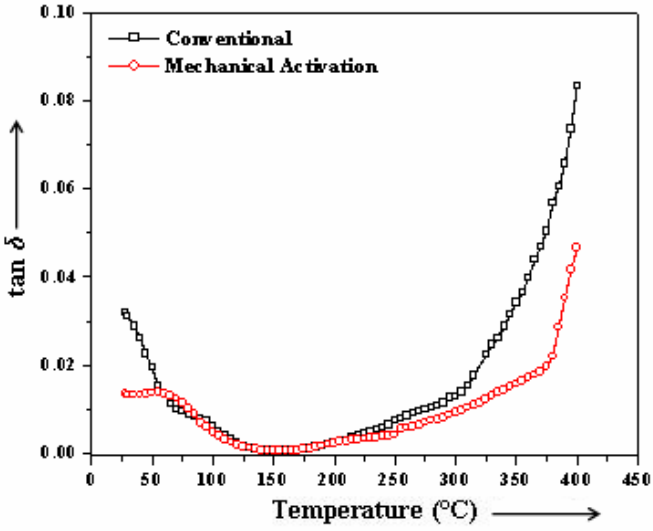

Fig. 6.31 Temperature variation of dielectric loss (tan δ) for the samples prepared by conventional and mechanical activation processes

Figs. 6.32 (a) and (b) show the variation of room temperature dielectric constant (ε'_r) and dielectric loss (tan δ) with frequency respectively for both the samples. It is observed that the room temperature dielectric constant of the sample prepared by mechanical activation is higher as compared to that of the

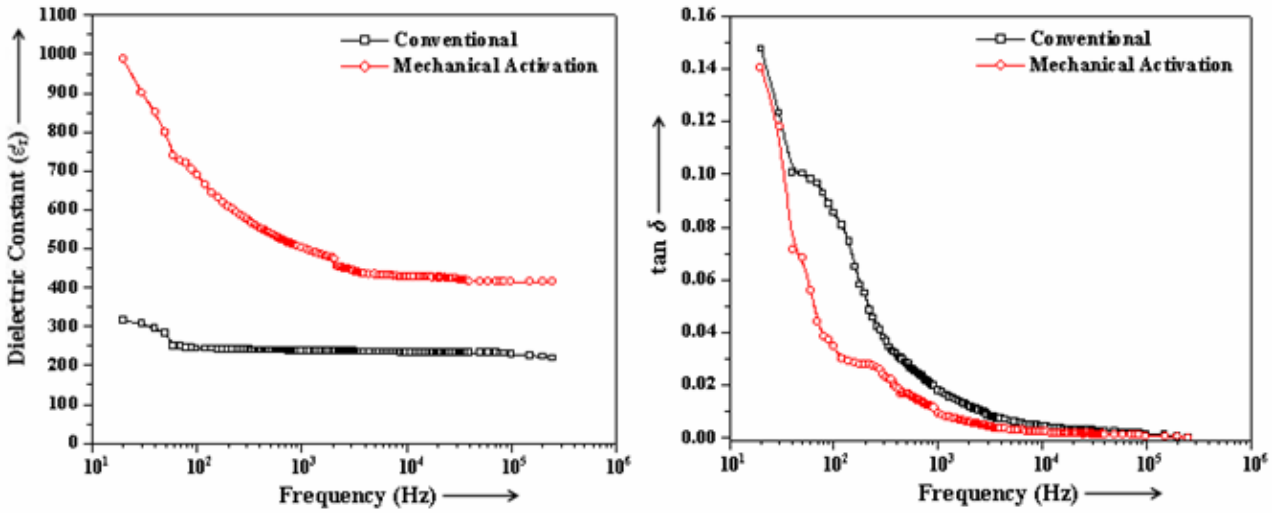

Fig. 6.32 Room temperature frequency variation of (a) dielectric constant (ε'_r) and (b) dielectric loss (tan δ) for the samples prepared by conventional and mechanical activation processes

sample prepared by conventional process, throughout the measured frequency range. Also, the room temperature dielectric loss is lower in the sample prepared by mechanical activation process.

6.2.6.2 Conductivity properties

DC conductivity

Fig. 6.33 shows the temperature variation of dc conductivity ($\sigma_{dc} = 1/\rho$) of the studied samples. In both the cases, the conductivity is constant at lower temperatures but at higher temperatures, it increases with temperature. This indicates negative temperature coefficient of resistance (NTCR) – type behaviour in $Ba_5SmTi_3Nb_7O_{30}$ compounds prepared by both the processes. The conductivity is found to be lower in specimen prepared by mechanical activation process throughout the studied temperature region. Due to smaller size of the grains (Fig. 6.28), there is comparatively higher number of grain boundaries in the sample prepared by mechanical activation method which results in higher contribution of grain boundaries towards the overall resistance.

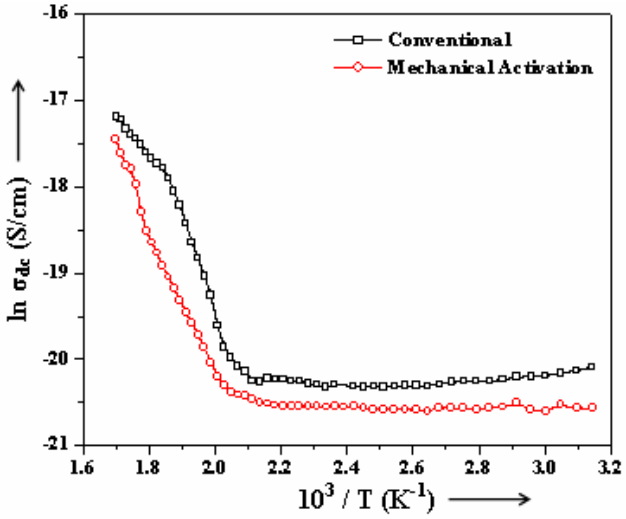

Fig. 6.33 Temperature variation of dc conductivity (ln σ_{dc}) of the samples prepared by conventional and mechanical activation processes

6.2.6.3 Ferroelectric properties

Fig. 6.34 illustrates the *P–E* hysteresis loops for both the samples at room temperature at a frequency of 100 Hz. The observed values of remanent polarization polarization ($2P_r$) and the coercive field ($2E_c$) are given in Table 6.8. The remanent

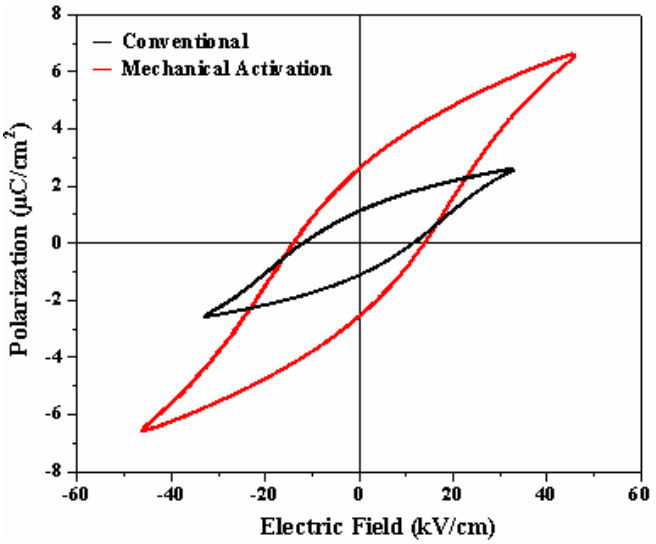

Fig. 6.34 *P-E* hysteresis loops of the samples prepared by conventional and mechanical activation processes

polarization ($2P_r$) value is found to be much higher in the specimen prepared by mechanical activation process than that in the conventionally prepared sample. Smaller grains induce strong internal stress which would results in increased degree of dipole orientation [56]. Thus the higher $2P_r$ value in the sample prepared by mechanical activation process can be attributed to its smaller granular sizes (Fig. 6.28).

6.2.6.4 Pyroelectric properties

The temperature variation of pyroelectric coefficient of both the synthesized samples is shown in Fig. 6.35. It is found to be higher in the sample prepared by the mechanical activation process. The maximum obtained pyroelectric coefficient is

80.7 $nCcm^{-2}{}^{o}C^{-1}$ in ball-milled sample as compared to 57.1 $nCcm^{-2}{}^{o}C^{-1}$ in the conventionally prepared sample. This enhanced pyroelectric activity in the sample prepared by mechanical activation method is due the increase of the spontaneous polarization in it as observed in Fig. 6.34.

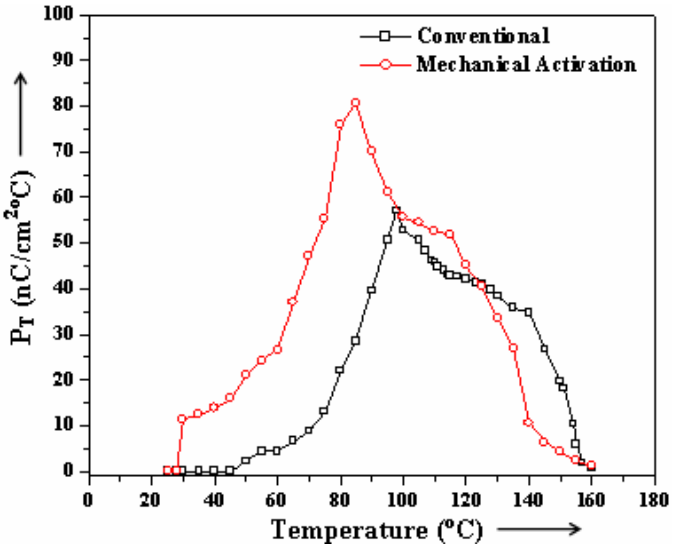

Fig. 6.35 Temperature variation of pyroelectric coefficient (P_T) of the samples prepared by both the processes

6.2.6.5 Piezoelectric properties

The measured values of piezoelectric coefficient (d_{33}) for both the samples are given in Table 6.8. The d_{33} value is also observed to be higher in the sample synthesized by mechanical activation process which can be understood in terms of its smaller grain size. Small grains have larger number of grain boundaries which results in the increase of internal electric fields generated by space charge layers at grain boundaries [57]. Moreover, a decrease in conductivity in mechanically activated sample (Fig. 6.33) improves the poling efficiency and hence the piezoelectric coefficient.

II. Microwave Sintering

6.2.7 Structural Characterization

6.2.7.1 X-ray diffraction

The room temperature X-ray diffractogram of $Ba_5SmTi_3Nb_7O_{30}$ sample sintered by microwave sintering is shown in Fig. 6.36. It is observed that single-

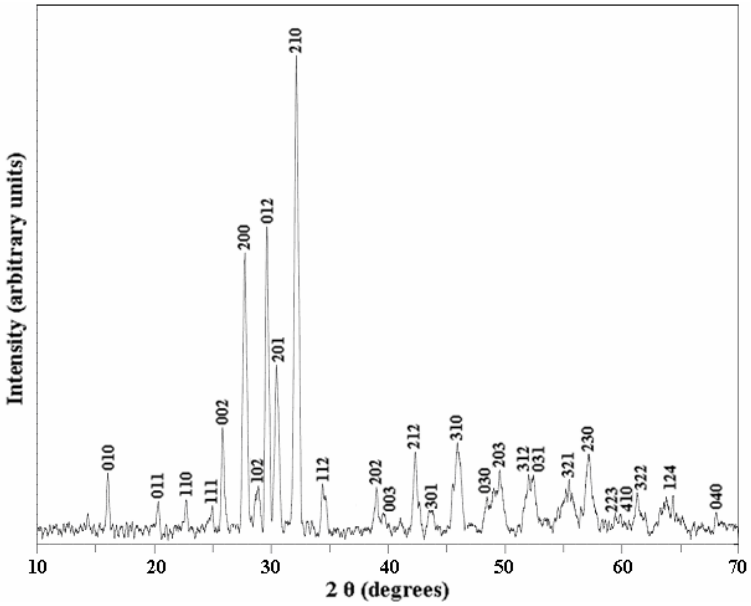

Fig. 6.36 XRD pattern of microwave sintered sample of $Ba_5SmTi_3Nb_7O_{30}$

phase $Ba_5SmTi_3Nb_7O_{30}$ compound is formed by microwave sintering. The refined lattice parameters and the unit cell volume of the sample prepared by microwave sintering is tabulated and are compared with that obtained in the sample prepared by conventional sintering in Table 6.9. The lattice parameters and the unit cell volume are observed to increase in microwave sintered sample as compared to conventional sintered sample.

Table 6.9 Comparison of different parameters in $Ba_5SmTi_3Nb_7O_{30}$ compound sintered by conventional and microwave sintering

Parameters	Method of Sintering	
	Conventional Sintering	**Microwave Sintering**
a (Å)	6.4106	6.4160
b (Å)	5.5595	5.5674
c (Å)	6.8112	6.8189
V ($Å^3$)	242.75	243.57
$\varepsilon'_{r\,max}$ at 100 kHz	303	167
γ	1.71	1.88
$2P_r$ ($\mu C/cm^2$)	2.3	1.3
$2E_c$ (kV/cm)	23.3	28.4

6.2.7.2 SEM analysis

Fig. 6.37 shows the SEM micrograph of the $Ba_5SmTi_3Nb_7O_{30}$ specimen sintered by microwave sintering. It reveals the uniform distribution of grains with average grain size of 2 μm within a short period of 2 hours of microwave sintering as compared to 10 hours of the conventional sintering.

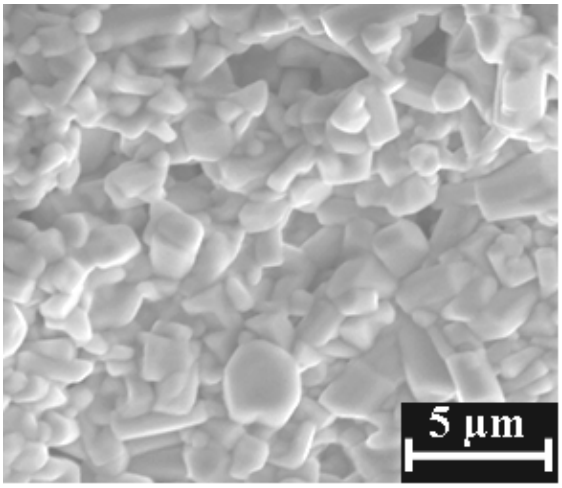

Fig. 6.37 SEM micrograph of microwave sintered sample of $Ba_5SmTi_3Nb_7O_{30}$

6.2.8 Electrical Characterization

6.2.8.1 Dielectric studies

Fig. 6.38 shows the temperature variation of dielectric constant (ε'_r) of the microwave sintered specimen of composition $Ba_5SmTi_3Nb_7O_{30}$ at frequencies namely 1 kHz, 10 kHz and 100 kHz. Like in conventional sintering, here also the

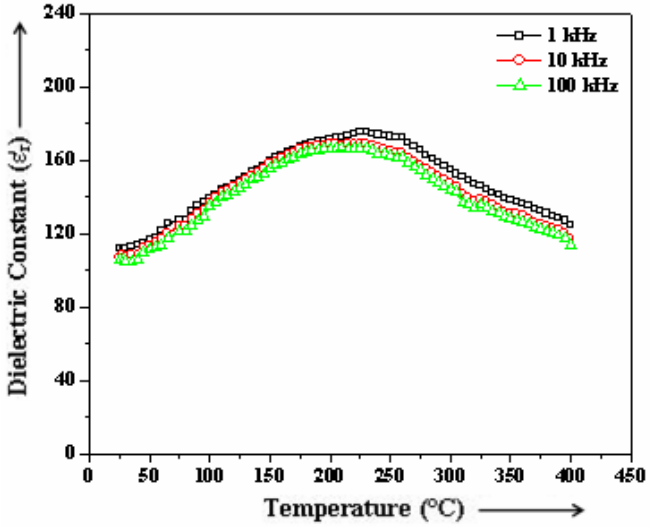

Fig. 6.38 Temperature variation of microwave sintered sample of $Ba_5SmTi_3Nb_7O_{30}$

Curie temperature (T_c) is found to be same for all the measured frequencies indicating the non-relaxor behaviour of the compound. Fig. 6.39 shows the comparison of the temperature variation of the dielectric constant (ε'_r) at 100 kHz of microwave sintered sample with that of conventional sintered sample. It is observed that ε'_r value of the sample sintered by conventional sintering is much higher compared to that of the sample sintered by microwave sintering (Table 6.9).

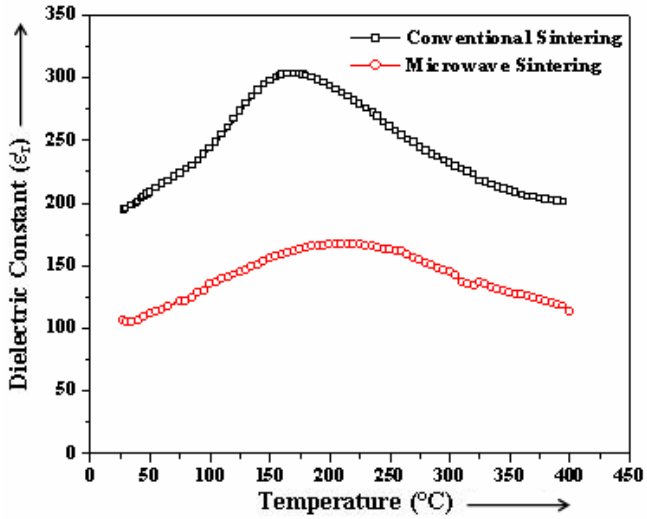

Fig. 6.39 Comparison of temperature variation of dielectric constant (ε'_r) at 100 kHz for samples sintered by conventional and microwave sintering

The dielectric peak is found to be broadened indicating the diffuse nature of the phase transition. The value of γ at 100 kHz is obtained from the slope of $\ln (1/\varepsilon'_r - 1/\varepsilon'_{r\,max})$ versus $\ln (T-T_c)$ curve and is listed in Table 6.9. It is found to be higher for the sample sintered by microwave sintering as compared to that for conventionally sintered sample indicating the increase in disorderness in the microwave sintered sample.

Fig. 6.40 shows the temperature variations of dielectric loss (tan δ) of $Ba_5SmTi_3Nb_7O_{30}$ compound prepared by microwave sintering at the selected frequencies of 1 kHz, 10 kHz and 100 kHz. Initially tan δ has smaller values at lower

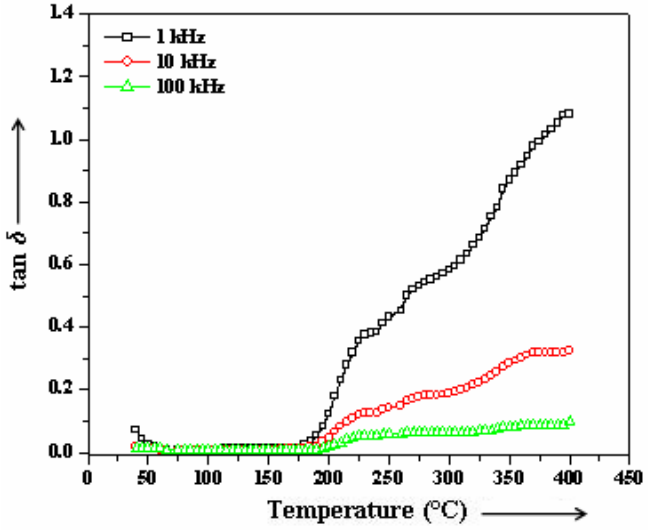

Fig. 6.40 Temperature variation of dielectric loss (tan δ) of microwave sintered sample of $Ba_5SmTi_3Nb_7O_{30}$

temperatures but it increases sharply at higher temperatures. This sharp increase of tan δ in high temperature region may be attributed to the increased mobility of space charges arising from the defects or vacancies (like oxygen vacancies) in the sample [54]. The comparison of the temperature variation of the dielectric loss (tan δ) at 100 kHz of microwave sintered sample with that of conventionally sintered sample is shown in Fig. 6.41. It is observed that dielectric loss value of the sample sintered by microwave sintering is higher compared to that of the sample sintered by conventional sintering.

Fig. 6.42 (a) and (b) show the comparison of variation of dielectric constant (ε_r') and dielectric loss (tan δ) as a function of frequency respectively at room temperature for $Ba_5SmTi_3Nb_7O_{30}$ samples sintered by both the methods. For both the

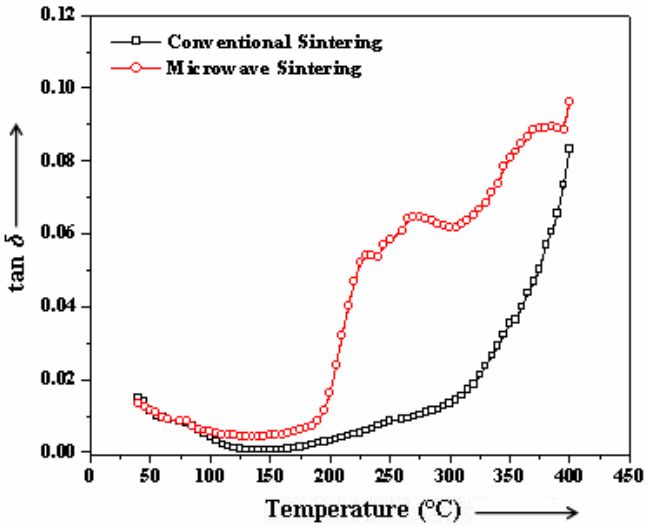

Fig. 6.41 Comparison of temperature variation of dielectric constant (ε'_r) at 100 kHz for the samples sintered by conventional and microwave sintering

samples, both dielectric constant and dielectric loss decrease upto about 1 kHz and remain nearly constant beyond this frequency. It is observed that the room temperature dielectric constant is higher and dielectric loss is lower in the conventionally sintered sample as compared to that in microwave sintered sample.

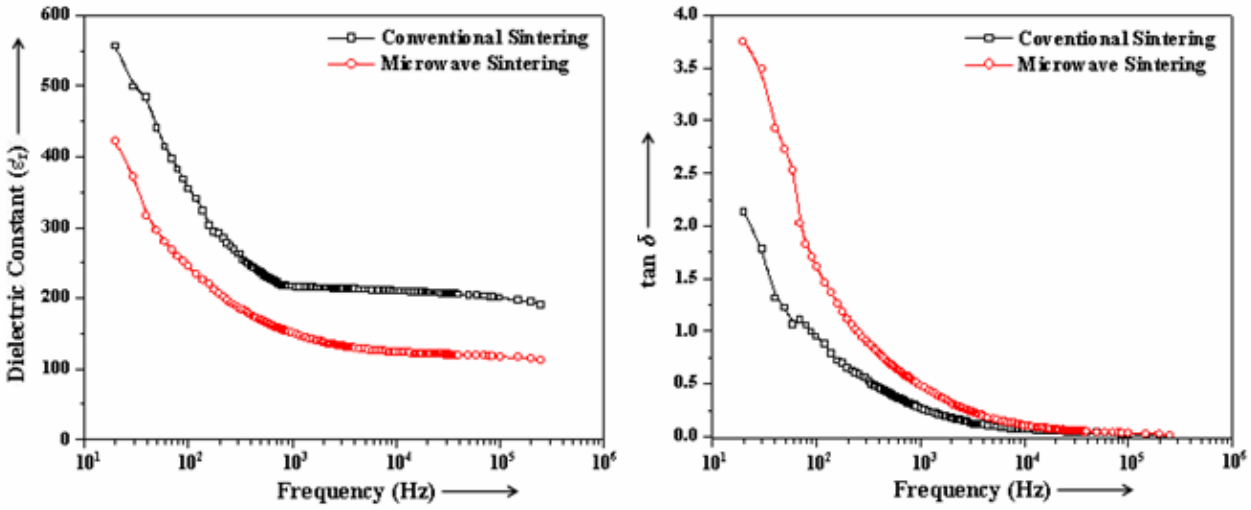

Fig. 6.42 Comparison of variation of (a) ε_r' and (b) tan δ with frequency for the samples sintered by conventional and microwave sintering

6.2.8.2 Conductivity studies

DC conductivity

The comparison of the temperature variation of dc conductivity for $Ba_5SmTi_3Nb_7O_{30}$ compound sintered by both conventional and microwave sintering methods is shown in Fig. 6.43. For both the samples, the conductivity is constant at lower temperatures but at higher temperatures, it increases with temperature indicating negative temperature coefficient of resistance (NTCR) – type behaviour of $Ba_5SmTi_3Nb_7O_{30}$ compound sintered by both the processes. The conductivity is higher in microwave sintered sample as compared to conventionally sintered sample which is due to the increased dielectric loss in microwave sintered sample.

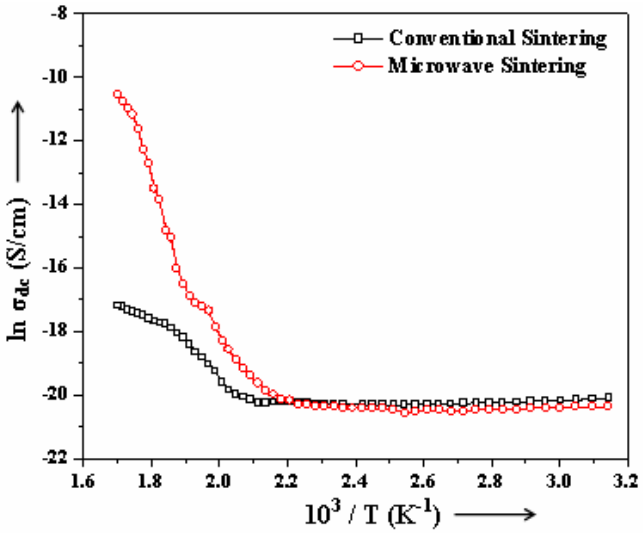

Fig. 6.43 Comparison of temperature variation of dc conductivity (ln σ_{dc}) for the samples sintered by conventional and microwave sintering

AC conductivity

Fig. 6.44 shows the temperature variation of ac conductivity at the selected frequencies of 1 kHz, 10 kHz and 100 kHz for $Ba_5SmTi_3Nb_7O_{30}$ samples sintered

by both the processes. For both the samples, there is a change in slope in the curve which can be attributed to the difference in activation energy in the paraelectric and ferroelectric phases. The ac conductivity is higher in microwave sintered sample as compared to conventionally sintered sample which can be ascribed to the higher dielectric loss (Fig. 6.41).

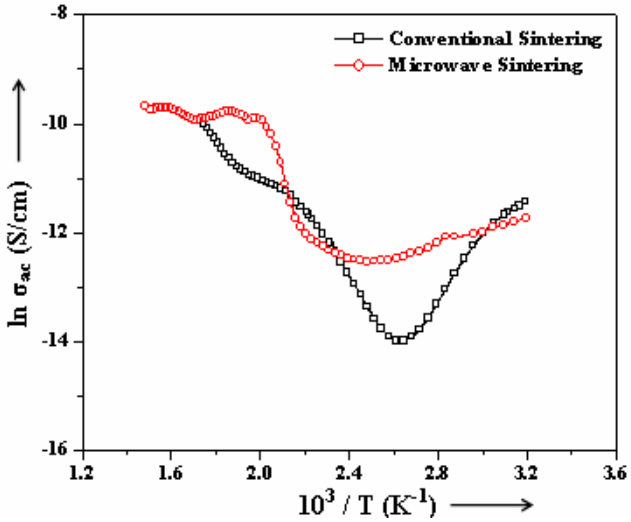

Fig. 6.44 Comparison of temperature variation of ac conductivity (ln σ_{ac}) for the samples sintered by conventional and microwave sintering

6.2.8.3 Impedance analysis

Fig. 6.45 shows the impedance (Z'-Z'') plots at different measuring temperatures of $Ba_5SmTi_3Nb_7O_{30}$ samples prepared by conventional sintering as well as microwave sintering. All the semicircles in the Cole-Cole plots exhibit some depression instead of a semicircle centered on the x-axis. Such a behaviour is indicative of non-Debye type of relaxation and it also manifests that there is a distribution of relaxation time instead of a single relaxation time in the material [56]. For both the samples, there is a presence of two semicircles at higher temperature (Fig. 6.45 inset) which exhibits the presence of both grain (bulk property) and grain boundary effects. The value of bulk resistances (R_b) at

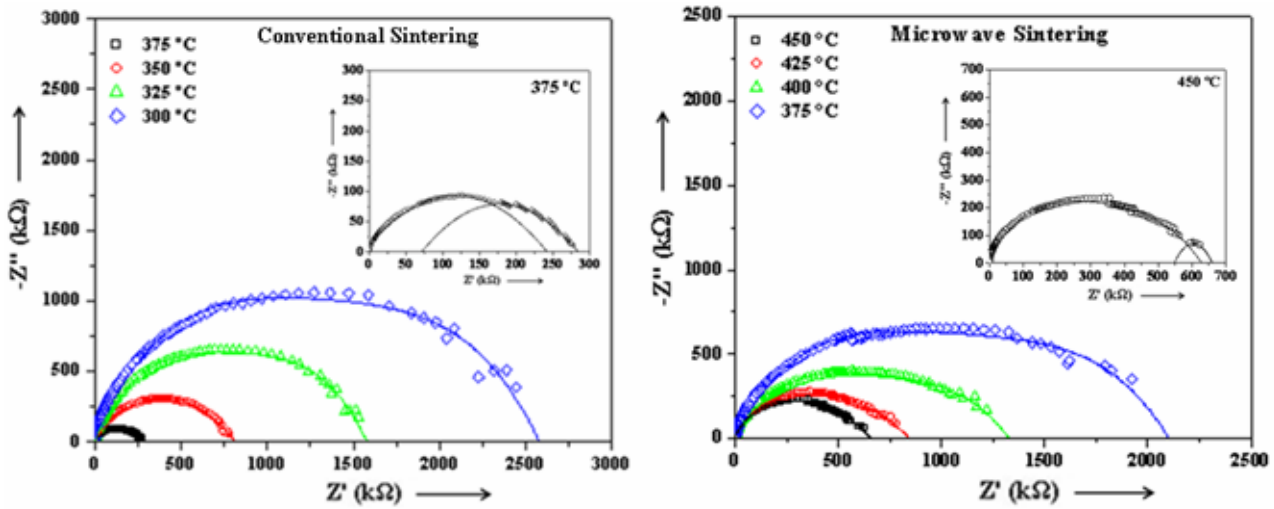

Fig. 6.45 Complex impedance spectrum at different temperatures for $Ba_5SmTi_3Nb_7O_{30}$ samples sintered by conventional and microwave sintering

different temperatures for samples sintered by both the methods have been obtained from the intercept of the semicircular arcs on the real axis (Z') and are given in Table 6.10. It is observed that R_b decreases with rise in the temperature for both the samples which again confirms the negative temperature coefficient of resistance (NTCR) behaviour of the $Ba_5SmTi_3Nb_7O_{30}$ compound. From these values of R_b, the bulk conductivity, σ_{bulk} has been obtained by using Eq. (2.31) and its temperature variation is shown in Fig. 6.46 for both the samples. The respective capacitances (C_b and C_{gb}) due to the grain and grain boundary effect

Table 6.10 Various parameters obtained from the Cole-Cole plots for $Ba_5SmTi_3Nb_7O_{30}$ samples sintered by conventional and microwave sintering

Method of Sintering	Temperature (°C)	R_b (kΩ)	C_b (nF)	R_{gb} (kΩ)	C_{gb} (nF)	E_a (eV)
Conventional Sintering	300	2590	0.38	-	-	0.99
	325	1610	0.35	-		
	350	800	0.31	-		
	375	240	0.30	45	3.85	
Microwave Sintering	375	2102	0.32	-	-	0.66
	400	1325	0.23	-	-	
	425	840	0.22	-	-	
	450	628	0.19	31	128.42	

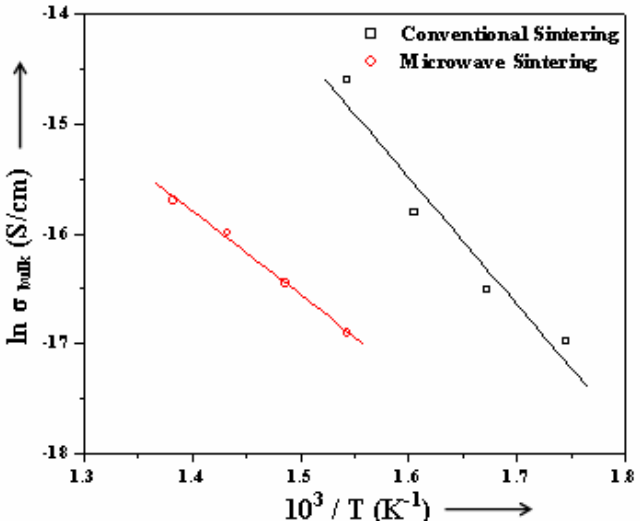

Fig. 6.46 Temperature variation of bulk conductivity for $Ba_5SmTi_3Nb_7O_{30}$ samples sintered by conventional and microwave sintering

can be calculated using the Eq. (2.30). The values of R_b, R_{gb}, C_b and C_{gb} obtained from Cole-Cole plots at different temperatures for both microwave and conventionally sintered samples are listed in Table 6.10. Fig. 6.47 shows the temperature variation of relaxation time due to bulk effect (τ_b) for both the samples. The activation energies (E_a) for both the samples have been calculated using Eq. (6.4) and are tabulated in Table 6.10. It is observed to be lower in the microwave sintered sample which is likely due to the increase of the degree of disorderness (γ) in this sample (Table 6.9).

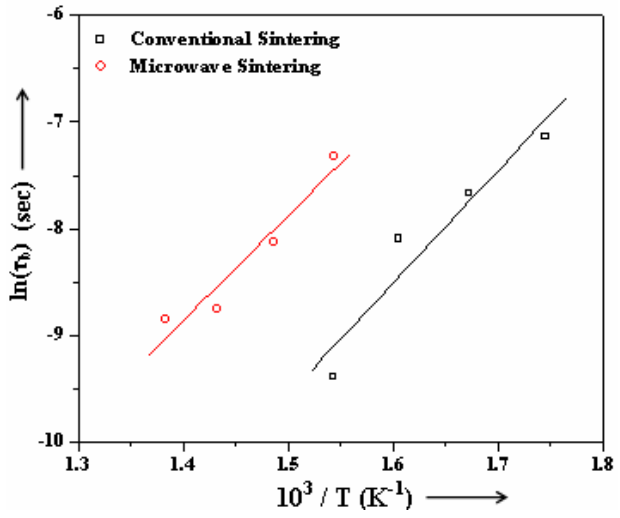

Fig. 6.47 Temperature variation of relaxation time for $Ba_5SmTi_3Nb_7O_{30}$ samples sintered by conventional and microwave sintering

6.2.8.4 Ferroelectric properties

Fig. 6.48 shows the *P–E* hysteresis loops for both the samples at room temperature at a frequency of 100 Hz. The observed values of remanent polarization ($2P_r$) and the coercive field ($2E_c$) of the samples are given in Table 6.9. The remanent polarization value is found to decrease in the microwave sintered sample as compared to the conventionally prepared sample. Microwave sintering is known to create more oxygen vacancies in the sample as compared to the conventionally sintered sample which causes pronounced pinning effect of ferroelectric domain walls leading to the decrease in the remanent polarization value [58].

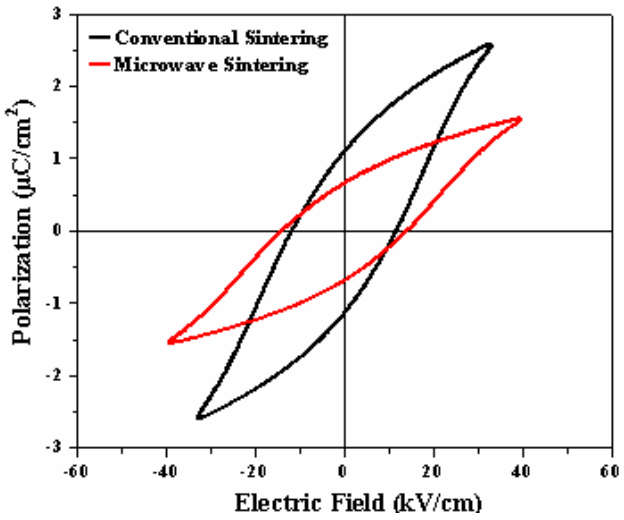

Fig. 6.48 *P-E* hysteresis loops of the samples sintered by conventional and microwave sintering

6.2.8.5 Pyroelectric properties

Fig. 6.49 shows the temperature variation of pyroelectric coefficient of the synthesized samples by both the methods. It is observed to decrease in the sample sintered by microwave. The maximum obtained pyroelectric coefficient is

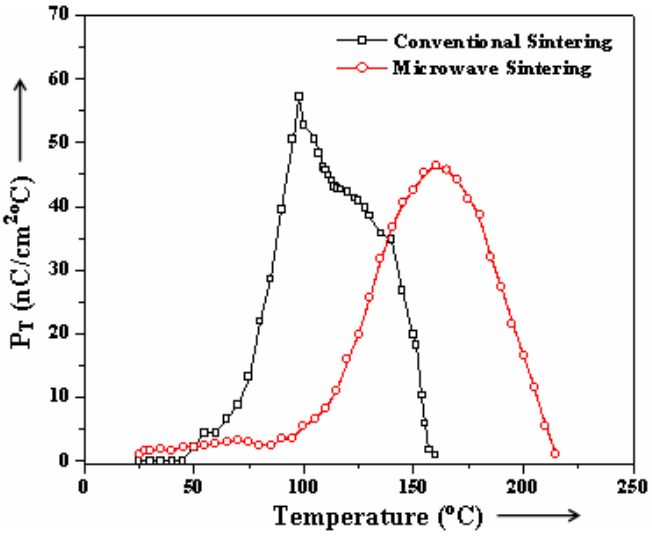

Fig. 6.49 Temperature variation of pyroelectric coefficient (P_T) for the samples sintered by both the processes

46.4 nCcm^{-2}°C^{-1} in microwave sintered sample as compared to 57.1 nCcm^{-2}°C^{-1} in the conventionally sintered sample. This reduced pyroelectric activity in the sample sintered by microwave is due the decrease of the spontaneous polarization in it as observed in Fig. 6.48.

6.3 CONCLUSIONS

Based on the above observations and discussions the following conclusions can be drawn from this chapter:

(i) The synthesized $Ba_5SmTi_3Nb_7O_{30}$ compound is single-phase having an orthorhombic TB-structure.

(ii) SEM and TEM micrographs reveal that the particles size milled for 20 hours reduces to nano-range.

(iii) Dielectric, ferroelectric, piezoelectric and pyroelectric properties have been observed to improve in $Ba_5SmTi_3Nb_7O_{30}$ compound prepared by mechanical

activation process at the optimized condition as compared to the conventional solid-state reaction process.

(iv) Microwave sintering results in the formation of phase and microstructures in short sintering time as compared to the conventional sintering.

(v) Microwave sintered sample has lower dielectric constant, higher diffusivity, higher dielectric loss, higher conductivity, lower remanent polarization ($2P_r$), lower pyroelectric coefficient (P_T) as compared to the conventional sintered sample.

REFERENCES

[1] K. Keizer, E. H. Janssen, K. J. de Vries and A. J. Burggraaf, Mater. Res. Bull. **8** (1973) 533.

[2] T. Yamamoto, Amer. Ceram. Soc. Bull. **71** (1992) 978.

[3] G. Arlt, Ferroelectrics **104** (1990) 217.

[4] E. R. Camargo, J. Frantti and M. Kakihana, J. Mater. Chem. **11** (2001) 1875.

[5] Y. Yoshikawa and K. Tsuzuki, J. Am. Ceram. Soc. **75** (1992) 2520.

[6] M. Cerqueira, R. S. Nasar, E. R. Leite, E. Longo and J. A. Varela, Mater. Lett. **35** (1998) 166.

[7] E. E. Oren, E. Taspinar, A. C. Tas, J. Am. Ceram. Soc. **80** (1997) 2714.

[8] S. Kim, M. Jun and S. Hwang, J. Am. Ceram. Soc. **82** (1999) 289.

[9] J. Tartaj, C. Moure, L. Lascano and P. Durán, Mater. Res. Bull. 36 (2001) 2301.

[10] J. B. Blum and S. R. Gurkovich, J. Mater. Sci. **20** (1985) 4479.

[11] D. M. Ibrahim and H. W. Hennicke, Trans. J. Br. Ceram. Soc. **80** (1981) 18.

[12] S. Sato, T. Murakata, H. Yanagi and F. Miyasaka, J. Mater. Sci. **29** (1994) 5657.

[13] J. Moon, T. Li, C. A. Randall and J. H. Adair, J. Mater. Res. **12** (1997) 189.

[14] C. R. Peterson and E. B. Slamovich, J. Am. Ceram. Soc. **82** (1999) 1702.

[15] A. Wu, P. M. Vilarinho, I. M. Miranda Salvado and J. L. Baptista, J. Am. Ceram. Soc. **83** (2000) 1379.

[16] B. G. Muralidharan, A. Sengupta, G. S. Rao and D. C. Agrawal, J. Mater. Sci. **30** (1995) 3231.

[17] R. Zimmermann-Chopin and S. Auer, J. Sol-Gel Sci. Technol. **3** (1994) 101.

[18] D. R. Chen, X. L. Jiao and R. R. Xu, J. Mater. Sci. Lett. **17** (1998) 53.

[19] Y. Narenda and G. L. Messing, J. Am. Ceram. Soc. **80** (1997) 915.

[20] R. H. Arendt, J. H. Rosolowski and J. W. Szymaszek, Mater. Res. Bull. **14** (1979) 703.

[21] C. C. Chiu, C. C. Li and S. B. Desu, J. Am. Ceram. Soc. **74** (1991) 38.

[22] J. Z. Jiang, F. W. Poulsen and S. Mørup, J. Mater. Res. **14** (1999) 1343.

[23] L. B. Kong, J. Ma, W. Zhu and O. K. Tan, J. Alloys Comp. **335** (2002) 290.

[24] R. Janot and D. Guérard, J. Alloys Comp. **333** (2002) 302.

[25] M. Zdujić, Ć. Jovalekić, L. Karanović, M. Mitrić, D. Poleti and D. Skala, Mater. Sci. Eng. A **245** (1998) 109.

[26] M. Simoneau, G. L'Esperance, J. L. Trudeau and R. Schulz, J. Mater. Res. **9** (1994) 535.

[27] Z. Q. Jin, W. Tang, J. R. Zhang, H. Lin and Y. W. Du, J. Magn. Mater. **182** (1998) 231.

[28] S. Wang, J. Ding, Y. Shi and Y. J. Chen J Magn. Mater. **219** (2000) 206.

[29] D. J. Fatemi, V. G. Harris, V. M. Browning and J. P. Kirkland, J. Appl. Phys. **83** (1998) 6767.

[30] J. M. Xue, D. M. Wan, S. E. Lee and J. Wang, J. Am. Ceram. Soc. **82** (1999) 1687.

[31] L. B. Kong, W. Zhu and O. K. Tan, Mater. Lett. **42** (2000) 232.

[32] L. B. Kong, J. Ma, W. Zhu and O. K. Tan, J. Alloys Comp. **322** (2001) 290.

[33] J. Wang, J. M. Xue, D. M. Wan and B. K. Gan, J. Solid State Chem. **154** (2000) 321.

[34] X.S. Gao, J.M. Xue, J. Wang, T. Yu and Z.X. Shen, J. Am. Ceram. Soc. **85** (2002) 565.

[35] S. K. Ang, J. M. Xue and J. Wang, J Alloys Comp **343** (2002) 156.

[36] L. B. Kong, J. Ma, H. Huang and R. F. Zhang, Mater. Res. Bull. **37** (2002) 1085.

[37] L. B. Kong, J. Ma, H. Huang, R. F. Zhang and W. X. Que, J. Alloys Comp. **337** (2002) 226.

[38] L. B. Kong, J. Ma, W. Zhu and O. K. Tan, Mater. Lett. **51** (2001) 108.

[39] K. Shantha and K. B. R. Varma, J. Am. Ceram. Soc. **83** (2000) 1122.

[40] A. Castro, P. Millán, J. Ricote and L. Pardo, J. Mater. Chem. **10** (2000) 767.

[41] C. H. Lu and C. H. Wu, J. Eur. Ceram. Soc. **22** (2002) 707.

[42] M. A. Janney and H. D. Kimrey, J. Amer. Ceram. Soc. **74** (1991) 1675.

[43] C. C. Chou, H. Y. Chang, I. N. Lin, B. J. Shaw and J. T. Tan, Jap. J. Appl.Phys. **37** (1998) 5269.

[44] C. L. Li, M. B. Suresh and C. C. Chou, J. Phys. Chem. Solids. **69** (2008) 611.

[45] C. Dong, J. Appl. Cryst. **32** (1999) 838.

[46] P. Scherrer, Gottin Nachr. **2** (1918) 98.

[47] W. R. Buessem, L. E. Cross and A. K. Goswami, J. Am. Ceram. Soc. **49** (1966) 33.

[48] G. Arlt, D. Hennings and G. de With, J. Appl. Phys. **58** (1985) 1619.

[49] W. Känzig, Phys. Rev. **98** (1955) 549.

[50] K. Uchino, E. Sadanaga and T. Hirose, J. Am. Ceram. Soc. **72** (1989) 1555.

[51] S. K. S. Parashar, R. N. P. Choudhary and B. S. Murty, J. Appl. Phys. **94** (2003) 6091.

[52] S. K. S. Parashar, R. N. P. Choudhary and B. S. Murty, J. Appl. Phys. **98** (2005) 104305.

[53] W. D. Callister, *Materials Science and Engineering*: *An Introduction* (Wiley, India, 2006).

[54] T. Friessnegg, S. Aggarwal, R. Ramesh, B. Nielsen, E. H. Poindexter and D. J. Keeble, Appl. Phys. Lett. **77** (2000) 127.

[55] S. Sen, R. N. P. Choudhary and P. Pramanik, Phys. B **387** (2007) 56.

[56] R. Koduri and M. Lopez, Ferroelectric Lett. **34** (2007) 113.

[57] Z. Zhang and R. Raj, J. Am. Ceram. Soc. **78** (1995) 3363.

[58] S. Mahajan, O. P. Thakur, D. K. Bhattacharya and K. Sreenivas, J. Am. Ceram. Soc. **92** (2009) 416.

CHAPTER 7

Chapter 7

Inferences & Suggestions for Future Work

6.1 INFERENCES

In this chapter, a recapitulation of the main results obtained in the present work has been summarized and inferences have been drawn. Also, the perspectives for the future work have been put forth.

In the present work, a comprehensive study of the structural and electrical behavioural changes due to systematic substitution at the A-site (A_1 and A_2) of tungsten bronze structured $Ba_5RTi_3Nb_7O_{30}$ (R=Rare-Earth) compounds of BaO-R_2O_3-TiO_2-Nb_2O_5 quaternary system was undertaken.

Firstly, the processing condition, i.e., calcination and sintering temperatures and durations to synthesize $Ba_5SmTi_3Nb_7O_{30}$ compound was optimized. It was found that the optimized sintering condition to prepare $Ba_5SmTi_3Nb_7O_{30}$ compound is 1300 ºC for 10 hours. The synthesized $Ba_5SmTi_3Nb_7O_{30}$ compound at this optimum preparation condition has orthorhombic crystal structure at room temperature with average grain size of about 2 µm. The compound shows a diffuse type of ferroelectric-paraelectric phase transition exhibiting non-relaxor behaviour with a Curie temperature (T_c) of 170 ºC. The compound has negative temperature coefficient of resistance (NTCR) behaviour. The remanent polarization ($2P_r$) value of the sample prepared at the optimum sintering condition is found to be 2.3 µC/cm^2. Maximum pyroelectric

coefficient (P_T) of the compound is found to be 57.1 $nCcm^{-2}{}^{o}C^{-1}$ and piezoelectric coefficient (d_{33} value) is found to be 8 pC/N at the optimized sintering condition.

Substitution of calcium at the barium site in $Ba_5SmTi_3Nb_7O_{30}$ compound i.e. $Ba_{5-x}Ca_xSmTi_3Nb_7O_{30}$ (x = 0-5) prepared at the optimized sintering condition is observed to effect the structural and electrical properties. The X-ray diffractograms show that single phase is maintained for x = 1 beyond which increasing presence of $Ca_3Nb_2Ti_3O_{14}$ as secondary phase is observed. The crystal structural distortion parameters, namely, orthorhombicity decreases and tetragonality increases with calcium substitution. Scanning electron micrographs reveal that calcium addition increases the average grain size and changes the shape of the grains from oval to rod like structure. Dielectric constant is observed to decrease with increase in calcium concentration. The compounds exhibit non-relaxor type ferroelectric-paraelectric diffuse phase transition with least diffusivity in x = 1 composition while for x = 5 the phase transition is not observed. Negative temperature coefficient of resistance (NTCR) behaviour is maintained even after addition of calcium. Remanent polarization ($2P_r$) value is observed to increase on calcium substitution for the specimen with x = 1.

The ionic radii of the rare-earths is observed to have profound effect on the structural, dielectric, ferroelectric, piezoelectric, pyroelectric and conductivity properties of $Ba_5RTi_3Nb_7O_{30}$ (R=Rare-Earth) and $CaBa_4RTi_3Nb_7O_{30}$ compounds. Lattice parameters and unit cell volume decrease with decrease in the ionic radii of the rare-earths. Average grain size increases with the decrease in the ionic radii of the rare-earths. All compounds exhibit non-relaxor type ferroelectric-paraelectric diffuse phase transition with increasing diffusivity as ionic radii of the rare-earths

decreases except in La-containing compounds (i.e. $Ba_5LaTi_3Nb_7O_{30}$ and $CaBa_4RTi_3Nb_7O_{30}$) where the nature of the compounds is observed to be relaxor. Dielectric constant decreases while Curie temperature increases with decrease in the ionic radii of the rare-earths. Conductivity of the specimen increases with the decrease in the ionic radii of the rare-earths. Remanent polarization ($2P_r$) value increases with the decrease in the ionic radii of the rare - earths. However, its value is higher in calcium containing compounds as compared to calcium free compounds. Decrease in the ionic radii of the rare-earths results in increase in the pyroelectric (P_T) and piezoelectric (d_{33} value) coefficients.

Mechanical activation process (i.e., high-energy ball milling) has successfully been used to synthesize nanocrystalline $Ba_5SmTi_3Nb_7O_{30}$ ferroelectric ceramics. This process skips the high energy consuming calcination step, making the preparation process simpler than the conventional technique. Dielectric, ferroelectric, piezoelectric and pyroelectric properties have been observed to improve in $Ba_5SmTi_3Nb_7O_{30}$ compound prepared by mechanical activation process at the optimized condition compared to the conventional solid-state reaction process revealing the superiority of this process over the conventional solid-state reaction method.

Microwave sintering results in the formation of phase and microstructures in short sintering time compared to the conventional sintering. However, $Ba_5SmTi_3Nb_7O_{30}$ sample sintered by microwave has lower dielectric constant, higher diffusivity, higher dielectric loss, higher conductivity, lower remanent polarization ($2P_r$), lower pyroelectric coefficient (P_T) compared to the conventionally sintered sample.

6.2 SCOPE FOR FURTHER STUDIES

As tungsten-bronze compounds are known to have good electro-optic coefficients [1-4], so electro-optic studies can be taken up in the $Ba_5RTi_3Nb_7O_{30}$ (R=Rare-Earth) compounds of $BaO\text{-}R_2O_3\text{-}TiO_2\text{-}Nb_2O_5$ quaternary system.

As mechanical activation process successfully synthesize nanocrystalline $Ba_5SmTi_3Nb_7O_{30}$ compound which enhances its structural and electrical properties as compared to the conventional solid-state reaction method, all other $Ba_5RTi_3Nb_7O_{30}$ (R=Rare-Earth) compounds of $BaO\text{-}R_2O_3\text{-}TiO_2\text{-}Nb_2O_5$ quaternary system can be prepared by this novel technique and their properties can be investigated.

Preparation of thin films can be taken up to understand the influence on electrical properties at such scales. This would help further, in undertaking commercialization of the studied compositions.

REFERENCES

[1] Y. Xu, C. J. Chen, R. Xu and J. D. Mackenzie, Phy. Rev. B **44** (1991) 35.

[2] R. R. Neurgaonkar and W. K. Cory, J. Opt. Soc. Amer. **3** (1986) 274.

[3] T. Yamazawa, T. Honma, H. Suematsu and T. Komatsu, J. Am. Ceram. Soc. **92** (2009) 2924.

[4] K. S. Rao and K. H. Yoon, J. Mater. Sci. **38** (2003) 391.

REPRINTS OF PUBLICATIONS

Journal of Alloys and Compounds 484 (2009) 40–44

Contents lists available at ScienceDirect

Journal of Alloys and Compounds

journal homepage: www.elsevier.com/locate/jallcom

Investigations of dielectric, pyroelectric and electrical properties of $Ba_5SmTi_3Nb_7O_{30}$ ferroelectric ceramic

Prasun Ganguly, A.K. Jha*, K.L. Deori

Thin Film & Materials Science Laboratory, Department of Applied Physics, Delhi College of Engineering (Faculty of Technology, University of Delhi), Bawana Road, Samaypur, Delhi 110042, India

ARTICLE INFO

Article history:
Received 26 February 2009
Received in revised form 7 May 2009
Accepted 10 May 2009
Available online 18 May 2009

Keywords:
Ceramics
Ferroelectrics
Solid-state reaction
X-ray diffraction
Dielectric response
Electrical properties

ABSTRACT

The polycrystalline sample of $Ba_5SmTi_3Nb_7O_{30}$ specimen was prepared by high-temperature solid-state reaction method and studied for their dielectric and electrical properties. X-ray diffraction (XRD) analysis reveals the formation of single-phase compound having orthorhombic crystal structure at room temperature. Microstructural analysis by scanning electron microscope (SEM) shows that the compound has well-defined grains, which are distributed uniformly throughout the sample. Detailed dielectric properties of the compound as a function of frequency and temperature show that the compound undergoes non-relaxor kind of ferroelectric–paraelectric phase transition of diffuse nature. Ferroelectric and pyroelectric studies of the compound have been discussed in this paper. The temperature dependence of ac and dc conductivity of the compound has been investigated. The conductivity study over a wide temperature range suggests that the compound has negative temperature coefficient of resistance (NTCR) behaviour.

1. Introduction

Since the discovery of ferroelectricity in Rochelle salt [1], efforts have been made continuously to find new ferroelectric materials. These efforts led to the discovery of large number of ferroelectric compounds. In the process, a large number of ferroelectric oxides of the perovskite family [2–5] and the tungsten–bronze (TB)-type structure [6–8] have been found. Some niobates with TB-type structure, such as barium sodium niobates [9], potassium lanthanum niobates [10] are considered to be interesting and more attractive because of their wide industrial applications. The TB-type structure consists of a complex array of distorted BO_6 octahedral sharing corners in such a way that three different types of interstices (A, B and C) are available for cation occupation in the general formula $[(A_1)_4(A_2)_2(C)_4][(B_1)_2(B_2)_8]O_{30}$, where A_1 and A_2 sites are usually filled by divalent or trivalent cations, B_1 and B_2 sites by tetravalent or pentavalent cations and C site being small, often remains empty giving the general formula $A_6B_{10}O_{30}$ for the tungsten–bronze structure [11]. Therefore, they provide various options for studying properties such as ferroelectric, pyroelectric, piezoelectric by cation substitution at different sites [12–18]. Recently, it has been found that rare-earth based $Ba_5RTi_3Nb_7O_{30}$ (R = Nd, Eu, Gd, Dy, Sm) compounds show diffuse phase transition with transition temperature above the room temperature [19,20]. In this class of materials, it is known that the processing conditions can change the symmetry of the compound [21]. These compounds are characterized by low activation energy and negative temperature coefficient of resistance [20,22]. Extensive literature survey reveals that comprehensive studies on $Ba_5SmTi_3Nb_7O_{30}$ compound are yet to be carried out. Impedance studies of this compound have been performed and reported elsewhere [23]. In this paper, structural, dielectric, ferroelectric, pyroelectric and conductivity studies of $Ba_5SmTi_3Nb_7O_{30}$ are reported.

2. Experimental

The polycrystalline sample of $Ba_5SmTi_3Nb_7O_{30}$ (BSTN) was prepared by solid-state reaction technique by taking high purity $BaCO_3$, TiO_2, Nb_2O_5 (all from M/s Aldrich, USA) and Sm_2O_3 (M/s Alfa Aesar, USA) in their stoichiometric proportions. The materials were thoroughly ground in an agate mortar and passed through sieve of extremely fine mesh size.

This powder mixture was then calcined at 1100 °C for 20 h in an alumina crucible. The calcined mixture was ground, passed through the sieve again. The mixture was then admixed with 5 wt.% polyvinyl alcohol (M/s Aldrich, USA) as a binder and pressed at ~300 MPa into disk shaped pellets of 15 mm diameter and 1.2 mm thickness. These pellets were then sintered at 1300 °C for 10 h. This is the optimized sintering condition found from the extensive studies reported elsewhere [24]. Also, this process yields a homogeneous specimen and the detail is reported elsewhere [23].

X-ray diffractogram of the sintered pellet was recorded using Philips (X'Pert Model) diffractometer in the range $10° \leq 2\theta \leq 70°$ with CuK_α radiation (λ = 1.5405 Å). The granular morphology of the sample was investigated using scanning electron microscope (Jeol, JSM – 840), operated at 20 kV. The sintered pellets were polished to a thickness of ~1 mm and coated with silver paste on both sides to act as elec-

* Corresponding author. Tel.: +91 9868242150; fax: +91 1127871023.
E-mail address: dr_jha_ak@yahoo.co.in (A.K. Jha).

0925-8388/$ – see front matter © 2009 Elsevier B.V. All rights reserved.
doi:10.1016/j.jallcom.2009.05.034

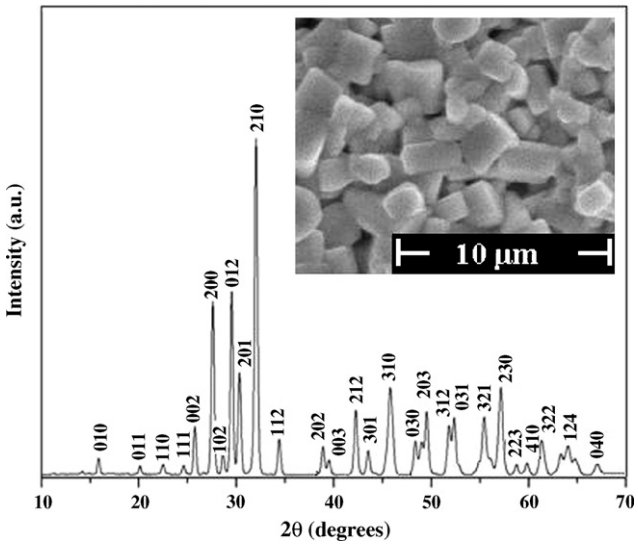

Fig. 1. X-ray diffraction pattern and SEM micrograph (inset) of $Ba_5SmTi_3Nb_7O_{30}$ compound.

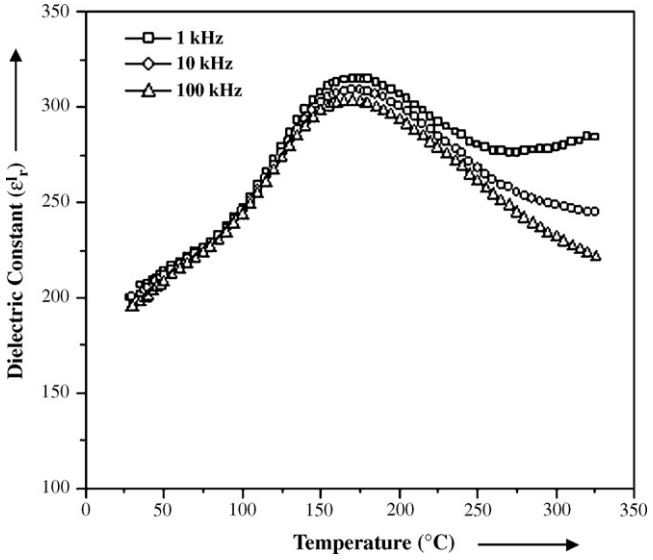

Fig. 2. Variation of dielectric constant (ε'_r) with temperature at 1 kHz, 10 kHz, and 100 kHz frequencies.

trodes and cured at 325 °C for 1 h. The dielectric measurements were carried out using HP 4284A LCR meter operating at oscillation amplitude of 1 V. The *P–E* hysteresis measurement was done at room temperature with ferroelectric tester (model Premier Precision II of Radiant Technologies). The measurement of the pyroelectric coefficient was performed using the Byer–Roundy technique [25]. The sample was first poled at 10 kV/cm at an elevated temperature (~100 °C) for 2 h in silicon oil. The poled sample was then placed in a programmable furnace, and the temperature was increased at a rate of 2 °C/min. The current generated in the specimen was measured using a high precision electrometer (Keithley 6517A). The dc electrical resistivity of the sample was measured from room temperature to 200 °C at constant electric field (60 V/cm), using a Keithley 6517A programmable electrometer.

3. Results and discussion

3.1. XRD and SEM analysis

Room temperature X-ray diffraction pattern of $Ba_5SmTi_3Nb_7O_{30}$ (BSTN) is shown in Fig. 1, which reveals the formation of single-phase compound. The lattice parameters were calculated using the observed interplanar spacing, *d*-values, obtained from the diffractogram and refined using the least square refinement method by a computer program package PowderX [26]. These refined lattice parameters are: $a = 6.4106$ Å, $b = 5.5595$ Å, and $c = 6.8112$ Å. The peaks were indexed using the observed *d*-values and the calculated lattice parameters. From these, it is found that BSTN has an orthorhombic TB-type structure. The SEM micrograph of the sample is shown in Fig. 1 (inset). Well-defined grains are seen to be homogeneously distributed throughout the sample. The average grain size of the compound is ~2 μm.

3.2. Dielectric properties

The dielectric constant (ε'_r) and dielectric loss ($\tan\delta$) of the specimen were measured from room temperature to 325 °C at different frequencies, namely, 1 kHz, 10 kHz, and 100 kHz. Fig. 2 shows the variation of dielectric constant with temperature at various frequencies. It is seen that the compound has a dielectric anomaly at 170 °C (which is the Curie temperature T_c) indicating the occurrence of ferroelectric–paraelectric phase transition. The compound has the same T_c at all these frequencies, suggesting that the compound does not have any relaxor behaviour [27]. The broad dielectric peaks (Fig. 2) indicate the diffuse nature of the phase transition. The diffusivity constant (γ) has been calculated using the formula [28]:

$$\ln\left(\frac{1}{\varepsilon'_r} - \frac{1}{\varepsilon'_{r\,\max}}\right) = \gamma \ln(T - T_c) + \text{constant} \quad (1)$$

where $\varepsilon'_{r\,\max}$ is the maximum value of ε'_r at $T = T_c$. The value of γ has been calculated from the slope of $\ln(1/\varepsilon'_r - 1/\varepsilon'_{r\,\max})$ versus $\ln(T - T_c)$ curve (Fig. 3) and is given in Table 1. At all the frequencies, the value of γ is found to be between 1 (obeying Curie–Weiss law) and 2 (for completely disordered system) confirming the diffuse phase transition. The diffuse nature of the phase transition can be explained in terms of oxygen vacancies. It is known that these TB structured compounds loses oxygen during sintering at high temperature [29,30], which using Kröger and Vink notation [31] can be represented:

$$O_o \rightarrow \tfrac{1}{2}O_2 \uparrow + V_o^{\bullet\bullet} + 2e^-$$

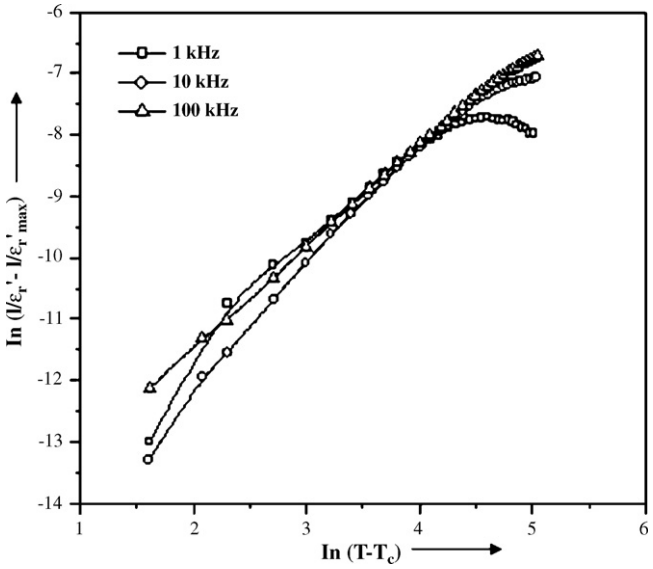

Fig. 3. Variation of $\ln(1/\varepsilon'_r - 1/\varepsilon'_{r\,\max})$ with $\ln(T - T_c)$ at 1 kHz, 10 kHz, and 100 kHz frequencies.

Table 1
Dielectric parameters and activation energy (ac conductivity) of $Ba_5SmTi_3Nb_7O_{30}$ compound.

Frequency (kHz)	$\varepsilon'_{r(R.T.)}$	$\varepsilon'_{r\max}$	Diffusivity (γ)	Activation energy, E_a (eV)	
				Ferroelectric phase	Paraelectric phase
1	206	315	1.28	0.38	0.95
10	201	309	1.59	0.35	0.57
100	193	303	1.71	0.28	0.40

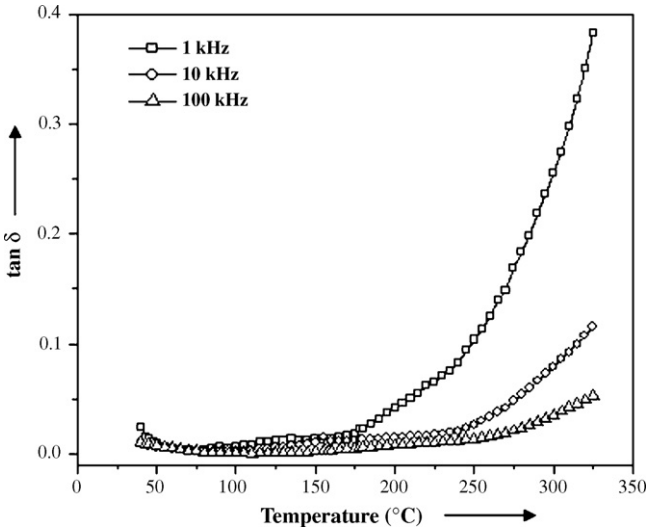

Fig. 4. Variation of dielectric loss ($\tan\delta$) with temperature at 1 kHz, 10 kHz, and 100 kHz frequencies.

where $V_o^{\bullet\bullet}$ denotes oxygen vacancies. The defects such as oxygen vacancies $V_o^{\bullet\bullet}$ induce disorderness in the system resulting in a diffuse type of ferroelectric–paraelectric phase transition [32].

Fig. 4 shows the variation of dielectric loss with temperature at selected frequencies. The variation of dielectric loss with temperature shows that the loss is almost constant at lower temperatures but at higher temperatures it increases sharply particularly at lower frequency. This sharp increase of dielectric loss in high temperature region may be attributed to the increased mobility of space charges arising from the defects or vacancies (like oxygen vacancies) in the sample [33].

Fig. 5 shows the variation of dielectric constant with frequency from 20 Hz to 500 kHz at room temperature. The dielectric constant decreases up to about 1 kHz and remains nearly constant beyond this frequency. The dielectric constant of a material has four polarization contributions: electronic, ionic, dipolar and space charge [34]. Response frequencies for ionic and electronic polarizations are $\sim 10^{13}$ Hz and 10^{16} Hz, respectively; and at frequencies beyond 1 kHz, contribution from space charge polarization is not expected [34]. Thus, the higher values of dielectric constant at lower frequencies can be attributed to the presence of defects such as oxygen vacancies, $V_o^{\bullet\bullet}$. These vacancies act as space charge which plays an important role in the polarization at lower frequencies [35,36]. Moreover, at lower frequencies, the dipoles can follow the field resulting in higher values of dielectric constant while at higher frequencies, the dipoles are unable to follow the rapidly changing field leading to the reduction in the values of dielectric constant.

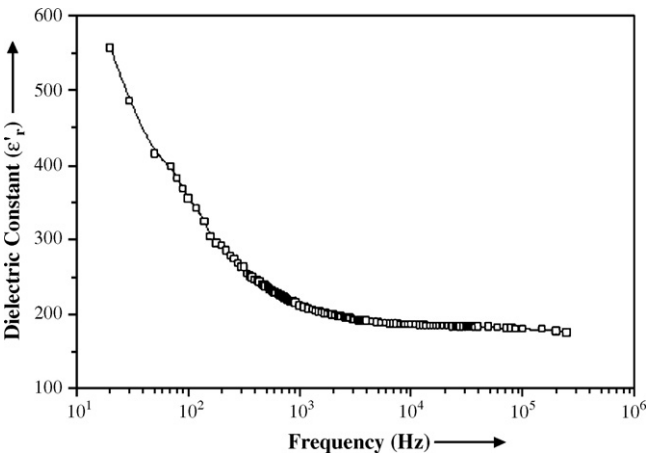

Fig. 5. Variation of dielectric constant (ε'_r) with frequency at room temperature.

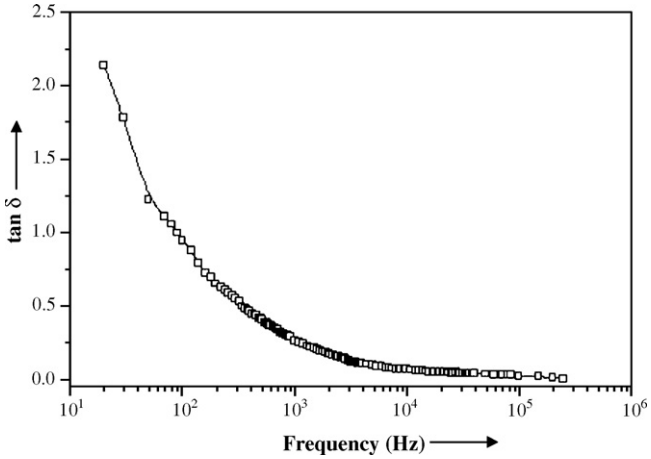

Fig. 6. Variation of dielectric loss ($\tan\delta$) with frequency at room temperature.

The variation of dielectric loss with frequency at room temperature is shown in Fig. 6. It also decreases sharply up to 1 kHz and beyond this it is nearly independent of frequency. As mentioned earlier, the higher values of dielectric loss at lower frequencies can also be understood in terms of oxygen vacancies that act as space charges and are dominant at lower frequencies [35,36].

3.3. Ferroelectric studies

To confirm the ferroelectric nature of the studied compound, *P–E* hysteresis loop was recorded at room temperature at a frequency of 50 Hz and is shown in Fig. 7. The remanent polarization (P_r) value is found to be 0.14 μC/cm^2 and the coercive field (E_c) is 5.02 kV/cm. It is well known that the polarization switching behaviour of ferroelectrics is strongly influenced by defects like oxygen vacancies [37]. These vacancies assemble near domain walls and the polarization reversal of these domains is suppressed due to "pinning" by these defects near the domain boundaries resulting in a smaller remanent polarization value [38].

3.4. Pyroelectric studies

The temperature variation of pyroelectric coefficient is shown in Fig. 8. The pyroelectric coefficient (P_T) was calculated using the

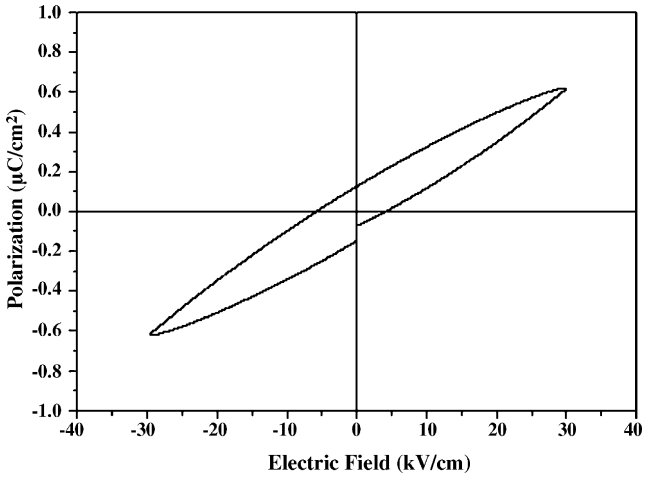

Fig. 7. *P–E* hysteresis loop at room temperature.

relation [39]:

$$P_T = \frac{P_I}{A(dT/dt)} \tag{2}$$

where P_I is the pyroelectric current, A is the area of the conducting surface of the sample and dT/dt is the rate of change of temperature. The pyroelectric current as well as pyroelectric coefficient passes through a peak at a temperature (98 °C) lower than the ferroelectric transition temperature (T_c). The maximum pyroelectric coefficient at this temperature is found to be 57.1 nC cm^{-2} °C^{-1}. The pyroelectric current is generated due to the change in spontaneous polarization with temperature. It is known that in diffuse phase transition, the rate of change of spontaneous polarization with temperature is maximum at a temperature below T_c [40], which is confirmed in the present work.

3.5. AC and DC conductivity

The total conductivity (σ_{tot}) of the material comprises the ac conductivity (σ_{ac}) and the dc conductivity (σ_{dc}):

$$\sigma_{tot} = \sigma_{ac}(\omega) + \sigma_{dc} \tag{3}$$

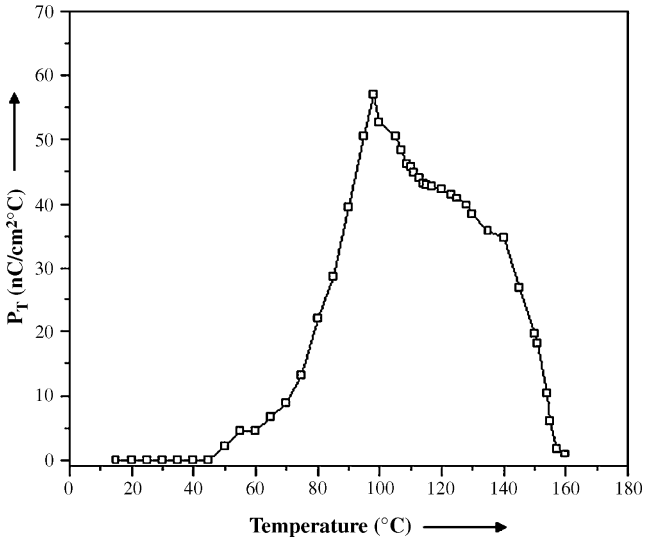

Fig. 8. Variation of pyroelectric coefficient (P_T) with temperature.

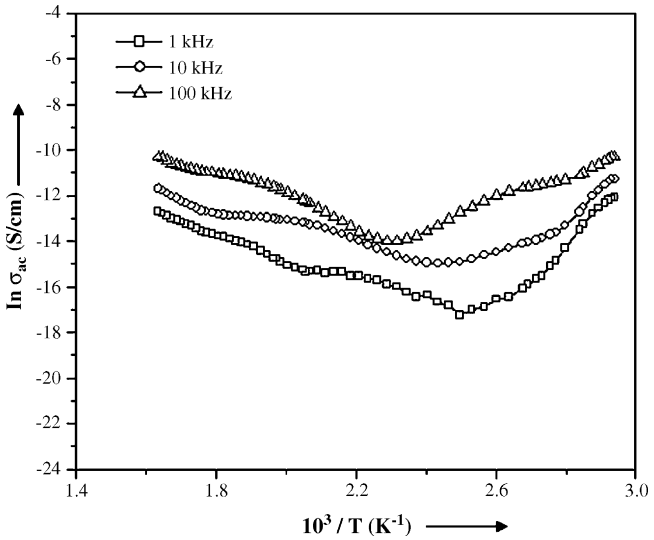

Fig. 9. Variation of ac conductivity with temperature at 1 kHz, 10 kHz, and 100 kHz frequencies.

The ac conductivity (σ_{ac}) and activation energy (E_a) of the sample have been calculated using the relation [41]:

$$\sigma_{ac} = \omega\varepsilon_r'\varepsilon_o \tan\delta = \sigma_o \exp\left(\frac{-E_a}{k_B T}\right) \tag{4}$$

where ω is the angular frequency, ε_o is the free space permittivity and k_B is the Boltzmann constant. The variation of ac conductivity as a function of temperature at 1 kHz, 10 kHz, and 100 kHz is shown in Fig. 9. The change in slope occurring near T_c can be attributed to the difference in activation energy in the paraelectric and ferroelectric phases. The activation energy, evaluated in the ferroelectric phase (low temperature) and paraelectric phase (high temperature) is summarized in Table 1.

Fig. 10 shows the variation of dc conductivity ($\sigma_{dc} = 1/\rho$) with absolute temperature (i.e. $\ln\sigma_{dc}$ vs. $10^3/T$). It is seen from the figure that at low temperatures the conductivity is constant. But at higher temperatures, it increases with temperature confirming that the compound has negative temperature coefficient of resistance (NTCR) behaviour, a typical characteristic of dielectric materials [42].

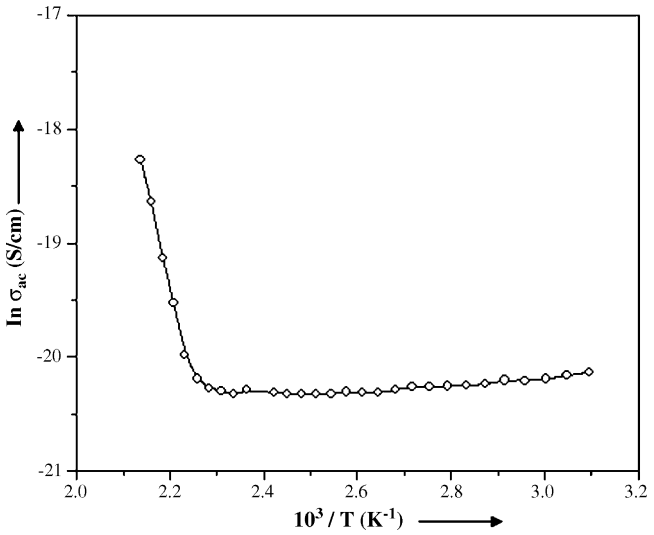

Fig. 10. Variation of dc conductivity with temperature.

4. Conclusion

The synthesized $Ba_5SmTi_3Nb_7O_{30}$ compound is in single phase having an orthorhombic tungsten–bronze crystal structure with an average grain size of about 2 μm, homogeneously distributed throughout the sample. The compound shows a diffuse type of ferroelectric–paraelectric phase transition exhibiting non-relaxor behaviour with a T_c of 170 °C. The *P*–*E* hysteresis loop at room temperature and the pyroelectric coefficients observed at different temperatures confirm the ferroelectric nature of the compound. Pyroelectric coefficient exhibits a peak at a temperature well below the T_c. The compound shows negative temperature coefficient of resistance (NTCR) behaviour.

Acknowledgment

One of the authors (PG) is grateful to Council of Scientific and Industrial Research (CSIR), New Delhi, India for the award of Senior Research Fellowship.

References

[1] J. Valasek, Phys. Rev. 17 (1921) 475–481.
[2] E.C. Subbarao, Ferroelectrics 5 (1973) 267–280.
[3] C.G.F. Stenger, A.J. Burggraaf, J. Phys. Chem. Solids 41 (1980) 17–23.
[4] V. Shrivastava, A.K. Jha, R.G. Mendiratta, Solid State Commun. 133 (2005) 125–129.
[5] I. Coondoo, A.K. Jha, S.K. Agarwal, J. Eur. Ceram. Soc. 27 (2007) 253–260.
[6] M.H. Fremcombe, Acta Crystallogr. 13 (1960) 131–140.
[7] W.L. Zhong, P.L. Zhang, H.C. Chen, F.S. Chen, Y.Y. Song, Ferroelectrics 74 (1987) 325–329.
[8] K.S. Singh, R. Sati, R.N.P. Choudhary, J. Mater. Sci. Lett. 11 (1992) 788–790.
[9] J.J. Rubin, L.G. Van Uitert, H.J. Leninstein, J. Cryst. Growth 1 (1967) 315–317.
[10] L.G. Van Uitert, S. Singh, H.J. Levinstein, J.E. Gensic, W.A. Bonner, Appl. Phys. Lett. 11 (1967) 161–162.
[11] P.B. Jasmieson, S.C. Abrahams, J.L. Bernstein, J. Chem. Phys. 48 (1965) 5048–5057.
[12] R.R. Neurgaonkar, W.F. Hall, J.R. Oliver, W.W. Ho, W.K. Cory, Ferroelectrics 87 (1998) 167–179.
[13] R.R. Neurgaonkar, J.G. Nelson, J.R. Oliver, L.E. Cross, Mater. Res. Bull. 25 (1990) 959–970.
[14] R.R. Neurgaonkar, J.G. Nelson, J.R. Oliver, Mater. Res. Bull. 27 (1992) 677–684.
[15] N. Wakiya, J.K. Wang, A. Saiki, K. Shinozaki, N. Mizutani, J. Eur. Ceram. Soc. 19 (1999) 1071–1075.
[16] Z.X. Cheng, S.J. Zhang, G.Y. Zhou, J.H. Liu, J.R. Han, H.C. Chen, Mater. Res. Bull. 35 (2000) 1107–1112.
[17] Y.K. Hwang, Y.U. Kwon, Mater. Res. Bull. 32 (1997) 1495–1502.
[18] B. Tribotte, J.M. Haussonne, G. Desgardin, J. Eur. Ceram. Soc. 19 (1999) 1105–1109.
[19] R.N.P. Choudhary, S.R. Shannigrahi, A.K. Singh, Bull. Mater. Sci. 22 (1999) 975–979.
[20] S.R. Shannigrahi, R.N.P. Choudhary, A. Kumar, H.N. Acharya, J. Phys. Chem. Solids 59 (1998) 737–742.
[21] X.H. Zheng, X.M. Chen, Solid State Commun. 125 (2003) 449–454.
[22] A. Panigrahi, R.N.P. Choudhary, B.N. Das, Indian J. Phys. 74A (2000) 147–149.
[23] P. Ganguly, A.K. Jha, K.L. Deori, Solid State Commun. 146 (2008) 472–477.
[24] P. Ganguly, A.K. Jha, K.L. Deori, J. Electroceram. 22 (2009) 257–262.
[25] C.B. Roundy, R.L. Byer, J. Appl. Phys. 44 (1973) 929–931.
[26] C. Dong, J. Appl. Cryst. 32 (1999) 838–1838.
[27] P.R. Das, R.N.P. Choudhary, B.K. Samantray, J. Alloys Compd. 448 (2008) 32–37.
[28] S.M. Pilgrim, A.E. Sutherland, S.R. Winzer, J. Am. Ceram. Soc. 73 (1990) 3122–3125.
[29] C.K. Suman, K. Prasad, R.N.P. Choudhary, J. Mater. Sci. 41 (2006) 369–375.
[30] C.K. Suman, K. Prasad, R.N.P. Choudhary, Mater. Chem. Phys. 82 (2003) 140–144.
[31] F.A. Kröger, H.J. Vink, Solid State Phys. 3 (1956) 307–335.
[32] V. Raghavan, Materials Science and Engineering, Prentice-Hall of India, New Delhi, 2004.
[33] T. Friessnegg, S. Aggarwal, R. Ramesh, B. Nielsen, E.H. Poindexter, D.J. Keeble, Appl. Phys. Lett. 77 (2000) 127–129.
[34] R.C. Buchanan, Ceramic Materials for Electronics: Processing, Properties and Applications, Marcel Dekker Inc., New York, 1991.
[35] Y. Noguchi, M. Miyayama, Appl. Phys. Lett. 78 (2001) 1903–1905.
[36] A. Chen, Y. Zhi, L.E. Cross, Phys. Rev. B 62 (2000) 228–236.
[37] W.L. Warren, D. Dimos, B.A. Tuttle, D.M. Smyth, J. Am. Ceram. Soc. 77 (1994) 2753–2757.
[38] Y. Noguchi, M. Miyayama, K. Oikawa, T. Kamiyama, M. Osada, M. Kakihana, Jpn. J. Appl. Phys. 41 (2002) 7062–7075.
[39] S.B. Lang, Source Book of Pyroelectricity, Gordan and Breach Science Publishers, New York, 1974.
[40] K. Uchino, Ferroelectric Devices, Marcel Dekker Inc., New York, 2000.
[41] W.D. Kingery, Introduction to Ceramics, Wiley, New York, 1960.
[42] V. Shrivastava, A.K. Jha, R.G. Mendiratta, Physica B 371 (2006) 337–342.

Solid State Communications 146 (2008) 472–477

Contents lists available at ScienceDirect

Solid State Communications

journal homepage: www.elsevier.com/locate/ssc

Complex impedance studies of tungsten–bronze structured $Ba_5SmTi_3Nb_7O_{30}$ ferroelectric ceramics

Prasun Ganguly, A.K. Jha *, K.L. Deori

Thin Film & Materials Science Laboratory, Department of Applied Physics, Delhi College of Engineering, Delhi – 110042, India

ARTICLE INFO

Article history:
Received 20 December 2007
Received in revised form
29 February 2008
Accepted 4 April 2008 by P. Chaddah
Available online 8 April 2008

PACS:
77.22.Gm
77.84.-s

Keywords:
A. Ferroelectrics
C. Complex impedance analysis
C. Grain boundaries
D. Dielectric response

ABSTRACT

This paper reports complex impedance analysis of polycrystalline tungsten–bronze structured $Ba_5SmTi_3Nb_7O_{30}$ prepared by a solid-state reaction method. X-ray diffractogram analysis reveals the formation of the compound in an orthorhombic crystal system. Scanning electron microscopy has been used to investigate the grain morphology of the material. Variation of dielectric constant (ε_r') with temperature at different frequencies shows that the compound has a dielectric anomaly of ferroelectric to paraelectric type at 170 °C, and exhibits diffuse phase transition. Impedance plots have been used as a tool to analyse the electrical characteristics of the sample as a function of frequency and temperature. Bulk resistance is observed to decrease with an increase in temperature, showing a typical negative temperature coefficient of resistance (NTCR) type behaviour. Nyquist or Cole–Cole plots show the existence of both grain and grain boundary effects only at a high temperature (375 °C). Relaxation time is found to decrease with a rise in temperature and it obeys the Arrhenius relationship. The corresponding activation energy is found to be about 0.95 eV. Variation of dc conductivity as a function of temperature has also been studied.

1. Introduction

Ferroelectric materials have received considerable attention of researchers owing to their wide industrial applications, such as multi-layer capacitors, transducers, actuators, ferroelectric random access memory, pyroelectric sensors, etc. Among various ferroelectric materials of different structural groups (e.g. perovskite, tungsten–bronze, spinel, pyrochlore [1–7]), rare-earth based compounds of tungsten–bronze (TB) family such as $Ba_5RTi_3Nb_7O_{30}$ (R = Dy, Sm, Nd, Eu, Gd) [8,9], $Ba_4R_2Ti_4Nb_6O_{30}$ (R = Y, Sm, Dy) [10], $Ba_2Na_3RNb_{10}O_{30}$ (R = La, Y, Gd, Eu, Dy) [11], $Ba_5Nd(Ti, Zr)Nb_7O_{30}$ [12], $Pb_2Bi_3DyTi_5O_{18}$ [13], etc. have attracted attention because of their interesting ferroelectric, pyroelectric, piezoelectric and nonlinear optical properties [14–20]. The crystal structure of this family is based on the framework of corner sharing distorted BO_6 octahedra in such a way that three different types of interstice (A, B and C) are available for cation occupation in the general formula $[(A_1)_4(A_2)_2(C)_4][(B_1)_2(B_2)_8]O_{30}$ [21]. In this formula, A_1 and A_2 sites are usually filled by divalent or trivalent cations, B_1 and B_2 sites by tetravalent or pentavalent cations and C site being small, often remains empty giving the general formula $A_6B_{10}O_{30}$ for the tungsten–bronze structure.

The structural, dielectric and ferroelectric properties of TB structured $Ba_5SmTi_3Nb_7O_{30}$ have been reported earlier [8,22,23]. However, hardly any report on electrical properties by means of complex impedance analysis, of this compound is available in the literature. The present paper summarizes the results of an extensive study made on the electrical properties of $Ba_5SmTi_3Nb_7O_{30}$ ceramics using Complex Impedance Spectroscopy (CIS).

2. Experimental

A polycrystalline sample of $Ba_5SmTi_3Nb_7O_{30}$ was prepared from high purity (>99%) $BaCO_3$, TiO_2, Nb_2O_5 (all from M/s Aldrich, USA) and Sm_2O_3 (M/s Alfa Aesar, USA) using a high-temperature solid-state reaction technique. These materials were taken in stoichiometric proportions, thoroughly ground in an agate mortar and then passed through sieve of appropriate size. The mixture was then calcined at 1100 °C for 20 h in an alumina crucible. The calcined mixture was ground and admixed with 4–5 wt% polyvinyl alcohol (PVA) as a binder and then pressed (300 MPa) into disk shaped pellet. The pellet was then sintered at 1300 °C for 10 h. This is the optimized sintering temperature found on making an extensive study and reported elsewhere [24].

An X-ray diffractogram of the sintered pellet was taken using a Philips (X'Pert Model) diffractometer in the range $10° \leq 2\theta \leq 70°$ using CuK_α radiation ($\lambda = 1.5405$ Å) with a scanning rate of 2°/min. A morphological study of the sample was carried out using a Scanning Electron Microscope (Jeol, JSM–840), operating

* Corresponding author. Tel.: +91 9868242150; fax: +91 11 27871023.
E-mail address: dr_jha_ak@yahoo.co.in (A.K. Jha).

0038-1098/$ – see front matter © 2008 Elsevier Ltd. All rights reserved.
doi:10.1016/j.ssc.2008.04.003

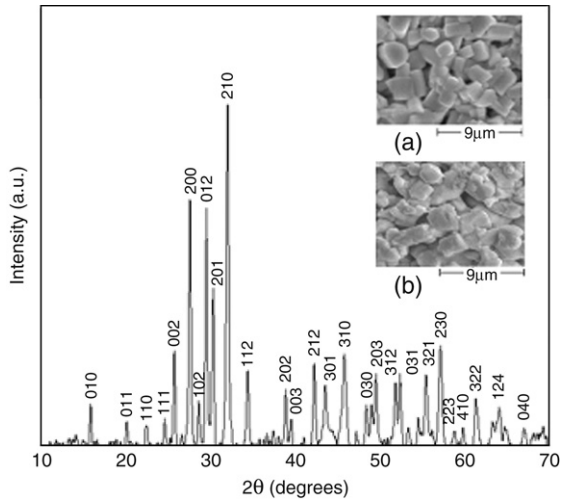

Fig. 1. X-ray diffraction pattern and SEM micrograph (inset) of (a) surface and (b) fractured $Ba_5SmTi_3Nb_7O_{30}$ compound.

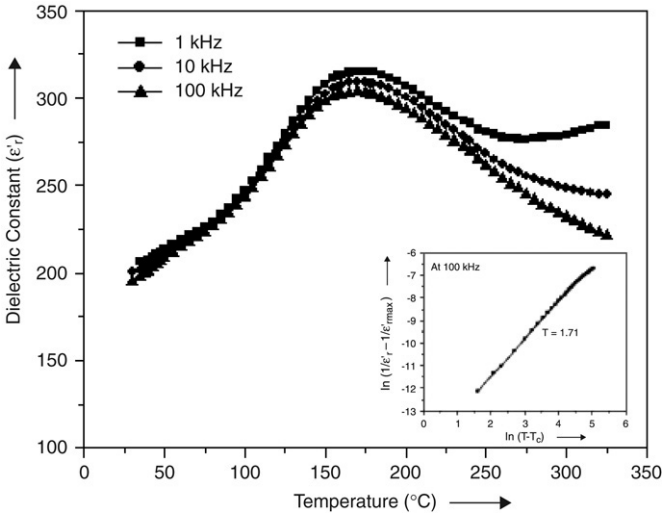

Fig. 2. Variation of dielectric constant (ε'_r) with temperature at 1 kHz, 10 kHz, 100 kHz frequencies and variation of $\ln(1/\varepsilon'_r - 1/\varepsilon'_{r\,\max})$ with $\ln(T - T_c)$ at 100 kHz (inset).

at 20 kV. The sintered pellet was polished and silver paste applied to both sides, then cured at 325 °C for 1 h. Dielectric and impedance measurements were carried out using an HP 4284A LCR meter operating at an oscillation amplitude of 1 V. Impedance measurements have been made in the temperature range of 300 °C to 375 °C at an interval of 25 °C and frequencies ranging from 20 Hz to 1 MHz.

3. Results and discussion

The room temperature X-Ray diffraction pattern of $Ba_5SmTi_3Nb_7O_{30}$ (BSTN) is shown in Fig. 1, which reveals the formation of a single-phase compound. Lattice parameters were calculated using the observed interplanar spacing d-values from the diffractograms and refined using the least square refinement method by a computer program package PowderX [25]. These refined lattice parameters are: $a = 6.4106$ Å, $b = 5.5595$ Å, $c = 6.8112$ Å. Peaks were indexed using the observed d-values and the calculated lattice parameters. From these, it is found that BSTN has an orthorhombic TB-type structure.

SEM micrographs of the surface and fractured sample are shown in Fig. 1 (inset). It can be seen from both micrographs that grains are homogeneously distributed throughout the sample. The average grain size of the compound is in the range of 2 μm.

The dielectric constant (ε'_r) of the specimen were measured from room temperature to 325 °C at frequencies of 1 kHz, 10 kHz and 100 kHz, as shown in Fig. 2. It is found that the compound has a dielectric anomaly at 170 °C indicating the occurrence of a ferroelectric–paraelectric phase transition. It is also observed that the compound has the same T_c for all the above frequencies, which suggests that the compound does not show any relaxor behaviour [26]. The dielectric peak is found to be broadened, indicating the existence of a diffuse phase transition. The diffusivity constant or degree of disorderness (γ) has been calculated using the formula [27]:

$$\ln(1/\varepsilon'_r - 1/\varepsilon'_{r\,\max}) = \gamma \ln(T - T_c) + \text{constant}. \quad (1)$$

The value of γ calculated from the slope of Fig. 2 (inset) is found to be 1.71 at 100 kHz. It is known that these TB structured compounds lose oxygen during sintering at high temperatures [28,29] which, using Kröger and Vink notation [30], can be represented:

$$O_O \rightarrow \frac{1}{2}O_2 \uparrow + V_O^{\bullet\bullet} + 2e^-$$

where $V_O^{\bullet\bullet}$ denotes oxygen vacancy. Defects such as oxygen vacancy $V_O^{\bullet\bullet}$ induce disorderness in the system [31] resulting in a diffuse type of ferro–paraelectric phase transition.

Complex impedance spectroscopy (CIS) have been used to study electrical properties of the compound. It is a useful nondestructive testing method for analyzing the electrical processes occurring in a compound on the application of a small ac signal as input perturbation. The resultant response (when plotted in a complex plane) appears in the form of a succession of semicircles representing contributions due to the bulk, grain boundaries and interfaces. A polycrystalline material usually shows both grain and grain boundary effects with different time constants leading to two successive semicircles [32]. Electrical properties of a material are often represented in terms of some complex parameters like complex impedance (Z^*), complex admittance (Y^*), complex modulus (M^*), complex permittivity (ε^*) and dielectric loss ($\tan\delta$). These frequency dependent parameters are related to each other by the following relations:

$$Z^*(\omega) = Z' - \mathrm{j}Z'' = R_s - \frac{\mathrm{j}}{\omega C_s} = \frac{1}{\mathrm{j}\omega C_0 \varepsilon^*} \quad (2)$$

$$Y^*(\omega) = Y' + \mathrm{j}Y'' = \frac{1}{R_p} + \mathrm{j}\omega C_p = \mathrm{j}\omega C_0 \varepsilon^* = \frac{1}{Z^*} \quad (3)$$

$$M^*(\omega) = M' + \mathrm{j}M'' = \frac{1}{\varepsilon^*} = \mathrm{j}\omega C_0 Z^* \quad (4)$$

$$\varepsilon^*(\omega) = \varepsilon' - \mathrm{j}\varepsilon'' \quad (5)$$

$$\tan\delta = \frac{Z'}{Z''} = \frac{Y'}{Y''} = \frac{M''}{M'} = \frac{\varepsilon''}{\varepsilon'} \quad (6)$$

where R_s and R_p are the series and parallel resistances respectively; C_s and C_p the series and parallel capacitances respectively; C_0 the geometrical capacitance; Z', Y', M', ε' and Z'', Y'', M'', ε'' denote the real and imaginary components of the impedance, admittance, modulus and permittivity respectively ($\mathrm{j} = \sqrt{-1}$).

Fig. 3 shows the variation of Z' with frequency at different measuring temperatures. It is observed that the value of Z' decreases with an increase of both frequency and temperature which indicates that conduction is increasing with rise in temperature and frequency. The coincidence of Z' values at higher frequencies at all temperatures indicates a possible release of space charge [33].

Fig. 4 shows the variation of Z'' with frequency at the above mentioned temperatures. Plots show that Z'' values attain a

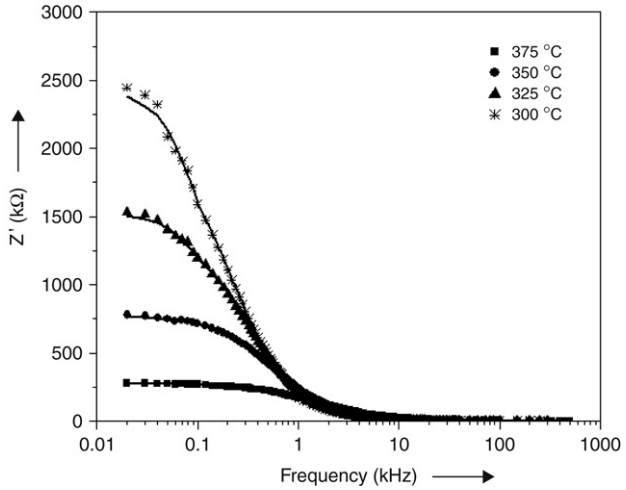

Fig. 3. Variation of the real part of impedance (Z') with frequency.

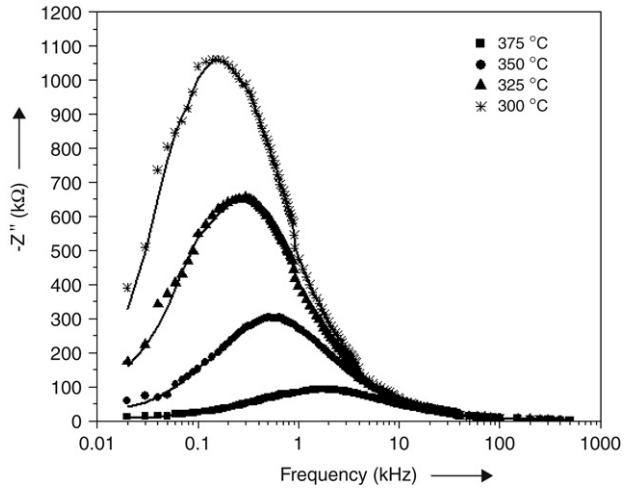

Fig. 4. Variation of the imaginary part of impedance (Z'') with frequency.

peak (Z''_{max}) at all measured temperatures. The magnitude of Z''_{max} decreases with temperature indicating an increasing loss in the resistive property of the sample. The value of Z''_{max}shifts to higher frequencies with increasing temperature. This indicates the occurrence of relaxation in the system [34]. Peak broadening with increase in temperature suggests the presence of temperature dependent electrical relaxation phenomenon in the material [35]. The relaxation process is due to the presence of immobile species at low temperature and defects/vacancies at higher temperatures.

Fig. 5 shows the normalized imaginary parts of impedance (Z''/Z''_{max}) as a function of frequency at the selected temperatures. The curve shows a peak with a slight asymmetric broadening at each temperature especially at higher temperatures. Asymmetric broadening of the peaks suggests the presence of electrical processes in the material with a spread of relaxation time [28].

Fig. 6 shows the plot of Z' versus Z'' (Nyquist or Cole–Cole plots) taken over a wide frequency range (20 Hz to 1 MHz) at different temperatures (300 °C, 325 °C, 350 °C and 375 °C). This range of temperature and frequency was selected as semicircles are formed in the Nyquist plots. All the semicircles exhibit some depression instead of a semicircle centered on the x-axis. Such behaviour is indicative of non-Debye type of relaxation and it also manifests that there is a distribution of relaxation time instead of a single relaxation time in the material [36]. The value of bulk resistance (R_b) at different temperatures has been obtained from the intercept of the semicircular arcs on the real axis (Z').

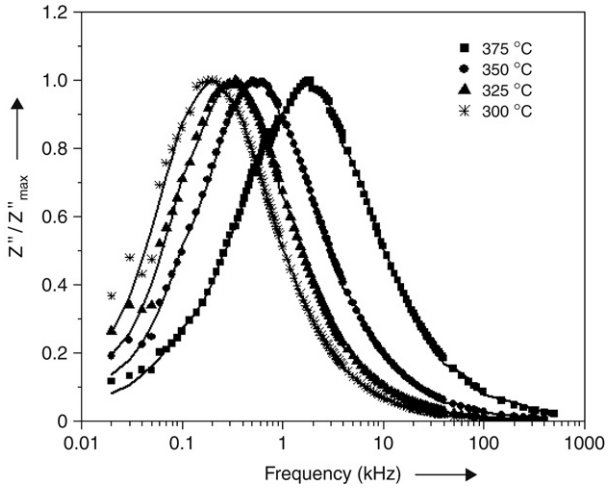

Fig. 5. Normalized imaginary part of impedance (Z''/Z''_{max}) as a function of frequency.

Table 1
Bulk resistance (R_b), bulk capacitance (C_b), grain boundary resistance (R_{gb}), grain boundary capacitance (C_{gb}) of BSTN compound

Temperature (°C)	R_b (kΩ)	C_b (nF)	R_{gb} (kΩ)	C_{gb} (nF)
300	2590	0.31	–	–
325	1610	0.30	–	–
350	800	0.38	–	–
375	240	0.35	285	0.61

It is observed (also given in Table 1) that R_b decreases with a rise in temperature. This manifests a negative temperature coefficient of resistance (NTCR) behaviour, a typical characteristic of dielectric materials [37,38]. However, the presence of two semicircles at higher temperature (375 °C) exhibits the presence of both grain (bulk property) and grain boundary effects. The high frequency semicircle corresponds to a bulk contribution, and the low frequency semicircle corresponds to a grain boundary effect [32]. The second intercept of each semicircle on real (Z')-axis gives the respective value of resistance (e.g. R_b and R_{gb}). The semicircles in the impedance spectrum have a characteristic peak occurring at a unique relaxation frequency ($\omega_r = 2\pi f_r$). It can be expressed as: $\omega_r RC = \omega_r \tau = 1$. Therefore,

$$f_r = \frac{1}{2\pi\tau} = \frac{1}{2\pi RC} \tag{7}$$

where τ is relaxation time. The respective capacitances (C_b and C_{gb}) due to grain and grain boundary effects can be calculated using this relation. The values of R_b, R_{gb}, C_b and C_{gb} obtained from Cole–Cole plots at different temperatures are listed in Table 1.

The relaxation time due to the bulk effect (τ_b) has been calculated using Eq. (7). Fig. 7 shows the variation of ln (τ_b) with the inverse of absolute temperature ($10^3/T$). It is observed that the value of τ_b decreases with an increase in temperature for all samples and its temperature dependence follows the Arrhenius relation:

$$\tau_b = \tau_0 \exp\left(\frac{-E_a}{k_B T}\right) \tag{8}$$

where τ_0 is the pre-exponential factor, k_B is Boltzmann constant and T the absolute temperature. The value of activation energy (E_a) as calculated from the slope of ln (τ_b) versus $10^3/T$ curve is observed to be 0.95 eV.

Electrical response of the materials can also be analyzed by complex modulus formalism, which provides an alternative approach based on polarization analysis. The complex modulus

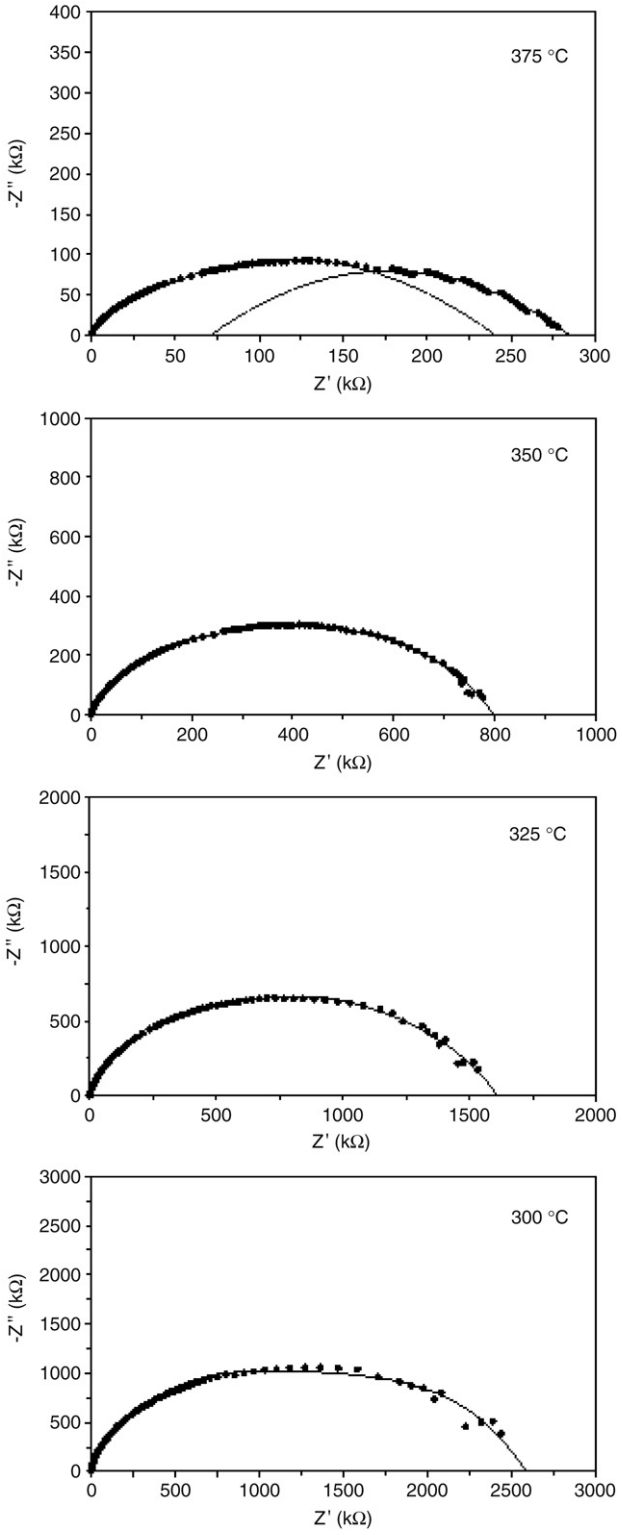

Fig. 6. Complex impedance spectrum (Cole–Cole plots) of BSTN at different temperatures.

(M^*) was calculated using the Eq. (4) where $M' = \omega C_0 Z''$ and $M'' = \omega C_0 Z'$, $C_0 = \varepsilon_0 A/t$ (ε_0 = permittivity of free space, A = area of the electrode surface and t = thickness of the sample). The complex modulus spectrum (M' versus M'') is shown in Fig. 8.

Fig. 9 shows the variation of M' with frequency at the temperatures mentioned earlier. It is characterized by a very low value (almost zero) of M' in the low frequency region then a continuous increase with an increase in frequency, having a

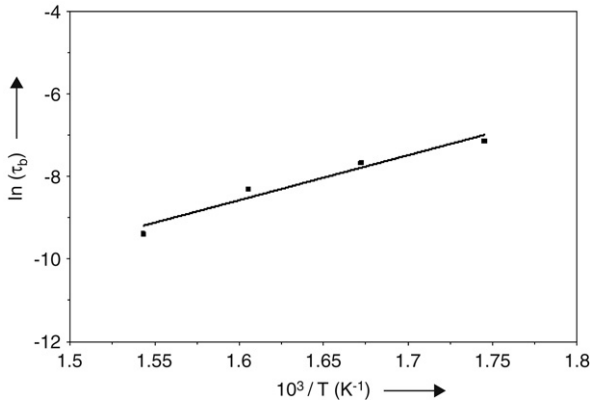

Fig. 7. Variation of $\ln(\tau_b)$ with the inverse of absolute temperature ($10^3/T$).

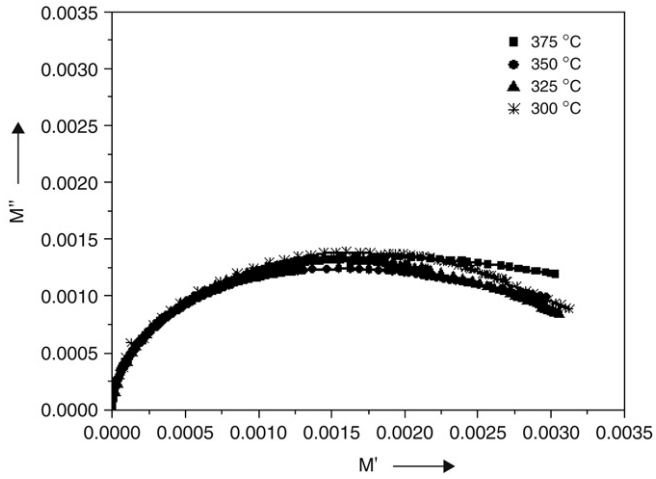

Fig. 8. Complex modulus spectrum (M' versus M'') at different temperatures.

tendency to saturate at a maximum asymptotic value in the high frequency region for all temperatures. This is attributed to the presence of conduction phenomena due to short-range mobility of charge carriers [39]. Fig. 10 shows the variation of M'' as a function of frequency. It shows that the maxima of the imaginary component of modulus (M''_{max}) shifts towards higher relaxation frequencies with a rise in temperature. This behaviour suggests that dielectric relaxation is thermally activated in which the hopping mechanism of charge carriers dominates intrinsically [34]. Asymmetric broadening of the peak indicates a spread of relaxation with different time constants, and hence the relaxation in the material is of a non-Debye type.

Scaling behaviour of the sample was studied by plotting normalized parameters (i.e. M''/M''_{max} versus log (f/f_{max}); f_{max} is frequency corresponding to M''_{max}) at different measuring temperatures (Fig. 11). The modulus scaling behaviour gives an insight into the dielectric processes occurring inside the material. The low frequency side of the peak in M''/M''_{max} versus log (f/f_{max}) curve represents the range of frequencies in which the charge carriers can move over a long distance (i.e., charge carriers can perform successful hopping from one site to the neighbouring site). The high frequency side of M''/M''_{max} versus log (f/f_{max}) curve represents the range of frequencies in which the charge carriers are spatially confined to their potential wells, and thus could make localized motions inside the well. The region where the peak occurs is an indication of the transition from long-range to short-range mobility with an increase in frequency [39]. The coincidence of all the peaks at different temperatures below the common value of log (f/f_{max}) $\sim 10^{-3}$ indicates temperature independent behaviour of the relaxation dynamic process occurring in the material [40].

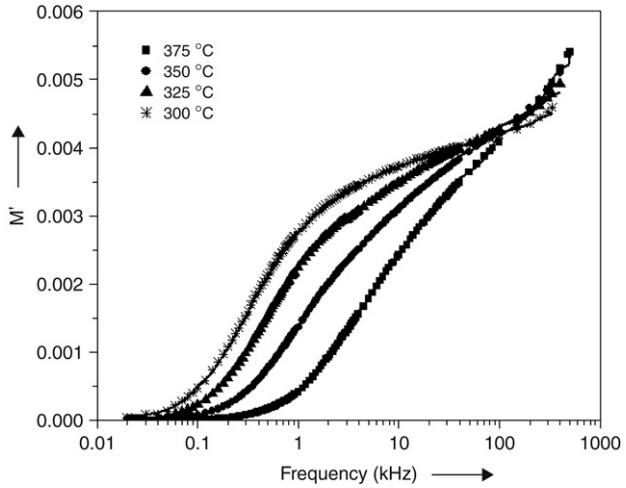

Fig. 9. Variation of the real part of modulus (M') with frequency.

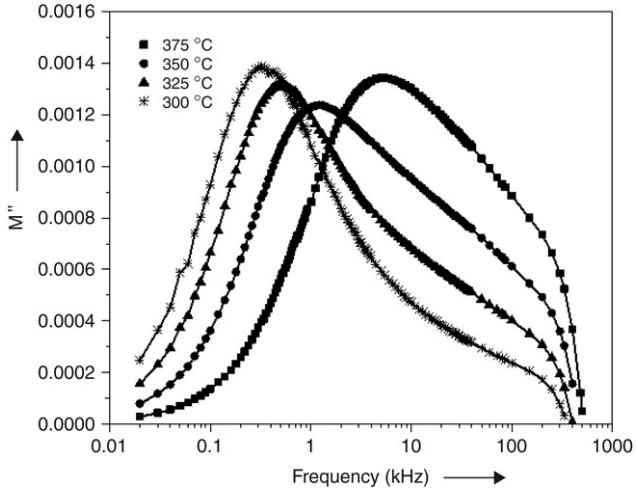

Fig. 10. Variation of the imaginary part of modulus (M'') with frequency.

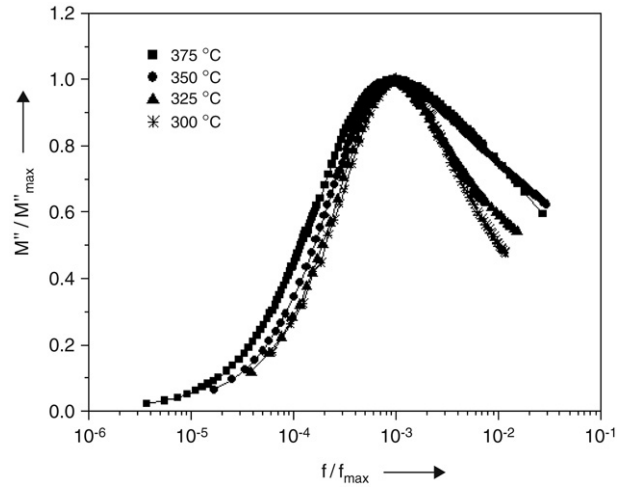

Fig. 11. Modulus scaling behaviour of BSTN at different temperatures.

The dc (bulk) conductivity, σ_{dc}, of the sample has been evaluated from the impedance spectrum using the relation:

$$\sigma_{dc} = \frac{t}{R_b A} \tag{9}$$

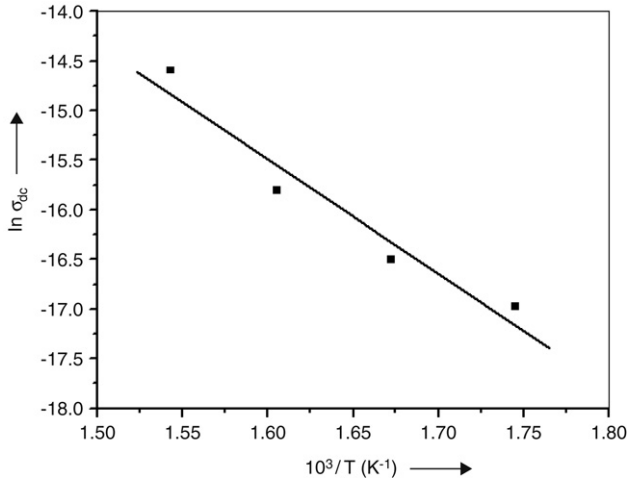

Fig. 12. Variation of ln σ_{dc} with inverse of temperature ($10^3/T$).

where R_b is the bulk resistance, t the thickness and A the surface area of the sample. Fig. 12 shows the variation of σ_{dc} with $10^3/T$. It is observed to increase with increasing temperature further confirming NTCR behaviour. The nature of the variation is linear and follows the Arrhenius relationship:

$$\sigma_{dc} = \sigma_{\mathrm{O}} \exp\left(\frac{-E_a}{k_B T}\right) \tag{10}$$

where E_a is the activation energy of conduction and T is the absolute temperature. The value of activation energy (E_a) as calculated from the slope of ln σ_{dc} versus $10^3/T$ curve is found to be 0.99 eV which is almost same as that obtained from the relaxation time (τ_b) versus temperature curve. This value of E_a is approximately the same as the energy required (~1 eV) for the motion of oxygen vacancies [36]. This confirms that the observed conductivity is due to a movement of oxygen vacancies in this material.

4. Conclusion

The synthesized BSTN sample has an orthorhombic TB crystal structure as revealed by XRD diffractogram. An SEM micrograph suggests that grains of average size ~2 μm are homogeneously distributed throughout the sample. Dielectric studies reveal that the compound has diffuse type ferro–paraelectric phase transition, and relaxor behaviour is not observed. Nyquist plots show both grain and grain boundary effects at 375 °C. It also shows that bulk resistance (R_b) decreases with increase in temperature, which manifests NTCR behaviour of the compound. Complex impedance analysis suggests dielectric relaxation to be of polydispersive non-Debye type. The electrical relaxation process occurring in the material has been found to be temperature dependent. The temperature dependence of the relaxation time (τ_b) is found to obey an Arrhenius law with activation energy (E_a) of 0.95 eV. Modulus analysis has established the possibility of a hopping mechanism for electrical transport processes in this material. The dc conductivity is observed to increase with increasing temperature further confirming NTCR behaviour.

References

[1] C.F.G. Stenger, A.J. Burggraaf, J. Phys. Chem. Solids 41 (1980) 17.
[2] C.F.G. Stenger, A.J. Burggraaf, J. Phys. Chem. Solids 41 (1980) 25.
[3] I. Coondoo, A.K. Jha, Solid State Commun. 142 (2007) 561.
[4] I. Coondoo, A.K. Jha, S.K. Agarwal, J. Eur. Cer. Soc. 27 (2007) 253.
[5] I. Coondoo, A.K. Jha, S.K. Agarwal, N.C. Soni, J. Electroceram. 16 (2006) 393.
[6] V. Shrivastava, A.K. Jha, R.G. Mendiratta, Solid State Commun. 133 (2005) 125.

[7] K.S. Singh, R. Sati, R.N.P. Choudhary, J. Mater. Sci. Lett. 11 (1992) 788.
[8] S.R. Shannigrahi, R.N.P. Choudhary, Atul Kumar, H.N. Acharya, J. Phys. Chem. Solids 59 (1998) 737.
[9] R.N.P. Choudhary, S.R. Shannigrahi, A.K. Singh, Bull. Mater. Sci. 6 (1999) 975.
[10] R. Palai, R.N.P. Choudhary, H.S. Tewari, J. Phys. Chem. Solids 62 (2001) 695.
[11] J.L. Mukherjee, J. Solid State Chem. 24 (1978) 163.
[12] A. Panigrahi, N.K. Singh, R.N.P. Choudhary, J. Solid State Chem. 63 (2002) 213.
[13] C.K. Suman, K. Prasad, R.N.P. Choudhary, Phys. Status Solidi 201 (2004) 3166.
[14] R.R. Neurgaonkar, W.F. Hall, J.R. Oliver, W.W. Ho, W.K. Cory, Ferroelectrics 87 (1998) 167.
[15] R.R. Neurgaonkar, J.G. Nelson, J.R. Oliver, Mater. Res. Bull. 25 (1990) 959.
[16] R.R. Neurgaonkar, J.G. Nelson, J.R. Oliver, Mater. Res. Bull. 27 (1992) 677.
[17] N. Wakiya, J.K. Wang, A. Saiki, K. Shinozaki, N. Mizutani, J. Eur. Ceram. Soc. 19 (1999) 1071.
[18] Z.X. Cheng, S.J. Zhang, G.Y. Zhou, J.H. Liu, J.R. Han, H.C. Chen, Mater. Res. Bull. 35 (2000) 1107.
[19] Y.K. Hwang, Y.U. Kwon, Mater. Res. Bull. 32 (1997) 1495.
[20] B. Tribotte, J.M. Haussonne, G. Desgardin, J. Eur. Ceram. Soc. 19 (1999) 1105.
[21] P.B. Jasmieson, S.C. Abrahams, L. Bernstein, J. Chem. Phys. 48 (1965) 5048.
[22] P.V. Bijumon, V. Kohli, Om Prakash, M.R. Varma, M.T. Sebastian, Mater. Sci. Eng. B 113 (2004) 13.
[23] X.H. Zheng, X.M. Chen, Solid State Commun. 125 (2003) 449.
[24] P. Ganguly, A.K. Jha, K.L. Deori, J. Electroceram. doi:10.1007/s10832-007-9337-6.
[25] C. Dong, J. Appl. Crystallogr. 32 (1999) 838.
[26] P.R. Das, R.N.P. Choudhary, B.K. Samantray, J. Alloys and Comp. 448 (2008) 32.
[27] S.M. Pilgrim, A.E. Sutherland, S.R. Winzer, J. Amer. Ceram. Soc. 73 (1990) 3122.
[28] C.K. Suman, K. Prasad, R.N.P. Choudhary, J. Mater. Sci. 41 (2006) 369.
[29] C.K. Suman, K. Prasad, R.N.P. Choudhary, Mat. Chem. Phys. 82 (2003) 140.
[30] F.A. Kröger, H.J. Vink, Solid State Phys. 3 (1956) 307.
[31] V. Raghavan, Materials Science and Engineering, Prentice-Hall of India, New Delhi, 2004, p. 194.
[32] B. Behera, P. Nayak, R.N.P. Choudhary, J. Alloys Comp. 436 (2007) 226.
[33] J. Plocharski, W. Wieczoreck, Solid State Ionics 28–30 (1988) 979.
[34] B. Behera, P. Nayak, R.N.P. Choudhary, Mat. Res. Bull. 43 (2008) 401.
[35] A.K. Jonscher, Nature 267 (1977) 673.
[36] S. Sen, R.N.P. Choudhary, P. Pramanik, Phys. B 387 (2007) 56.
[37] R.C. Buchanan, Principles of Electronic Ceramics, Marcel Dekkar, New York, 1991, p. 250.
[38] V. Shrivastava, A.K. Jha, R.G. Mendiratta, Phys. B 371 (2006) 337.
[39] P.S. Das, P.K. Chakraborty, B. Behera, R.N.P. Choudhary, Phys. B 395 (2007) 98.
[40] S. Saha, T.P. Sinha, Phys. Rev. B 65 (2002) 134103.

Journal of Alloys and Compounds 495 (2010) 7–12

Contents lists available at ScienceDirect

Journal of Alloys and Compounds

journal homepage: www.elsevier.com/locate/jallcom

Structural and electrical properties of $Ba_{5-x}Ca_xSmTi_3Nb_7O_{30}$ ($x = 0–5$) ferroelectric ceramics

Prasun Ganguly, A.K. Jha *

Thin Film & Materials Science Laboratory, Department of Applied Physics, Delhi Technological University (Formerly Delhi College of Engineering), Bawana Road, Delhi 110042, India

ARTICLE INFO

Article history:
Received 26 December 2009
Received in revised form 15 January 2010
Accepted 21 January 2010
Available online 2 February 2010

Keywords:
Ceramics
Ferroelectrics
Solid state reaction
Dielectric response
X-ray diffraction
Scanning electron microscopy

ABSTRACT

Samples of the compositions $Ba_{5-x}Ca_xSmTi_3Nb_7O_{30}$ ($x = 0–5$), where Ba has been replaced by Ca in steps, were synthesized by solid state reaction method and studied for their structural, dielectric and electrical properties. X-ray diffraction analysis shows the formation of the compounds in an orthorhombic structure at room temperature. Scanning electron micrographs reveal that the average grain size of the compounds increases with increase in calcium content. Detailed studies of dielectric properties as a function of temperature at different frequencies suggest that the synthesized compounds undergo non-relaxor type ferroelectric–paraelectric phase transition of diffuse nature with a decrease in the value of dielectric constant as calcium content increases. When barium is completely replaced by calcium (i.e., $Ca_5SmTi_3Nb_7O_{30}$), the compound does not show any phase transition. The ferroelectric nature of the studied compounds was confirmed by recording the polarization–electric field (P–E) hysteresis loops at room temperature. The remanent polarization value is observed to be highest in the sample with $x = 1$. The temperature variation of P–E loop in the Ca free compound has been reported. The dc and ac conductivity study over a wide temperature range suggests that the compounds have negative temperature coefficient of resistance (NTCR) behaviour.

1. Introduction

From the first report of ferroelectricity in $BaTiO_3$ [1], there has been an increasing interest in developing and searching new ferroelectric materials for device applications, which has led to the discovery of numerous ferroelectric materials. During the process, a large number of ferroelectric oxides of different structural families such as perovskite, spinel, tungsten–bronze (TB), etc., have been discovered. Some of the ferroelectric niobates of TB structure have excellent properties such as pyroelectric, electro-optic, photorefractive, piezoelectric, etc., useful for device applications [2–6]. The TB-type structure consists of a complex array of distorted BO_6 octahedral sharing corners in such a way that three different types of interstices (A, B and C) are available for cation occupation in the general formula $[(A_1)_4(A_2)_2(C)_4][(B_1)_2(B_2)_8]O_{30}$ [7] where A_1 and A_2 sites are usually filled by divalent or trivalent cations, B_1 and B_2 sites by tetravalent or pentavalent cations and C site being small, often remains empty giving the general formula $A_6B_{10}O_{30}$. There is a scope for substitution by variety of cations at many interstitial sites (i.e., A_1, A_2, B_1 and B_2) that can tailor the physical properties of the compound for various device applications. In order to find some new TB niobate ceramics, some work has been carried out in $BaO–R_2O_3–TiO_2–Nb_2O_5$ (R = rare earth) quaternary systems [8–11]. These compounds were found to be interesting because of their nature of diffuse phase transition with transition temperature well above room temperature [12]. Detailed literature survey shows that even though a lot of work has been done on the TB-compounds, not much work has been reported in the $Ba_{5-x}Ca_xRTi_3Nb_7O_{30}$ (R = rare earth); $x = 0–5$, compounds. This prompted the authors to make a detailed study of $Ba_{5-x}Ca_xSmTi_3Nb_7O_{30}$ (BCSTN) ($x = 0, 1, 2, 3, 4$ and 5) compounds and studied for their structural, dielectric, ferroelectric and electrical properties.

2. Experimental

The polycrystalline samples of BCSTN were prepared by solid state reaction technique by taking high purity $CaCO_3$, $BaCO_3$, TiO_2, Nb_2O_5 (all from M/s Aldrich, USA) and Sm_2O_3 (M/s Alfa Aesar, USA) in their stoichiometric proportions. The materials were thoroughly ground in an agate mortar and passed through sieve of extremely fine mesh size. This powder mixture was then calcined at 1100 °C for 20 h in an alumina crucible. The calcined mixture was ground, passed through the sieve again. The mixture was then admixed with 5 wt.% polyvinyl alcohol (M/s Aldrich, USA) as a binder and then pressed at ~300 MPa into disk shaped pellets. These pellets were then sintered at 1300 °C for 10 h. This sintering condition is the optimized sintering condition and the details are reported elsewhere [13].

X-ray diffractogram of the sintered pellets were recorded using Bruker diffractometer (model D8 Advance) in the range $20° \leq 2\theta \leq 70°$ with Cu Kα radiation

* Corresponding author. Tel.: +91 9868242150; fax: +91 11 27871023.
E-mail address: dr_jha_ak@yahoo.co.in (A.K. Jha).

0925-8388/$ – see front matter © 2010 Elsevier B.V. All rights reserved.
doi:10.1016/j.jallcom.2010.01.118

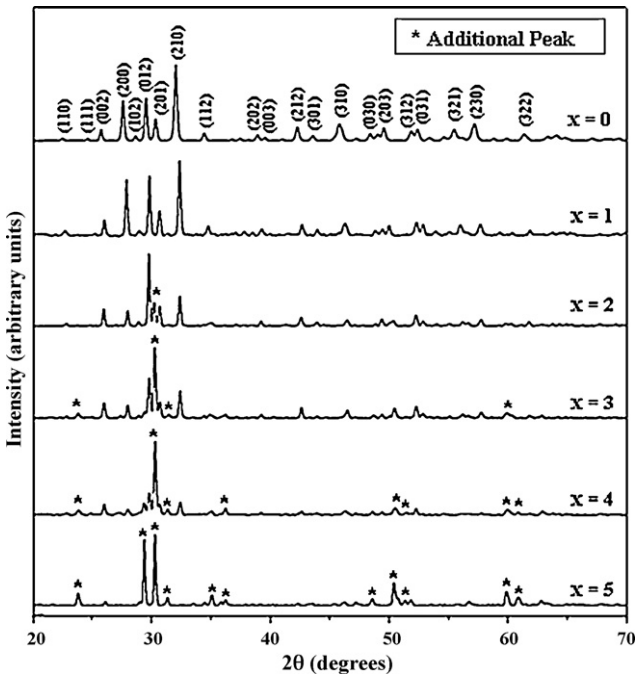

Fig. 1. X-ray diffraction patterns of $Ba_{5-x}Ca_xSmTi_3Nb_7O_{30}$ (x = 0–5) compounds.

(λ = 1.5405 Å) with a scanning rate of 1°/min. The granular morphology of the samples was investigated using scanning electron microscope (JEOL, JSM-840), operated at 20 kV. The sintered pellets were polished and silver pasted on both sides and cured at 325 °C for 1 h. The dielectric measurements were carried out using a precision LCR meter (Agilent 4284A) operating at oscillation amplitude of 1 V. The polarization–electric field (P–E) hysteresis loops were recorded using a P–E loop tracer based on Sawyer–Tower circuit. The dc electrical resistivity of the samples was measured from room temperature to 300 °C at constant electric field (60 V/cm), using a Keithley 6517A programmable electrometer.

3. Results and discussion

3.1. XRD and SEM analysis

Fig. 1 shows the XRD patterns of the various BCSTN sintered samples. It is observed in the diffractogram that the specimen remains single phase only up to x = 1. For the samples with $x \geq 2$, additional peaks are also observed which indicates the formation of secondary phase. As the calcium concentration increases, the splitting as well as the intensity of additional peaks increased. A comparison of the additional peaks with standard XRD patterns (JCPDS file No. 30-0270) shows the formation of $Ca_3Nb_2Ti_3O_{14}$ as secondary phase. Lattice parameters were calculated from the X-ray diffractograms and refined using least square refinement method by a computer program package – PowderX [14] – are listed in Table 1. A decrease in the lattice constants is observed which can be understood as ionic radius of Ca^{2+} (1.00 Å) is less than that of Ba^{2+} (1.36 Å) [15]. The crystal structural distortion parameters, namely, orthorhombicity $[2(a-b)/(a+b)]$ and tetragonal strain (c/a) have been calculated and plotted as a function of calcium concentration (Fig. 2). It is observed that the tetragonality increases while orthorhombicity decreases as calcium content is increased.The SEM micrographs of the Ca free and Ca-substituted samples are shown in Fig. 3 which shows considerable increase in grain size with increasing Ca content. The average grain size in the sample with x = 0 is ~2 μm while in the sample with $1 \leq x \leq 5$ the size is found to be in the range of ~10–17 μm. The shape of grains changes from oval to rod like structure with increase in Ca content. Similar shape change of grains on addition of calcium has been reported earlier also [16]. However, it can be seen that the size of rod like structure reduces in barium free sample.

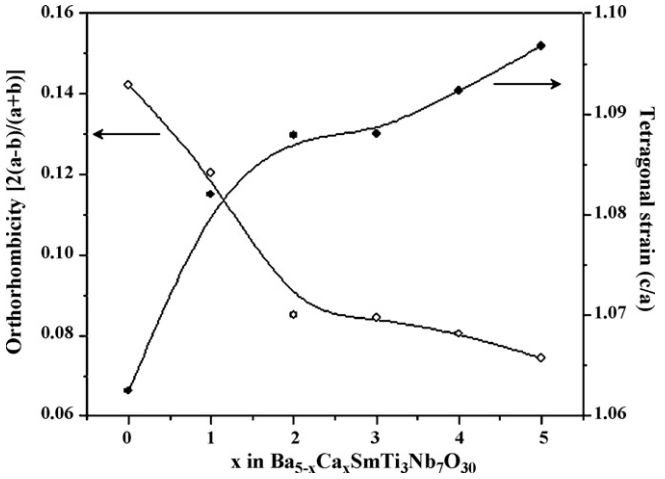

Fig. 2. Compositional variation of orthorhombicity and tetragonal strain.

3.2. Dielectric properties

Fig. 4 shows the temperature dependence of dielectric constant (ε'_r) and dielectric loss ($\tan\delta$) for all the compounds at different frequencies (1, 10 and 100 kHz). It is observed that the compounds with x = 0–4 undergo ferroelectric–paraelectric phase transition of diffuse type at the Curie temperature (T_c), whereas the compound with x = 5 does not show any dielectric anomaly in the measured temperature range. It is also observed that all the compounds have the same T_c at all the above mentioned frequencies, suggesting that the compounds do not show any relaxor behaviour. This result is somewhat different from the earlier results obtained in $Ba_5SmTi_3Nb_7O_{30}$ ceramic reported by Shannigrahi et al. [8] where the sample was sintered at 1250 °C for 24 h and the specimen shows relaxor behaviour, lower T_c, higher $\varepsilon'_{r\,max}$ values. In this class of materials, it is known that sintering process strongly influences phase constitutes, grain size, grain uniformity, internal stress, etc. [17]. Hence these differences in result may be due to the difference in sintering temperature used in both the studies. Moreover, it is known that concentration of oxygen vacancies increases with increase in sintering temperature in this compound [13] and the relaxor behaviour diminishes due to defects such as oxygen vacancy as polar clusters formed by oxygen vacancies never freezes [18]. So, in the present work, a higher sintering tem-

Table 1
Different parameters of $(Ba_{1-x}Ca_x)_5SmTi_3Nb_7O_{30}$ (x = 0–5) compounds.

x	a (Å)	b (Å)	c (Å)	T_c (°C)	$\varepsilon'_{r\,max}$ at 100 kHz	γ	$2P_r$ (μC/cm^2)	$2E_c$ (kV/cm)	E_a (eV)
0	6.4106	5.5595	6.8112	170	303	1.71	2.3	23.3	0.57
1	6.3078	5.5914	6.8250	198	243	1.10	2.5	36.7	1.10
2	6.2608	5.7506	6.8111	30	220	1.50	1.0	10.3	0.59
3	6.2629	5.7556	6.8139	80	147	1.52	0.8	18.4	0.40
4	6.2480	5.7650	6.8244	85	64	1.60	0.7	22.9	0.38
5	6.1924	5.7484	6.7915	–	38	–	–	–	0.45

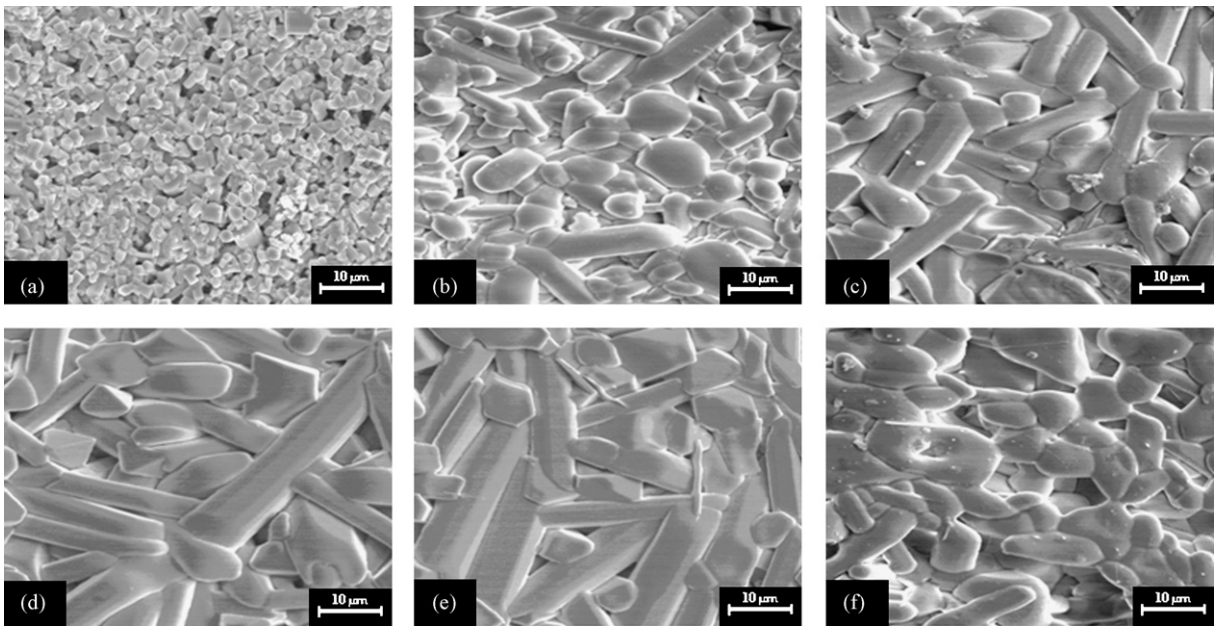

Fig. 3. SEM micrographs of $(Ba_{1-x}Ca_x)_5SmTi_3Nb_7O_{30}$ samples with (a) $x = 0$, (b) $x = 1$, (c) $x = 2$, (d) $x = 3$, (e) $x = 4$ and (f) $x = 5$.

perature (1300 °C) compared to the earlier work [8] results in an increased concentration of oxygen vacancies that possibly mask the relaxor behaviour of the compound. Further, the dielectric constant decreases as the concentration of calcium increases (Table 1). This is possibly due to the decrease in the net polarization of the compounds with increase in Ca concentration as the ionic polarizability, α_I of Ca is 3.16 Å^3 compared to that of Ba 6.40 Å^3 [19]. However, T_c increases from 170 °C (in Ca free specimen) to 198 °C

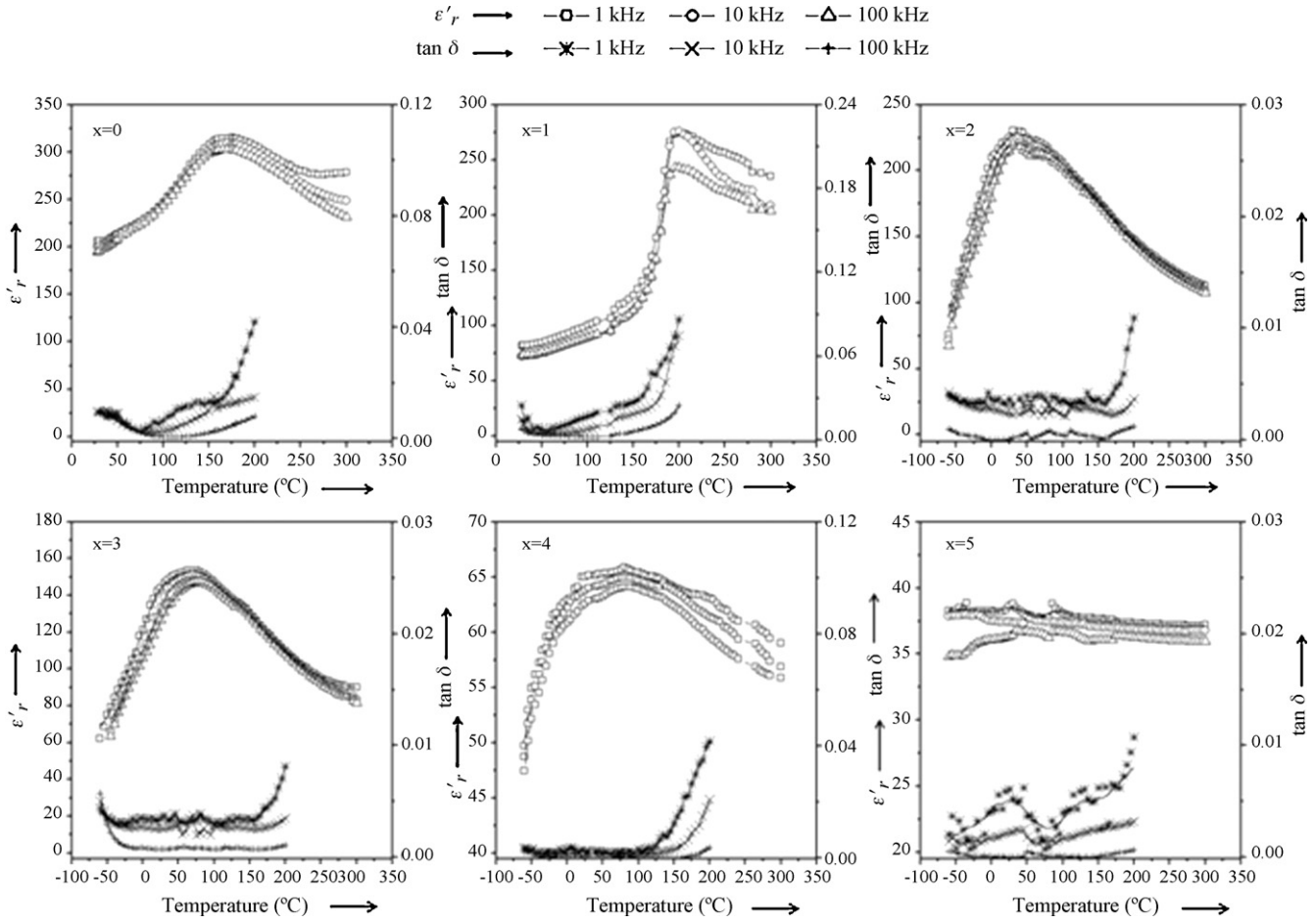

Fig. 4. Variation of dielectric constant (ε'_r) and dielectric loss ($\tan\delta$) with temperature at 1, 10 and 100 kHz frequencies of $(Ba_{1-x}Ca_x)_5SmTi_3Nb_7O_{30}$ compounds.

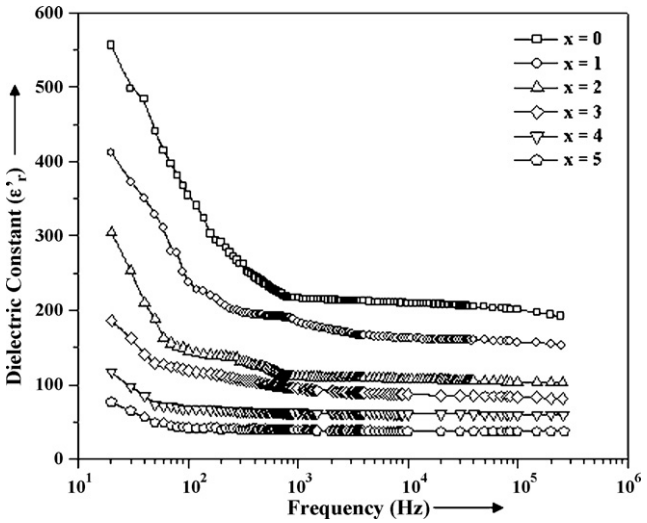

Fig. 5. Variation of dielectric constant (ε_r') with frequency at room temperature.

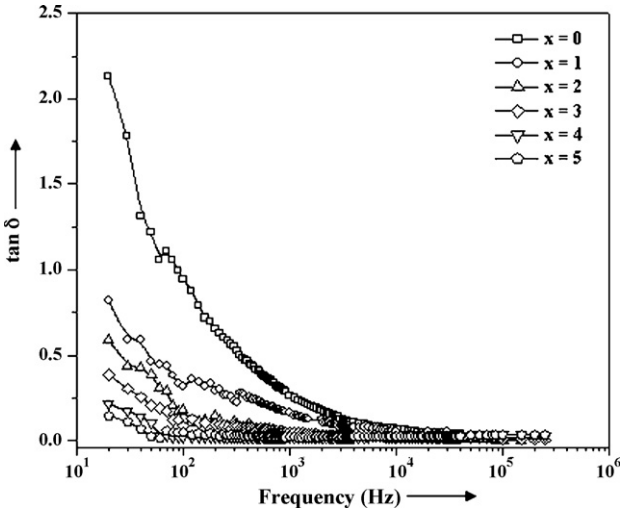

Fig. 6. Variation of dielectric loss ($\tan\delta$) with frequency at room temperature.

in calcium ($x=1$) containing specimen. Larger value of tetragonal strain (c/a) on adding Ca (Fig. 2) indicates that a larger amount of thermal energy is required for the phase transition resulting in an increase in T_c. Another possible reason for the increase in the transition temperature could be attributed to the reduced value of the tolerance factor due to the partial substitution of smaller cation Ca at Ba-site [16]. However, for higher concentration of calcium (i.e., $x \geq 2$), T_c decreases sharply (Table 1). This is likely due to the formation of the secondary phase at these concentrations. At all the frequencies, the dielectric peak is found to be broadened indicating the existence of diffuse phase transition. The diffusivity constant (γ) have been calculated using the empirical relation [20]:

$$\ln\left(\frac{1}{\varepsilon_r'} - \frac{1}{\varepsilon_{r\,\max}'}\right) = \gamma \ln(T - T_c) + \text{constant} \quad (1)$$

where $\varepsilon_{r\,\max}'$ is the maximum ε_r' value at $T=T_c$. The value of γ at 100 kHz for all the samples are obtained from the slope of $\ln((1/\varepsilon_r') - (1/\varepsilon_{r\,\max}'))$ versus $\ln(T-T_c)$ curve and are listed in Table 1. For all the studied compositions, γ is found to be between 1 (obeying Curie–Weiss law) and 2 (for completely disordered sys-

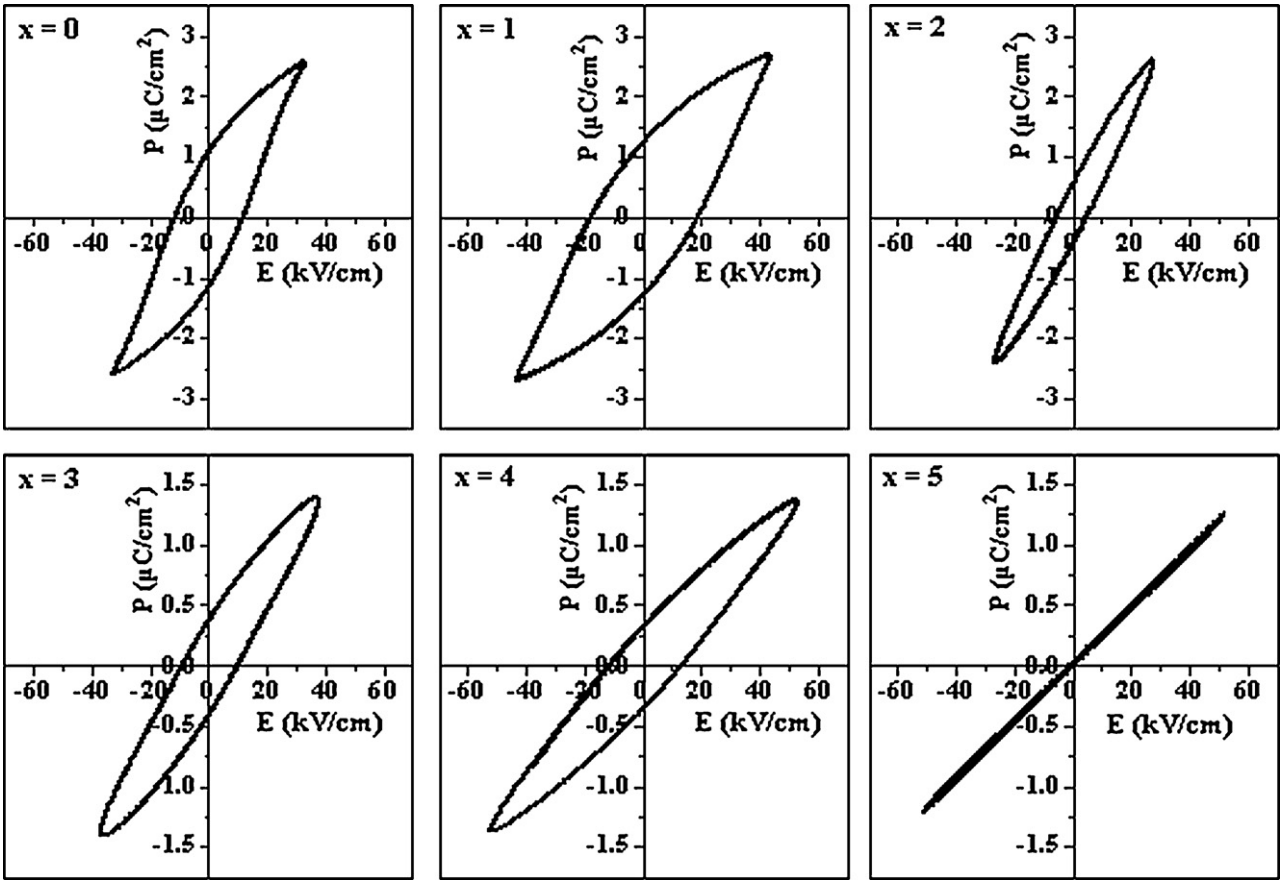

Fig. 7. *P–E* hysteresis loops of $Ba_{5-x}Ca_xSmTi_3Nb_7O_{30}$ ($x=0$–5) compounds at room temperature.

tem) confirming the diffuse phase transition in all the samples. The value of γ is found to decrease from Ca free to $x = 1$ compound but it increases as concentration of calcium is further increased. It suggests that the composition with $x = 1$ is more ordered than other compositions [21]. For all the BCSTN compounds, at the above mentioned frequencies, the variation of dielectric loss with temperature (Fig. 4) shows that the loss is almost constant initially but at higher temperatures it increases sharply. This sharp increase of dielectric loss in high temperature region may be attributed to the increased mobility of space charges arising from the defects or vacancies (like oxygen vacancies) in the sample [22].

Fig. 5 shows the variation of dielectric constant with frequency from 20 Hz to 500 kHz at room temperature for all the compounds. For all the compositions, the dielectric constant decreases up to about 1 kHz and remains nearly constant beyond this frequency. The dielectric constant of a material has four polarization contributions: electronic, ionic, dipolar and space charge [23]. Response frequencies for ionic and electronic polarizations are $\sim 10^{13}$ and 10^{16} Hz, respectively; and at frequencies beyond 1 kHz, contribution from space charge polarization is not expected [23]. Thus, the higher values of dielectric constant at lower frequencies can be attributed to the presence of space charges in the structure which exist as defects such as oxygen vacancies [24,25]. Moreover, at lower frequencies, the dipoles can follow the alternating field resulting in higher values of dielectric constant while at higher frequencies the dipoles are unable to follow the rapidly changing field leading to the reduction in the values of dielectric constant.

The variation of dielectric loss with frequency at room temperature for all the compounds is shown in Fig. 6. It also decreases sharply up to 1 kHz and beyond this it is nearly independent of frequency. As discussed above, this can also be understood as the unability of the dipoles to follow the rapidly oscillating field at higher frequencies leading to the reduction in the values of dielectric loss. It can also be seen from Figs. 5 and 6 that the dielectric constant and dielectric loss at room temperature decreases with increase in calcium concentration.

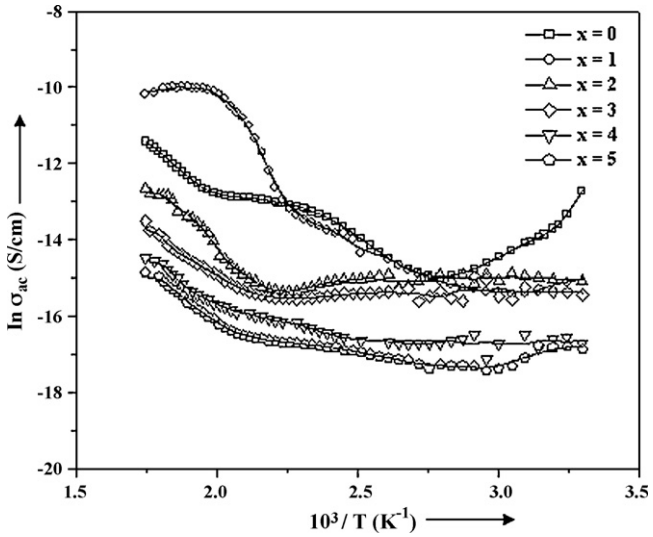

Fig. 9. Variation of ac conductivity ($\ln \sigma_{ac}$) with inverse of temperature ($10^3/T$) at 100 kHz frequency of $(Ba_{1-x}Ca_x)_5SmTi_3Nb_7O_{30}$ compounds.

3.3. Ferroelectric studies

To confirm the ferroelectric nature of the studied compounds, hysteresis loops were recorded at room temperature at a frequency of 100 Hz. Fig. 7 shows the variation of polarization as a function of electric field for all the compounds. The observed values

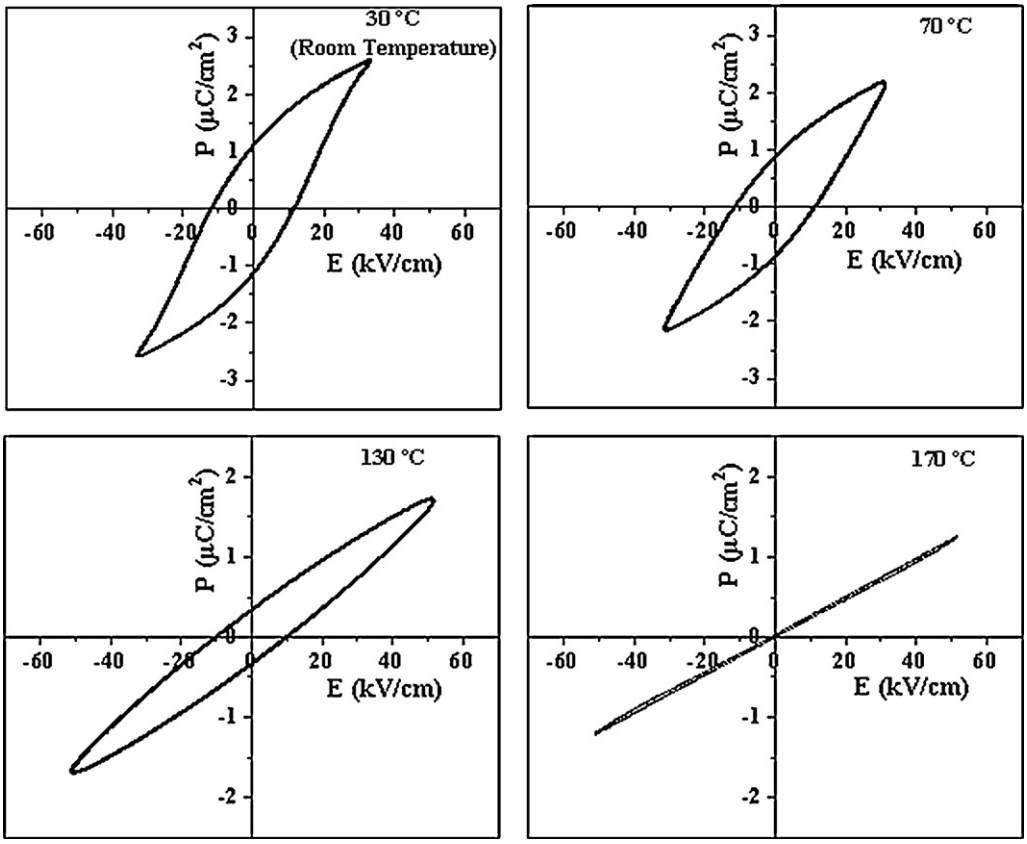

Fig. 8. Temperature variation of *P–E* hysteresis loop in $x = 0$ (i.e., $Ba_5SmTi_3Nb_7O_{30}$) compound.

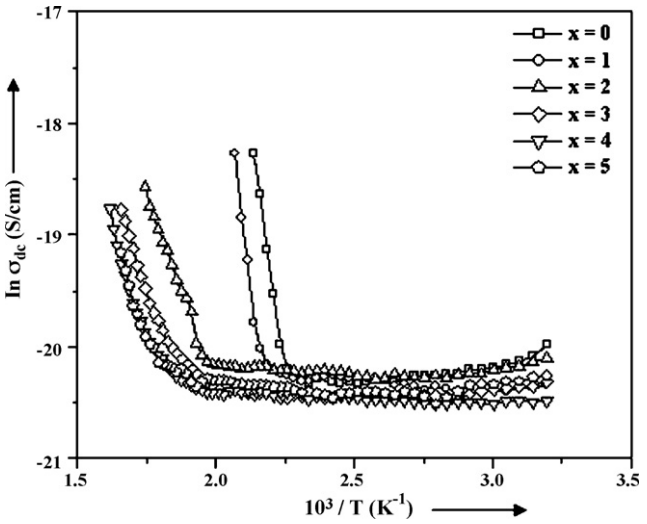

Fig. 10. Variation of dc conductivity ($\ln \sigma_{dc}$) with inverse of temperature ($10^3/T$) of $(Ba_{1-x}Ca_x)_5SmTi_3Nb_7O_{30}$ compounds.

of remanent polarization ($2P_r$) and the coercive field ($2E_c$) for all the compounds are given in Table 1. The remanent polarization ($2P_r$) is found to increase on Ca substitution, i.e., for the specimen with $x = 1$. The increase in remanent polarization could be correlated to the pronounced structural distortion arising due to the partial substitution of smaller cation Ca at Ba-site [16]. But for higher concentration of calcium, $2P_r$ decreases and finally the loop becomes a straight line for $x = 5$ confirming that the compound is no longer ferroelectric on completely replacing barium by calcium, which is in conformity with dielectric observations. The temperature variation of *P–E* hysteresis loop for $x = 0$ (i.e., $Ba_5SmTi_3Nb_7O_{30}$) specimen is shown in Fig. 8. It can be seen that the remanent polarization ($2P_r$) value decreases with increasing temperature and finally it becomes zero at the transition temperature (T_c), i.e., 170 °C.

3.4. AC and DC conductivity

The total conductivity (σ_{tot}) of the material comprises the ac conductivity (σ_{ac}) and the dc conductivity (σ_{dc}):

$$\sigma_{tot} = \sigma_{ac}(\omega) + \sigma_{dc} \quad (2)$$

The ac conductivity (σ_{ac}) and activation energy (E_a) of the sample have been calculated using the relation [26]:

$$\sigma_{ac} = \omega \varepsilon_r' \varepsilon_o \tan\delta = \sigma_o \exp\left(\frac{-E_a}{k_B T}\right) \quad (3)$$

where ω is the angular frequency, ε_o the free space permittivity and k_B the Boltzmann constant. The variation of ac conductivity as a function of inverse of temperature ($10^3/T$) for all the compositions at 100 kHz is shown in Fig. 9 and the calculated values of E_a of the samples are given in Table 1. The conductivity of the compounds at higher temperature is higher, which is a common behaviour in most of the dielectric ceramics [27,28]. The nature of variation of σ_{ac} over a wide temperature range supports the thermally activated conduction process in these materials. This is due to the presence of defects like oxygen vacancies whose mobility increases at higher temperatures [22].

Fig. 10 shows the variation of dc conductivity ($\sigma_{dc} = 1/\rho$) with inverse of temperature ($10^3/T$) for all the compositions. It can be seen from the figure that at low temperatures the conductivity is constant. But at higher temperatures, it increases with temperature indicating negative temperature coefficient of resistance (NTCR)-type behaviour in all the studied BCSTN compounds.

4. Conclusion

X-ray diffractograms confirm the formation of orthorhombic TB-structure in all the BCSTN compounds with decrease in orthorhombicity and increase in tetragonality on increasing the calcium concentration. Single phase is maintained for $x = 1$ beyond which increasing presence of $Ca_3Nb_2Ti_3O_{14}$ as secondary phase is indicated by XRD studies. Microstructural studies reveal that there is an increase in average grain size on substitution of calcium. The dielectric studies show that the value of dielectric constant decreases on addition of calcium. The Curie temperature (T_c), however, increases from 170 °C (for $x = 0$) to 198 °C (for $x = 1$). All the compounds exhibit non-relaxor type ferroelectric–paraelectric diffuse phase transition with least diffusivity in $x = 1$ composition except $x = 5$ where the compound does not show any phase transition. Negative temperature coefficient of resistance (NTCR) behaviour is being observed in all the compounds.

Acknowledgments

One of the authors (PG) is grateful to Council of Scientific and Industrial Research (CSIR), New Delhi, India for the award of Senior Research Fellowship.

References

[1] B. Wul, Nature 157 (1946) 808.
[2] N.S. Vandamme, A.E. Sutherland, L. Jones, K. Bridger, S.R. Winzer, J. Am. Ceram. Soc. 74 (1991) 1785–1792.
[3] R.R. Neurgaonkar, W.F. Hall, J.R. Oliver, W.W. Ho, W.K. Cory, Ferroelectrics 87 (1998) 167–179.
[4] R.R. Neurgaonkar, W.K. Cory, J. Opt. Soc. Am. B 3 (1986) 274–282.
[5] D. Liu, Y. Liu, S.Q. Huang, X. Yao, J. Am. Ceram. Soc. 76 (1993) 2129–2132.
[6] A. Panigrahi, N.K. Singh, R.N.P. Choudhary, J. Mater. Sci. Lett. 18 (1999) 1579–1581.
[7] P.B. Jasmieson, S.C. Abrahams, J.L. Bernstein, J. Chem. Phys. 48 (1965) 5048–5057.
[8] S.R. Shannigrahi, R.N.P. Choudhary, A. Kumar, H.N. Acharya, J. Phys. Chem. Solids 59 (1998) 737–742.
[9] P. Ganguly, A.K. Jha, K.L. Deori, J. Alloys Compd. 484 (2009) 40–44.
[10] R. Palai, R.N.P. Choudhary, H.S. Tewari, J. Phys. Chem. Solids 62 (2001) 695–700.
[11] P.R. Rao, S.K. Ghosh, P. Koshy, J. Mater. Sci.: Mater. Electron. 12 (2001) 729–732.
[12] J.L. Mukherjee, C.P. Khattak, K.P. Gupta, F.F.Y. Wang, J. Solid State Chem. 24 (1978) 163–167.
[13] P. Ganguly, A.K. Jha, K.L. Deori, J. Electroceram. 22 (2009) 257–262.
[14] C. Dong, J. Appl. Cryst. 32 (1999) 838.
[15] R.D. Shannon, C.T. Prewitt, Acta Crystogr. B 25 (1969) 925–946.
[16] R.R. Das, P. Bhattacharya, W. Perez, R.S. Katiyar, Ceram. Int. 30 (2004) 1175–1179.
[17] X.H. Zheng, X.M. Chen, Solid State Commun. 125 (2003) 449–454.
[18] L. Zhang, X.M. Chen, Solid State Commun. 149 (2009) 1317–1321.
[19] R.D. Shannon, J. Appl. Phys. 73 (1993) 348–366.
[20] S.M. Pilgrim, A.E. Sutherland, S.R. Winzer, J. Am. Ceram. Soc. 73 (1990) 3122–3125.
[21] T. Badapanda, S.K. Rout, S. Panigrahi, T.P. Sinha, Curr. Appl. Phys. 9 (2009) 727–731.
[22] T. Friessnegg, S. Aggarwal, R. Ramesh, B. Nielsen, E.H. Poindexter, D.J. Keeble, Appl. Phys. Lett. 77 (2000) 127–129.
[23] R.C. Buchanan, Ceramic Materials for Electronics: Processing, Properties and Applications, Marcel Dekker, Inc., New York, 1991.
[24] Y. Noguchi, M. Miyayama, Appl. Phys. Lett. 78 (2001) 1903–1905.
[25] A. Chen, Y. Zhi, L.E. Cross, Phys. Rev. B 62 (2000) 228–236.
[26] W.D. Kingery, Introduction to Ceramics, Wiley, New York, 1960.
[27] K.S. Singh, R. Sati, R.N.P. Choudhary, Pramana 38 (1992) 161–166.
[28] K.S. Rao, T.N.V.K.V. Prasad, A.S.V. Subrahmanyam, J.H. Lee, J.J. Kim, S.H. Cho, Mater. Sci. Eng. B 98 (2003) 279–285.

Physica B 405 (2010) 3154–3158

Contents lists available at ScienceDirect

Physica B

journal homepage: www.elsevier.com/locate/physb

Impedance spectroscopy analysis of $Ba_5NdTi_3Nb_7O_{30}$ ferroelectric ceramic

Prasun Ganguly, A.K. Jha *

Thin Film & Materials Science Laboratory, Department of Applied Physics, Delhi Technological University (Formerly Delhi College of Engineering), Bawana Road, Delhi 110042, India

ARTICLE INFO

Article history:
Received 1 October 2009
Received in revised form
17 April 2010
Accepted 19 April 2010

Keywords:
Solid-state reaction
X-ray diffraction
Dielectric response
Impedance spectroscopy

ABSTRACT

The polycrystalline sample of $Ba_5NdTi_3Nb_7O_{30}$, a member of tungsten bronze family, was prepared by solid-state reaction method. X-ray diffraction (XRD) analysis shows the formation of single-phase compound with an orthorhombic structure. Scanning electron micrograph of the material shows uniform grain distribution throughout the sample. Variation of dielectric constant (ε'_r) with temperature at different frequencies shows that the compound has a dielectric anomaly of ferroelectric to paraelectric type at 100 °C, and exhibits non-relaxor kind of diffuse phase transition. Studies of electrical properties of $Ba_5NdTi_3Nb_7O_{30}$ using the complex impedance spectroscopy (CIS) technique show the decrease in bulk resistance with rise in temperature indicating a typical negative temperature coefficient of resistance (NTCR)-type behaviour. A possible hopping mechanism for electrical transport in the system is evident from the modulus analysis.

1. Introduction

Since the discovery of ferroelectricity in $BaTiO_3$ [1], a number of ferroelectric oxides of perovskite structure and tungsten bronze (TB) structure have been studied. Some niobates with the TB structure have attracted much attention due to their interesting ferroelectric, pyroelectric, piezoelectric, and nonlinear optical properties for applications in various electrical devices, such as transducers, actuators, capacitors, and ferroelectric random access memory [2–7]. The TB structure consists of a complex array of distorted BO_6 octahedra sharing corners in such a way that three different types of interstices (A, B, and C) are available for a wide variety of cations giving the general formula $[(A_1)_4(A_2)_2(C)_4][(B_1)_2(B_2)_8]O_{30}$, where A_1 and A_2 sites are usually filled by divalent or trivalent cations, B_1 and B_2 sites by tetravalent or pentavalent cations and C site being small, often remains empty giving the general formula $A_6B_{10}O_{30}$ for the tungsten bronze structure [8]. It has been found that physical properties can be improved by different ionic substitutions at the above-mentioned sites. A number of compounds such as $Ba_5RTi_3Nb_7O_{30}$, $Ba_3R_3Ti_5Nb_5O_{30}$, and $Ba_4R_2Ti_4Nb_6O_{30}$ have been studied in $BaO–R_2O_3–TiO_2–Nb_2O_5$ (R=Nd, Sm, Gd, Dy, and Y) system in order to find new TB niobate ceramics [6,7,9–15]. It has been found that this family has phase transition of diffuse nature with transition temperature above the room temperature [16,17]. Detailed literature survey shows that, though a lot of work has been done on different members of TB structural family, hardly any report on electrical properties by means of complex impedance analysis of $Ba_5NdTi_3Nb_7O_{30}$ compound is available in the literature. The present report summarizes the results of an extensive study made on the electrical properties of $Ba_5NdTi_3Nb_7O_{30}$ ceramics using complex impedance spectroscopy (CIS).

2. Experimental

The polycrystalline sample of $Ba_5NdTi_3Nb_7O_{30}$ was prepared by the solid-state reaction technique by taking high purity $BaCO_3$, Nd_2O_3, TiO_2, and Nb_2O_5 (all from M/s Aldrich, USA) in their stoichiometric proportions. The materials were thoroughly ground in an agate mortar and passed through sieve of extremely fine mesh size. This powder mixture was then calcined at 1100 °C for 20 h in an alumina crucible. The calcined mixture was ground and passed through the sieve again. The mixture was then admixed with 5 wt% polyvinyl alcohol (M/s Aldrich, USA) as a binder and pressed at ~200 MPa into disk shaped pellet. This pellet was then sintered at 1300 °C for 10 h. This is the optimized sintering condition found from the extensive studies and reported elsewhere [18].

X-ray diffractogram of the sintered pellet was recorded using Bruker diffractometer (model D8 Advance) in the range $10° < 2\theta < 70°$ with CuK_α radiation ($\lambda = 1.5405$ Å) with a scanning rate of 1°/min. The granular morphology of the sample was investigated using Scanning Electron Microscope (Zeiss, EVO® MA 10), operated at 20 kV. The sintered pellets were polished and coated with silver paste on both sides to act as electrodes and cured at 325 °C for 1 h. Dielectric and impedance measurements were carried out using an Agilent 4284A LCR meter operating at

* Corresponding author. Tel.: +91 9868242150; fax: +91 11 27871023.
E-mail address: dr_jha_ak@yahoo.co.in (A.K. Jha).

0921-4526/$ - see front matter © 2010 Elsevier B.V. All rights reserved.
doi:10.1016/j.physb.2010.04.035

an oscillation amplitude of 1 V. Impedance measurements have been made in the temperature range of 350–425 °C at an interval of 25 °C and frequencies ranging from 20 Hz to 500 kHz.

3. Results and discussion

3.1. Structural and microstructural analysis

Room temperature X-ray diffraction pattern of $Ba_5NdTi_3Nb_7O_{30}$ (BNTN) is shown in Fig. 1, which reveals the formation of single-phase compound. The lattice parameters were calculated using the observed interplanar spacing d-values from the diffractograms and refined using the least square refinement method by a computer program package PowderX [19]. These refined lattice parameters are: $a=6.4483$ Å, $b=5.5642$ Å, and $c=6.8198$ Å. The peaks were indexed using the observed d-values and the calculated lattice parameters. From these, it is found that BNTN has an orthorhombic TB-type structure. The SEM micrograph of the sample is shown in Fig. 1 (inset). It can be seen that the grains are homogeneously distributed over the entire sample. The average grain size of the compound is in the range of 2 μm.

3.2. Dielectric studies

The dielectric constant (ε'_r) of the specimen was measured from room temperature to 300 °C at the frequencies of 1, 10, and 100 kHz and is shown in Fig. 2. It is found that the compound has a dielectric anomaly at 100 °C (the Curie temperature T_c) suggesting the occurrence of ferroelectric–paraelectric phase transition. It is also observed that the compound has the same T_c at all the above-mentioned frequencies indicating that the compound does not show a relaxor behaviour [20]. The dielectric peak is found to be broadened indicating the existence of diffuse phase transition. The diffusivity constant or degree of disorderness (γ) was calculated using the formula [21]:

$$\ln(1/\varepsilon'_r - 1/\varepsilon'_{rmax}) = \gamma \ln(T - T_c) + \text{constant} \quad (1)$$

The value of γ calculated from the slope of Fig. 2 (inset) is found to be 1.4 at 100 kHz which is between 1 (obeying Curie–Weiss law) and 2 (for completely disordered system) indicating a diffuse kind of phase transition as indeed observed. The diffuse nature of the phase transition can be explained in terms of oxygen vacancies. It is known that these TB structured compounds lose oxygen during sintering at high temperature [22,23], which using Kröger and Vink notation [24] can be represented as

$$O_o \rightarrow \frac{1}{2}O_2\uparrow + V_o^{\bullet\bullet} + 2e^-$$

where $V_o^{\bullet\bullet}$ denotes oxygen vacancies. The defects such as oxygen vacancies $V_o^{\bullet\bullet}$ induce disorderness in the system resulting in a diffuse type ferroelectric–paraelectric phase transition [25].

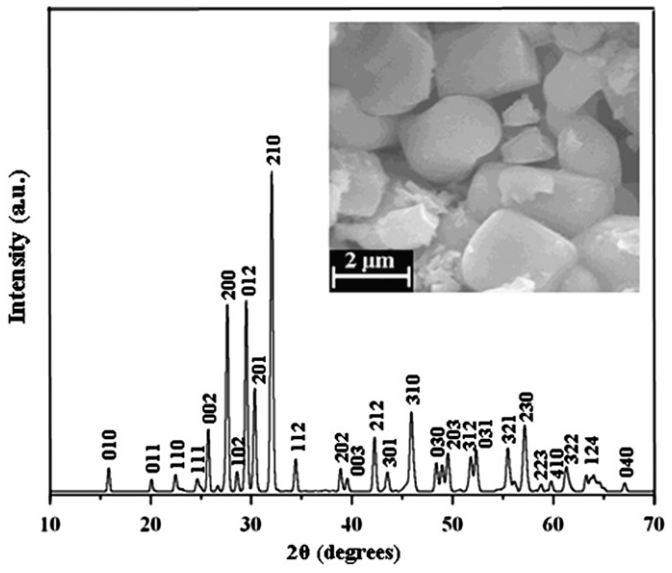

Fig. 1. X-ray diffraction pattern and SEM micrograph (inset) of $Ba_5NdTi_3Nb_7O_{30}$ compound.

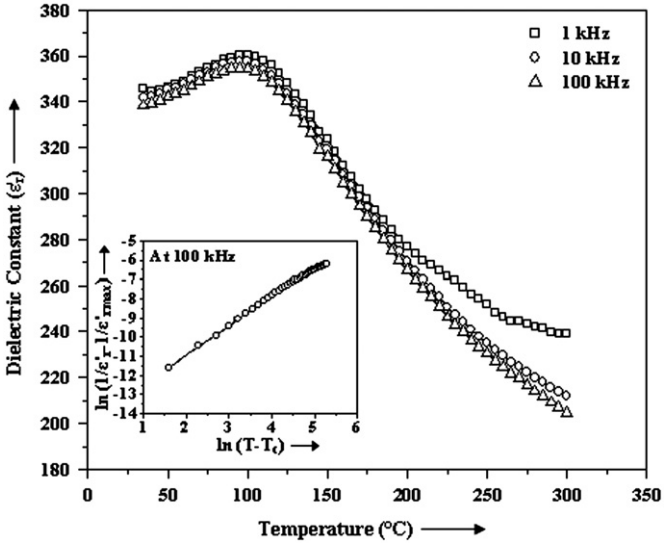

Fig. 2. Variation of dielectric constant (ε'_r) with temperature at 1, 10, and 100 kHz frequencies and variation of $\ln(1/\varepsilon'_r - 1/\varepsilon'_{rmax})$ with $\ln(T-T_c)$ at 100 kHz (inset).

3.3. Impedance studies

Complex impedance spectroscopy (CIS) technique [26] is a non-destructive powerful technique for the characterization of electrical behaviour of electroceramics material. This technique shows the response of a specimen to a sinusoidal perturbation and gives the impedance as a function of frequency. The resultant response (when plotted in a complex plane) appears in the form of a succession of semicircles representing electrical phenomena inside the material due to the bulk, grain boundary, and interface. The frequency dependence of electrical properties of a material is often represented in terms of complex impedance (Z^*), complex admittance (Y^*), complex modulus (M^*), complex permittivity (ε^*), and dielectric loss ($\tan\delta$). They are related to each other as follows:

$$Z^*(\omega) = Z' - jZ'' = R_s - \frac{j}{\omega C_s} = \frac{1}{j\omega C_0 \varepsilon^*} \quad (2)$$

$$Y^*(\omega) = Y' + jY'' = \frac{1}{R_p} + j\omega C_p = j\omega C_o \varepsilon^* = \frac{1}{Z^*} \quad (3)$$

$$M^*(\omega) = M' + jM'' = \frac{1}{\varepsilon^*} = j\omega C_o Z^* \quad (4)$$

$$\varepsilon^*(\omega) = \varepsilon' - j\varepsilon'' \quad (5)$$

$$\tan\delta = \frac{Z'}{Z''} = \frac{Y'}{Y''} = \frac{M''}{M'} = \frac{\varepsilon''}{\varepsilon'} \quad (6)$$

where C_o is the geometrical capacitance, R_s, R_p and C_s, C_p are the series and parallel resistances and capacitances, respectively; Z', Y', M', ε' and Z'', Y'', M'', ε'' denote the real and imaginary

components of the impedance, admittance, modulus, and permittivity, respectively.

The plot of Z' versus Z'' (Nyquist or Cole–Cole plots) at different temperatures (350, 375, 400, and 425 °C) taken over a wide frequency range (20 Hz–500 kHz) is shown in Fig. 3. All the semicircles exhibit some depression instead of a semicircle centered on the real axis. Such behaviour is indicative of non-Debye type relaxation and it also indicates that there is a distribution of relaxation time instead of a single relaxation time

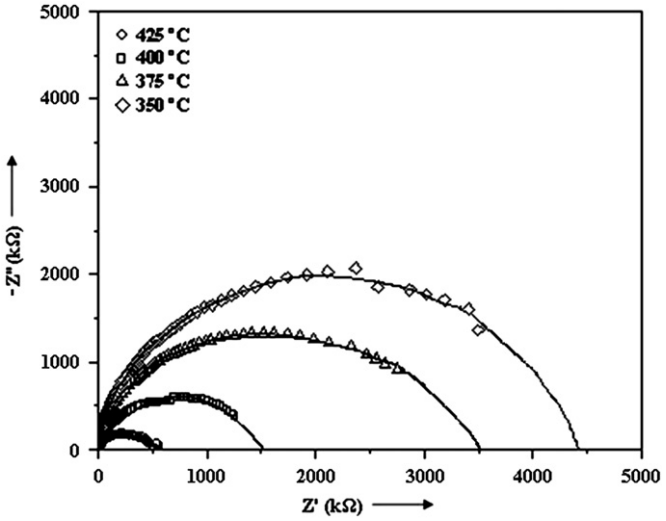

Fig. 3. Complex impedance spectrum (Nyquist plots) of $Ba_5NdTi_3Nb_7O_{30}$ at different temperatures.

Table 1
Bulk resistances and capacitances of $Ba_5NdTi_3Nb_7O_{30}$ compound.

Temperature (°C)	R_b (kΩ)	C_b (pF)
350	4480	250
375	3508	190
400	1538	200
425	514	170

in the material [27]. Each of these semicircles could be represented by a single parallel RC combination. The values of bulk resistance (R_b) at different temperatures have been obtained from the intercept of the semicircular arcs on the real axis (Z') and are given in Table 1. It is observed that R_b decreases with the rise in temperature. This manifests the negative temperature coefficient of resistance (NTCR) behaviour, a typical characteristic of these dielectric materials [28]. The semicircles in the impedance spectrum have a characteristic peak occurring at a unique relaxation frequency ($\omega_r = 2\pi f_r$). It can be expressed as: $\omega_r RC = \omega_r \tau = 1$. Therefore

$$f_r = \frac{1}{2\pi\tau} = \frac{1}{2\pi RC} \tag{7}$$

where τ is relaxation time. The corresponding capacitances (C_b) due to the grain effect can be calculated using this relation. The values of R_b and C_b obtained from Cole–Cole plots at different temperatures are listed in Table 1.

Fig. 4 (a) shows the variation of Z'' with frequency at various temperatures. The plots show that the Z'' values attain a peak (Z''_{max}) at all the temperatures and the magnitude of Z''_{max} decreases with increase in measuring temperature. Further, it is observed that the value of Z''_{max} shifts to higher frequencies with increase in temperature. The observed peak broadening on increasing temperature suggests the presence of temperature dependent relaxation processes in the compound [29]. The contribution towards relaxation process is possibly due to electrons at low temperature and defects/vacancies at higher temperature [20].

Fig. 4(b) shows the normalized imaginary parts of the impedance (Z''/Z''_{max}) as a function of frequency at the selected temperatures. The curve shows peak with a slight asymmetric broadening at each temperature especially at higher temperatures. The asymmetric broadening of the peaks suggests the presence of electrical processes in the material with a spread of relaxation time [22].

3.4. Modulus studies

Electrical response of the materials can also be analyzed by complex modulus formalism, which provides an alternative approach based on the polarization analysis. Complex impedance

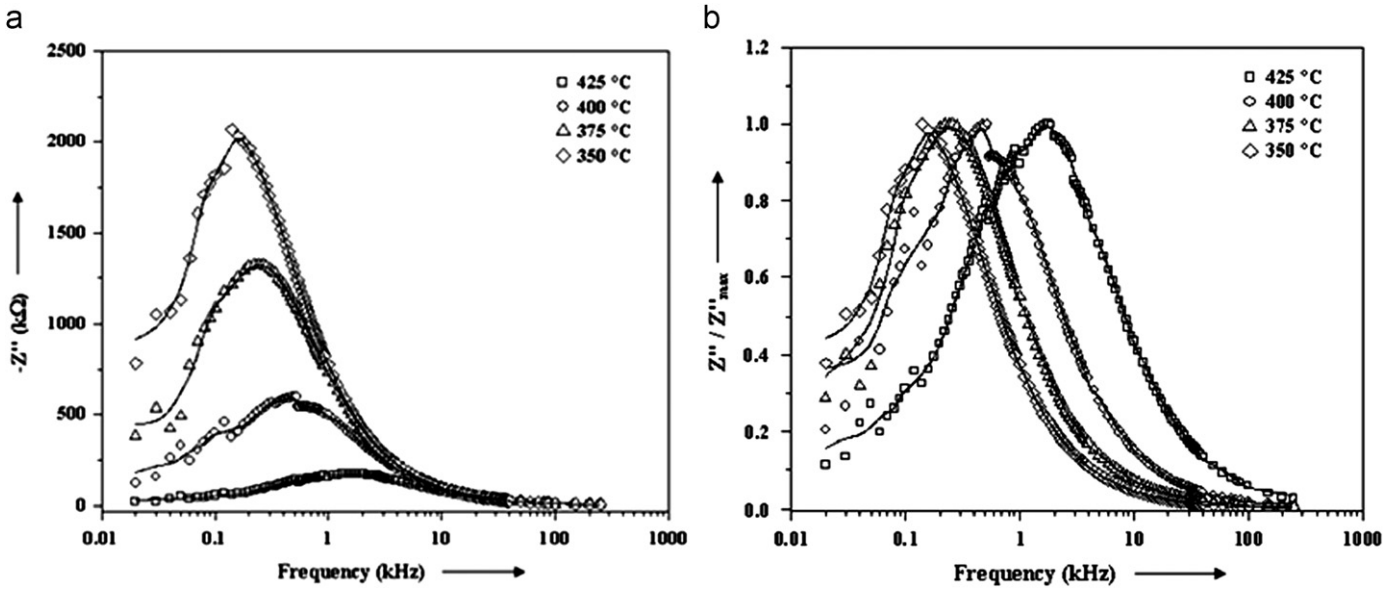

Fig. 4. (a) Variation of imaginary part of impedance (Z'') with frequency. (b) Normalized imaginary part of impedance (Z''/Z''_{max}) as a function of frequency.

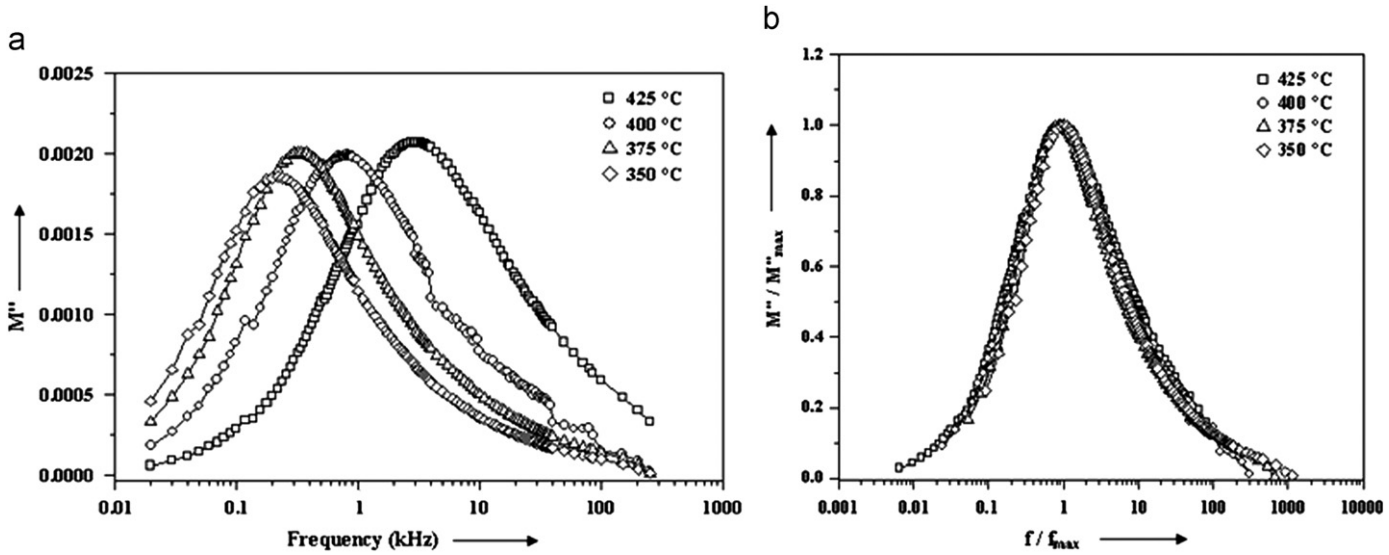

Fig. 5. (a) Variation of imaginary part of modulus (M'') with frequency. (b) Modulus scaling behaviour at different temperatures.

spectrum gives more emphasis to elements with the larger resistance whereas complex modulus plots highlight those with smaller capacitance [30]. The complex modulus (M^*) was calculated using Eq. (4) where $M'=\omega CoZ''$ and $M''=\omega CoZ'$, $C_o=\varepsilon_o A/t$ (ε_o=permittivity of free space, A=area of the electrode surface, and t=thickness of the sample). Fig. 5(a) shows the variation of M'' as a function of frequency. It exhibits that the maxima of the imaginary component of modulus (M''_{max}) shifts towards higher relaxation frequency with rise in temperature. This behaviour suggests that the dielectric relaxation is thermally activated in which hopping mechanism of charge carriers dominates intrinsically [29]. The asymmetric broadening of the peak indicates the spread of relaxation with different time constant, and hence the relaxation in the material is of non-Debye type. The scaling behaviour of the sample was studied by plotting normalized parameters (i.e. $M''/M''max$ versus $\log(f/f_{max})$; f_{max} is frequency corresponding to M''_{max}) at different measuring temperatures and is shown in Fig. 5 (b). The modulus scaling behaviour gives an insight into the dielectric processes occurring inside the material [30]. The low frequency side of the peak in M''/M''_{max} versus $\log(f/f_{max})$ curve represents the range of frequencies in which the charge carriers can cover a longer distance by successfully hopping from one site to another site. The high frequency side of M''/M''_{max} versus $\log(f/f_{max})$ curve represents the range of frequencies in which the charge carriers are spatially confined to their potential wells, and therefore can make only localized motions inside the well. The region where the peak occurs is an indication of the transition from the long-range to the short-range mobility with increase in frequency [30]. The overlapping of all the curves/peaks of different temperatures indicates temperature independent behaviour of the dynamic processes occurring in the material [31].

3.5. Conductivity studies

The dc (bulk) conductivity, σ_{dc}, of the sample has been evaluated from the impedance spectrum using the relation

$$\sigma_{dc}=\frac{t}{R_bA} \tag{8}$$

where R_b is the bulk resistance, t the thickness, and A the surface area of the sample. Fig. 6 shows the variation of $\ln\sigma_{dc}$ with $10^3/T$. It is observed to increase with increase in temperature further

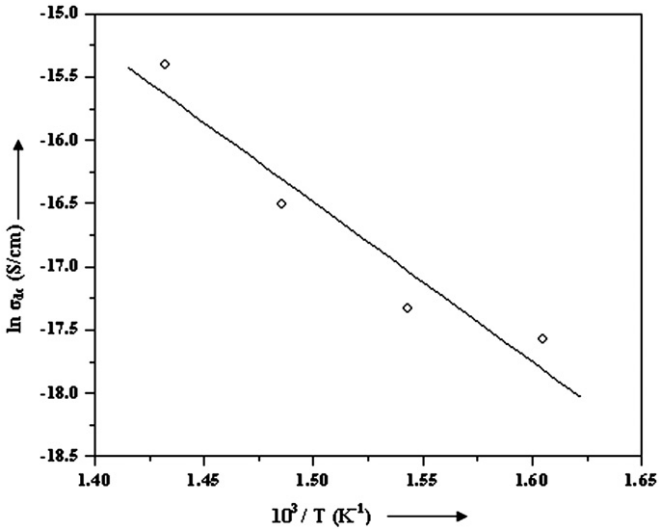

Fig. 6. Variation of $\ln\sigma_{dc}$ with inverse of temperature ($10^3/T$).

confirming the NTCR behaviour. The nature of variation is linear and follows the Arrhenius relationship

$$\sigma_{dc}=\sigma_o\exp\left(\frac{-E_a}{k_BT}\right) \tag{9}$$

where E_a is the activation energy of conduction and T is the absolute temperature. The value of activation energy (E_a) as calculated from the slope of $\ln\sigma_{dc}$ with $10^3/T$ curve is found to be 1.09 eV. This value of E_a is approximately the same as the energy required ($\sim$1 eV) for the motion of oxygen vacancies [27]. This confirms that the observed conductivity is due to the movements of oxygen vacancies in the material.

4. Conclusion

The synthesized $Ba_5NdTi_3Nb_7O_{30}$ compound is single phase having an orthorhombic tungsten–bronze crystal structure with uniform distribution of grains of average size $\sim$2 μm throughout the sample. The compound shows a diffuse type of ferroelectric–paraelectric phase transition having non-relaxor behaviour with a

T_c of 100 °C. Complex impedance analysis suggests dielectric relaxation to be of polydispersive non-Debye type with a temperature dependent behaviour. Modulus analysis has established the possibility of hopping mechanism for electrical transport process in this material. The dc conductivity is found to increase with increase in temperature confirming negative temperature coefficient of resistance (NTCR) behaviour of the compound. The activation energy for conduction (E_a) of the material is found to be 1.09 eV, which is almost the same as the energy required for the motion of oxygen vacancies confirming the conductivity is due to the movements of oxygen vacancies in the material.

Acknowledgments

One of the authors (PG) is grateful to Council of Scientific and Industrial Research (CSIR), New Delhi, India, for the award of Senior Research Fellowship.

References

[1] B. Wul, Nature 157 (1946) 808.
[2] N.S. Vandamme, A.E. Sutherland, L. Jones, K. Bridger, S.R. Winzer, J. Am. Ceram. Soc. 74 (1991) 1785.
[3] R.R. Neurgaonkar, W.F. Hall, J.R. Oliver, W.W. Ho, W.K. Cory, Ferroelectrics 87 (1998) 167.
[4] R.R. Neurgaonkar, W.K. Cory, J. Opt. Soc. Am. B 3 (1986) 274.
[5] D. Liu, Y. Liu, S.Q. Huang, X. Yao, J Am. Ceram. Soc. 76 (1993) 2129.
[6] A. Panigrahi, N.K. Singh, R.N.P. Choudhary, J. Mater. Sci. Lett. 18 (1999) 1579.
[7] P.P. Rao, S.K. Ghosh, P. Koshy, J. Mater. Sci.: Mater. Electron. 12 (2001) 729.
[8] P.B. Jasmieson, S.C. Abrahams, J.L. Bernstein, J. Chem. Phys. 48 (1965) 5048.
[9] P. Ganguly, A.K. Jha, K.L. Deori, J. Alloys Compd. 484 (2009) 40.
[10] P. Ganguly, A.K. Jha, K.L. Deori, Solid State Commun. 146 (2008) 472.
[11] P. Ganguly, S. Devi, A.K. Jha, K.L. Deori, Ferroelectrics 381 (2009) 111.
[12] R. Palai, R.N.P. Choudhary, H.S. Tewari, J. Phys. Chem. Solids 62 (2001) 695.
[13] X.H. Zheng, X.M. Chen, J. Mater. Res. 17 (2002) 1664.
[14] L. Fang, H. Zhang, J.B. Yan, W.M. Yang, Chin. J. Inorg. Chem. 18 (2002) 1131.
[15] X.H. Zheng, X.M. Chen, Solid State Commun. 125 (2003) 449.
[16] J.L. Mukherjee, C.P. Khattak, K.P. Gupta, F.F.Y. Wang, J. Solid State Chem. 24 (1978) 163.
[17] R.N.P. Choudhary, S.R. Shannigrahi, A.K. Singh, Bull. Mater. Sci. 22 (1999) 975.
[18] P. Ganguly, A.K. Jha, K.L. Deori, J. Electroceram. 22 (2009) 257.
[19] C. Dong, J. Appl. Cryst. 32 (1999) 838.
[20] P.R. Das, R.N.P. Choudhary, B.K. Samantray, J. Alloys Compd. 448 (2008) 32.
[21] S.M. Pilgrim, A.E. Sutherland, S.R. Winzer, J. Am. Ceram. Soc. 73 (1990) 3122.
[22] C.K. Suman, K. Prasad, R.N.P. Choudhary, J. Mater. Sci. 41 (2006) 369.
[23] C.K. Suman, K. Prasad, R.N.P. Choudhary, Mater. Chem. Phys. 82 (2003) 140.
[24] F.A. Kröger, H.J. Vink, Solid State Phys. 3 (1956) 307.
[25] V. Raghavan, in: Materials Science and Engineering, Prentice-Hall of India, New Delhi, 2004.
[26] J.R. MacDonald, in: Impedance Spectroscopy Emphasising Solid Materials and Systems, Wiley, New York, 1987.
[27] S. Sen, R.N.P. Choudhary, P. Pramanik, Physica B 387 (2007) 56.
[28] V. Shrivastava, A.K. Jha, R.G. Mendiratta, Physica B 371 (2006) 337.
[29] B. Behera, P. Nayak, R.N.P. Choudhary, Mater. Res. Bull. 43 (2008) 401.
[30] P.S. Das, P.K. Chakraborty, B. Behera, R.N.P. Choudhary, Physica B 395 (2007) 98.
[31] S. Saha, T.P. Sinha, Phys. Rev. B 65 (2002) 1341031.

J Electroceram (2009) 22:257–262
DOI 10.1007/s10832-007-9337-6

Enhancement of dielectric properties by optimization of sintering condition in tungsten–bronze structured $Ba_5SmTi_3Nb_7O_{30}$ ferroelectric ceramics

Prasun Ganguly · A. K. Jha · K. L. Deori

Received: 29 March 2007 / Accepted: 25 September 2007 / Published online: 14 November 2007

Abstract In this work, polycrystalline $Ba_5SmTi_3Nb_7O_{30}$ tungsten–bronze structured ferroelectric ceramics were synthesized by solid-state reaction technique at different sintering temperatures and durations. The X-ray diffractograms reveal the formation of the compounds in orthorhombic crystal system. The density of the compound is observed to increase with increase in sintering temperature and duration. Scanning electron microscopy (SEM) has been used for the microstructural investigation. Detailed dielectric properties of the compounds have been studied as a function of frequency and temperature. The variations of dielectric constant (ε_r') with temperature show that the compounds undergo a diffuse type ferro-paraelectric phase transition. The dielectric constant is found to increase with the increasing sintering temperature and duration. In all the samples, the variation of dielectric loss (tan δ) with temperature is observed to be almost constant initially but it increases as temperature is increased and a peak is observed only when the material is sintered at higher temperature for longer duration. The frequency dependence of dielectric constant and loss shows a decreasing trend up to nearly 10 kHz and beyond this frequency there is almost no variation. Also, the diffusivities of the samples have been calculated and it is found to increase with increasing sintering temperature and duration.

Keywords Tungsten–bronze structure · Sintering temperature and duration · Dielectric properties · Diffusivity

P. Ganguly (✉) · A. K. Jha · K. L. Deori
Thin Films & Materials Science Laboratory,
Department of Applied Physics, Delhi College of Engineering,
Delhi 110042, India
e-mail: gangulyprasun@yahoo.co.in

A. K. Jha
e-mail: dr_jha_ak@yahoo.co.in

1 Introduction

Since the discovery of ferroelctricity in $BaTiO_3$ [1], large number of new ferroelectric materials have been discovered having significant industrial and commercial applications. Materials in different structural groups like perovskite, tungsten–bronze (TB), spinel, pyrochlore are now well known [2–7]. Some niobates and tantalates with TB structure have attracted attention because of their interesting ferroelectric, pyroelectric, piezoelectric and nonlinear optical properties [8–14]. The TB-type structure consists of a complex array of distorted BO_6 octahedra sharing corners in such a way that three different types of interstices (A, B and C) are available for cation occupation in the general formula $[(A_1)_4(A_2)_2(C)_4][(B_1)_2(B_2)_8]O_{30}$ [15]. In this formula, A_1 and A_2 sites are usually filled by divalent or trivalent cations, B_1 and B_2 sites by tetravalent or pentavalent cations and C site being small, often remains empty giving the general formula $A_6B_{10}O_{30}$ for the tungsten–bronze structure. In this family, researchers have shown interest in $Ba_2Na_3RNb_{10}O_{30}$ (R=La, Y, Gd, Eu and Dy) [16], $K_2LaNb_5O_{15}$ [17], $Ba_4NaNb_{10}O_{30}$ [18], $Ba_5SmTi_3Nb_7O_{30}$ [19] compounds. However, to the best of our knowledge, not much work has been reported on $Ba_5SmTi_3Nb_7O_{30}$ compound by systematically varying the sintering condition. In this work, we have systematically studied the effect of sintering temperature and duration on the structure and properties of $Ba_5SmTi_3Nb_7O_{30}$.

2 Experimental

The polycrystalline samples of $Ba_5SmTi_3Nb_7O_{30}$ (BSTN) were prepared by solid-state reaction technique by taking high purity $BaCO_3$, TiO_2, Nb_2O_5 (all from M/s Aldrich, USA) and Sm_2O_3 (M/s Alfa Aesar, USA) in their

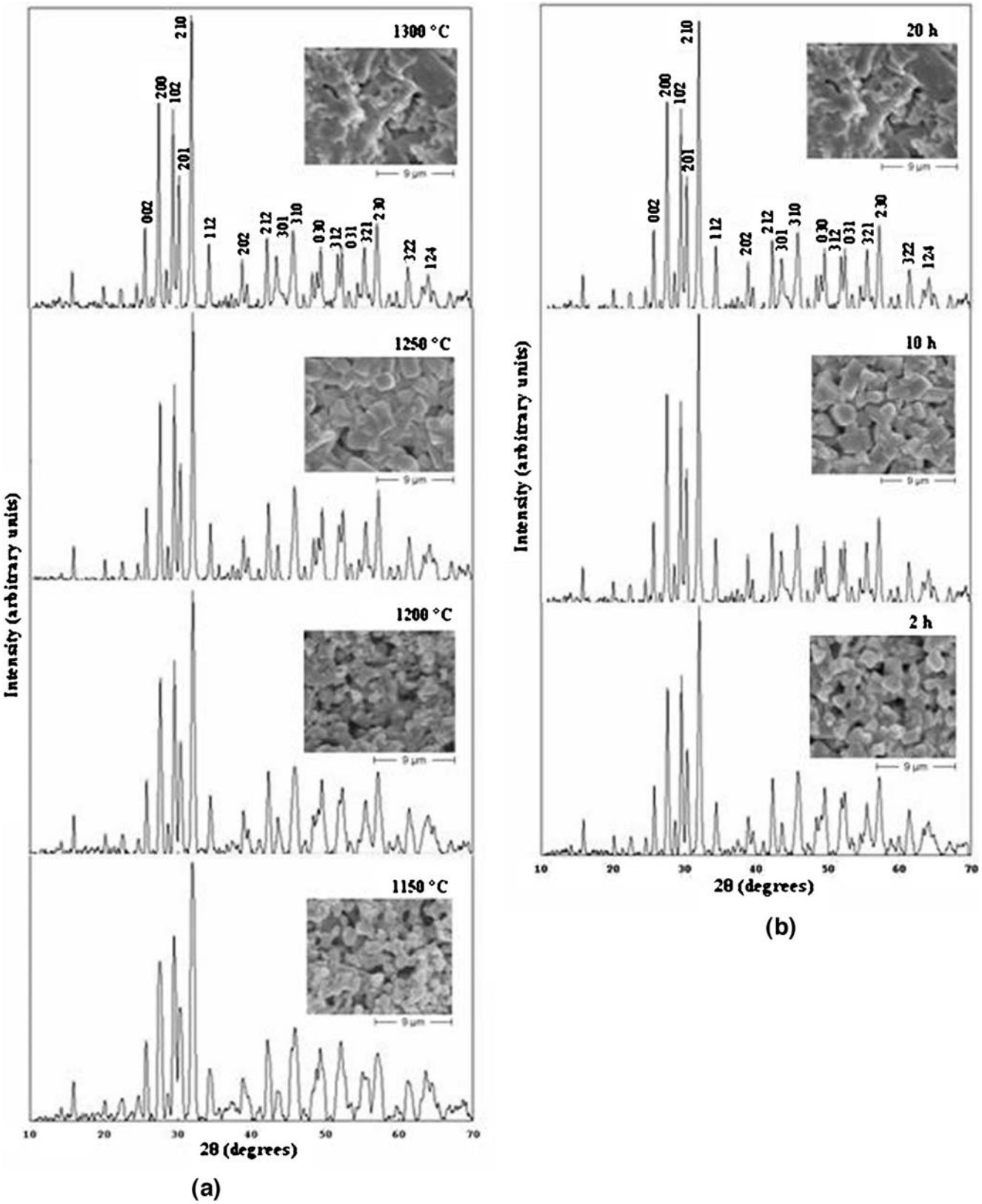

Fig. 1 XRD patterns of $Ba_5SmTi_3Nb_7O_{30}$ sintered at (**a**) different temperatures for 20 h and (**b**) different durations at 1300°C. In inset the respective SEM micrographs of the samples are shown

Table 1 Lattice parameters, relative density, average grain size, dielectric properties (at 100 kHz) and diffusivity of $Ba_5SmTi_3Nb_7O_{30}$ synthesized at various sintering conditions.

Sintering Conditions	a (Å)	b (Å)	c (Å)	Relative Density (%)	Average Grain Size (μm)	$\varepsilon'_{R.T.}$	ε'_{max}	T_c (°C)	γ
1150°C; 20 h	6.5198	5.6101	6.9338	62.41	1.4	64.9838	86.3004	210	1.34
1200°C; 20 h	6.5398	5.5728	6.9253	65.66	1.8	88.3513	132.3420	180	1.47
1250°C; 20 h	6.5374	5.5397	6.9001	74.84	2.6	154.0528	232.2804	170	1.73
1300°C; 20 h	6.4050	5.5566	6.8005	90.23	4.2	259.1363	416.0325	165	1.95
1300°C; 10 h	6.4106	5.5595	6.8112	80.34	2.2	193.5925	303.1267	170	1.71
1300°C; 2 h	6.3858	5.5435	6.7648	70.14	1.6	136.4142	207.0189	185	1.45

stoichiometric proportions. The materials were thoroughly ground in an agate mortar and passed through sieve of appropriate size. This powder mixture was then calcined at 1100°C for 20 h in an alumina crucible. The calcined mixture were ground and admixed with 4–5 wt.% polyvinyl alcohol (PVA) as a binder and then pressed at ~300 MPa into disk shaped pellets. These pellets were then sintered at different sintering conditions. One set of pellets were sintered at temperatures from 1150 to 1300°C at an interval of 50°C for 20 h and another set of pellets were sintered at 1300°C for 2 h, 10 h and 20 h.

X-ray diffractograms of all the sintered pellets were recorded using Philips (X'Pert Model) diffractometer in the

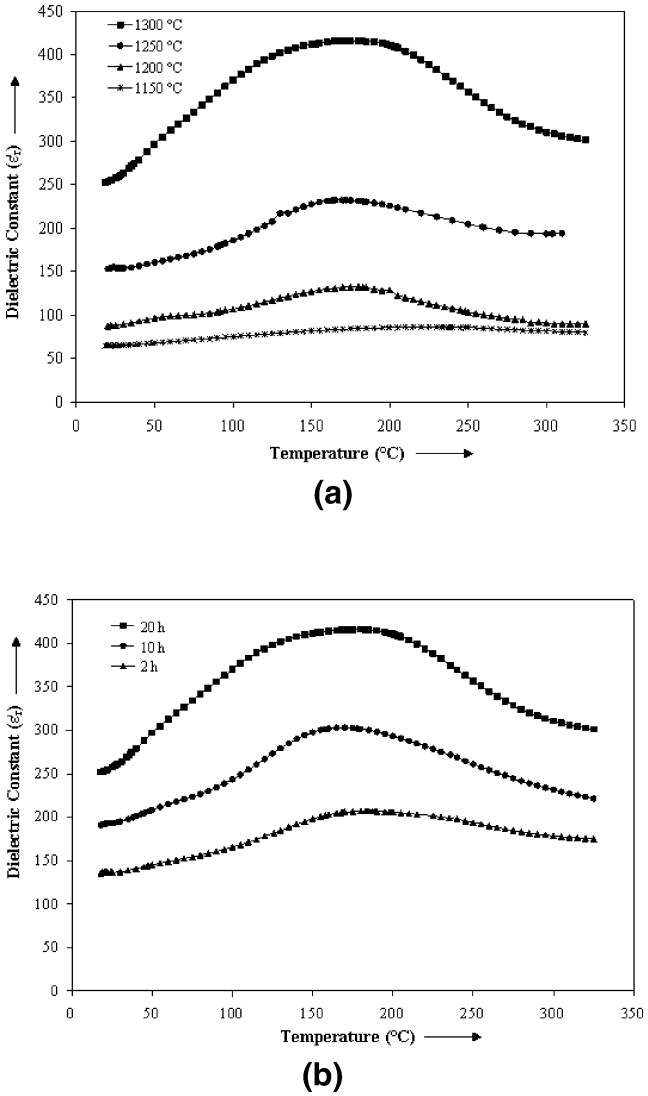

Fig. 2 Variation of dielectric constant with temperature at different (**a**) sintering temperature and (**b**) sintering time at 100 kHz

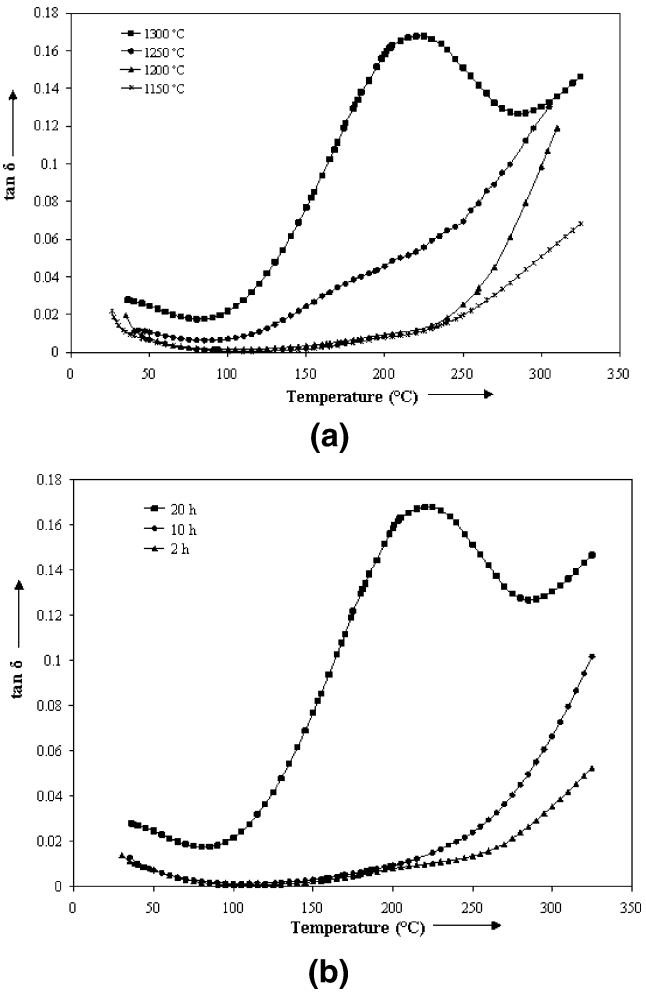

Fig. 3 Variation of dielectric loss (tan δ) with temperature at different (**a**) sintering temperature and (**b**) sintering time at 100 kHz

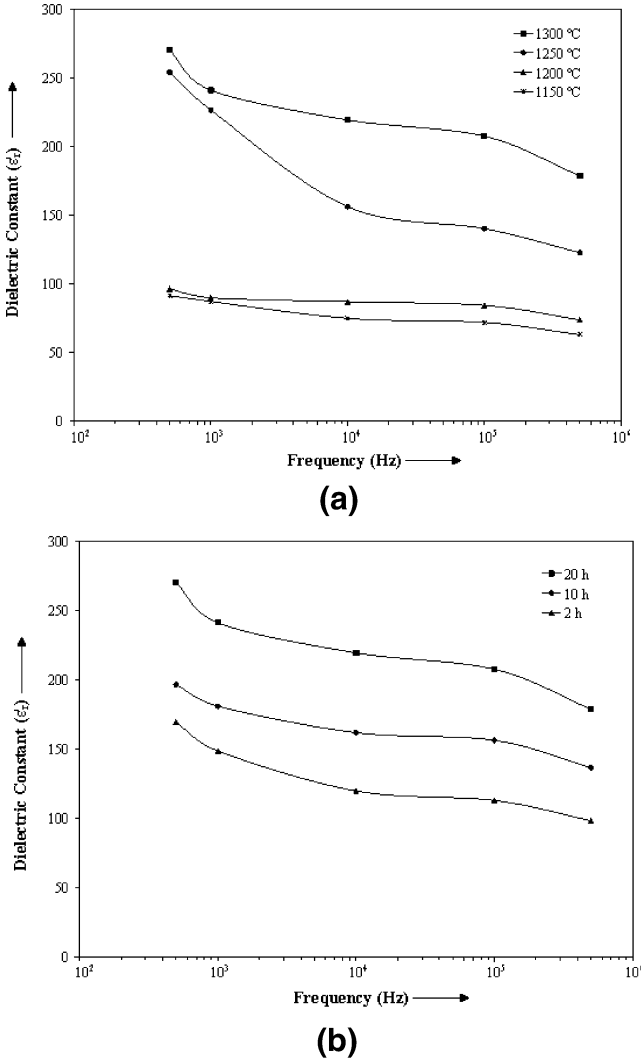

Fig. 4 Variation of dielectric constant (ε_r') with frequency at different (**a**) sintering temperature and (**b**) sintering time at room temperature

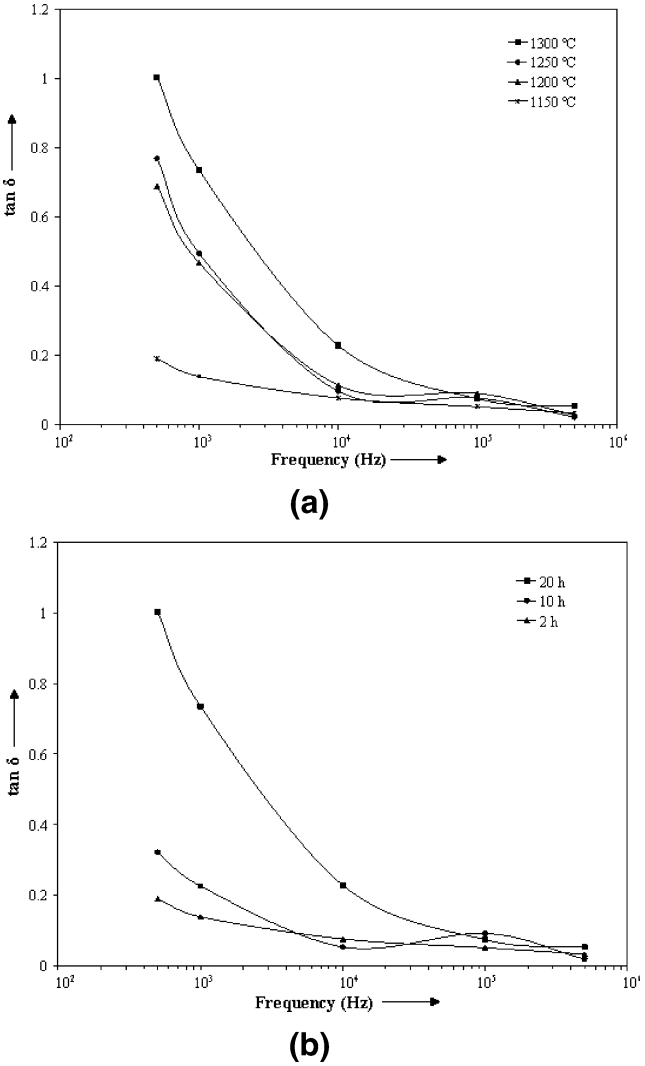

Fig. 5 Variation of dielectric loss (tan δ) with frequency at different (**a**) sintering temperature and (**b**) sintering time at room temperature

range $10° \leq 2\theta \leq 70°$ with CuK_α radiation (λ=1.5405 Å). The densities of the sintered pellets were measured using Archimedes principle in a laboratory made set-up with ethylene glycol. The microstructural study of the samples was carried out using Scanning Electron Microscope (Jeol, JSM—840), operated at 20 kV. The sintered pellets were polished and coated with silver paste on both sides to act as electrodes and cured at 325°C for 1 h. The dielectric measurements were carried out using HP 4284A LCR meter operating at oscillation amplitude of 1 V.

3 Results and discussion

Figure 1(a) and (b) shows the X-ray diffraction patterns of all the studied samples which reveal the formation of single-phase compounds. However, some peaks of the samples with lower sintering temperature are merged indicating incomplete growth of the phase. The lattice parameters of the samples were calculated (Table 1) using the observed interplanar spacing *d*-values from the diffractograms and refined using the least square refinement method by a computer program package PowderX [20]. The observed decrease in lattice parameters on increase in sintering temperature is possibly due to increased formation of oxygen vacancies discussed later in the text. The peaks have been indexed using the observed d and the calculated lattice parameters. From these results, it is found that BSTN samples sintered at above mentioned sintering conditions have an orthorhombic crystal with a TB-type structure.

The values of the relative density of the samples are given in Table 1. It is observed that relative density increases as the sintering temperature and time increases. This is possibly due to decrease in the porosity and increase in the grain size of

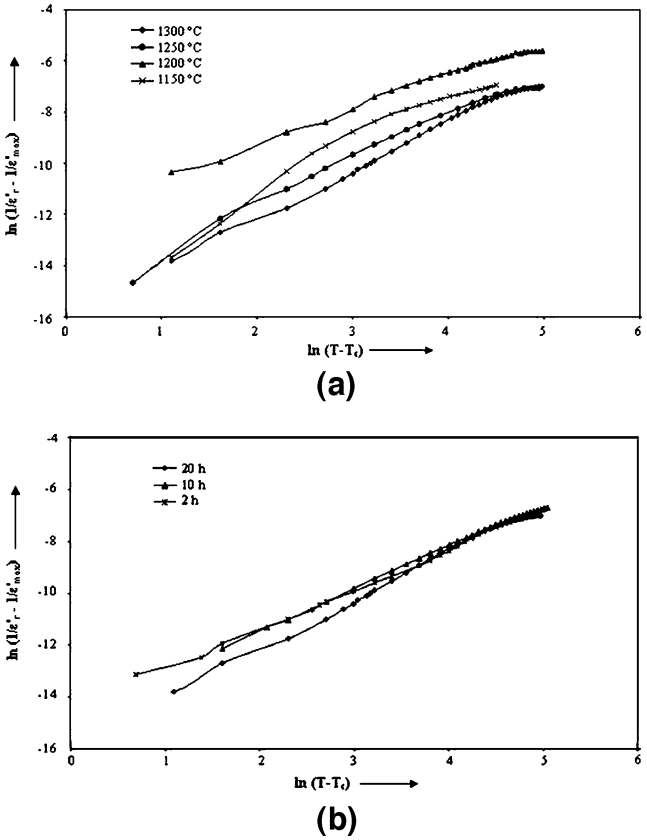

Fig. 6 Variation of $\ln\left(1/\varepsilon'_r - 1/\varepsilon'_{\max}\right)$ with ln $(T–T_c)$ as a function of (**a**) sintering temperature and (**b**) sintering duration

the specimens as seen in SEM micrographs (Fig. 1(a) and (b) inset) with increase in the sintering temperature and time, also given in Table 1.

The dielectric constant $\left(\varepsilon'_r\right)$ and dielectric loss (tan δ) of the studied samples sintered at various sintering temperatures were measured from room temperature to 325°C at 100 kHz frequency. The maximum dielectric constant $\left(\varepsilon'_{\max}\right)$ and room temperature dielectric constant $\left(\varepsilon'_{R.T}\right)$ value of all the samples are given in Table 1 with their curie temperatures (T_c). In all the samples, a diffuse type of ferro-paraelectric phase transition is observed. Figure 2(a) and (b) shows the temperature variation of dielectric constant at 100 kHz for different sintering temperature and time. It is found that ε'_r increases as sintering temperature and duration of the BSTN samples increases. The increase in ε'_r can be understood by the increase in the grain size with increase in sintering temperature and time (Table 1). The higher sintering temperature for longer duration enhances the average grain size, making the domain wall motion easier resulting in an increased dielectric constant [21]. Also, it is known that these TB structured compounds are expected to lose oxygen during sintering at high temperature [22, 23] as per the reaction which can be represented by Kröger and Vink notation [24]:

$$O_o \rightarrow \frac{1}{2}O_2 \uparrow + V_o^{\bullet\bullet} + 2e^-$$

where $V_o^{\bullet\bullet}$ denotes oxygen vacancies. The defects such as oxygen vacancies $V_o^{\bullet\bullet}$, act as space charge. So as we increase the sintering temperature and duration in this material more and more oxygen vacancies are created. The increase in ε'_r value is known to be related to the oxygen ions or oxygen vacancies created during sintering [25]. This could be another possible cause for the increase in ε'_r as sintering temperature and duration of the BSTN samples increases.

Figure 3(a) and (b) depicts the temperature variation of dielectric loss at 100 kHz for different sintering conditions. It is observed that the loss increases with temperature. The loss is found to be higher in the sample which is sintered at higher sintering temperature for longer duration. The source of dielectric loss in insulating ceramics is space charge polarization and/or domain wall relaxation [26]. From the above discussion it is reasonable to believe that the space charge, in the form of oxygen vacancies, is primarily responsible for an appreciable increase in dielectric loss in the samples sintered at higher sintering temperature for longer durations. Also the loss increases with increase in temperature as the oxygen vacancy induced polarization becomes dominant at high temperatures [27]. Unlike other samples, a peak is observed in the tan δ versus temperature curve of the specimen sintered at 1300°C for 20 h. This could be the relaxation peak whose formation is attributed to the oxygen vacancies [28, 29] which are present in large concentration in this highly sintered sample of BSTN.

Figure 4(a) and (b) shows the frequency variation of ε'_r over the range 500 Hz to 500 kHz at room temperature of the studied samples. It is observed that ε'_r decreases steadily for samples sintered at 1250°C and 1300°C (for all durations) as the frequency increases from 500 Hz to 10 kHz and remains almost constant at frequencies above 10 kHz. However, the samples sintered at 1150°C and 1200°C, show no appreciable variation in ε'_r values in the entire frequency range. The dielectric constant of a material has four polarization contributions: electronic, ionic, dipolar and space charge [30]. In the present work, contribution from the dipolar polarization is not expected as the applied electric field of about 6 V/cm is too small to alter the orientation of the dipoles. Response frequencies for electronic and ionic polarizations are ~10^{16} and 10^{13} Hz, respectively; and at frequencies above 10 kHz, contribution from space charge polarization is not expected [30]. As discussed above, as we increase the sintering temperature and time in the BSTN samples, more and more oxygen vacancies are generated. The defects such as oxygen vacancies, $V_o^{\bullet\bullet}$, acting as space charge play an important role in the polarization which becomes dominant at lower frequencies [31, 32]. The high value of ε'_r for low frequencies in case of samples sintered at higher temperatures (1250–1300°C) can thus be attributed to the presence of such space charges. Moreover, higher relative density

and larger grains size supports the observation of high ε'_r value in the samples sintered at higher temperatures (1250–1300°C). The small amount of oxygen vacancies in the samples sintered at lower temperature (1150–1200°C) results in negligible variation of ε'_r value with frequency.

Figure 5(a) and (b) shows the variation of tan δ with frequency at room temperature. It also decreases sharply upto 10 kHz for all the samples and beyond this it is almost independent of frequency. This can also be understood in terms of space charge as the source of dielectric loss in these materials is space charge polarization [26].

In all the samples, broad peak in dielectric constant vs. temperature curve is observed. The broadening of the dielectric peaks may be attributed to the occurrence of more disordering in the system on increasing sintering temperature and time. The degree of disorderness or the diffusivity constant (γ) has been calculated using the formula [33]

$$\ln\left(1/\varepsilon'_r - 1/\varepsilon'_{\max}\right) = \gamma \ln(T - T_c) + \text{constant}$$

The value of γ for all the samples at 100 kHz obtained from the slope of the curve $\ln\left(1/\varepsilon'_r - 1/\varepsilon'_{\max}\right)$ versus ln (T–T_c), as shown in Fig. 6(a) and (b), has been found to be between 1 (obeying Curie-Weiss law) and 2 (for completely disordered system) (Table 1). It is found to increase with sintering temperature and duration indicating increase in disorderness in the system with increase in sintering temperature and time. This could be due to the defects (here oxygen vacancy) induced disorderness [34] which increases with increase in sintering temperature and duration.

4 Conclusions

For all sintering conditions undertaken in the present work, BSTN shows an orthorhombic crystal system with a TB-type structure. The density and the average grain size increases with increase in sintering temperature and time. The dielectric constant $\left(\varepsilon'_r\right)$ as well as dielectric loss (tan δ) increases significantly by increasing sintering temperature and time. However, a peak in the dielectric loss versus temperature curve has been observed only when the material is sintered at higher temperature for longer duration. The disorderness in the system is found to increase as the sintering temperature and duration is increased.

References

1. B.K. Wul, L.M. Goldman, C.R. Acad. Sci. URSS **46**, 133(1945)
2. I. Coondoo, A.K. Jha, S.K. Agarwal, N.C. Soni, J. Electroceram **16**, 393(2006)
3. I. Coondoo, A.K. Jha, S.K. Agarwal, J. Eur. Cer. Soc **27**, 253(2007)
4. V. Shrivastava, A.K. Jha, R.G. Mendiratta, Solid State Comm **133**, 125(2005)
5. C.F.G. Stenger, A.J. Burggraaf, J. Phys. Chem. Solids **41**, 17(1980)
6. C.F.G. Stenger, A.J. Burggraaf, J. Phys. Chem. Solids **41**, 25(1980)
7. K.S. Singh, R. Sati, R.N.P. Choudhary, J. Mater. Sci. Lett **11**, 788 (1992)
8. R.R. Neurgaonkar, W.F. Hall, J.R. Oliver, W.W. Ho, W.K. Cory, Ferroelectrics **87**, 167(1998)
9. R.R. Neurgaonkar, J.G. Nelson, J.R. Oliver, Mater. Res. Bull **25**, 959(1990)
10. R.R. Neurgaonkar, J.G. Nelson, J.R. Oliver, Mater. Res. Bull **27**, 677(1992)
11. N. Wakiya, J.K. Wang, A. Saiki, K. Shinozaki, N. Mizutani, J. Eur. Ceram. Soc **19**, 1071(1999)
12. Z.X. Cheng, S.J. Zhang, G.Y. Zhou, J.H. Liu, J.R. Han, H.C. Chen, Mater. Res. Bull **35**, 1107(2000)
13. Y.K. Hwang, Y.U. Kwon, Mater. Res. Bull **32**, 1495(1997)
14. B. Tribotte, J.M. Haussonne, G. Desgardin, J. Eur. Ceram. Soc **19**, 1105(1999)
15. P.B. Jasmieson, S.C. Abrahams, L. Bernstein, J. Chem. Phys **48**, 5048(1965)
16. J.L. Mukherjee, J. Solid State Chem **24**, 163(1978)
17. H. Iwaski, Mater. Res. Bull **6**, 251(1971)
18. K.V. Masuno, J. Phys. Soc. Jpn **19**, 323(1964)
19. S.R. Shannigrahi, R.N.P. Choudhary, A. Kumar, H.N. Acharya, J. Phys. Chem. Solids **59**, 737(1998)
20. C. Dong, J. Appl. Cryst **32**, 838(1999)
21. H.T. Martirena, J.C. Burfoot, J. Phys. C: Solid State Phys **7**, 3162 (1976)
22. C.K. Suman, K. Prasad, R.N.P. Choudhary, J. Mat. Sci **41**, 369 (2006)
23. C.K. Suman, K. Prasad, R.N.P. Choudhary, Mat. Chem. & Phys **82**, 140(2003)
24. F.A. Kröger, H.J. Vink, Solid State Phys **3**, 307(1956)
25. P. Goel, K.L. Yadav, Mat. Lett **60**, 3183(2006)
26. I.S. Zheludev, *Physics of Crystalline Dielectrics, Vol I: Crystallography & Spontaneous Polarization* (Plenum, New York (1971)
27. T. Friessnegg, S. Aggarwal, R. Ramesh, B. Nielsen, E.H. Poindexter, D.J. Keeble, Appl. Phys. Lett **77**, 127(2000)
28. W.P. Lu, X.Y. Mao, X.B. Chen, J. Appl. Phys **95**, 1973(2004)
29. W.P. Lu, J. Zhu, H. Sun, X.B. Chen, J. Mat. Res **20**, 971(2005)
30. R.C. Buchanan, *Ceramic Materials for Electronics: Processing, Properties and Applications* (Marcel Dekker, New York (1986), p. 38
31. Y. Noguchi, M. Miyayama, Appl. Phys. Lett **78**, 1903(2001)
32. A. Chen, Y. Zhi, L.E. Cross, Phys. Rev. B **62**, 228(2000)
33. S.M. Pilgrim, A.E. Sutherland, S.R. Winzer, J. Am. Ceram. Soc **73**, 3122(1990)
34. V. Raghavan, *Materials Science and Engineering* (Prentice-Hall of India, New Delhi (2004), p. 194

Ferroelectrics, 381:111–119, 2009

ISSN: 0015-0193 print / 1563-5112 online
DOI: 10.1080/00150190902869772

Taylor & Francis
Taylor & Francis Group

Dielectric and Pyroelectric Studies of Tungsten—Bronze Structured $Ba_5SmTi_3Nb_7O_{30}$ Ferroelectric Ceramics

PRASUN GANGULY, SHEELA DEVI, A. K. JHA,* AND K. L. DEORI

Thin Film & Materials Science Laboratory, Department of Applied Physics, Delhi College of Engineering (Faculty of Technology, University of Delhi) Delhi–110042, India

In the present work, sample of composition $Ba_5SmTi_3Nb_7O_{30}$ was prepared by solid-state reaction method. X-ray diffraction (XRD) analysis reveals the formation of single-phase compound with an orthorhombic structure. The grain morphology of the sample has been investigated by scanning electron microscopy. Dielectric properties of the compound have been studied as a function of temperature and frequency. The variation of dielectric constant (ε'_r) with temperature at different frequencies shows that the compound has a dielectric anomaly of ferroelectric to paraelectric type at 170°C, and exhibits non-relaxor kind of diffuse phase transition. At different frequencies, the variation of dielectric loss (tan δ) with temperature shows at lower temperatures the loss is almost constant and increases sharply at higher temperatures. The frequency dependence of dielectric constant and loss show a decreasing trend upto 10 kHz and beyond this frequency they remain almost constant. The variation of pyroelectric coefficient with temperature is reported in the present work. Pyroelectric figure of merit have been calculated from the pyroelectric coefficients.

Keywords Dielectric constant; dielectric loss; curie temperature; pyroelectric coefficient

Introduction

Due to the interesting dielectric, ferroelectric, pyroelectric, piezoelectric and nonlinear optical properties for applications in various devices such as transducers, actuators, capacitors, and ferroelectric random access memory, more and more attentions are being paid to the dielectric ceramics with tungsten bronze (TB) structure [1–5]. The TB structure consists of a complex array of distorted BO_6 octahedra sharing corners in such a way that three different types of interstices (A, B and C) are available for a wide variety of cation substitution in the general formula $[(A_1)_4(A_2)_2(C)_4][(B_1)_2(B_2)_8]O_{30}$ [6]. In the given formula, A_1 and A_2 sites are usually filled by divalent or trivalent cations, B_1 and B_2 sites by tetravalent or pentavalent cations and C site being small, often remains empty giving the general formula $A_6B_{10}O_{30}$ for the filled tungsten-bronze structure. It has been found that

Received August 3, 2008; in final form December 31, 2008.
*Corresponding author. E-mail: dr_jha_ak@yahoo.co.in

different ionic substitutions at the above mentioned sites can play an important role in tailoring the physical properties. Some compounds such as $Ba_5RTi_3M_7O_{30}$, $Ba_4R_2Ti_4M_6O_{30}$, $Ba_3R_3Ti_5M_5O_{30}$ have been studied in BaO-R_2O_3-TiO_2-M_2O_5(R = Dy, La, Nd, Sm; M = Nb, Ta) system [4, 5, 7–13]. Some works on TB structured $Ba_5SmTi_3Nb_7O_{30}$have been reported earlier [10, 13–15]. However, no report on the pyroelectric property of this compound is found in the literature. The present paper reports the dielectric and pyroelectric studies of $Ba_5SmTi_3Nb_7O_{30}$.

Experimental

The polycrystalline sample of $Ba_5SmTi_3Nb_7O_{30}$ was prepared from high purity (>99%) $BaCO_3$, TiO_2, Nb_2O_5 (all from M/s Aldrich, USA) and Sm_2O_3(M/s Alfa Aesar, USA) using high-temperature solid-state reaction technique. These materials were taken in stoichiometric proportions, thoroughly ground in an agate mortar and then passed through sieve of appropriate size. The mixture was then calcined at 1100°C for 20 hours in an alumina crucible. The calcined mixture was ground and admixed with 4–5 wt.% polyvinyl alcohol (PVA) as a binder and then pressed (300 MPa) into disk shaped pellet. The pellet was then sintered at 1300°C for 10 hours. This is the optimized sintering temperature found on making an extensive study and reported elsewhere [16].

X-ray diffractogram of the sintered pellet was recorded using a Philips (X'Pert Model) diffractometer in the range $10^\circ \leq 2\theta \leq 70^\circ$ using CuK_α radiation ($\lambda = 1.5405$ Å) with a scanning rate of 2°/min. The morphological study of the sample was carried out using Scanning Electron Microscope (Jeol, JSM – 840), operated at 20 kV. The sintered pellet was polished and silver pasted on both sides and cured at 325°C for 1hour. The dielectric measurements were carried out using HP 4284A LCR meter operating at oscillation amplitude of 1 V. The measurement of the pyroelectric coefficient was performed using the Byer-Roudy technique [17]. The sample was first poled at 10 kV/cm at an elevated temperature (∼100°C) for 2 h in silicon oil. The poled sample was then placed in a programmable furnace, and the temperature was increased at a rate of 2°C/min. The current generated in the specimen was measured using a high precision electrometer (Keithley 6517A).

Results and Discussion

1. XRD and SEM Analysis

Room temperature X-Ray diffraction pattern of $Ba_5SmTi_3Nb_7O_{30}$ (BSTN) is shown in Fig. 1, which reveals the formation of single—phase compound. The lattice parameters were calculated using the observed interplanar spacing d-values from the diffractograms and refined using the least square refinement method by a computer program package PowderX [18]. These refined lattice parameters are: $a = 6.4106$ Å, $b = 5.5595$ Å, $c = 6.8112$ Å. The peaks were indexed using the observed d-values and the calculated lattice parameters. From these, it is found that BSTN has an orthorhombic TB-type structure.

The SEM micrograph of the sample is shown in Fig. 1 (inset). It can be seen from the micrograph that the grains are homogeneously distributed throughout the sample. The average grain size of the compound is in the range of 2 μm.

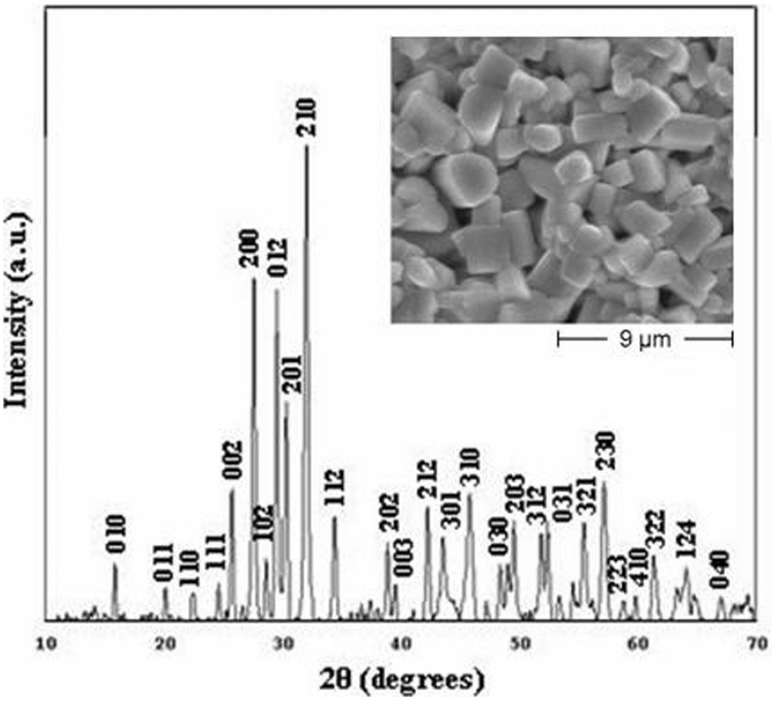

Figure 1. X-Ray diffraction pattern and SEM micrograph (inset) of $Ba_5SmTi_3Nb_7O_{30}$ compound.

2. Dielectric Properties

The dielectric constant (ε'_r) and dielectric loss (tan δ) of the specimen were measured from room temperature to 325°C at the frequencies of 1 kHz, 10 kHz and 100 kHz, shown in Fig. 2 and Fig. 3 respectively. It is found that the compound has a dielectric anomaly at 170°C indicating the occurrence of ferroelectric-paraelectric phase transition. It is also observed that the compound has same T_c at all the frequencies, which suggests that the compound does not show any relaxor behaviour [19]. The dielectric peak is found to be broadened indicating the existence of diffuse phase transition. The diffusivity constant or degree of disorderness (γ) has been calculated using the formula [20]:

$$\ln\left(\frac{1}{\varepsilon'_r} - \frac{1}{\varepsilon'_{r\,\max}}\right) = \gamma \ln (T - T_c) + \text{constant} \tag{1}$$

The value of γ calculated from the slope of Fig. 2 (inset) is found to be 1.71 at 100 kHz which is between 1 (obeying Curie-Weiss law) and 2 (for completely disordered system) thus confirming the diffused phase transition [21]. It is known that these TB structured compounds lose oxygen during sintering at high temperature [22, 23] which using Kröger and Vink notation [24] can be represented:

$$O_\circ \rightarrow \frac{1}{2} O_2 \uparrow + V_\circ^{\cdot\cdot} + 2e^-$$

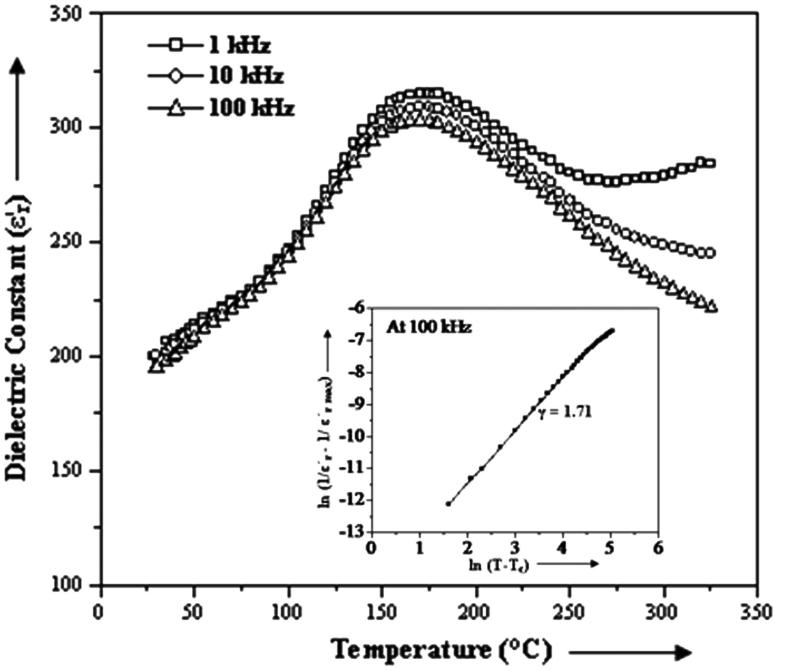

Figure 2. Variation of dielectric constant (ε'_r) with temperature at 1 kHz, 10 kHz, 100 kHz frequencies and variation of ln $(1/\varepsilon'_r - 1/\varepsilon'_{r\,max})$ with ln $(T - T_c)$ at 100 kHz (inset).

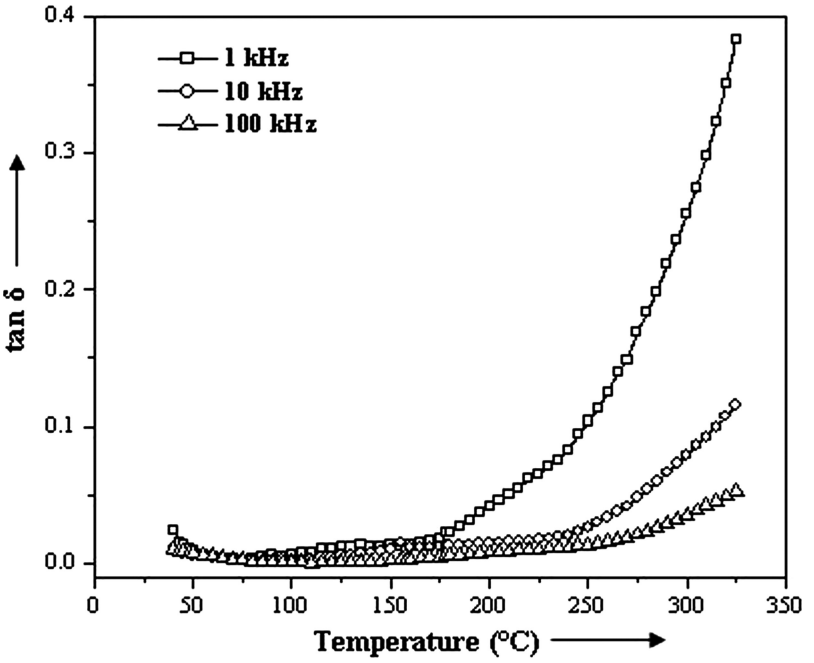

Figure 3. Variation of dielectric loss (tan δ) with temperature at 1 kHz, 10 kHz, 100 kHz frequencies.

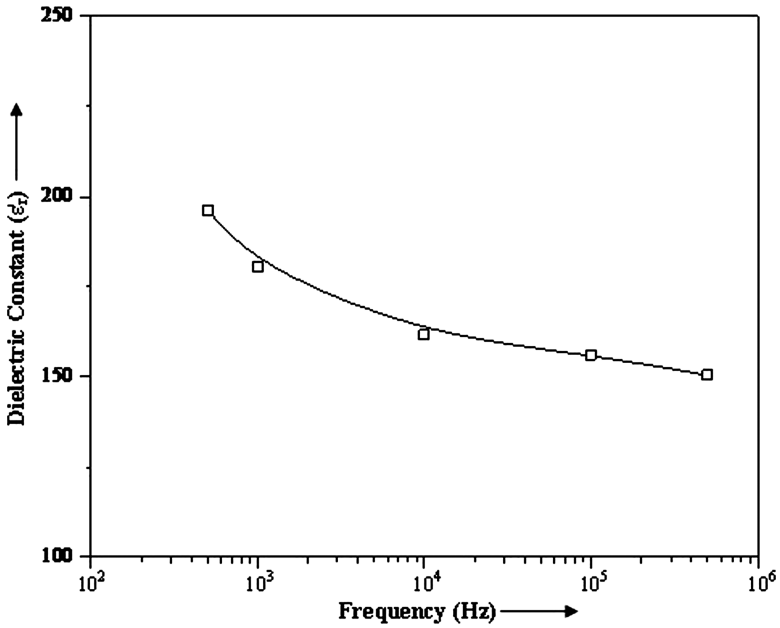

Figure 4. Variation of dielectric constant (ε'_r) with frequency at room temperature.

where $V_o^{\cdot\cdot}$ denotes oxygen vacancies. The defects such as oxygen vacancies $V_o^{\cdot\cdot}$ induce disorderness in the system [25] resulting in a diffuse type ferroelectric—paraelectric phase transition.

At the above mentioned frequencies, the variation of dielectric loss (tan δ) with temperature shows that at low temperature the loss is almost constant but at higher temperatures it increases sharply. The source of dielectric loss in these ceramics is space charge polarization/domain wall relaxation [26]. The presence of defects like oxygen vacancies, $V_o^{\cdot\cdot}$, that act as space charges which are more active at higher temperatures [27] explain the observed higher losses at higher temperatures.

Figure 4 shows the frequency variation of ε'_r over the range 500 Hz to 500 kHz at room temperature of the studied sample. It is observed that ε'_r decreases steadily as the frequency increases from 500 Hz to 10 kHz and remains almost constant at frequencies above 10 kHz. The dielectric constant of a material has four polarization contributions: electronic, ionic, dipolar and space charge [28]. In the present work, contribution from the dipolar polarization is not expected, as the applied electric field is 6 V/cm, which is too small to alter the orientation of the dipoles. Response frequencies for electronic and ionic polarizations are $\sim 10^{16}$ and 10^{13} Hz, respectively; and at frequencies above 10 kHz, contribution from space charge polarization is not expected [28]. The defects such as oxygen vacancies, $V_o^{\cdot\cdot}$, acting as space charge play an important role in the polarization which are dominant at lower frequencies [29, 30]. The high value of ε'_r for low frequencies can thus be attributed to the presence of such space charges.

Figure 5 shows the variation of tan δ with frequency at room temperature. It also decreases sharply upto 10 kHz and beyond this it is almost independent of frequency. The higher values of dielectric loss at low frequencies can also be understood in terms of oxygen vacancies that act as space charge which are active at low frequencies [29,30].

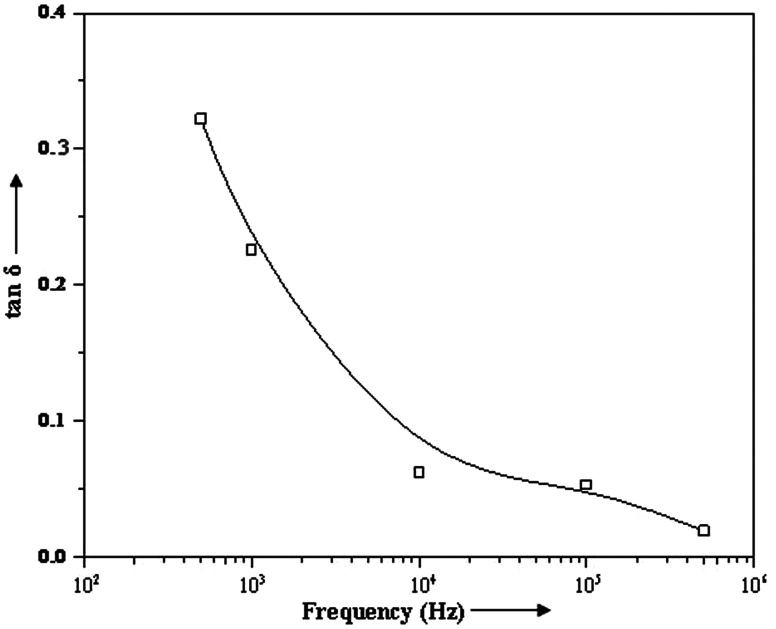

Figure 5. Variation of dielectric loss (tan δ) with frequency at room temperature.

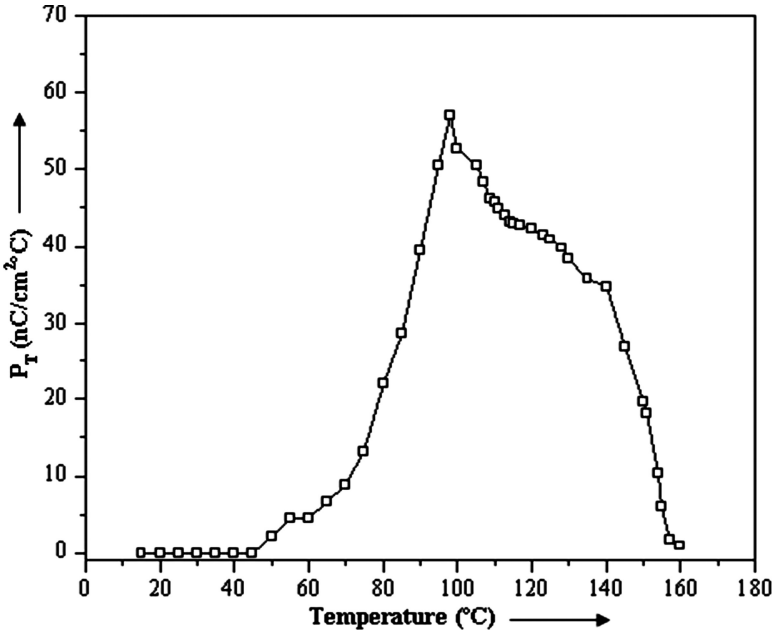

Figure 6. Variation of pyroelectric coefficient (P_T) with temperature.

3. Pyroelectric Studies

The temperature variation of pyroelectric coefficient is shown in Fig. 6. The pyroelectric coefficient (P_T) was calculated using the relation [31]:

$$P_T = \frac{P_I}{A\left(\frac{dT}{dt}\right)} \tag{2}$$

where P_I is the pyroelectric current, A the area of the conducting surface of the sample and dT/dt is the rate of change in temperature. The pyroelectric current as well as pyroelectric coefficient passes through a peak at a temperature (98°C) lower than the ferroelectric transition temperature (T_c). The maximum pyroelectric coefficient at this temperature was found to be 57.1 $nCcm^{-2\circ}C^{-1}$ which is smaller compared to the reported values for other ferroelectric oxide [32]. The pyroelectric current is generated due to the spontaneous polarization change with temperature. It is known that in diffuse kind of phase transition, the rate of change of spontaneous polarization with temperature is maximum at temperature well below T_c [33] which is in conformity with the observed diffuse phase transition. Pyroelectric figure of merit (R_v) have been calculated from the pyroelectric coefficients and dielectric constant at 100 kHz by using the following formula [34]:

$$R_v = \frac{P_I}{\varepsilon_r'} \tag{3}$$

and its variation with temperature is shown in Fig. 7. It suggests that the compound as a pyroelectric sensor has maximum efficiency at temperature 98°C which is lower than the curie temperature of the compound.

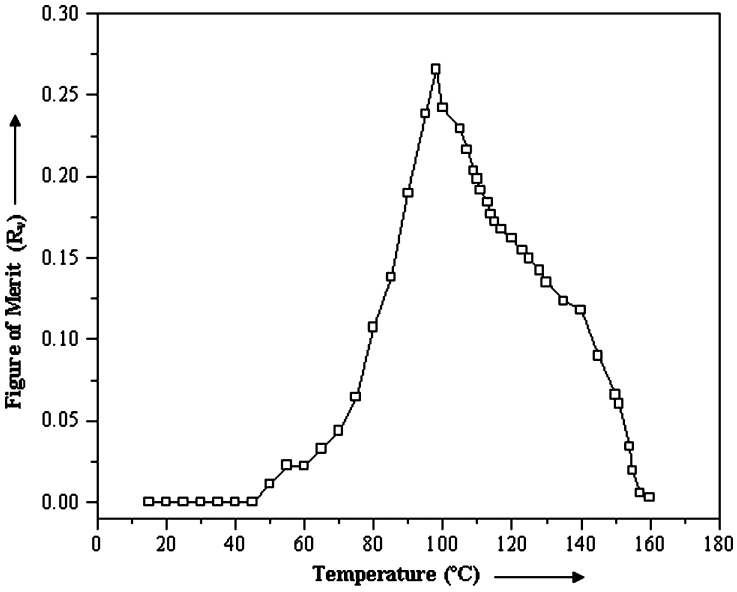

Figure 7. Variation of pyroelectric figure of merit (R_v) with temperature.

Conclusions

The synthesized BSTN compound is in single phase having an orthorhombic TB crystal structure. Grains of average size $\sim 2\ \mu$m are homogeneously distributed throughout the sample. The compound has a diffuse type of ferroelectric—paraelectric phase transition and it shows non-relaxor behaviour. The maximum pyroelectric coefficient (P_I) in this compound has been found to be 57.1 nC/cm$^2{}^\circ$C at around 98°C. The variation of pyroelectric coefficient with temperature confirms the diffuse phase transition in the compound.

References

1. R. R. Neurgaonkar, W. F. Hall, J. R. Oliver, W. W. Ho, and W. K. Cory, Tungsten bronze $Sr_{1-x}Ba_xNb_2O_6$, A case history of versatility. *Ferroelectrics* **87**, 167–179 (1998).
2. R. R. Neurgaonkar and W. K. Cory, Progress in photorefractive tungsten bronze crystals. *J. Opt. Soc. Amer.* **3**, 274–276 (1986).
3. D. Liu, Y. Li, S. Q. Huang, and X. Yao, Phase structure and dielectric properties of Bi_2O_3-ZnO-Nb_2O_5 based dielectric ceramics.*J. Amer. Ceram. Soc.* **76**, 2129–2132 (1986).
4. A. Panigrahi and N. K. Singh, Structural and electrical properties of $Ba_5RTi_3Nb_7O_{30}$[R = Eu, Gd] ceramics. *J. Mater. Sci. Lett.* **18**, 1579–1581 (1999).
5. R. P. Rao, S. K. Ghosh, and P. Koshy, Dielectric and ferroelectric properties of $Ba_3M_3Ti_5Nb_5O_{30}$ (M = Sm or Y) ceramics. *J. Mater. Sci. Mater. Electron.* **12**, 729–732 (2001).
6. P. B. Jasmieson, S. C. Abrahams, and L. Bernstein, Ferroelectric tungsten bronze type crystal structures.1.Barium Strontium Niobate $Ba_{0.27}Sr_{0.75}Nb_2O_{5.78}$. *J. Chem. Phys.* **48**, 5048–5057 (1965).
7. P. Koshy, L. P. Kumari, and M. T. Sebastian, Preparation, characterization and dielectric properties of $Ba_3Ln_3Ti_5Nb_5O_{30}$ (Ln = La, Nd) ceramics. *J. Mater. Sci. Mater. Electron.* **9**, 43–45 (1998).
8. Z. Y. Xu and X. M. Chen, Effects of Ca and Sr substitution on dielectric properties in $Ba_3Sm_3Ti_5Ta_5O_{30}$ ceramics. *J. Mater. Sci. Mater. Electron.* **11**, 219–223 (2000).
9. X. M. Chen and J. S. Yang, Dielectric characteristics of ceramics in BaO-Nd_2O_3-TiO_2-Ta_2O_5 system. *J. Eur. Ceram. Soc.* **19**, 139–142 (1999).
10. S. R. Shannigrahi, R. N. P. Choudhary, A. Kumar, and H. N. Acharya, Phase transition in $Ba_5RTi_3Nb_7O_{30}$(R = Dy, Sm) ferroelectric ceramics. *J. Phys. Chem. Solid.* **59**, 737–742 (1998).
11. R. Palai, R. N. P. Choudhary, and H. Stewari, Structural and dielectric properties of $Ba_4R_2Ti_4Nb_6O_{30}$ (R = Y, Sm and Dy) ferroelectric ceramics. *J. Phys. Chem. Solid.* **62**, 695–700 (2001).
12. X. H. Zheng and X. M. Chen, Dielectric ceramics with tungsten—bronze structure in the BaO-Nd_2O_3-TiO_2-Nb_2O_5system. *J. Mater. Res.* **17**, 1664–1670 (2002).
13. X. H. Zheng and X. M. Chen, Crystal structure and dielectric properties of ferroelectric ceramics in the BaO-Sm_2O_3-TiO_2-Nb_2O_5 system. *Solid State Comm.* **125**, 449–454 (2003).
14. P. V. Bijumon, V. Kohli, O. Prakash, M. R. Varma, and M. T. Sebastian, Dielectric properties of $Ba_5MTi_3A_7O_{30}$ [M = Ce, Pr, Nd, Sm, Gd, Dy and Bi; A = Nb, Ta] ceramics. *Mater. Sci. & Eng. B*. **113**, 13–18 (2004).
15. P. Ganguly, A. K. Jha, and K. L. Deori, Complex impedance studies of tungsten-bronze structured $Ba_5SmTi_3Nb_7O_{30}$ ferroelectric ceramics. *Solid State Comm.* **146**, 472–477 (2008).
16. P. Ganguly, A. K. Jha, and K. L. Deori, Enhancement of dielectric properties of optimization of sintering condition in tungsten-bronze structured $Ba_5SmTi_3Nb_7O_{30}$ ferroelectric ceramics. *J. Electroceram.* **22**, 257–262 (2009).
17. C. B. Roundy and R. L. Byer, Sensitive $LiTaO_3$ pyroelectric detector. *J. Appl. Phys.* **44**, 929–931 (1973).
18. C. Dong, Powder X: Windows-95 based program for powder X-ray diffraction data processing. *J. Appl. Cryst.* **32**, 838–838 (1999).

19. P. R. Das, R. N. P. Choudhary, and B.K. Samantray, Diffuse ferroelectric phase transition in $Na_2Pb_2Nd_2W_2Ti_4Nb_4O_{30}$ ceramic. *J. Alloys and Comp.* **448**, 32–37 (2008).
20. S. M. Pilgrim, A. E. Sutherland, and S. R. Winzer, Diffuseness as a useful parameter for relaxor ceramics. *J. Amer. Ceram. Soc.* **73**, 3122–3125 (1990).
21. R. Clarke and J. C. Burfoot, The diffuse phase transition in potassium strontium niobate. *Ferroelectrics* **8**, 505–506 (1974).
22. C. K. Suman, K. Prasad, and R. N. P. Choudhary, Complex impedance studies on tungsten-bronze electroceramic: $Pb_2Bi_3LaTi_5O_{18}$. *J. Mater. Sci.* **41**, 369–375 (2006).
23. C. K. Suman, K. Prasad, and R. N. P. Choudhary, Electrical properties of $Pb_2Bi_3NdTi_5O_{18}$ ceramic.*Mat. Chem. & Phys.* **82**, 140–144 (2003).
24. F. A. Kröger and H. J. Vink, Relations between the concentrations of imperfections in crystalline solids. *Solid State Phys.* **3**, 307–335 (1956).
25. V. Raghavan, Materials Science and Engineering. New Delhi: Prentice-Hall of India; 2004.
26. I. S. Zheludev, Physics of Crystalline Dielectrics, Electrical Dielectrics. New York: Plenum Press; 1971.
27. T. Friessnegg, S. Aggarwal, R. Ramesh, B. Nielsen, E. H. Poindexter, and D. J. Keeble, Vacancy formation in (Pb,La)(Zr,Ti)O_3 capacitors with oxygen deficiency and the effect on voltage offset. *Appl. Phys. Lett.* **77**, 127–129 (2000).
28. R. C. Buchanan, Ceramic Materials for Electronics: Processing, Properties and Applications. New York: Marcel Dekker Inc., 1986.
29. Y. Noguchi and M. Miyayama, Large remanant polarization of vanadium-doped $Bi_4Ti_3O_{12}$. *Appl. Phys. Lett.* **78**, 1903–1905 (2001).
30. A. Chen, Y. Zhi, and L. E. Cross, Oxygen-vacancy-related low-frequency dielectric relaxation and electrical conduction in Bi:$SrTiO_3$. *Phys. Rev. B.* **62**, 228–236 (2000).
31. S. B. Lang, Source Book of Pyroelectricity. New York: Gordan and Breach Science Publishers, 1974.
32. K. S. Rao, T. N. V. K. V. Prasad, A. S. V. Subrahmanyam, J. H. Lee, J. J. Kim, and S. H. Cho, Dielectric and pyroelectric properties of BSNN ceramics: effect of Ba/Sr ratio and La_2O_3 addition. *Mat. Sci & Engg. B.* **98**, 279–285 (2003).
33. K. Uchino, Ferroelectric Devices. New York: Marcel Dekker Inc., 2000.
34. B. M. Jin, S. Erdei, and A. S. Bhalla, Pyroelectric measurements on various kinds of doped TGS single crystals. Proceedings of the Ninth IEEE International Symposium on Applications of Ferroelectrics. 825–828 (1994).

About the Author

The author received his B. Sc. (Hons.) Physics and M. Sc. (Physics) with specialization in Condensed Matter Physics from University of Delhi, Delhi. He cleared the National Eligibility Test (NET) for lectureship conducted by Council of Scientific and Industrial Research (CSIR) and University Grants Commission (UGC). He is presently a Senior Research Fellow of CSIR. He has also worked as a CSIR - Research Intern in National Physical Laboratory, Delhi.